TUM School of Natural Sciences
Technische Universität München

Polar Intermetallic Fe/Co/Ni-rich Germanides and Silicides: Synthesis and Characterization

Thomas Braun, M.Sc.

Vollständiger Abdruck der von der TUM School of Natural Sciences der Technischen Universität München zur Erlangung des akademischen Grades eines

Doktors der Naturwissenschaften (Dr. rer. nat.)

genehmigten Dissertation.

Vorsitzende(r):	Prof. Dr. Hubert A. Gasteiger
Prüfer der Dissertation:	
	1. Prof. Dr. Thomas F. Fässler
	2. Prof. Dr. Tom Nilges

Die Dissertation wurde am 12.10.2022 bei der Technischen Universität München eingereicht und durch die TUM School of Natural Sciences am 15.11.2022 angenommen.

"Der Zauber steckt immer im Detail."

Theodor Fontane

Danksagung

Zuallererst möchte ich mich bei meinem Doktorvater *Professor Dr. Thomas F. Fässler* und meinem Mentor *Dr. Viktor Hlukhyy* bedanken, die es mir ermöglicht haben, diese Dissertation anzufertigen. Ich habe mich am Lehrstuhl immer Willkommen gefühlt und zusammen mit Viktor eine eigene Nachwuchsgruppe zu bilden, war sehr spannend. Vielen Dank für das interessante Forschungsthema, das mir entgegengebrachte Vertrauen, die Unterstützung und Geduld.

Darüber hinaus gibt es noch weitere Personen, die mir während der Promotion zur Seite standen:

Hervorzuheben sind dabei *Manuela Donaubauer*, die als Lehrstuhlsekretärin immer verfügbar war und bei organisatorischen Fragen stets hilfsbereit war und *Maria Müller*, die sozusagen als Mädchen für alles immer bereit war zu helfen. Maria hat mich sehr dabei unterstützt, das MPMS SQUID Magnetometer wöchentlich mit flüssigem Helium zu füllen und hat darüber hinaus Messungen von DTA und EDX Proben durchgeführt.

Wilhelm Klein für die Unterstützung beim Messen von Einkristallen an der Drehanode sowie beim Einkauf von Milch und Kaffee für die Kaffeekasse.

Marina Boyko, die mich im Umgang mit dem MPMS eingewiesen hat und *Ralf Stehle* für die Hilfe und Erklärungen in Bezug auf Helium-Kannen und die Heliumrückführung zum WMI.

Oksana Storcheva für die Organisation und Hilfe der Saalpraktika, die ich im Rahmen meiner Lehrtätigkeit betreuen durfte. In diesem Zusammenhang auch die technischen Mitarbeiter *Richard Wetzel*, *Sara Garofalo*, *Thomas Miller* und *Tobias Kubo*, die stets hilfsbereit waren und viel Humor mitbrachten.

Sabine Zeitz, *Ingrid Werner* †, *Philipp Keil* und *Laura A. Jantke* für die angenehme Zeit als Bürokollegen. Sabine danke ich auch für die schönen Filmabende, die mich tiefer in den Marvel Kosmos eingeführt haben.

Clara Berg, *David Henseler*, *Maximilian Huber*, *Clemens Kaußler*, *Alfred Rabenbauer*, *Annika Schulz*, *Dardan Ukaj*, *Sabine Zeitz*, die bei mir Forschungspraktika und/oder Bachelorarbeiten durchgeführt haben.

Alle übrigen Kolleginnen und Kollegen, mit denen ich am Lehrstuhl zusammenarbeiten durfte: *Alex, Annette, Anton, Benedikt, Christian, Christina, Christopher, David M, Dominik, Elke, Felix, Frank, Henrik, Irina, Jan, Jasmin, Jingwen, Kevin, Kerstin, Lavinia, Lorenz, Manuel, Michael, Nicole, Sabine F., Samuel, Sebastian, Stefan, Tassilo, Terrance, Thomas W., Vincent, Yasmin.*

Prof. Dr. Tom Nilges und seiner Arbeitsgruppe für die Zusammenarbeit und der gemeinsamen Nutzung von Laborgeräten. Seiner Mitarbeiterin *Anna Vogel* für das Messen von Thermoelektrischen Eigenschaften.

Prof. Antti Karttunen für die Rechnungen an Pentakisdodekaedern für die Struktur in $BaNi_{16}Si_{12}$.

Ich danke meinen Freunden, die mir in meiner Freizeit Gesellschaft geleistet und so mein Leben bereichert haben. Meine Kommilitonen *Matthias Edelmann, Alexander Jussupow, Michael Wiedemann, Sebastian Wienhold und Theresa Zach*, die mich durch das Studium begleitet haben.

Meiner Familie danke ich für den Rückhalt, die Familienfeiern und Reisen.

Mein größter Dank gebührt meinen Eltern, die mich immer unterstützt haben und für mich da waren. Ohne sie wäre ich heute nicht derselbe Mensch und nicht da, wo ich heute bin.

Abstract

In this work the phase systems $Ae - T - X$ with Ae = Mg, Ca, Sr, Ba, T = Fe, Co, Ni and X = Si, Ge were investigated. The main objective was to find new compounds with chains, layers or framework of transition metal atoms. These are considered as potential candidates towards superconductivity. Compositions of known related compounds were attempted with new element combinations. Synthesis was done from the elements in different kinds of high temperature furnaces. Arc melting, inductive heating and resistive heating was used, keeping the reagents under inert argon atmosphere. In some cases the elements or reaction products were activated using a ball mill for further reaction. Both, single crystal and powder X-ray diffraction methods were used to investigate the crystal structure of new compounds. Composition of single crystals were validated using energy dispersive X-ray spectroscopy in combination with scanning electron microscopy (SEM-EDX). Thermal stability and (reversible) phase transitions were checked with differential thermal analysis (DTA). Magnetic properties and testing for superconductivity were performed with a magnetometer, using a superconducting quantum-interference device (SQUID) as sensor.

For new compounds, electronic structure calculations were performed using TB-LMTO-ASA method, to obtain Band Structure, Density of States (DOS), Crystal Orbital Hamilton Population (COHP) and Electron Localization Function (ELF).

The first part of this thesis deals with layered compounds, where the transition metal atoms are arranged in layers within a polyanionic network. The following compounds and solid solutions were investigated: $CaFe_2Ge_2$, $SrNi_2Si_2$, $Sr_{1-x}Ca_xCo_2Ge_2$, $Sr_{1-x}Ba_xCo_2Ge_2$, $Y_{1-x}Ca_xFe_2Ge_2$, $CaFe_{2-x}Co_xGe_2$, $Ca_{1-x}Co_6Ge_6$, $CaFe_6Ge_6$, SrNiSi, $SrNi_2Si$ and $BaNi_2Si$. The 122-family based on the $ThCr_2Si_2$-type was of special interest because many of its members were found to be superconducting under certain conditions. Attempts were made to find new materials with this physical property. For $Ca_{1-x}Co_6Ge_6$ and $CaFe_6Ge_6$, different superstructures were found, where channels are filled either randomly or with certain order. SrNiSi makes a very rare structure within the 111-family and was found with two different stacking variants.

The second part deals with those compounds that were accidentally found, with transition metal atoms being incorporated all over the three-dimensional network. After identification of the composition, synthesis with corresponding stoichiometry was done to obtain them as main phase for characterization. Following compounds were discovered: $BaNi_{16}Si_{12}$, $SrNi_5Si_3$, $CaCo_{8.8}Si_{4.2}$, $SrNi_{9.3}Ge_{3.7}$, $Mg_6Co_{15.6}Si_{7.4}$, $Mg_6Co_{16}Ge_7$ and Laves phase $MgCo_{2-x}Ge_x$. Very interesting is the structure of $BaNi_{16}Si_{12}$ that contains catalan pentakis dodecahedra as coordination polyhedra with the highest coordination number among intermetallic compounds. Such polyhedron has never been observed before among intermetallic compounds and only been modeled on theoretical level.

Zusammenfassung

In dieser Arbeit wurden Phasen in den Systemen $Ae - T - X$ mit Ae = Mg, Ca, Sr, Ba, T = Fe, Co, Ni und X = Si, Ge untersucht. Die Hauptaufgabe war das auffinden von neuen Verbindungen mit Ketten, Schichten oder Netzwerken aus Übergangmetallatomen. Diese werden als potentielle Kandidaten für die Supraleitung angesehen. Unterschiedliche Zusammensetzungen von ähnlichen bekannten Verbindungen wurden mit neuen Kombinationen von Elementen ausprobiert. Die Synthesen wurden aus den Elementen in verschiedenen Arten von Hochtemperaturöfen durchgeführt. Diese sind Lichtbogenschmelzen, induktives Erhitzen und Widerstandsheizung, wobei die Reagenzien unter inerter Argonatmosphäre gehalten wurden. In manchen Fällen mussten die Elemente oder Reaktionsprodukte mittels Kugelmühle aktiviert werden, um die weitere Reaktion zu ermöglichen. Sowohl Einkristall- als auch Pulver-Röntgendiffraktometrie wurden eingesetzt, um die Kristallstruktur von neuen Verbindungen zu untersuchen. Die Zusammensetzung der Einkristalle wurde mittels energiedispersiver Röntgenspektroskopie in Verbindung mit einem Rasterelektronenmikroskop validiert (SEM-EDX). Mittels Differenzthermoanalyse (DTA) wurden die Temperaturbeständigkeit und (reversible) Phasenübergange untersucht. Magnetische Eigenschaften und Tests auf Supraleitfähigkeit wurden mit einem Magnetometer durchgeführt, das ein supraleitendes Quanteninterferenzgerät (SQUID) als Sensor nutzt.

Für neue Verbindungen wurden elektronische Eigenschaften unter Nutzung der TB-LMTO-ASA Methode berechnet, um die Bandstruktur, Zustandsdichte (DOS), Hamilton Population im Kristallorbital (COHP) und die lokalisierte Elektronen-Lokalisierung-Funktion (ELF) zu erhalten.

Der erste Teil Arbeit befasst sich mit schichtartigen Strukturen, wo die Übergangsmetallatome innerhalb eines polyanionischen Netzwerks in Schichten angeordnet sind. Die folgenden Verbindungen und festen Lösungen wurden untersucht: $CaFe_2Ge_2$, $SrNi_2Si_2$, $Sr_{1-x}Ca_xCo_2Ge_2$, $Sr_{1-x}Ba_xCo_2Ge_2$, $Y_{1-x}Ca_xFe_2Ge_2$, $CaFe_{2-\mathrm{x}}Co_\mathrm{x}Ge_2$, $Ca_{1-\mathrm{x}}$ Co_6Ge_6, $CaFe_6Ge_6$, SrNiSi, $SrNi_2Si$ und $BaNi_2Si$. Die 122-Strukturfamilie, basierend auf dem $ThCr_2Si_2$-Typ war von besonderem Interesse, da einige ihrer Vertreter unter bestimmten Bedingungen supraleitend sind. Versuche wurden unternommen, neue Materialien mit dieser physikalischen Eigenschaft zu finden. Für $Ca_{1-x}Co_6Ge_6$ und $CaFe_6Ge_6$ wurden unterschiedliche Überstrukturen beobachtet, in denen die Kanäle entweder willkürlich oder nach bestimmten Ordnungsschema besetzt sind. SrNiSi bildet eine sehr seltene Struktur innerhalb der 111-Familie aus und wurde mit zwei verschiedenen Stapelungsvarianten entdeckt.

Der zweite Teil behandelt Verbindungen, die zufällig entdeckt wurden und bei denen die Übergangsmetallatome am gesamten dreidimensionalen Netzwerk beteiligt sind. Nach ihrer Identifizierung und dem Bestimmen der Zusammensetzung wurde die Synthese mit entsprechender Stöchiometrie der Elemente durchgeführt, um sie als Hauptphase zu erhalten und diese zu untersuchen. Folgende Verbindungen wurden gefunden: $BaNi_{16}Si_{12}$, $SrNi_5Si_3$, $CaCo_{8.8}Si_{4.2}$, $SrNi_{9.3}Ge_{3.7}$, $Mg_6Co_{15.6}Si_{7.4}$, $Mg_6Co_{16}Ge_7$ und die Laves Phase $MgCo_{2-x}Ge_x$. Besonders spannend ist die Verbindung $BaNi_{16}Si_{12}$, die Catalanische Pentakisdodekaeder als Koordinationspolyeder enthält, das die höchste Koordinationszahl unter den intermetallischen Verbindungen besitzt. Solch ein Polyeder wurde noch nie in intermetallischen Verbindungen nachgewiesen und existiert nur auf Basis theoretischer Modellrechnungen.

Declaration

This work has been written as publication-based thesis. Peer-reviewed articles published in journals as well as supporting information and manuscripts are provided in chapter 5, contribution of co-authors is given in table 2.2. Chapter 1 contains some introduction and literature about the topic and deals with the relevance, scope and outline of this work. Chapter 2 summarizes experimental and computational methods used to synthesize and characterize investigated compounds. Results are presented and discussed in chapter 3 and a conclusion is provided in chapter 4.

Nomenclature

ABS	automated background subtraction
AF	arc furnace
ASA	atomic-sphere approximation
bcc	body centered cubic
ccp	cubic close packed
CN	coordination number
COHP	crystal orbital Hamilton population
iCOHP	integrated crystal orbital Hamilton population
cT	collapsed tetragonal
DOS	density of states
iDOS	integrated density of states
pDOS	projected density of states
DTA	differential thermal analysis
EDX	energy dispersive X-ray spectroscopy
ELF	electron localization function
EN	electronegativity
FC	field-cooled
hcp	hexagonal close packed
HFF	high frequency furnace
HTS	high temperature superconductor
IF	induction furnace
LDA	local density approximation
LMTO	linear muffin tin orbital
RF	resistance furnace
SEM	scanning electron microscope
SQUID	superconducting quantum-interference device
TB	tight-binding
tcp	tetrahedrally close packed

VEC	valence electron concentration
XRD	X-ray diffraction
PXRD	powder X-ray diffraction
SXRD	single crystal X-ray diffraction
ZFC	zero-field-cooled

Contents

List of Tables

List of Figures

1 Introduction

1.1 Atomic Arrangement in Inorganic Solids

Elemental metals are known to commonly form solids with a regular ordered arrangement of close (bcc = body centered cubic; $CN = 8 + 6$) or closest (ccp = cubic close packed or hcp = hexagonal close packed; $CN = 12$) packed atoms. This leads to maximization of nearest neighbors and a high coordination number (CN); electrons are shared isotropically and are delocalized (historically called *electron gas*). Nonmetals forge covalent bonds, sharing electrons between distinct atoms with typical angles about 90°, 109.5°, 120° or 180°. These bonds are directed and therefore anisotropic. Since for close packed structures all angles are 60°, atomic arrangement must be different and peculiar structures are formed with larger gaps between atoms. The structures are a geometrical compromise between many weaker contacts (coordination) and fewer strong contacts (bonding).

In materials containing different elements, difference in electronegativity (EN), atomic radii and valence electron concentration (VEC) have impact on the accomplished structure. A simple classification is done by the van Arkel-Ketelaar triangle [1]. It distinguishes between metallic (ΔEN and ΣEN small), covalent (ΔEN small, ΣEN large) and ionic interactions (ΔEN large, ΣEN medium). This works well for mixed metals, simple salts, compounds of group 13 to 17 and Zintl phases. However, this classical view does not describe the situation in intermetallics composed of several metals. Already for binary systems, there are examples where different kinds of bonding occurs, e.g. in the K–Pb-system. KPb and K_4Pb_9 are Zintl phases with single bonds or deltahedral clusters and shared skeletal electrons. KPb_2 (= K_4Pb_8), which has close composition to K_4Pb_9, however, forms an intermetallic Laves phase [2]. There have been arguments in the past century whether intermetallic phases may be called compounds, which assumes a stoichiometrically sharp composition. Eduard Zintl's work provided a lot of research in this field [3].

1.1.1 Alloys and Phases

Mixtures of a metal with other elements are generally called alloys, when the material maintains its metallic properties. It is not specified how these elements mix with each other [4]. On the one hand there are heterogeneous materials, where domains of different composition are present (e.g. iron-carbon-alloys). These domains can be embedded as grains in a matrix of the main component metal, where the secondary elements precipitate [5]. On the other hand, homogeneous phases with an equal distribution throughout the solid may occur. Thus, an alloy can also exhibit different phases that coexist in the solid.

1.1.2 Compounds and Solid Solutions

Starting with the structure of a metal A and partially substituting it with another metal B, $A_{1-x}B_x$-mixtures can be obtained. If the atoms of B randomly replace atoms of A without changing the structure, it is called a solid solution. In many cases, however, a regular pattern forms, where the distribution of A and B follows a specific order. These can be coloring variants of parent structures or completely new structure types. Hume-Rothery [6] investigated many intermetallic phases and found a dependence of formed structures on the valence electron concentration. For the example of brass, the composition of copper and zinc separates the series $\mathrm{Cu}_{1-x}\mathrm{Zn}_x$ into several regions. Each makes its own structural phase. Some phases have composition close to stoichiometric compounds, e.g. CuZn, $\mathrm{Cu_5Zn_8}$ or $\mathrm{CuZn_3}$, however, they show a phase width and are not sharp. Hume-Rothery observed limitations to solid solutions that are described by some rules, named after him [7]: (1) the atomic radius of the solute may not differ more than 15% to the host atom; (2) crystal structures of solute and solvent must be similar; (3) best solubility occurs for atoms with same valency; atoms of higher valency prefer a solvent of lower valency; (4) electronegativity of both species has to be similar, a large difference leads to formation of intermetallic compounds. In contrast to solutions, these compounds have a defined composition with no or very small homogeneity range. They show as sharp lines in the phase diagram, e.g. CoSn and $\mathrm{Co_2Sn}$ in Co–Sn-system [5].

1.1.3 Structure and Bonding in Intermetallic Compounds

In intermetallic compounds the structural arrangement depends on sterical as well as electronical factors. In contrast to simple cubic or hexagonal close packed metals, a compound with atoms of difference size requires a more complex structure to gain the best compromise of optimized volume and maximized atomic contacts. Frank and Kasper [8] determined polyhedra with coordination numbers 12, 14, 15 and 16 that only contain triangular faces. The basic principle is to avoid octahedral voids that are larger in size than tetrahedral voids. These compounds are therefore called tetrahedrally close packed (TCP). All faces have to be triangular as a quadrangular face represents the cross-section of an octahedral void. For structures with very differently sized atoms, pseudo Frank-Kasper phases with polyhedra of even larger coordination numbers can be achieved [9]. Important TCP structures are e.g. Laves phases, $CaCu_5$-type [10] and $NaZn_{13}$-type [11]. Besides packing effects also electronical effects are important for intermetallic structures [12]. Atomic distances can be considerably shorter than the sum of the atomic radii when bonding interactions take place. The presence of atoms with different electronegativity leads to coexisting ionic, metallic and covalent interactions. This type of compounds is called *polar intermetallic phases*, however, that term is still controversial [13]. It is not clear defined whether electropositive elements like alkaline, alkaline earth or rare earth metals must be present. These exhibit cationic character, their electrons are transferred to the more electronegative species X. Similar to Zintl phases, the additional electrons cause changes to the X-substructure [3]. Intermetallic compounds cover a broad range and the transition from valence compounds to intermetallics is not sharp [2, 12, 14]. In polar intermetallic compounds with more than two elements, combination of electropositive main group, early transition metal or rare earth metal together with a late transition metal and semi-metal is possible. The obtained structures vary from quite simple to highly complex. Very versatile are nickel-based compounds, e.g. $MgNi_{2-x}Ge_x$ that adopts the structure of cubic Laves phase $MgCu_2$ for small x (small VEC) and ordered superstructures of $MgCu_2$ or $MgZn_2$ with increasing VEC [15]. A complex example is $Ca_{15}Ni_{68}Ge_{37}$ with a large unit cell that contains 120 atoms and combines different structural motifs of simple binary/ternary compounds [16]. Compounds with d-metal substructures are not only topologically interesting but also exhibit considerable physical properties. Among these are magnetic ordering and superconductivity, that are covered in section 1.2.

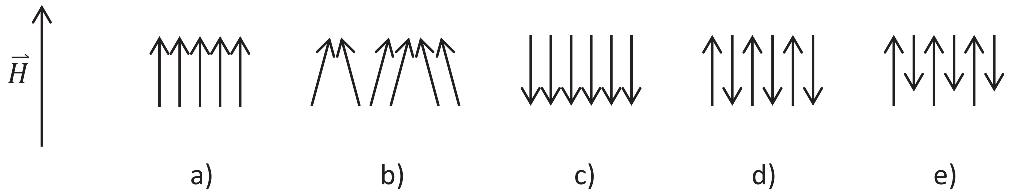

Figure 1.1: Schematic representation of different types of magnetism in an external magnetic field $\vec{H}$. a) ferromagnetism, b) paramagnetism, c) diamagnetism, d) antiferromagnetism and e) ferrimagnetism. Arrows are magnetic moments that sum up to the total magnetization.

1.2 Magnetism and Superconductivity

1.2.1 Fundamental Properties

Intermetallic compounds are of interest to physicists due to their versatile magnetic properties. Especially with rare earth elements, numerous experiments were reported, investigating effects like permanent magnets, heavy fermions, Kondo lattices, valence fluctuations, magnetostriction, spin glass behavior and random anisotropy [17]. All effects are based on the order of atomic magnetic moments with or without an external magnetic field. Some are related to the reaction of magnetism with changing field and/or temperature. For crystalline materials with unique directions, an anisotropic response can be observed. At a stable temperature and field, different magnetic responses are possible (fig. 1.1):

- ferromagnetic, with all magnetic moments orientated parallel to an external field
- paramagnetic, with non-maximal alignment, the degree is linear to the field strength
- diamagnetic, with an anti-parallel alignment to the magnetic field, similar to paramagnetism with negative sign
- anti-ferromagnetic, with paired spins, that cancel out each other
- ferrimagnetic, which is a derived from an anti-ferromagnetic order with unequal spins. A reduced momentum remains that behaves paramagnetically

Magnetization M in dependence of an external field H depends on the magnetic susceptibility χ of a compound, as shown in eq. (1.1). Susceptibility is commonly expressed as molar susceptibility (eq. (1.2)). In a solid compound different types of magnetism are present that sum up to the total susceptibility. These are in general diamagnetic contributions of paired electrons and paramagnetic contributions of unpaired spins. Also different magnetic substructures may coexist and terms of eq. (1.3) can be further subdivided.

$$M = \chi \cdot H \tag{1.1}$$

$$\chi_\mathrm{m} = \chi \cdot \frac{m}{MW} \tag{1.2}$$

$$\chi = \chi_\mathrm{dia} + \chi_\mathrm{para} \tag{1.3}$$

All compounds have diamagnetic contribution of core electrons. Its value can be estimated via molar weight MW using eq. (1.4) [18].

$$\chi_\mathrm{dia} = -\frac{MW}{2} 10^{-6}\,\mathrm{emu\,mol^{-1}} \tag{1.4}$$

In metals, delocalized electrons can create temperature-independent Pauli-paramagnetism but also temperature-dependent Curie-paramagnetism. The latter changes to ferro- or antiferromagnetism below a certain specific temperature and is explained in more detail in section 1.2.2

1.2.2 Magnetic Transitions

A temperature-dependent change of magnetic behaviour is well known for Curie-paramagnetism. Above a specific Curie temperature T_C, paramagnetism is observed, whereas below this temperature, ferromagnetic order establishes. In the paramagnetic region, reciprocal magnetic susceptibility is directly proportional to temperature, which is described by the Curie-Weiss-law (eq. (1.5)). The Curie constant C is determined by Avogadro constant N_A, Boltzmann constant k_B and magnetic moment μ of a particle. Θ is called Weiss constant and is positive, negative or zero.

$$\chi_\mathrm{m} = \frac{C}{T - \Theta} \quad \text{with} \quad C = \frac{N_\mathrm{A} \cdot \mu^2}{3k_\mathrm{B}} \tag{1.5}$$

The Weiss constant can be derived by fitting the reciprocal susceptibility at high temperatures and extrapolation to $y = 0$, as shown in fig. 1.2a. A value of zero means the sample is Curie paramagnetic. A positive value shows ferro- or ferrimagnetism below this temperature. In literature this temperature is often

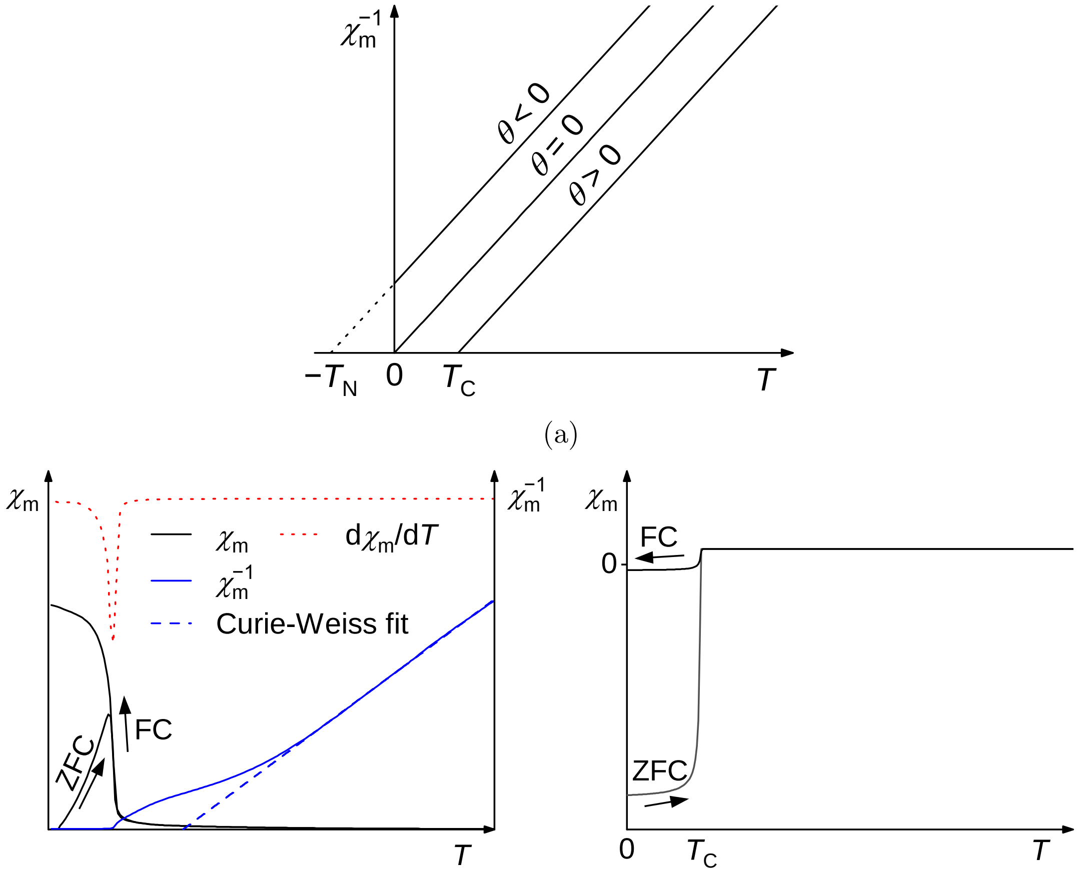

(a)

(b)

(c)

Figure 1.2: (a) Different types of paramagnetism following the Curie-Weiss law. $\theta = 0$ represents ideal Curie-paramagnetism. T_C is the Curie temperature of a ferromagnet and T_N an estimate of the Néel temperature of an antiferromagnet. (b) Example of ferromagnetism with spin freezing at low temperatures (black line), showing the difference between zero-field-cooled (ZFC) and field-cooled (FC) magnetic susceptibility. The freezing temperature T_f at the deflection point appears as extremum in the derivative (red line). The Curie-Weiss fit (blue line) illustrates that T_f and θ may be at different temperatures. (c) Schematic change in susceptibility below superconducting transition temperature T_C (not confuse with Curie temperature).

called Curie temperature T_C, which is the transition temperature to paramagnetic state. For negative Θ-values, samples are antiferromagnetic below the so-called Néel temperature T_N, which is the absolute value of the intersection between fit and x-axis. Below a certain freezing temperature T_f magnetic moments of individual crystallites are locked in random directions, when cooling in zero-field (zero-field-cooled, ZFC) [19, 20]. By cooling with applied field (field-cooled), all moments are aligned and show a higher value. The difference is related to the coercivity [20]. Figure 1.2b shows an example with diverging ZFC and FC scans and corresponding Curie-Weiss plot of the FC scan. It illustrates that the freezing temperature T_f, which can be determined from the first derivative of FC curve, can be at a lower temperature than the intersection of the Curie-Weiss-fit with the x-axis [21]. These are ferromagnetic Curie temperature T_C and paramagnetic Curie temperature θ_p, which represent the transition temperatures for short- and long-range order, respectively.

T_C is also used to describe critical temperatures of superconductors, below which a material enters a state with no electrical resistivity and may not be mistaken as Curie temperature. In a superconducting phase magnetic fields are expelled from the bulk, which is called Meissner–Ochsenfeld effect and can be seen in magnetic measurements by a sudden drop in susceptibility to negative values. A schematic measurement is given in fig. 1.2c. Classical type-I superconductors can be explained with formation of Cooper pairs. Two electrons form a quasi particle with total spin of zero, allowing them to behave like bosons. As a result, Bose-Einstein condensation is possible which does not follow the Pauli exclusion principle of fermions. In this state, all electrons occupy the same quantum state. The BCS model developed by Bardeen, Cooper and Schrieffer works well for low temperatures and describes a phonon-mediated mechanism. However, this model fails at temperatures above 30 K because too much thermal agitation separates the cooper pairs. Also type-I superconductivity is suppressed above a critical magnetic field H_C. However, most intermetallic superconductors are of type-II. These possess two critical field strengths $H_{C,1}$ and $H_{C,2}$ where the Shubnikov phase is formed, a mixed state with the superconducting state being penetrated by flux tubes. Moreover type-II superconductors can reach temperatures far above the BCS limit [22, 23]. Theories and models to calculate and predict critical temperatures for these high temperature superconductors (HTS) are still discussed controversially and are tackled e.g. with machine learning [24].

In compounds such as $Ba_{1-x}K_xFe_2As_2$, a reversible phase transition from tetragonal to orthorhombic structure is accompanied by a change of magnetic ordering [25, 26].

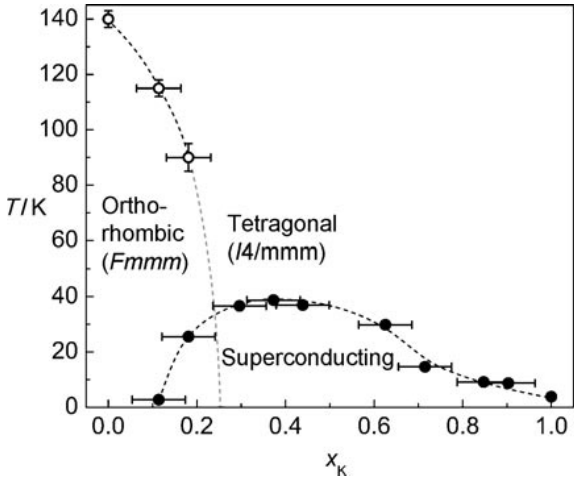

Figure 1.3: Phase diagram of $Ba_{1-x}K_xFe_2As_2$ that shows structural (open symbol) and critical (filled symbol) phase transition temperatures with dependence on the degree of substitution x [25].

The transition temperatures are composition-dependent and while partial substitution suppresses the magneto-structural transition, superconductivity emerges. This is illustrated in fig. 1.3. Intermetallic compounds with reversible structural transition are therefore of interest in search for new superconductors.

Known high temperature superconductors (HTS) generally have some disadvantages towards application [27]. Cuprates that are already superconducting when cooled with liquid nitrogen are hard and brittle and cannot be fabricated into wires easily. Other compounds that work best under high pressure, cannot be handled practically. Thus while room temperature superconductivity was observed for a carbon-hydrogen-sulfur system above 260 GPa [28], intermetallic compounds are still interesting materials for further investigation. The classic superconductor Nb_3Sn ($T_C = 18\,K$, discovered in 1954) is still popular in application, e.g. for NMR and MRI instruments [29–31].

1.2.3 Layered Superconductors

Compounds of very different structure and nature were found to be superconductors at low temperatures. Many of them have been attributed to the class of layered superconductors [32]. Among these are graphite intercalation compounds, (intercalated) transition metal dichalcogenides, cuprates, AlB_2-type, $ThCr_2Si_2$-type and related compounds. Even some layered organic materials show superconductivity.

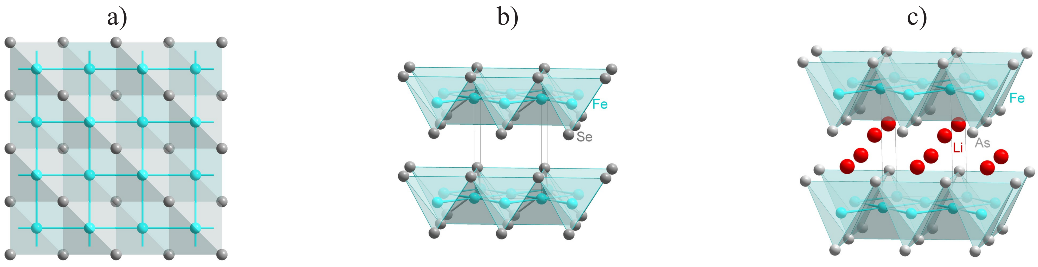

11: anti-PbO-type

111: CeFeSi-type

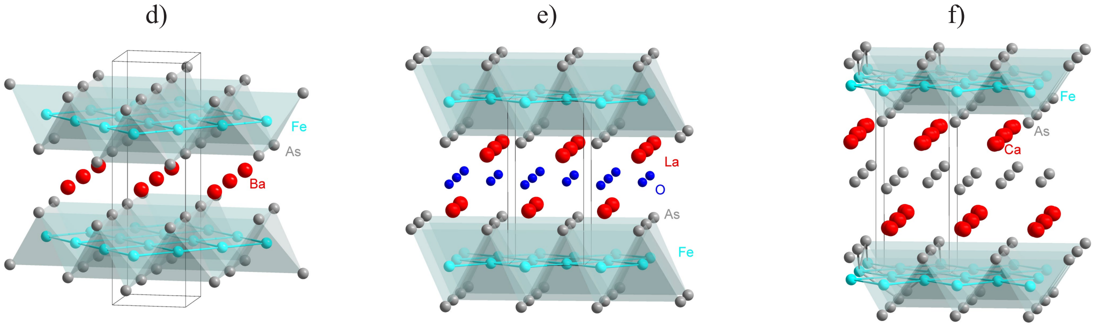

122: $ThCr_2Si_2$-type

1111: CuZrSiAs-type

112: $Ca_{0.79}La_{0.21}FeAs_2$-type

Figure 1.4: Selected intermetallic iron pnictide and chalcogenide superconductors of different structure types. a) Common structure motif of iron square lattice, each transition metal atom is tetrahedrally coordinated by p-element atoms. b) FeSe [33], c) LiFeAs [34], d) $Ba_{0.6}K_{0.4}Fe_2As_2$ [35], e) $LaO_{0.89}F_{0.11}FeAs$ [36], f) $Ca_{0.79}La_{0.21}FeAs_2$ [37]. They represent the classes 11, 111, 122, 1111 and 112, respectively. Iron is is drawn in cyan, electropositive metals in red and p-elements in grey, oxygen in blue.

One very intensively investigated class of superconductors are iron pnictides and chalcogenides [38–40]. They have a common structural motif, shown in fig. 1.4a: a square planar iron layer with each atom being tetrahedrally coordinated by the p-block element. By intercalation of other elements between these layers, various structure types have been obtained. Some examples are shown in fig. 1.4b–f. FeSe ($T_C = 8\,K$ [33]), LiFeAs ($T_C = 18\,K$, [34]), $Ba_{0.6}K_{0.4}Fe_2As_2$ ($T_C = 38\,K$ [35]), $LaO_{0.89}F_{0.11}FeAs$ ($T_C = 26\,K$ [36]) and $Ca_{0.79}La_{0.21}FeAs_2$ ($T_C = 45\,K$ [37]). They represent the classes 11, 111, 122, 1111 and 112, respectively. Research has shown, that in these systems superconductivity is not limited to iron as transition metal and pnictogenides or chalcogenides as p-element. For instance $SrNi_2P_2$ with $T_C = 1.4\,K$ [41], YFe_2Ge_2 with $T_C = 1.8\,K$ [42] and $SrNi_2Ge_2$ with $T_C = 0.9\,K$ [43] were reported. Besides compounds with square quadratic nets, there are also other intermetallics with superconducting properties, that contain hexagonal substructures. Laves phase Mg_2Ir_3Si ($T_C = 3.8\,K$ [44]) and $CaCu_5$-derivative $LaRu_3Si_2$ ($T_C = 7.8\,K$ [45]) contain a Kagomé-lattice of transition metal. AlB_2-type $SrNi_{0.3}Si_{2-x}$ ($T_C = 7.8\,K$ [46]) and $FePSe_3$ ($T_C = 5.5\,K$ at 30 GPa [47]) make a hexagonal honeycomb-lattice.

1.3 Scope and Outline of This Work

Motivation of this thesis was to find novel polar intermetallic compounds, based on iron, cobalt or nickel, that contain chains, layers or networks of transition metal. Inspired by various results on iron pnictides and structurally related compounds, these materials are considered as potential superconductors. This work focused on a search fo new $Ae - T - X$ compounds with electropositive Ae = Mg, Ca, Sr, Ba, transition metals T = Fe, Co or Ni and tetrelides X = Si, Ge. For substitution experiments, adjacent elements in the periodic table like phosphorus or yttrium were used. Compositions were chosen in the earth alkaline poorer region with at least a third atom-% of transition metal, where samples are expected to be metallic. Of special interest were structures that contain one-, two- or three-dimensionally infinite T-substructures, that may be suitable as parent compounds for new superconducting materials.

Experimental methods and procedures that were used for synthesis and characterization are described in chapter 2. This includes computational methods to calculate band structure, density of states, crystal orbital Hamilton population and electron localization function. Samples were prepared starting from the elements by applying high temperatures (typically from 800 °C to 3000 °C). Phase analysis was performed using powder X-ray based diffraction methods. Thermal stability was investigated by differential thermal analysis and magnetic properties were measured with a SQUID system.

All compounds discovered within this thesis are collected in section 3.1, drawn into a comprehensive ternary composition triangle. In many cases, existing structures were obtained with new combination of elements. For SrNiSi (section 3.2.1.3) and $BaNi_{16}Si_{12}$ (section 3.3.3) new unique structure types were discovered. In section 3.2 all investigated structures are discussed that exhibit a two-dimensional arrangement of transition metals, forming layers within the polyanionic network. $CaFe_2Ge_2$ and $SrNi_2Si_2$ as new members of $ThCr_2Si_2$-type structure family are reported as well as related experiments with solid solutions. Structures of $Ca_{1-x}Co_6Ge_6$ and $CaFe_6Ge_6$

show multiple order variants, either disordered or forming superstructures with long-range order. SrNiSi exists with two stacking variants of a peculiar planar Ni–Si-layer. $SrNi_2Si$ and $BaNi_2Si$ represent another type of layered structure, that are not flat, but corrugated. Section 3.3 deals with all other compounds, that contain networks with transition metal contribution in all three dimensions. These are cobalt germanides $MgCo_{2-x}Ge_x$ and $Mg_6Co_{16}Ge_7$, cobalt silicides $CaCo_{8.79(1)}Si_{4.21}$ and nickel silicides $SrNi_5Si_3$, $SrNi_{9.26(9)}Si_{3.74}$ and $BaNi_{16}Si_{12}$. The last one marks two records with respect to the amount of alkaline earth atoms and the size of coordination polyhedra.

A conclusion is given in chapter 4. Publications and manuscripts are included in chapter 5, they contain information on experiments and discussion of results. A complete list of all publications and manuscripts in preparation is given in chapter 6

References

[1] T. L. Meek, L. D. Garner, *Journal of Chemical Education* **2005**, *82*, 325, DOI `10.1021/ed082p325`.

[2] T. F. Fässler, S. Hoffmann, *Zeitschrift für Kristallographie - Crystalline Materials* **1999**, *214*, DOI `10.1524/zkri.1999.214.11.722`.

[3] H. Schäfer, *Annual Review of Materials Science* **1985**, *15*, 1–42, DOI `10.1146/annurev.ms.15.080185.000245`.

[4] *Lexikon der Physik, Gesamtausgabe in 5 Bänden + 1 Registerband*, (Eds.: U. Kilian, C. Weber, W. Greulich), Spektrum Akademischer Verlag, Heidelberg, **2000**.

[5] R. Pöttgen, D. Johrendt, *Intermetallics, Synthesis, structure, function*, 2nd edition, De Gruyter, Berlin and Boston, **2019**, 314 pp.

[6] W. Hume-Rothery, *Journal of the Institute of Metals* **1926**, *35*, 319–335.

[7] U. Mizutani, *Hume-Rothery Rules for Structurally Complex Alloy Phases*, CRC Press, **2016**, DOI `10.1201/b10324`.

[8] F. C. Frank, J. S. Kasper, *Acta Crystallographica* **1958**, *11*, 184–190, DOI `10.1107/S0365110X58000487`.

[9] B. Pansu, J.-F. Sadoc, *European physical journal. E, Soft matter and Biological Physics* **2017**, *40*, 102, DOI `10.1140/epje/i2017-11592-6`.

[10] W. Haucke, *Zeitschrift für anorganische und allgemeine Chemie* **1940**, *244*, 17–22, DOI `10.1002/zaac.19402440103`.

[11] E. Zintl, W. Haucke, *Zeitschrift für Elektrochemie und angewandte physikalische Chemie* **1938**, *44*, 104–111.

[12] F. Gladisch, S. Steinberg, *Crystals* **2018**, *8*, 80, DOI `10.3390/cryst8020080`.

[13] C. Hoch, *Crystals* **2019**, *9*, 267, DOI `10.3390/cryst9050267`.

[14] C. Zheng, R. Hoffmann, *Zeitschrift für Naturforschung, B: A Journal of Chemical Sciences* **1986**, *41*, 292–320, DOI `10.1515/znb-1986-0304`.

[15] L. Siggelkow, V. Hlukhyy, T. F. Fässler, *Zeitschrift für anorganische und allgemeine Chemie* **2017**, *643*, 1424–1430, DOI `10.1002/zaac.201700180`.

[16] L. Siggelkow, V. Hlukhyy, B. Wahl, T. F. Fässler, *European Journal of Inorganic Chemistry* **2011**, *2011*, 4012–4024, DOI `10.1002/ejic.201100347`.

[17] D. Gignoux, D. Schmitt, *Journal of Magnetism and Magnetic Materials* **1991**, *100*, 99–125, DOI `10.1016/0304-8853(91)90815-R`.

[18] G. A. Bain, J. F. Berry, *Journal of Chemical Education* **2008**, *85*, 532, DOI `10.1021/ed085p532`.

[19] I. A. Campbell, S. Senoussi, *Philosophical Magazine B* **1992**, *65*, 1267–1274, DOI `10.1080/13642819208215092`.

[20] P. A. Joy, P. S. A. Kumar, S. K. Date, *Journal of physics. Condensed matter : an Institute of Physics journal* **1998**, *10*, 11049–11054, DOI `10.1088/0953-8984/10/48/024`.

[21] E. Petrovský, A. Kapička, *Journal of Geophysical Research: Solid Earth* **2006**, *111*, DOI `10.1029/2006JB004507`.

[22] C. P. Poole, *Handbook of superconductivity*, Academic Press, San Diego, CA, **2000**, 709 pp.

[23] R. Sharma, *Superconductivity, Basics and Applications to Magnets*, Springer International Publishing, Cham, **2015**, 427 pp.

[24] S. R. Xie, Y. Quan, A. C. Hire, B. Deng, J. M. DeStefano, I. Salinas, U. S. Shah, L. Fanfarillo, J. Lim, J. Kim, G. R. Stewart, J. J. Hamlin, P. J. Hirschfeld, R. G. Hennig, *npj Computational Materials* **2022**, *8*, DOI `10.1038/s41524-021-00666-7`.

[25] M. Rotter, M. Pangerl, M. Tegel, D. Johrendt, *Angewandte Chemie (International ed. in English)* **2008**, *47*, 7949–7952, DOI `10.1002/anie.200803641`.

[26] D. Johrendt, H. Hosono, R.-D. Hoffmann, R. Pöttgen, *Zeitschrift für Kristallographie - Crystalline Materials* **2011**, *226*, 435–446, DOI `10.1524/zkri.2011.1363`.

[27] X. Geng, J. Yi in *Nano-sized multifunctional materials, Synthesis, properties and applications*, (Ed.: N. H. Hong), Micro & nano technologies series, Elsevier, Amsterdam, Kidlington, Oxford, and Cambridge, MA, **2019**, pp. 117–144, DOI `10.1016/B978-0-12-813934-9.00006-2`.

[28] E. Snider, N. Dasenbrock-Gammon, R. McBride, M. Debessai, H. Vindana, K. Vencatasamy, K. V. Lawler, A. Salamat, R. P. Dias, *Nature* **2020**, *586*, 373–377, DOI `10.1038/s41586-020-2801-z`.

[29] B. T. Matthias, T. H. Geballe, S. Geller, E. Corenzwit, *Physical Review* **1954**, *95*, 1435, DOI `10.1103/PhysRev.95.1435`.

[30] X. Xu, *Superconductor Science and Technology* **2017**, *30*, 093001, DOI `10.1088/1361-6668/aa7976`.

[31] C. Yao, Y. Ma, *iScience* **2021**, *24*, 102541, DOI `10.1016/j.isci.2021.102541`.

[32] R. A. Klemm, *Layered Superconductors: Volume 1*, Oxford University Press, **2011**, DOI `10.1093/acprof:oso/9780199593316.001.0001`.

[33] F.-C. Hsu, J.-Y. Luo, K.-W. Yeh, T.-K. Chen, T.-W. Huang, P. M. Wu, Y.-C. Lee, Y.-L. Huang, Y.-Y. Chu, D.-C. Yan, M.-K. Wu, *Proceedings of the National Academy of Sciences of the United States of America* **2008**, *105*, 14262–14264, DOI `10.1073/pnas.0807325105`.

[34] X. C. Wang, Q. Q. Liu, Y. X. Lv, W. B. Gao, L. X. Yang, R. C. Yu, F. Y. Li, C. Q. Jin, *Solid State Communications* **2008**, *148*, 538–540, DOI `10.1016/j.ssc.2008.09.057`.

[35] M. Rotter, M. Tegel, D. Johrendt, *Physical review letters* **2008**, *101*, 107006, DOI `10.1103/PhysRevLett.101.107006`.

[36] Y. Kamihara, T. Watanabe, M. Hirano, H. Hosono, *Journal of the American Chemical Society* **2008**, *130*, 3296–3297, DOI `10.1021/ja800073m`.

[37] N. Katayama, K. Kudo, S. Onari, T. Mizukami, K. Sugawara, Y. Sugiyama, Y. Kitahama, K. Iba, K. Fujimura, N. Nishimoto, M. Nohara, H. Sawa, *Journal of the Physical Society of Japan* **2013**, *82*, 123702, DOI `10.7566/JPSJ.82.123702`.

[38] H. Hosono, A. Yamamoto, H. Hiramatsu, Y. Ma, *Materials Today (Oxford, United Kingdom)* **2018**, *21*, 278–302, DOI `10.1016/j.mattod.2017.09.006`.

[39] Q. Si, R. Yu, E. Abrahams, *Nature Reviews Materials* **2016**, *1*, 3202, DOI `10.1038/natrevmats.2016.17`.

[40] P. D. Johnson, G. Xu, W.-G. Yin, *Iron-Based Superconductivity*, *Vol. 211*, Springer International Publishing, Cham, **2015**, DOI `10.1007/978-3-319-11254-1`.

[41] F. Ronning, E. D. Bauer, T. Park, S.-H. Baek, H. Sakai, J. D. Thompson, *Physical Review B* **2009**, *79*, 134507, DOI `10.1103/PhysRevB.79.134507`.

[42] Y. Zou, Z. Feng, P. W. Logg, J. Chen, G. Lampronti, F. M. Grosche, *physica status solidi (RRL) - Rapid Research Letters* **2014**, *8*, 928–930, DOI `10.1002/pssr.201409418`.

[43] T. L. Hung, I. A. Chen, C. H. Huang, C. Y. Lin, C. W. Chen, Y. B. You, S. T. Jian, M. C. Yang, Y. Y. Hsu, J. C. Ho, Y. Y. Chen, H. C. Ku, *Journal of Low Temperature Physics* **2013**, *171*, 148–155, DOI `10.1007/s10909-012-0832-z`.

[44] K. Kudo, H. Hiiragi, T. Honda, K. Fujimura, H. Idei, M. Nohara, *Journal of the Physical Society of Japan* **2020**, *89*, 013701, DOI `10.7566/JPSJ.89.013701`.

[45] S. Li, B. Zeng, X. Wan, J. Tao, F. Han, H. Yang, Z. Wang, H.-H. Wen, *Physical Review B* **2011**, *84*, 214527, DOI `10.1103/PhysRevB.84.214527`.

[46] S. Pyon, K. Kudo, M. Nohara, *Journal of the Physical Society of Japan* **2012**, *81*, 023702, DOI `10.1143/JPSJ.81.023702`.

[47] Y. Wang, J. Ying, Z. Zhou, J. Sun, T. Wen, Y. Zhou, N. Li, Q. Zhang, F. Han, Y. Xiao, P. Chow, W. Yang, V. V. Struzhkin, Y. Zhao, H.-K. Mao, *Nature communications* **2018**, *9*, 1914, DOI `10.1038/s41467-018-04326-1`.

2 Experimental Methods and Procedures

2.1 Handling of Chemicals

2.1.1 Starting Materials

All experiments were conducted starting from pure elements, as listed in table 2.1. Air sensitive educts were stored in an glovebox (MBRAUN, H_2O and $O_2 < 0.1\,\mathrm{ppm}$), filled with argon (purity 4.8, Westfalen AG) to prevent oxidation. Alkaline earth metals were cleaned from the oxidized surface by scraping. Powdered silicon and germanium was obtained via ball milling.

Table 2.1: Chemicals used for syntheses. Air-sensitive elements were kept under inert conditions in an argon-filled glovebox.

Element	purity	shape	Supplier
Barium	99.5%	ingots	ChemPur
Calcium	99.5% (redistilled)	pieces	Alfa Aesar
Cobalt	99.9+%	ingots	Alfa Aesar
Iron	99.98%	granules	Alfa Aesar
Iron	99.9%	powder	Chempur
Germanium	99.999%	pieces	Evochem GmbH
Magnesium granules	99.8%	granules	Alfa Aesar
Nickel	99.98%	wire	Alfa Aesar
Red Phosphorous	97%	powder	Sigma-Aldrich
Silicon	99.999%	granules	Alpha Aesar
Strontium	98% (redistilled)	pieces	ChemPur
Yttrium	99.9%	chips	Chempur

2.1.2 Mechanical Alloying

For some reactions it was necessary to activate the educts prior to thermal treatment via planetary ball milling (FRITSCH Pulverisette6 classic line). Calcium lumps had to be cut into pieces smaller 2 mm to obtain a fine powder with no bigger particles. All components (in total about 1.2 g to 1.5 g) were loaded into a hardened steel ball mill jar (15 ml, 3 ball with Ø = 10 mm, 1 cm) under inert glovebox atmosphere and closed with a gas-tight lock-system. A program with following parameter had been used: 600 rpm for 72 rounds of 10 min milling followed by a pause of 5 min in reverse mode. This high rotational speed was necessary to downsize calcium particles, larger batch with more material helped reducing abrasion of balls and jar.

Powdered samples were pelletized prior to annealing to enhance reactivity by reducing diffusion pathways between particles and to reduce surface contact with reaction container. A house-made press mould with Ø = 6 mm had been used, applying 2 t for half a minute with a hydraulic press (Specac Atlas 15T).

2.1.3 High-Temperature Treatment

Ampule Materials and Treatment In order to protect reagents from air and moisture, the reactions were performed in sealed containers. Depending on the type of reaction, different ampule materials were chosen. For synthesis in muffle furnaces, silica glass tubes (ilmasil PN, Qsil) with 1 mm wall thickness and outer diameter of 10, 15 or 18 mm were used. Tubes were closed on one side in a H_2/O_2-torch; and if required graphitized. To graphitize a drop of acetone was vaporized and steam pyrolized at the bottom and walls of the ampule by glowing it in the colorless flame. Subsequently the tubes were washed with acetone and dried overnight at 120 °C. Quality of the obtained graphite film was checked with a light bulb. After adding the reagents, sample space was evacuated, purged with argon and sealed under static vacuum. Metal ampules made of niobium or tantalum were prepared from tubes (Ø = 10 mm, 0.5 mm wall thickness) cut into pieces from 3 cm to 5 cm. The ends were arc-welded either by squeezing and crimping them flat or by inserting a lid, that was punched out from a respective metal sheet (0.5 mm thickness). For cleaning purpose, the prepared metal ampules and lids had been sonicated subsequently for 10 min in glacial acetic acid, deionized water and acetone, then dried for several hours at 120 °C.

Different instruments and techniques were used for thermal treatment, depending on the type of reaction and target:

Arc Furnace (AF) For fast reactions of elements with high boiling point, the elements were melted in a modified mini arc melting system (MAM-1, Edmund Bühler GmbH) inside the glove box. Via arc melting, temperatures above 3000 °C can be reached within seconds. A copper block with cavity was used as hearth, mounted in a water-cooled fixture and set up as counter electrode. Alkaline earth elements were placed under the other starting materials and carefully melted to avoid excessive evaporation. Melting reguli were turned upside down and remelted 2 times to 3 times to ensure homogeneity.
The AF was also used to seal metal ampules by welding caps and/or walls together. In this case another copper block was used that fits an ampule holder made of brass.

Induction Furnace / High Frequency Furnace (IF / HFF) Fast heating and cooling of samples within metal ampules was performed via inductive heating (TIG 2.5/300, Hüttinger Elektronik, Freiburg) and the temperature was observed with a single-color pyrometer (Keller ITS, CellaTemp PA 35) for values higher than 600 °C. Since the bottom of the ampule is monitored and the furnace power is adjusted by hand in % of maximal output, temperatures are approximate values, especially below 600 °C. A water-cooled jacket, that can be evacuated and purged with argon, protects the hot ampule.

Resistance Furnace (RF) Longtime reactions, taking from days to weeks were performed in resistance furnaces. Temperatures can be controlled very precisely and programmed with different setpoints, ramps and dwelling times. Samples were either placed in a muffle furnace (Nabertherm, P330 or B180 controller) or tube furnace (HTM Reetz GmbH, Loba 1200-40-600 with Eurotherm 2416 controller). To protect the samples and metal ampules from oxidation, the they were sealed in silica when placed in muffle furnaces. For use with tube furnaces, reusable protection vessels were used that are made of silica glass (ilmasil PN, Qsil). They are approximately 50 cm long tubes that fit into the oven space, have a closed bottom and a ground-joint cap with valve. These vessels were repeatedly evacuated, purged with argon and finally kept under static vacuum.

2.2 Characterization

2.2.1 Powder X-ray Diffraction Methods

With powder X-ray diffraction (PXRD) , the phase purity of samples was verified, solid solutions investigated, new phases detected and structural models confirmed. Data were collected with a STOE StadiP powder diffractometer in transmission geometry. Depending on the absorption caused by high concentration of heavy elements such as barium and tin, different X-ray sources were used. To overcome absorption problem, Mo $K_{\alpha 1}$-radiation ($\lambda = 0.710\,73$ Å, typical 2θ-range 2 to 50) and in all other cases Cu $K_{\alpha 1}$-radiation ($\lambda = 1.540\,60$ Å, typical 2θ-range 5 to 100) were chosen. The latter is diffracted almost twice as much, resulting in better resolution with reflections being more separated by each other. Both diffractometers are equipped with a Ge(111) monochromator and DECTRIS MYTHEN 1K detector. Samples were grinded to fine powder and either fixed on Scotch Magic Tape or sealed in mark-tubes ($\varnothing = 0.3$ mm). In some cases with heavy absorbers, the samples were diluted with diamond powder. Data were collected and corrected to external Si standard with the diffractometer software package WinXPOW [1]. Simple profile fitting, cell indexing, calculation of theoretical patterns for structural models and phase analysis can be done with this software. For Rietveld refinement, FullProf suite [2] or Bruker Topas [3] were used.

2.2.2 Single Crystal X-Ray Diffraction

New structures were investigated by single crystal X-Ray diffraction (SXRD). Crystals were picked under an optical microscope either under air or in a glovebox. In the first case, nail polish was used to fix crystals on thin glass fibers. In the second case air or moisture sensitive crystals were fixed on glass fibers with oil and either sealed in a glass mark-tube or kept in a closed vial. Nitrogen jet cooling was used to freeze the oil in position and protect exposed crystals. Different diffractometer were used with respect to availability and crystal quality. All were equipped with a molybdenum source (Mo K_{α}-radiation ($\lambda = 0.710\,73$ Å): Xcalibur3 (Oxford Diffraction), equipped with fine focused radiation source, graphite monochromator and Sapphire 3 CCD detector; data were processed by CrysAlis RED and absorption corrected by SCALE3 ABSPACK [4, 5]. D8 Kappa Apex II (Bruker AXS) with Apex II detector, equipped with a FR591 rotating anode as radiation source; the diffractometer software [6] contains Saint[7] to deduce data and Sadabs [8] for absorption correction. The rotating anode is also used by STOE IPDS 2T with graphite monochromator and image plate detector; the data collection and processing was performed with X-Area software collection [9], absorption correction was done numerically with X-Red 32 [10] and X-Shape [11], scaling and exclusion of outliers done with Laue Analyzer LANA [12]. The fourth used diffractometer was a STOE STADIVARI with Genix 3D Mo HF as X-ray source, graded multilayer mirror monochromator and DECTRIS Pilatus 300 K detector; the same software than for the IPDS was used.

The crystal structures were solved with direct methods using ShelXS [13] and refined with ShelXL [14, 15] based on full-matrix least squares against F^2. To check for the correct composition, occupancy parameters were refined in separate series of least-squares cycles. In the last cycles, ideal occupancies were assumed again for fully occupied sites. Electron-density (Fourier) synthesis was investigated to avoid missed residual peaks.

2.2.3 Energy-Dispersive X-ray Spectroscopy

Further investigations of single crystals were performed with a Hitachi TM-1000 Tabletop scanning electron microscope (SEM) (15 kV, equipped with an energy dispersive X-ray (EDX) analyzer (SWIFT-ED-TM). Sample have been fixed with carbon tape on an aluminium-sample holder. Besides the crystal size and shape that were observed via SEM, it was possible to prove the presence or absence of specific elements and measure element compositions with EDX. In the case of crystalline materials, diffraction effects may occur and can hit the EDX-detector, resulting in wrong compositions where the statistical weighting of the elements is not accurate [16].

2.2.4 Differential Thermal Analysis

Phase transitions and thermal stability were examined with differential thermal analysis (DTA) using a Netzsch DSC 404 Pegasus. Custom-made niobium ampules were used as sample holder and reference. Before usage they had been cleaned as described in section 2.1.3 and dried under vacuum for 30 min at 1000 °C. Samples were pulverized to enhance surface contact with the ampule and sealed in the arc furnace under argon atmosphere. Empty reference and filled ampule were placed in the instrument, the chamber evacuated and purged with argon three times.

Heating/cooling cycles were performed with $10\,^{\circ}\mathrm{C\,min^{-1}}$ two to three times under a constant argon flow of $75\,\mathrm{mL\,min^{-1}}$. The device was controlled and data recorded using the PROTEUS thermal analysis program [17].

2.2.5 Magnetic Measurements

Magnetic properties of phase pure samples and tests for superconductivity on multiphase samples were recorded with a MPMS XL5 magnetometer by Quantum Design, cooled with liquid helium. It uses a superconducting quantum interference device (SQUID) to probe magnetic dipole moments in an applied homogeneous magnetic field. Powder samples were filled into a gelatin capsule and mounted in a plastic straw by pinching small holes into it. For samples of very weak magnetism, the empty holder was measured and automatically subtracted during the measurement using the "Automated Background Subtraction"-mode (ABS).

For magnetization measurements, field-dependent $M(H)$-scans were performed at 300 K and 1.8 K. Fields were scanned from 0 Oe to 50 000 Oe for para- or diamagnetic samples and between −50 000 Oe and 50 000 Oe in case of (ferro)magnetic hysteresis. Temperature-dependent Magnetization $M(T)$ was measured at various fields either by cooling with an applied field (field-cooled, FC) or warming in an applied field after cooling in a zero field (zero-field-cooled, ZFC). Superconductivity was tested between 1.8 K and 30 K at 15 Oe, where a sudden drop in magnetization caused by the Meissner effect occurring below the critical temperature.

Samples were centered, measurement parameter operated and data recorded by MultiVu software [18]. The magnetization values M [emu] were corrected for diamagnetic sample holder contribution (if not measured with ABS) and normalized to amount of substance. This molar magnetization M_m can be expressed in μ_a [μ_B], considering all atoms carrying a magnetic moment in the compound normalized to the Bohr magneton, which is a a measure how well the spins are aligned with the field. Dividing M_m by the applied field gives the magnetic susceptibility X_m. To correct for diamagnetic contribution X_D of paired electrons, the approximation

$$X_\mathrm{D} = -\frac{MW}{2}10^{-6}\,\mathrm{emu\,mol^{-1}} \quad [19]$$

was used.

2.3 Computational Methods

DFT-based calculations were performed to gain a broader understanding of investigated compounds, using the Stuttgart TB-LMTO-ASA software package [20, 21]. Structure data taken from XRD refinements were used as input parameter. Basis functions are so-called "Linear Muffin Tin Orbitals" (LMTO) with a spherical potential around atoms and a constant flat potential between them. In interstitial regions the tail parts of MTOs don't cancel each other out and interact with each other [22]. They are "blown up" to reach space filling and minimize empty space (atomic-sphere approximation, ASA). In case of voids within the structure, empty spheres are inserted. Atomic radii as well as position and radii of empty spheres were determined automatically after Jepsen and Andersen [23]. The tight-binding (TB) method simplifies interaction of electrons to simple two-center form [24]; exchange and correlation terms were treated within the local density approximation (LDA) and parameterized according to von Barth and Hedin [25]. Downfolding of orbitals with minor contribution to bonding was performed to obtain a minimal basis set and to avoid ghost bands [23, 26]. The calculations were performed without spin polarization and integration of the Brillouin zone was done via tetrahedron method [27]. With these techniques, band structure, density of states (DOS), projected DOS, crystal orbital Hamilton population (COHP) [28] and the electron localization function (ELF) [29] as well as integrated iDOS and $-$iCOHP were obtained. The $-$iDOS value represents the number of electrons and the iCOHP the type and strength of bonding interactions, positive values were considered as bonding, negative as anti-bonding.

2.4 Experimental and Computational Contribution of Co-Authors

This work was funded by the German Research Foundation and TUM Graduate School, affiliated to the subgroup of Dr. Viktor Hlukhyy in the chair of inorganic chemistry with focus on novel materials (Prof. Dr. Thomas F. Fässler). As corresponding author, V. Hlukhyy supervised all manuscripts; his contribution to the work included: setting tasks and goals, discussion of the synthetic routes and results, help in solving the crystal structures and guidance in the preparation of the manuscripts. A list of co-authors and their contribution to publications and manuscripts is given in table 2.2.

Table 2.2: List of co-authors with specified contribution to the included publications and manuscripts.

Author	Publication	Contribution
David Henseler	$BaNi_{16}Si_{12}$ section 5.7	Syntheses, phase analysis
Antii J. Karttunen	$BaNi_{16}Si_{12}$ section 5.7	Quantum chemical calculations
Annika Schultz	$Mg_6Co_{15.64(9)}Si_{7.36}$, $Mg_6Co_{16}Ge_7$, $MgCo_{2-x}Ge_x$ (section 5.9)	Syntheses, phase analysis
Sabine Zeitz	$SrNi_2Si$, $BaNi_2Si$ (section 5.5)	Syntheses, phase analysis

References

[1] WinXPOW, version 3.05, Darmstadt, Germany: STOE & Cie GmbH, **2011**.

[2] J. Rodriguez-Carvajal, FullProf: A Program for Rietveld Refinement and Pattern Matching Analysis, At the Satellite Meeting on Powder Diffraction of the XV IUCr Congress, Toulouse, France, **1990**.

[3] Bruker, General profile and structure analysis software for powder diffraction data, version 6, Madison, Wisconsin (USA): Bruker AXS inc., **2016**.

[4] CrysAlis RED, version 1.171.33.34d, Abingdon, Oxfordshire, England: Oxford Diffraction Ltd., **2009**.

[5] SCALE3 ABSPACK, CrysAlis Software Package, version 1.171.33.34d, Abingdon, Oxfordshire, England: Oxford Diffraction Ltd., **2015**.

[6] Bruker, APEX Suite of Crystallographic Software, Madison, Wisconsin (USA): Bruker AXS inc., **2008**.

[7] SAINT, Madison, Wisconsin (USA): Bruker AXS inc., **2001**.

[8] SADABS, Madison, Wisconsin (USA): Bruker AXS inc., **2001**.

[9] X-Area, version 1.76, Darmstadt, Germany: STOE & Cie GmbH, **2015**.

[10] X-RED32, version 1.63.1, Darmstadt, Germany: STOE & Cie GmbH, **2016**.

[11] X-SHAPE, version 2.18, Darmstadt, Germany: STOE & Cie GmbH, **2015**.

[12] LANA, version 1.68.1, Darmstadt, Germany: STOE & Cie GmbH, **2016**.

[13] G. M. Sheldrick, SHELXS-2014, Program for the Determination of Crystal Structure, Göttingen, Germany: University of Göttingen, **2014**.

[14] G. M. Sheldrick, *Acta crystallographica. Section C, Structural chemistry* **2015**, *71*, 3–8, DOI `10.1107/S2053229614024218`.

[15] G. M. Sheldrick, SHELXL-2014, Program for Crystal Structure Refinement, Göttingen, Germany: University of Göttingen, **2014**.

[16] D. Shindo, T. Oikawa, *Analytical Electron Microscopy for Materials Science*, Springer Japan, Tokyo, **2002**, 162 pp., DOI `10.1007/978-4-431-66988-3`.

[17] NETZSCH Proteus Thermal Analysis, version 6.1.0, Selb, Germany: NETZSCH-Gerätebau GmbH, **2016**.

[18] MPMS MultiVu, version 1.61, San Diego: Quantum Design Inc., **2013**.

[19] G. A. Bain, J. F. Berry, *Journal of Chemical Education* **2008**, *85*, 532, DOI `10.1021/ed085p532`.

[20] R. W. Tank, O. Jepsen, O. K. Andersen, The STUTTGART TB-LMTO-ASA program, Stuttgart: Max-Planck-Institut für Festkorperförschung, **1998**.

[21] M. van Schilfgarde, T. A. Paxton, O. Jepsen, O. K. Andersen, TB-LMTO-ASA, version 4.7, Stuttgart, Germany, **1994**.

[22] O. K. Andersen, A. V. Postnikov, S. Y. Savrasov, *MRS Proceedings* **1991**, *253*, DOI `10.1557/PROC-253-37`.

[23] O. Jepsen, O. K. Andersen, *Zeitschrift für Physik B: Condensed Matter* **1995**, *97*, 35–47, DOI `10.1007/BF01317585`.

[24] O. K. Andersen, O. Jepsen, *Physical review letters* **1984**, *53*, 2571–2574, DOI `10.1103/PhysRevLett.53.2571`.

[25] U. v. Barth, L. Hedin, *Journal of Physics C: Solid State Physics* **1972**, *5*, 1629–1642, DOI `10.1088/0022-3719/5/13/012`.

[26] R. W. Tank, C. Arcangeli, *Physica Status Solidi B: Basic Solid State Physics* **2000**, *217*, 89–130, DOI `10.1002/(SICI)1521-3951(200001)217:1<89::AID-PSSB89>3.0.CO;2-C`.

[27] P. E. Blöchl, O. Jepsen, O. K. Andersen, *Physical review. B, Condensed matter* **1994**, *49*, 16223–16233, DOI `10.1103/PhysRevB.49.16223`.

[28] R. Dronskowski, P. E. Blöchl, *Journal of Physical Chemistry* **1993**, *97*, 8617–8624, DOI `10.1021/j100135a014`.

[29] A. Savin, R. Nesper, S. Wengert, T. F. Fässler, *Angewandte Chemie International Edition in English* **1997**, *36*, 1808–1832, DOI `10.1002/anie.199718081`.

3 Results and Discussion

3.1 Investigated Compounds

see section 5.1 $CaFe_2Ge_2$ with square-planar iron layers – Closing a gap in the row of CaT_2Ge_2 (T = Mn–Zn)
Braun, T.; Hlukhyy, V. *J. of Solid State Chem.* **276**, 368–375 (2019)

see section 5.2 Trends in $ThCr_2Si_2$-Type Tetrelides with Iron, Cobalt or Nickel—Disorder and Distortion
Braun, T.; Hlukhyy, V. *Manuscript for publication*

see section 5.3 Structural Order-Disorder in $CaFe_6Ge_6$ and $Ca_{1-x}Co_6Ge_6$
Braun, T.; Hlukhyy, V. *J. of Solid State Chem.* **in press**, 123742 (2022)

see section 5.4 SrNiSi with Two Different Stacking Variants — An Electron Deficient Zintl-Phase
Braun, T.; Hlukhyy, V. *Manuscript for publication*

see section 5.5 $SrNi_2Si$ and $BaNi_2Si$ – New Layered Silicides with Fused Nickel Six-membered Rings in a Boat Conformation
Braun, T.; Zeitz, S.; Hlukhyy, V. *Z. Anorg. Allg. Chem.* **645**, 388–395 (2019)

see section 5.6 $SrNi_5Si_3$ – First Tetrelide with $LaCo_5P_3$-Type Structure
Braun, T.; Hlukhyy, V. *Manuscript for publication*

see section 5.7 Alkaline Earth Metal Poorest Ordered Compound $BaNi_{16}Si_{12}$ with Catalan Pentakis Dodecahedra—A New Record for Coordination Number
Braun, T.; Henseler, D.; Karttunen, A. J.; Hlukhyy, V. *Manuscript for publication*

see section 5.8 Synthesis and Crystal Structure of $CaCo_{8.79(1)}Si_{4.21}$ and $SrNi_{9.26(8)}Ge_{3.74}$ with $Ce_2Ni_{17}Si_9$-type
Braun, T.; Hlukhyy, V. *Manuscript for publication*

see section 5.9 Synthesis and Crystal Structure of *G*-Phases $Mg_6Co_{15.64(9)}Si_{7.36}$, $Mg_6Co_{16}Ge_7$ and Laves Phase $MgCo_{2-x}Ge_x$

Braun, T.; Schulz, A.; Hlukhyy, V. *Manuscript for publication*

New materials with chains, layers or networks of transition metal were expected in the alkaline earth poorer region of ternary intermetallic compounds. Different combinations $Ae_xT_yX_z$ with Ae = Mg, Ca, Sr, Ba, T = Fe, Co, Ni and X = Si, Ge

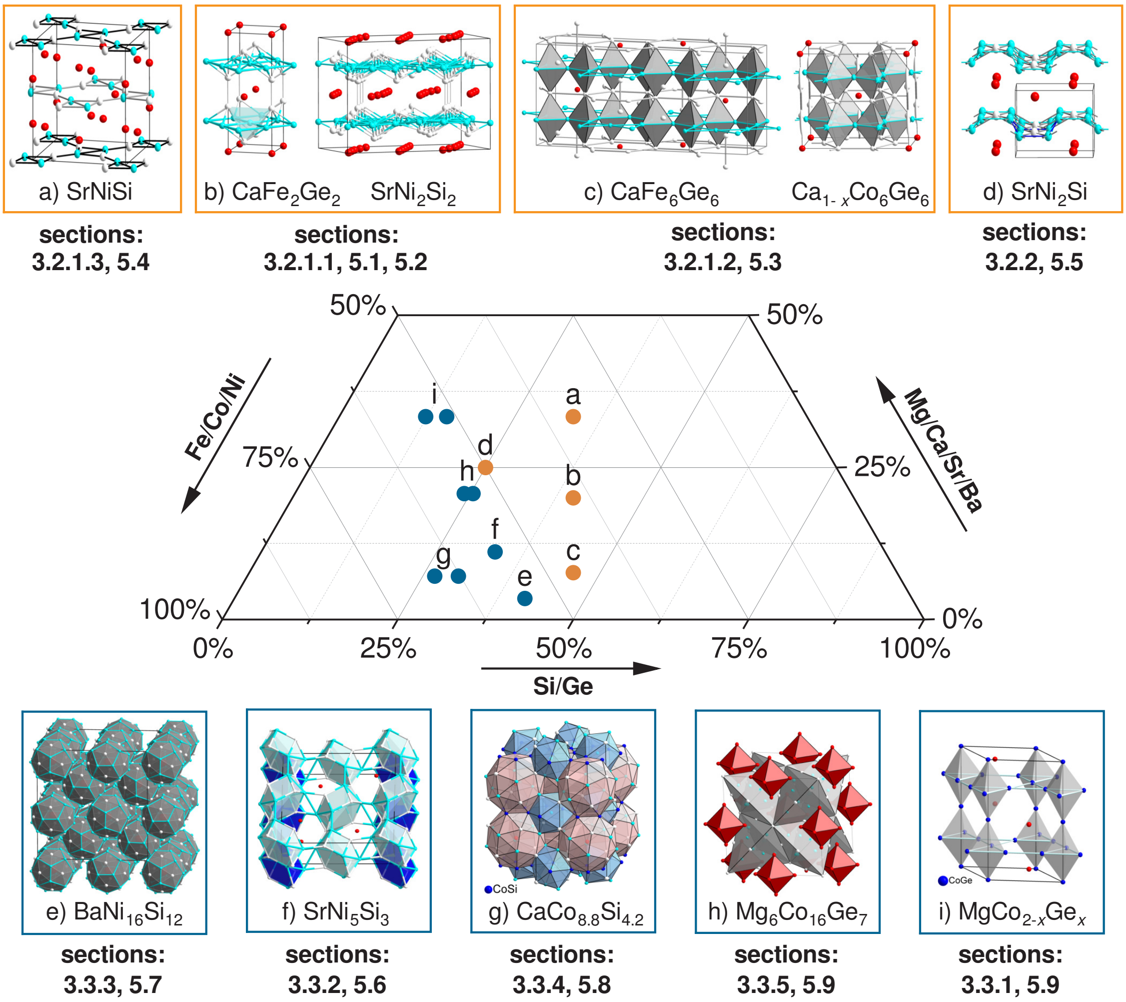

Figure 3.1: Ternary composition triangle the in $Ae - T - X$-system (Ae = Mg, Ca, Sr, Ba; T = Fe, Co, Ni; X = Si, Ge). Alkaline earth metals are drawn in red, transition metals in cyan, tetrels in white and mixed occupancy in blue. For each structure type, representative compounds are shown. Characteristic polyhedra were chosen, pointing out different building principles. To keep it clearly represented, only the new phases are shown without binary and ternary phases from literature.

were tried and obtained compounds are collected in a ternary composition triangle (fig. 3.1). Compositions were limited to the transition metal rich region, where enough transition metal atoms are present in the structure to develop linked units. Otherwise they would too likely be isolated and not form desired substructures within the crystal structure. Most of the detected phases adopt known structure types that have been achieved with a new combination of elements in this thesis: $CaFe_2Ge_2$ [1], $Ca_{1-x}Co_6Ge_6$, $CaFe_6Ge_6$ [2], $SrNi_5Si_3$, $CaCo_{8.8}Si_{4.2}$, $SrNi_{9.3}Ge_{3.7}$, $Mg_6Co_{15.6}Si_{7.4}$, $Mg_6Co_{16}Ge_7$, $SrNi_2Si$, $BaNi_2Si$ [3], $MgCo_{2-x}Ge_x$. In addition, distortion variant ($SrNi_2Si_2$) or own types ($BaNi_{16}Si_{12}$, SrNiSi) were found. All structures have in common that T and X atoms form a polyanionic network that embeds cationic alkaline earth atoms. The exact structure has to be regarded for each compound individually, because atomic radii differences as well as valency and electronic properties determine the atomic arrangement. Especially nickel compounds such as SrNiSi, $SrNi_2Si_2$ and $SrNi_5Si_3$ behave differently than their homologs.

The 111-composition is a good example for the structural variety, which ranges from polyanionic units that are extended in only one dimension, to such with two or three dimensionsional polyanionic networks. SrNiGe and BaNiGe with anti-SnClF-type make nickel-germanium ladders in one direction, CaNiGe contains two dimensional squared layers of Ni, coordinated tetrahedrally by germanium, and MgNiGe with TiNiSi-type (also known as MgSrSi-type) has a 3D network of nickel and germanium [4, 5]. Taking into account also other transition metals and elements from the pnictogen group, many structure types are found in the ICSD database [6]: AlB_2, SrPtSb, Laves(2H)-$MgZn_2$, Laves(4H)-$MgNi_2$, $Mg(Cu_{0.5}Al_{0.5})_2$, ZrNiAl, ZrBeSi, CaPtAs, LiGaGe, AlLiSi (half-Heusler), $CeCu_2$, SrAgGe, EuAuGe, HoPdGe, CaAuSn, TiNiSi, LaIrSi, CaPdAl, PbClF, BaPdP, CaPtP, CaPdAs, anti-SnClF, MgCuAs, MgAgSb, MgAgAs, CaPdSi and EuNiGe.

Various compositions were tried, since it is not always possible to predict the structure on basis of the stoichiometric formula, involved elements, their respective valency, valence electron concentration or difference of atomic radii. Unknown phases in multi-phase samples were identified and characterized. With the refined formula a direct synthesis was possible; promising samples were investigated for superconductivity.

3.2 Structures with Transition Metals Atoms Ordered in Layers

All solid compounds consist of a three dimensional packing of atoms. However, as in polar intermetallic compounds ionic and covalent bonds coexist, polyanionic fragments can be regarded separately. These fragments can be layers that are stacked and intercalated by electropositive atoms like alkaline, alkaline earth or rare earth metals that compensate the anionic charge. A famous example is the family of iron pnictides with layers of edge-sharing $FeAs_4$-tetrahedra. Some examples are illustrated in fig. 1.4 and more complex variants are reported in the literature [7]. The layers are stacked with different sequences and combined with other types, such as As-honeycomb- or LaO-layers in 112-type $Ca_{0.79}La_{0.21}FeAs_2$ or 1111-type $LaO_{0.89}F_{0.11}FeAs$, respectively [8, 9].

In most intermetallic compounds, some distances between atoms are too large to form covalent bonds, but close enough for interactions that may be metallic or coordinative. Depending on the distance between the layers and the orientation of the terminating atoms in adjacent layers, a three-dimensional network can occur. For example, in the collapsed $ThCr_2Si_2$-type, inter-layer bonding occurs. In this case of a three-dimensional framework, it is still possible that atoms of a specific kind are limited to certain crystallographic layers, forming quasi-two-dimensional structures. Such layered compounds have been of interest for physical properties, especially with respect to magnetism and superconductivity [10, 11].

In this work several compounds were investigated with transition metal atoms in layers. These can be divided into planar ones, where the metal form a plane that is surrounded by main group elements (section 3.2.1) and into corrugated ones, where both elements are in the same plane (section 3.2.2).

3.2.1 Planar Layered Structures

3.2.1.1 122 Family with Transition Metal Arranged in Squared Lattice

see section 5.1 $CaFe_2Ge_2$ with square-planar iron layers – Closing a gap in the row of CaT_2Ge_2 (T = Mn–Zn)
Braun, T.; Hlukhyy, V. *J. of Solid State Chem.* **276**, 368–375 (2019)

see section 5.2 Trends in $ThCr_2Si_2$-Type Tetrelides with Iron, Cobalt or Nickel—Disorder and Distortion
Braun, T.; Hlukhyy, V. *Manuscript for publication*

A large compound family in intermetallics is based on variants of the $BaAl_4$-structure, where atoms on specific sites are replaced by a third element. Among different coloring variants, a common representative is the $ThCr_2Si_2$-type, also known as $CeAl_2Ga_2$-type [12, 13]. In the body-centered tetragonal space group $I4/mmm$, cationic alkaline earth or rare earth atoms Ae occupy the $2a$ Wyckoff position (0 0 0), d-metal atoms T occupy $4d$ (0 $^1/_2$ $^1/_4$) and p-elements X are on $4e$ (0 0 z). The resulting structure contains square planar T layers, where each atom is tetrahedrally coordinated by X atoms. These edge-sharing tetrahedra form layers that are a common structural motif among layered superconductors (see section 1.2.3 and fig. 1.4). Depending on the X-atom's z-parameter and cell height c, these layers can be connected by inter-layer bonds between X-atoms that form dumbbells. Compounds with these bonds are termed collapsed tetragonal (cT) structures. The opposite are uncollapsed tetragonal structures (ucT), with well-separated layers. ucT-compounds are also called $BaZn_2P_2$- or $TlCu_2Se_2$-type in the ICSD [6] or

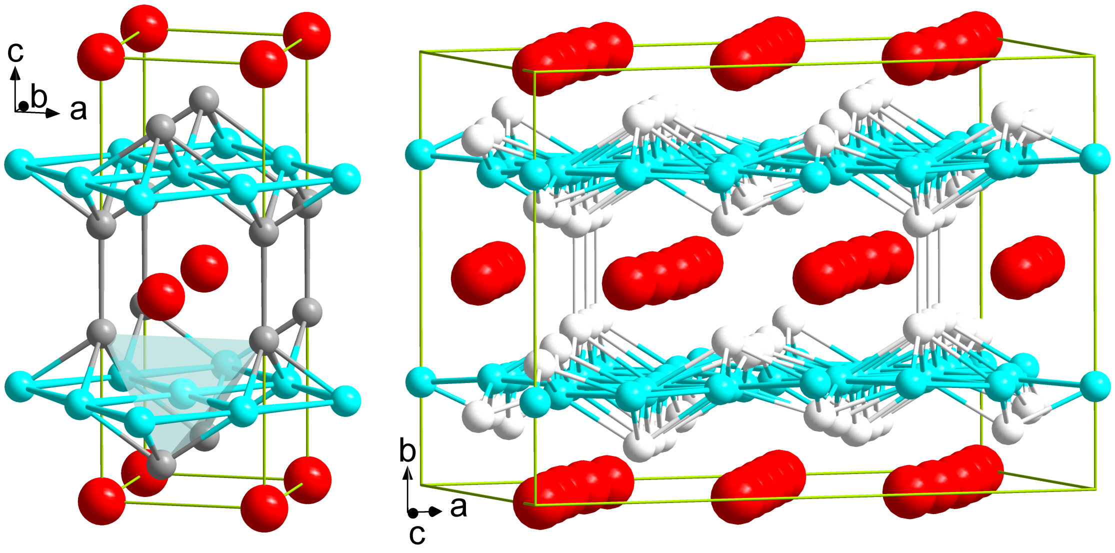

(a) (b)

Figure 3.2: (a) Crystal structure of $CaFe_2Ge_2$ [1], a Fe@Ge_4-tetrahedron is shown in blue. (b) Structural model of $SrNi_2Si_2$, which demonstrates the presence of Si-dumbbells as well as broken Si–Si-bonds. Alkaline earth atoms are drawn in red, transition metal in cyan and tetrelides in white/grey.

Pearson database [14], respectively. According to M. Shatruk [15], only about 10% of $ThCr_2Si_2$-type compounds are ucT. In addition some compounds are polymorph and a reversible transition between cT and ucT can be induced by temperature, external pressure or chemical pressure. This was reported for compounds $SrNi_2P_2$ or in $Sr_{1-x}Ca_xCo_2P_2$, where the large size of strontium breaks inter-layer bonds [16, 17]. Similar behavior was observed when substituting the main group element in $SrNi_2P_{2-x}As_x$ [18].

As part of this thesis, $CaFe_2Ge_2$ (fig. 3.2a) was successfully prepared using a ball mill approach. In contrast to isostructural homologes CaT_2Ge_2 (T = Mn–Zn), the iron compound appears to be metastable. It does not form directly from a stoichiometric melt and decomposes during annealing at high temperatures. Structural parameter of this compound do fit well into the series of aliovalent isotypes, as discussed in section 5.2. Also magnetic properties show values that follow the trend reported for the $CaMn_{2-x}Fe_xGe_2$ series [19], with a ferromagnetic Curie temperature of 44 K. The metastable character of $CaFe_2Ge_2$ is surprising since the structure type forms independent of a specific valence electron concentration and atomic radius of iron is similar to those of cobalt and manganese. The tetrahedron angle (111.2°) is only slightly distorted from regular geometry, which should be ideal for superconductivity [20]. Electronic structure calculations show a DOS peak at the Fermi level and the ELF-plot confirms a Ge–Ge-bond between the layers, which is a requirement for cT structures. Since also famous $(Ba_{1-x}K_x)Fe_2As_2$ ($T_C = 38\,K$) needed substitution to become superconducting [21], some solid solutions were investigated with $CaFe_2Ge_2$ as parent compound: $Y_{1-x}Ca_xFe_2Ge_2$, $CaFe_{2-x}Co_xGe_2$ and $CaFe_2Ge_{2-x}P_x$. A shift in lattice parameter indicated that substitution was successful, however, the degree of substitution was difficult to control since secondary reactions are an issue, which affects the stoichiometry. Magnetic measurements did not reveal any sign of superconductivity, which is in line with results on $La_{0.59}Ca_{0.41}Fe_2Ge_2$ and $CaMn_{2-x}Fe_xGe_2$ [19, 22].

Similar to the previous compound, also $SrNi_2Si_2$ marks a gap in the system of alkaline earth transition metal tetrelides. Its synthesis is possible by melting and annealing the elements, however, the crystal structure (fig. 3.2b) is not trivial. It contains a mixture of formed and broken Si–Si-dumbbells, which results in a superstructure of $ThCr_2Si_2$-type with a large unit cell. This is already known for the low-temperature modification of $SrNi_2P_2$, but for $SrNi_2Si_2$ a more complex model is required. The results discussed in section 5.2 indicate that even modulation is present and crystals of large size and good quality are necessary to collect sufficient amount of satellite reflections. In this work it was possible to obtain an averaged structure model, that was acceptable to identify the new phase. However, the precise structure solution could not be obtained. Tested samples were not superconductive down to 1.8 K.

The ternary compounds $CaCo_2Ge_2$, $SrCo_2Ge_2$ and $BaCo_2Ge_2$ all form stable compounds with high phase purity via arc melting. Being isovalent, the Ge–Ge-distance depends on the size of the alkaline earth atom. Larger atoms increase the chemical strain and lead from a cT structure in $CaCo_2Ge_2$ to a ucT one in $BaCo_2Ge_2$. The strontium compound shows an intermediate distance of 2.88 Å [23] and ELF calculations by Cuervo-Reyes and Nesper [24] demonstrate that electrons do not form covalent bonds but also no lone pairs. In this work, solid solutions $Sr_{1-x}Ca_xCo_2Ge_2$ and $Sr_{1-x}Ba_xCo_2Ge_2$ were synthesized to target the region where a transition from cT to ucT happens. An instability created by substitution might lead to a magnetic phase change or superconductivity. According to Aryal [25], $CaCo_2Ge_2$ is a weak ferromagnetic at low temperatures, $SrCo_2Ge_2$ shows paramagnetism [26]. Solid solution between these two compounds is possible for the full range and the structural parameter follow Vegard's law. Since no special behavior was observed for a specific composition, midway sample $Sr_{0.46}Ca_{0.54}Co_2Ge_2$ was measured. No ferromagnetic transition was observed and is thus expected to be found for $1 > x > 0.54$. Substitution of strontium with barium was successful and lead to a change in lattice parameter. However, $hk3$- and $hk6$-reflections appear broadly, whereas $hk0$-reflections are sharp, which is a sign of internal strain or modulation in certain directions. Three samples with $x = 0.25, 0.5, 0.75$ were tested, all showed paramagnetism with ferromagnetic contribution by secondary phases.

Besides compounds with square lattice of transition metal, also hexagonal planes with Kagomé nets were investigated and are part of the next section.

3.2.1.2 166 Family with Transition Metal in Kagomé Lattice

see section 5.3 Structural Order-Disorder in $CaFe_6Ge_6$ and $CaCo_6Ge_6$
Braun, T.; Hlukhyy, V. *J. of Solid State Chem.* **in press**, 123742 (2022)

RT_6X_6-compounds (R = rare earth metal, T = Mn, Fe, Co, X = Ge, Sn, Ga) are composed of a framework made of vertex-sharing trigonal bipyramids with open hexagonal channels. This structural motif can be derived from $CaCu_5$ when all

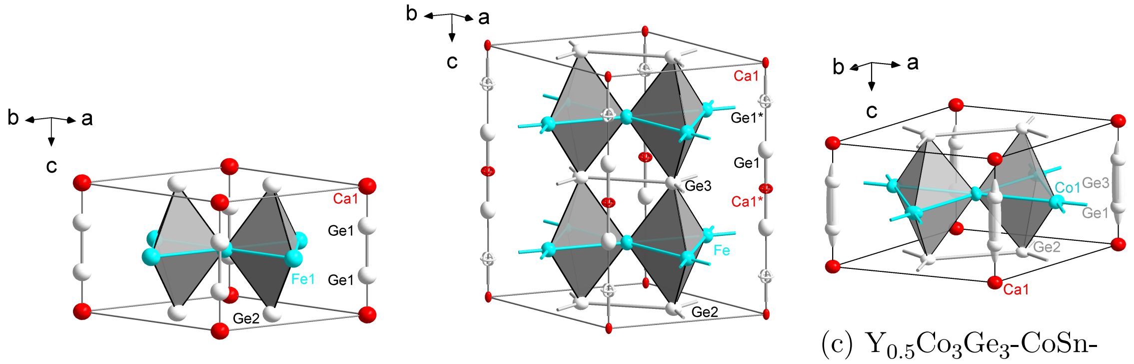

(a) $Y_{0.5}Co_3Ge_3$-type (b) $MgFe_6Ge_6$-type (c) $Y_{0.5}Co_3Ge_3$-CoSn-intergrowth

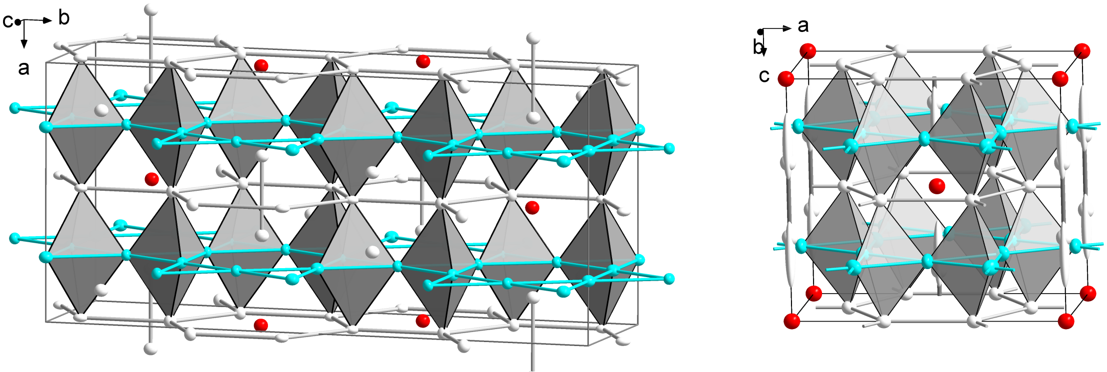

(d) $TbFe_6Sn_6$-type (e) $ScFe_6Ga_6$-CoSn-intergrowth

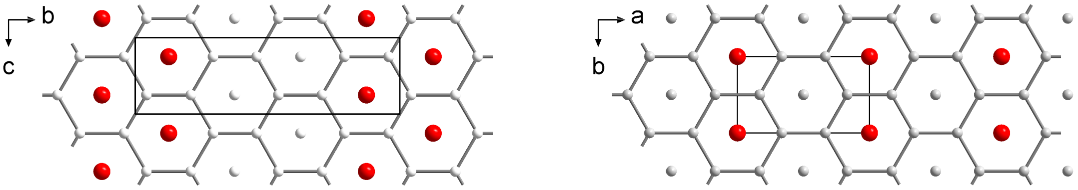

(f) (g)

Figure 3.3: (a), (b), (d) and (f) Crystal structures of $CaFe_6Ge_6$. (c) and (e) Crystal structures of $Ca_{1-x}Co_6Ge_6$. (f) and (g) illustrate the phase shift of stacking sequence between adjacent channels of ordered $CaFe_6Ge_6$ and $Ca_{1-x}Co_6Ge_6$, respectively. A plane can either contain the center of a Ge_2-dumbbell or a calcium atom.

apical atoms are replaced by X and all basal atoms by T, like it is the case for CoSn-structure [27]. Interestingly, while calcium is placed in the honeycomb layer, additional tin atoms in CoSn are situated in the narrower Kagomé-layer with a larger void remaining [28]. By filling every second void with an R-atom, Sn-atoms are pushed into adjacent voids forming dumbbells. The ordering sequence in a structure within and between channels can be random ($\mathrm{Y_{0.5}Co_3Ge_3}$-type) or regular, resulting in different superstructures [29–32]. 166 compounds are counted to layered compounds since the transition metal atoms are arranged in crystallographic layers. This enables the formation of magnetic order and interesting physical properties [11]. Superconductivity was observed in related $\mathrm{LaRu_3Si_2}$-system, where Si-dumbbells in channel are replaced by another lanthanum atom, but the TX-framework is analog [33].

In this work the compounds $\mathrm{CaFe_6Ge_6}$ and $\mathrm{Ca_{1-x}Co_6Ge_6}$ (fig. 3.3) were investigated. Both form from the elements via arc melting, crystallizing with disorder. By annealing, atoms in the channels rearrange themselves to form long-range order, which also includes the relation of guest atoms in adjacent channels to each other. Due to the hexagonal nature of the host lattice, three possible orientations of an orthorhombic supercell, that are rotated by 60° with respect to each other, can form if an ordering originates in different domains. Such a process is known as microtwinning [34, 35]. Thus, the crystal structures had to be solved as three-component twins to refine models without disorder and avoid pseudo-symmetry. For $\mathrm{CaFe_6Ge_6}$, unit cells of three different ordering types were identified from single crystals: (I) $\mathrm{Y_{0.5}Co_3Ge_3}$-type (fig. 3.3a) shows complete disorder (superposition of 50 % Ca atoms and 50 % $\mathrm{Ge_2}$-dumbbells). (II) $\mathrm{MgFe_6Ge_6}$-type (fig. 3.3b) has a doubled c-axis and the stacking sequence is in phase between adjacent channels. In the ordered structure model, all calcium atoms are in one layers and all dumbbells in the other. Positional disorder with split position (78 %/22 %) was observed and confirmed by diffuse scattering in constructed reciprocal lattice sections. It may result of an incomplete ordering process that has been quenched. (III) An orthorhombic superstructure with $\mathrm{TbFe_6Sn_6}$-type (fig. 3.3d), where the stacking sequence changes phase after every second channel in a row, which is illustrated in fig. 3.3f. The third modification is the most stable one and is easily obtained by annealing at elevated temperatures. Like with iron, also the cobalt containing compound $\mathrm{Ca_{1-x}Co_6Ge_6}$ was found with multiple modifications: (I) a small hexagonal cell with disorder (fig. 3.3c) and (II) a larger orthorhombic superstructure with doubled height of the unit cell (fig. 3.3e). In both structures calcium deficiency was observed. Due to defect of Ca atoms, the adjacent germanium atoms in channels may relax and shift back to the height of Kagomé-layer, forming a $Y_{0.5}Co_3Ge_3$-CoSn- or $ScFe_6Ga_6$-CoSn-intergrowth, respectively. This type of structure is known to adapt to chemical strain [36, 37]. Atomic displacement ellipsoids of these atoms are very elongated so that their ends overlap with the position of dumbbells. Diffuse scattering in constructed reciprocal lattice sections prove that there was no missed order or modulation. $Ca_{1-x}Co_6Ge_6$ is very reluctant to order and a crystal with ordered superstructure was only found by chance. The position of calcium alternates within adjacent channels row by row (fig. 3.3g).

Magnetic properties and electronic structure calculations are discussed in section 5.3. Application of $CaFe_6Ge_6$ as precatalyst for alkaline oxygen evolution reaction was reported by Yang et al. [38].

3.2.1.3 SrNiSi with Ni-Dumbbells in Flat Nets

see section 5.4 SrNiSi with Two Different Stacking Variants — An Electron Deficient Zintl-Phase
Braun, T.; Hlukhyy, V. *Manuscript for publication*

In the previous section a structure family was investigated that can adopt many different superstructures, based on the same parent type. In contrast, intermetallic compounds in the 111-family, composed of an element with low electronegativity, a d-metal and a p-block element, adopt a lot of structure types with very different arrangement and motifs. Many examples are listed in section 3.1; one of them is the PbClF-type, found for CaNiGe that contains square planar layers, identical to those in the 122-family (section 3.2.1.1) [4]. For SrNiGe and BaNiGe, these layers are broken into ribbons due to larger size of alkaline earth atoms [5]. Among isoelectronic silicon-homologes, only SrNiSi did form, however, with a completely different structure (fig. 3.4). Structural motif is a NiSi-layer similar to those of BaPdP [39]. In contrast to the pnictide compound, silicon atoms are within the plane instead of a split position close above/below it. Two modifications of SrNiSi were found with different stacking variants of the same layer (fig. 3.4): (I) Layers are stacked and shifted in $\vec{b}$ direction with respect to each other. The stacking sequence AB is described with an orthorhombic unit cell in the space group *Cmca*. By looking along the $(\vec{a} - \vec{b})$ direction (fig. 3.4c), all layers align and have the same orientation. (II) Layers are stacked and shifted alternately in $\vec{a}$ and $\vec{b}$ direction. Stacking sequence

AB(AB)' is described by a larger tetragonal unit cell with space group $I4_1acd$. Along the $(\vec{c}-\vec{a})$ direction (fig. 3.4d), all layers align, however, due to additional shift in a second directions, orientation turns by 90° after every second layer as can be seen by orientation of Ni–Ni-dumbbells.

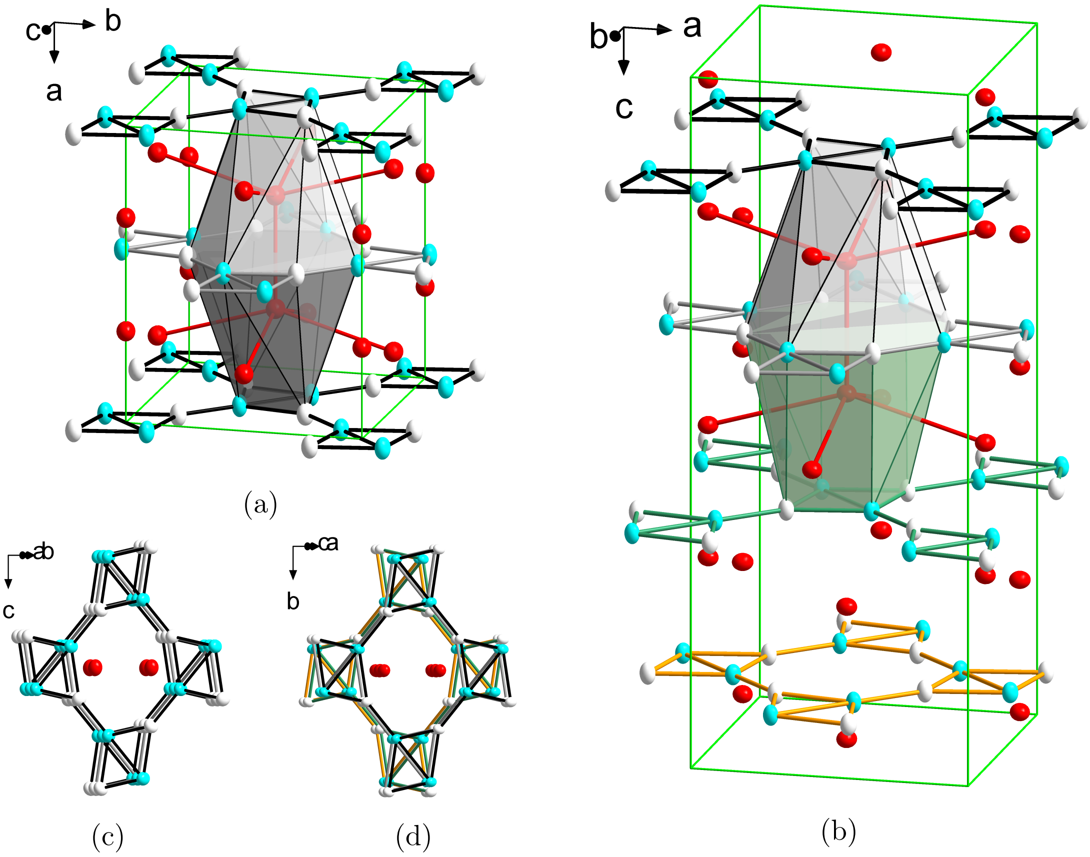

(a)

(c)

(d)

(b)

Figure 3.4: Crystal structure of SrNiSi: orthorhombic modification (a, c) or tetragonal modification (b, d), respectively. The view on the orthorhombic or tetragonal structure along $(\vec{a}-\vec{b})$ or $(\vec{c}-\vec{a})$ direction, respectively, emphasizes stacking differences. Alkaline earth atoms are drawn in red, transition metal in cyan and tetrelides in white/grey. Bonds have been drawn in different colors for each individual layer.

The chemical environment of both modifications is very similar, since layers are isolated from each other. This shows in electronic structure calculations that result in almost identical DOS curves. Also simulated powder XRD patterns are close to each other and only differ in the intensity and position of weak reflections. The Fermi level of both modifications lies on a peak, which is a sign of magnetic or structural instability according to the Stoner criterion. However, due to secondary phases, no magnetic properties could be determined, a test for superconductivity in a multi-phase sample did not show superconductivity.

ELF calculations were performed to compare SrNiSi with BaPdP. They are quite identical for both modifications of SrNiSi. Electrons are more localized within the Ni–Si-layer than in the Pd–P-layer. Ni–Ni has an attractor whereas no bonding interaction between palladium atoms is observed. In addition, phosphorus atoms have pronounced lone pairs that are decreased in the silicide compound. Since BaPdP is a Zintl compound with band gap at the Fermi level [39, 40], the electron-poorer, but isostructural SrNiSi may be considered as electron-deficient Zintl phase.

3.2.2 Corrugated Layered Structures

see section 5.5 $SrNi_2Si$ and $BaNi_2Si$ – New Layered Silicides with Fused Nickel Six-membered Rings in a Boat Conformation
Braun, T.; Zeitz, S.; Hlukhyy, V. *Z. Anorg. Allg. Chem.* **645**, 388–395 (2019)

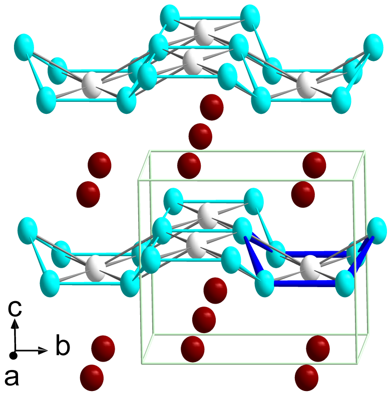

Figure 3.5: Crystal structure of $SrNi_2Si$ [3]. Strontium is drawn in red, nickel in cyan and silicon in white. Contacts forming one hexagon are tinted blue to highlight chair conformation.

Except from structures with flat layers, also compounds with other geometry were investigated. $SrNi_2Si$ and $BaNi_2Si$ exhibit a corrugated layer (fig. 3.5). They are part of the system AeNi2X (Ae = Ca, Sr, Ba and X = Si, Ge), in which the $CaNi_2Si$- and $BaNi_2Ge$-type were reported [3, 41–43]. The first is isostructural to the $LiCu_2Sn$-type [44], but does show separate Ni_2Si-layers; the latter is an ordered variant of $TiCu_3$. Both compounds contain Ni–X-networks, where nickel adopts a hexagonal substructure with each hexagon being centered by a X-atom. Layers are intercalated by alkaline earth atoms and interlayer-distances are so large that they can be considered as isolated from each other. In contrast to section 3.2.1, layers are not flat, but corrugated and X-atoms are placed within the nickel plane. It was observed that depending on the ratio of atomic radii ${}^{r(Ae)}/_{r(X)}$, either $CaNi_2Si$-type or $BaNi_2Ge$-type are formed. The first was found for $CaNi_2Si$ and $SrNi_2Ge$, where the nickel-net has chair conformation like in grey arsenic, the latter was found for $SrNi_2Si$, $BaNi_2Si$ and $BaNi_2Ge$, with the nickel-net in boat conformation (highlighted in blue in fig. 3.5).

In this work, the compounds $SrNi_2Si$ and $BaNi_2Si$ were synthesized and characterized to investigate the change from chair to boat conformation and look for a potentially (reversible) phase transition between both configurations (section 5.5). Signals in differential thermal analysis are present for both compounds that are absent in $CaNi_2Si$ and the germanides, which may indeed be caused by a structural phase change. However, no high temperature phase could be isolated as powder or single crystal to prove that assumption. Electronic structure calculations showed metallic properties and the ELF-visualization confirmed the 2-dimensional character of the layers, which is in agreement with corresponding paths in the band structure.

3.3 Structures with 3D-Networks of Transition Metal Atoms

Polar intermetallic compounds are able to form various different structures. Whereas some trends can be observed for certain systems, the example of ternary 111 compounds (see sections 3.1 and 3.2.1.3) perfectly demonstrates how difficult it is to make reliable predictions. Many different 111-structure types were found. Even if valence electron concentration, valency of main group element and atomic radii follow a trend, there are always exceptions. Looking for new compounds with chains or nets of transition metal, also such with three-dimensional networks were discovered and investigated. After identifying the composition, attempts were made to obtain phase purity as good as possible and electronic structure calculations were performed for solved structures. They are different from those in section 3.2 with regard to position of transition metals that are not limited to certain layers, and contribute to polyanionic networks in all three dimensions.

3.3.1 Laves Phase $MgCo_{2-x}Ge_x$ with Vertex-Sharing Trigonal Bipyramids of Co Atoms

see section 5.9 Synthesis and Crystal Structures of G-Phases $Mg_6Co_{15.64(9)}Si_{7.36}$, $Mg_6Co_{16}Ge_7$ and Laves Phase $MgCo_{2-x}Ge_x$
Braun, T.; Hlukhyy, V. *Manuscript for publication*

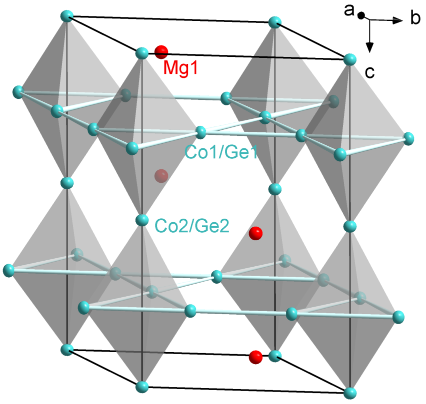

Figure 3.6: Crystal structure of $MgCo_{2-x}Ge_x$ Laves phase, crystallizing with disordered $MgZn_2$-type.

Kagomé nets and trigonal bipyramids were found in the 166 family (section 3.2.1.2). A more common class with this structure motive are Laves phases. For instance Mg_2Ir_3Si is a fully ordered Laves phase with iridium atoms making Kagomé nets (basal plane of pyramids) and silicion forming honeycomb nets (vertices of pyramids) [45]. This compound as well as Li_2IrSi_3, where position of iridium and silicon is inverted, are superconductors (7 K and 3.7 K, respectively) [45–47].

In this thesis , the Laves phase $MgCo_{2-x}Ge_x$ (fig. 3.6) was investigated for $x = 0.5$ and 0.75. Resulting solid solutions have refined formulas $MgCo_{1.63(2)}Ge_{0.37}$ and $MgCo_{1.54(7)}Ge_{0.46}$, which corresponds to $x = 0.37$, 0.46. They adopt disordered hexagonal $MgZn_2$-type (structural parameter given in section 5.9). Both layers contain cobalt as well as germanium atoms with mixed occupancy. Whereas Kagomé nets are mainly occupied by cobalt (85 %–88 %), hexagonal nets contain less (71 % or 55 %, respectively) and more germanium. Since cobalt is found on both positions, a 3-dimensional network is formed. Substitution of cobalt with germanium occurs primarily in the hexagonal layer to maintain a metallic Kagomé subnet. This is in agreement with results observed for the homologous system $MgNi_{2-x}Ge_x$. However, whereas for $x = 0.5$ the fully ordered structure Mg_2Ni_3Ge was reported [48], the cobalt compound remained disordered with $x = 0.46$, which is very close to 0.5. No formation of superstructure reflections or diffuse scattering was observed. Electronic structure calculations show a DOS maximum for $x = 0.46$, which might explain the preferred formation of disordered solid solution over the ordered variant.

A stoichiometric sharp compound with no disorder is discussed in the next section. It belongs to the class of compounds with metal:nonmetal-ratio of 2:1.

3.3.2 $SrNi_5Si_3$ with Complex Ni-Substructure

see section 5.6 $SrNi_5Si_3$ – first tetrelide with $LaCo_5P_3$-Type Structure
Braun, T.; Hlukhyy, V. *Manuscript for publication*

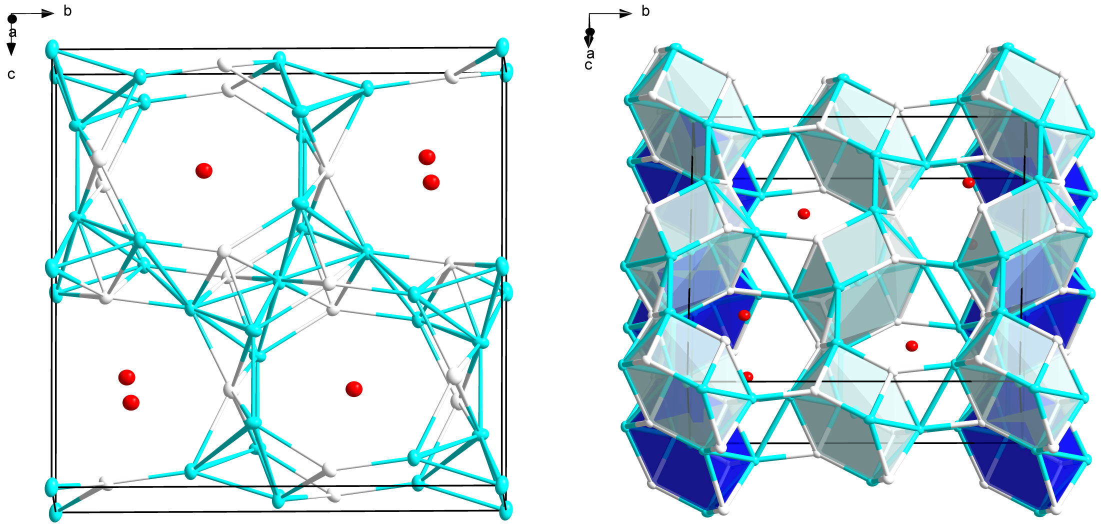

(a) (b)

Figure 3.7: (a) Crystal structure of $SrNi_5Si_3$. (b) Highlighted Ni@$[NiSi]_6$-hexagonal prisms with different colors for clearer visibility. Sr is drawn in red, Ni in cyan and Si in white.

The 153-family comprises of eight different structure types, illustrated in section 5.6. Whereas tetrelides adopt either YNi_5Si_3- or UCu_5Si_3-type [49, 50], the $SrNi_5Si_3$ forms with $LaCo_5P_3$-type, which is normally formed by pnictides. Despite typical representation with trigonal prism of transition metal atoms and rare-earth or alkaline earth atoms that coordinate a p-element, another representation (fig. 3.7) is more comprehensive: the structure can be considered as built-up by hexagonal prism with alternating vertices of nickel and silicon atoms. These Ni@$[NiSi]_6$-units form face-sharing blocks along *a*-direction, which share vertices along *c*-direction to form zigzag-sheets that are connected by short Ni–Ni- and Ni–Si-contacts along *b*-direction. Such hexagonal building blocks were reported for nickel germanides $SrNi_3Ge_2$ and $Ba_2Ni_5Ge_4$ [42, 51]. Band structure calculations were compared to isostructural $SrNi_5P_3$ and $SrNi_5As_3$ [52]. The DOS near the Fermi level is dominated by nickel states, where with pnictides a pseudogap at $-3\,\mathrm{eV}$ occur, that is not so pronounced with silicon. The fact that this structure type is formed with different valence electron concentration indicates that size effect can play crucial role in its formation. Synthesis always contained $Ni_{31}Si_{12}$ and $SrNi_{6.3}Si_{6.7}$ as secondary phases. Magnetic measurements did not show superconductivity.

Hexagonal nickel-silicon prisms are also found in $BaNi_{16}Si_{12}$ (section 3.3.3) with a different connectivity pattern.

3.3.3 $BaNi_{16}Si_{12}$ as BCC-Packing of Ni-Dodecahedra

see section 5.7 Alkaline Earth Metal Poorest Ordered Compound $BaNi_{16}Si_{12}$ with Catalan Pentakis Dodecahedra—A New Record for Coordination Number
Braun, T.; Henseler, D.; Karttunen, A. J.; Hlukhyy, V. *Manuscript for publication*

By arc melting of the elements, $BaNi_{16}Si_{12}$ can be obtained with high phase purity. Looking at stoichiometric compounds with no partial substitution, this composition marks the lowest amount of alkaline earth metal in a polar intermetallic compounds. $BaNi_{16}Si_{12}$ crystallizes in an own type with a large unit cell of cubic symmetry: $a = 18.0482(1)\,\text{Å}$, space group $Fd\bar{3}c$. All 464 atoms of the unit cell are described by 5 Wyckoff positions. Barium atoms are coordinated by a Catalan pentakis dodecahedron, made of 20 nickel and 12 silicon atoms. This polyhedron was observed for the first time in a solid compound. To date it is the largest coordination polyhedron among intermetallic compounds; larger polyhedra like fullerenes act more like a cage than a coordination sphere [53]. In $BaNi_{16}Si_{12}$ these polyhedra are packed with body centered cubic (bcc) arrangement. Regarding coordination sphere of Ni2@Ni_6Si_6 and Ni3@Ni_6Si_6, two types of hexagonal prism were found: one with alternating atoms of nickel and silicon and another where atoms alternate within the hexagon and are the same along edges. The first polyhedron has also been observed in $SrNi_5Si_3$ (section 3.3.2). By edge-sharing, eight polyhedra (four of each kind)

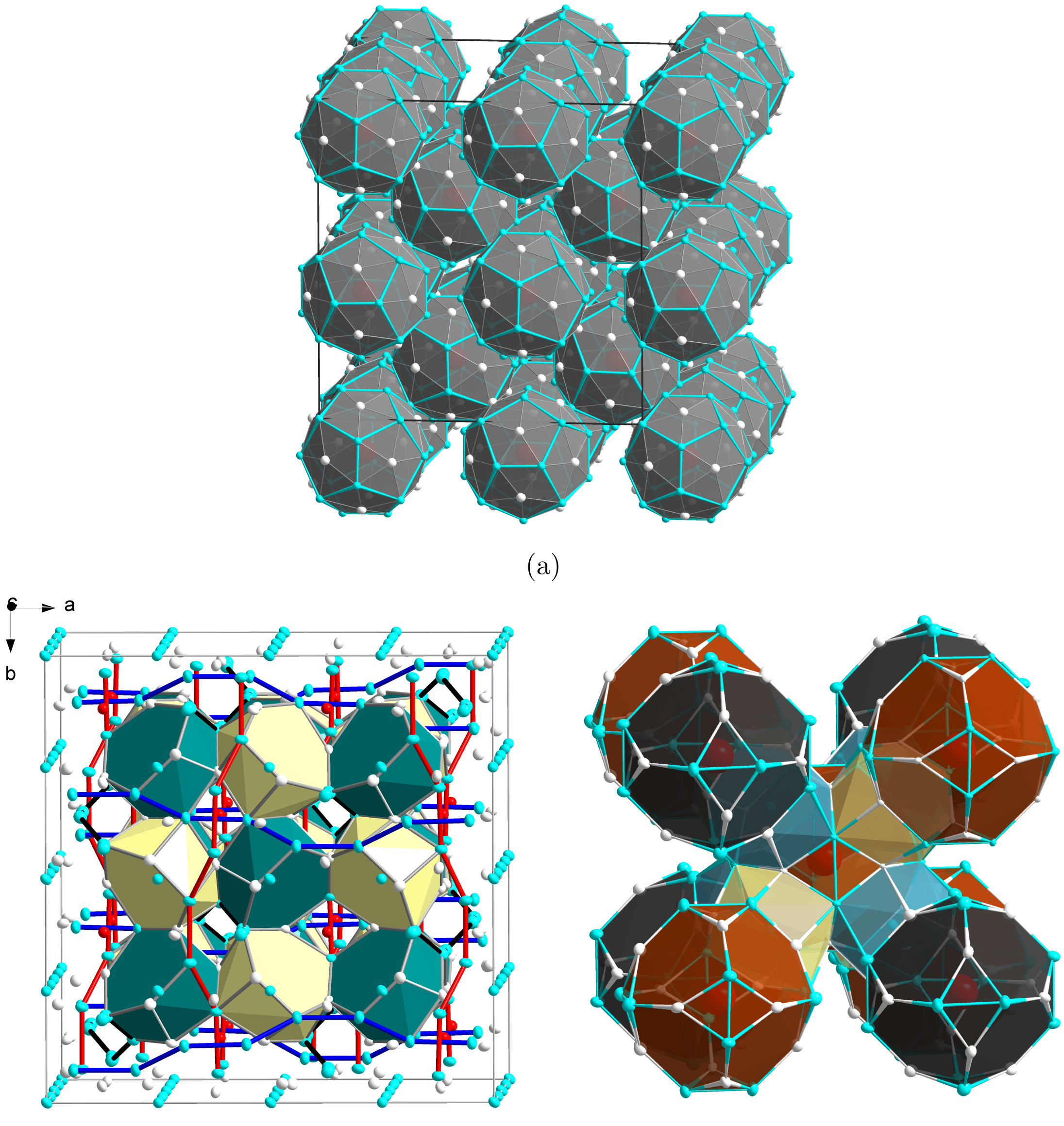

(a)

(b)

(c)

Figure 3.8: Crystal structure of $BaNi_{16}Si_{12}$ with emphasis on (a) packing of barium centered pentakis dodecahedra, (b) nickel centered Ni–Si-prisms (according to central atom Ni2 or Ni3 in yellow or blue, respectively) and (c) Ni–Si-network that is created by prism edges after removing central atoms, representing the connectivity between hexagonal prisms. Barium atoms are drawn in red, nickel in cyan and silicon in white. Colors of polyhedra were chosen depending on constitution or orientation.

surround each barium cation. When removing the central nickel atoms Ni2 and Ni3, the connectivity between prisms becomes visible (fig. 3.8c). Edges form a spherical pattern of hexagons and distorted squares with a short Ni–Ni-contact. It reminds of the layers found in SrNiSi (sections 3.2.1.3 and 5.4), but coiled up. Of course, the polyhedral view only highlights certain aspects in the solid, the Ni–Si-network contains a lot more contacts. Another interesting details if found when looking at shortest Ni–Ni-distances. One-dimensional chains are obtained that perpetuate the structure in all three dimension. They contribute to edges of the hexagonal prism as well as contacts between them. Taking also longer Ni–Ni-distances into account, they are part of a three-dimensional polyanionic structure.

Inspired by so-called *rattling* structures, such as $Ba_8Ni_xSi_{46-x}$, thermoelectric properties were measured. Electric conductivity drops with increasing temperature, which is typical for metals and leads to poor ZT factors. This is in agreement with band structure calculations that show bands crossing the Fermi level. The geometry of isolated $Ba@Ni_{20}Si_{12}$ cluster was optimized and used to simulate Raman bands. The calculation showed a true local minimum for this structure, similar to results reported for hypothetical $Au_{20}Si_{12}$, $Cu_{20}Si_{12}$ and $B_{12}@Mg_{20}B_{12}$ pentakis dodecahedra [54–56]. The difference in electrons in the nickel silicide might be compensated by condensation of these clusters in the solid with additional bonds in the necks.

In magnetic measurements $BaNi_{16}Si_{12}$ gives almost no signal, so in-situ subtraction of the sample holder was required, using the Automated Background Subtraction. Weak paramagnetism was observed after correcting for the diamagnetic contribution of core electrons. No transition into superconducting state was detected down to 1.8 K

3.3.4 $CaCo_{8.79(1)}Si_{4.21}$ and $SrNi_{9.26(9)}Si_{3.74}$ with face- and vertex-sharing Co/Ni-tetrahedra

see section 5.8 Synthesis and Crystal Structure of $CaCo_{8.79(1)}Si_{4.21}$ and $SrNi_{9.26(8)}Ge_{3.74}$ with $Ce_2Ni_{17}Si_9$-type
Braun, T.; Hlukhyy, V. *Manuscript for publication*

Similar to the previous structure, also $CaCo_{8.79(1)}Si_{4.21}$ (fig. 3.9) and $SrNi_{9.26(9)}Si_{3.74}$ have alkaline earth atoms centered in large polyhedra. Both compounds could be obtained with high phase purity by arc melting and subsequent annealing. They crystallize with tetragonal space group $I4/mcm$ in a distorted coloring variant of

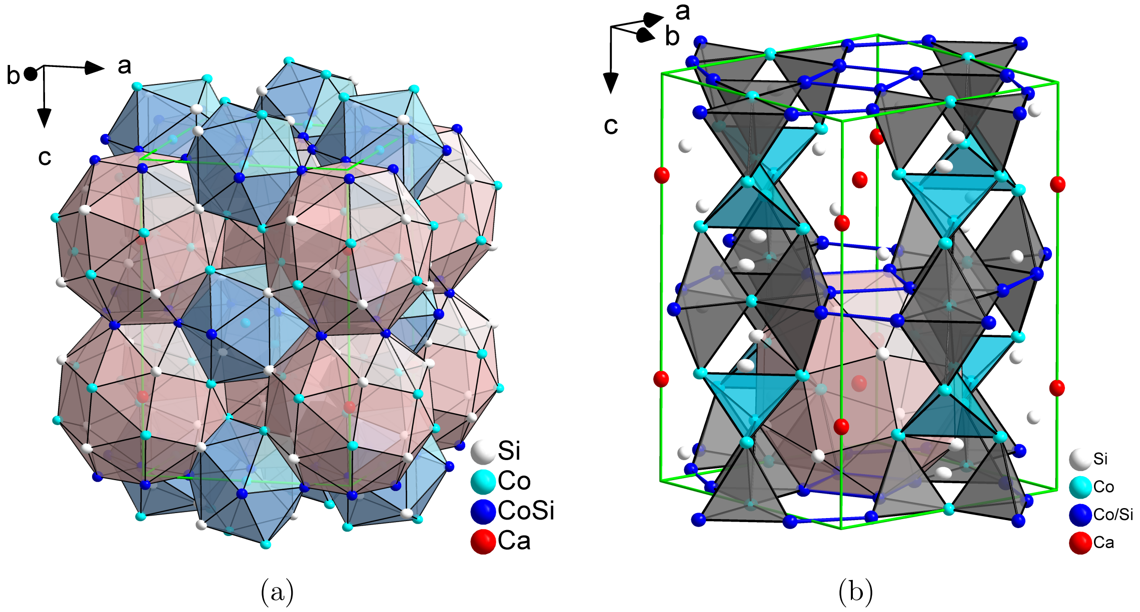

(a) (b)

Figure 3.9: (a) Crystal structure of $CaCo_{8.79(1)}Si_{4.21}$, highlighting the packing of nickel and calcium centered polyhedra. (b) Alternative representation with nickel tetrahedra.

$NaZn_{13}$ [57]. The structure represents a packing of $T@T_{8\pm x}X_{4\mp x}$ (T = Co, Ni, X = Si, Ge) icosahedra and $A@T_{16\pm x}X_{8\mp x}$ (A = Ca, Sr) snub cubes (24 vertices). Due to the mixed occupancy, they were assigned to $Ce_2Ni_{17}Si_9$-type (= $CeNi_{9-x}Si_{4+x}$) [58], which is isostructural to $LaFe_9Si_4$-type for $x = 0$. An alternative representation focuses on face- and vertex-sharing nickel tetrahedra, forming trigonal bipyramids. Even though both structures seem similar, mixed occupancy is found on different atomic sites. Electronic structure calculations showed a DOS peak at the Fermi level of $CaCo_{8.79}Si_{4.21}$ that is absent in the strontium nickel germanide. Since such a peak may indicate a magnetic instability, field dependent measurements were performed. Ferromagnetism was observed, which is in contrast to results on $LaCo_{13-x}Si_x$ [59], where ferromagnetism only occurs for $x < 4$.

In contrast to these compounds, alkaline earth metal atoms are not isolated in the structures of section 3.3.5, but form octahedral units.

3.3.5 $Mg_6Co_{15.64(9)}Si_{7.36}$ and $Mg_6Co_{16}Ge_7$ with Interconnected Stella Quadrangula of Co Atoms

see section 5.9 Synthesis and Crystal Structure of *G*-Phases $Mg_6Co_{15.64(9)}Si_{7.36}$, $Mg_6Co_{16}Ge_7$ and Laves Phase $MgCo_{2-x}Ge_x$
Braun, T.; Schulz, A.; Hlukhyy, V. *Manuscript for publication*

$Mg_6Co_{15.64(9)}Si_{7.36}$ and $Mg_6Co_{16}Ge_7$ (fig. 3.10) belong to the *G*-phases, that were discovered in 1938 and whose crystal structure was solved in 1956 for $Mg_6Cu_{16}Si_7$ [60–62]. Transition metal atoms form a stella quadrangula [63], with vertices being the centers of $CuSi_4$-tetrahedra. Together they form Cu_8Si_{10} supertetrahedra that are connected via edges. In the crystal structure octahedral Mg_6-clusters are cubic face-centered and supertetrahedra occupy all tetrahedral "voids". For $Mg_6Co_{15.64}Si_{7.36}$, mixed occupancy was observed in the central cobalt tetrahedron. In $Mg_6Co_{16}Ge_7$ full occupied sites were observed within standard deviation of refined occupations. Electronic structure calculations show metallic properties; the exact stoichiometric composition of the silicide matches a DOS minimum at the Fermi level. The samples did not show superconductivity at 15 Oe when cooling down to 1.8 K.

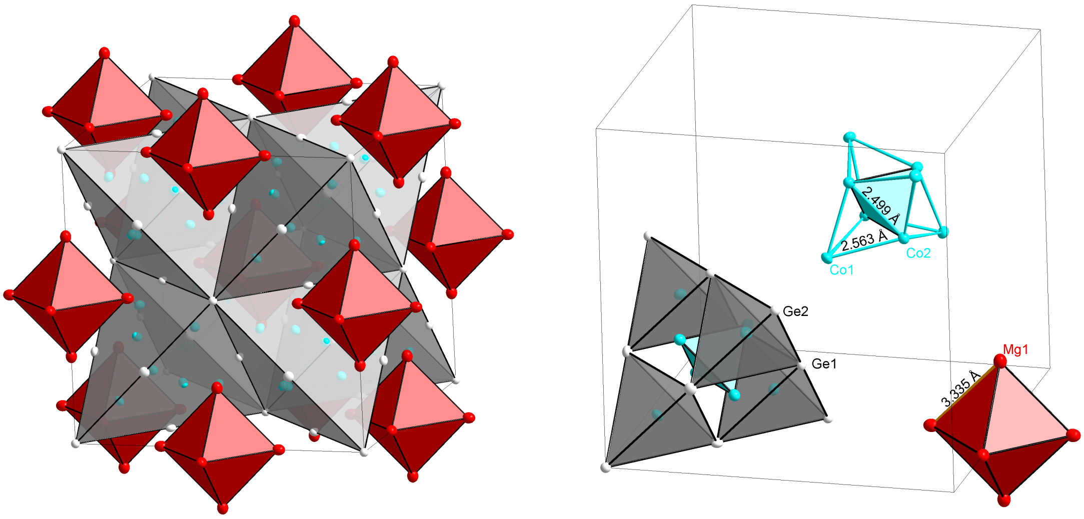

(a) (b)

Figure 3.10: (a) Crystal structure of $Mg_6Co_{16}Ge_7$, highlighting the packing of Ni_8Ge_{10} supertetrahedra and Mg-octahedra. (b) Illustration of nickel stella quadrangular and its relation orientation in the supertetrahedron.

References

[1] T. Braun, V. Hlukhyy, *Journal of Solid State Chemistry* **2019**, *276*, 368–375, DOI `10.1016/j.jssc.2019.05.032`.

[2] T. Braun, V. Hlukhyy, *Journal of Solid State Chemistry* **2022**, *in press*, 123742, DOI `https://doi.org/10.1016/j.jssc.2022.123742`.

[3] T. Braun, S. Zeitz, V. Hlukhyy, *Zeitschrift für anorganische und allgemeine Chemie* **2019**, *645*, 388–395, DOI `10.1002/zaac.201800500`.

[4] V. Hlukhyy, N. Chumalo, V. Zaremba, T. F. Fässler, *Zeitschrift für anorganische und allgemeine Chemie* **2008**, *634*, 1249–1255, DOI `10.1002/zaac.200700534`.

[5] V. Hlukhyy, L. Siggelkow, T. F. Fässler, *Inorganic chemistry* **2013**, *52*, 6905–6915, DOI `10.1021/ic302681t`.

[6] FIZ Karlsruhe, ICSD, Inorganic Crystal Structure Database, version 4.7.0, Karlsruhe, Germany: Leibniz Institute for Information Infrastructure, **2022**.

[7] H. Ogino, S. Sato, K. Kishio, J.-i. Shimoyama, T. Tohei, Y. Ikuhara, *Applied Physics Letters* **2010**, *97*, 072506, DOI `10.1063/1.3478850`.

[8] Y. Kamihara, T. Watanabe, M. Hirano, H. Hosono, *Journal of the American Chemical Society* **2008**, *130*, 3296–3297, DOI `10.1021/ja800073m`.

[9] N. Katayama, K. Kudo, S. Onari, T. Mizukami, K. Sugawara, Y. Sugiyama, Y. Kitahama, K. Iba, K. Fujimura, N. Nishimoto, M. Nohara, H. Sawa, *Journal of the Physical Society of Japan* **2013**, *82*, 123702, DOI `10.7566/JPSJ.82.123702`.

[10] R. A. Klemm, *Layered Superconductors: Volume 1*, Oxford University Press, **2011**, DOI `10.1093/acprof:oso/9780199593316.001.0001`.

[11] N. V. Baranov, E. G. Gerasimov, N. V. Mushnikov, *The Physics of Metals and Metallography* **2011**, *112*, 711–744, DOI `10.1134/S0031918X11070039`.

[12] Z. Ban, M. Sikirica, *Acta Crystallographica* **1965**, *18*, 594–599, DOI `10.1107/S0365110X6500141X`.

[13] O. S. Zarechnyuk, P. I. Kripyakevich, E. I. Gladyshevskii, *Soviet Physics. Crystallography* **1965**, *9*.

[14] P. Villars, K. Cenzual, Pearson's Crystal Data, Crystal Structure Database for Inorganic Compounds (on DVD), Materials Park, Ohio, USA: ASM International, **2019**.

[15] M. Shatruk, *Journal of Solid State Chemistry* **2019**, *272*, 198–209, DOI `10.1016/j.jssc.2019.02.012`.

[16] F. Ronning, E. D. Bauer, T. Park, S.-H. Baek, H. Sakai, J. D. Thompson, *Physical Review B* **2009**, *79*, 134507, DOI `10.1103/PhysRevB.79.134507`.

[17] S. Jia, A. J. Williams, P. W. Stephens, R. J. Cava, *Physical Review B* **2009**, *80*, 165107, DOI `10.1103/PhysRevB.80.165107`.

[18] V. Keimes, A. Hellmann, D. Johrendt, A. Mewis, T. Woike, *Zeitschrift für anorganische und allgemeine Chemie* **1998**, *624*, 830–836, DOI `10.1002/(SICI)1521-3749(199805)624:5<830::AID-ZAAC830>3.0.CO;2-6`.

[19] R. Welter, B. Malaman, *Journal of Alloys and Compounds* **2003**, *354*, 35–46, DOI `10.1016/S0925-8388(02)01354-3`.

[20] C.-H. Lee, A. Iyo, H. Eisaki, H. Kito, M. Teresa Fernandez-Diaz, T. Ito, K. Kihou, H. Matsuhata, M. Braden, K. Yamada, *Journal of the Physical Society of Japan* **2008**, *77*, 083704, DOI `10.1143/JPSJ.77.083704`.

[21] M. Rotter, M. Tegel, D. Johrendt, *Physical review letters* **2008**, *101*, 107006, DOI `10.1103/PhysRevLett.101.107006`.

[22] V. Gvozdetskyi, V. Hlukhyy, R. Gladyshevskii, *Chemistry of Metals and Alloys* **2015**, *8*, 123–128.

[23] W. Dörrscheidt, N. Niess, H. Schäfer, *Zeitschrift für Naturforschung, Teil B: Anorganische Chemie, Organische Chemie* **1976**, *31*, 890–891, DOI `10.1515/znb-1976-0634`.

[24] E. Cuervo-Reyes, R. Nesper, *Physical Review B* **2014**, *90*, 064416, DOI `10.1103/PhysRevB.90.064416`.

[25] L. R. Aryal, Master's Thesis, University of Houston, Houston, **2013**, 93 pp.

[26] S. Jia, P. Jiramongkolchai, M. R. Suchomel, B. H. Toby, J. G. Checkelsky, N. P. Ong, R. J. Cava, *Nature Physics* **2011**, *7*, 207–210, DOI `10.1038/nphys1868`.

[27] O. Nial, *Zeitschrift für anorganische und allgemeine Chemie* **1938**, *238*, 287–296, DOI `10.1002/zaac.19382380213`.

[28] S. I. Simak, U. Häußermann, I. A. Abrikosov, O. Eriksson, J. M. Wills, S. Lidin, B. Johansson, *Physical review letters* **1997**, *79*, 1333–1336, DOI `10.1103/PhysRevLett.79.1333`.

[29] W. Buchholz, H.-U. Schuster, *Zeitschrift für anorganische und allgemeine Chemie* **1981**, *482*, 40–48, DOI `10.1002/zaac.19814821105`.

[30] G. Venturini, *Zeitschrift für Kristallographie - Crystalline Materials* **2006**, *221*, DOI `10.1524/zkri.2006.221.5-7.511`.

[31] G. Venturini, H. Ihou-mouko, C. Lefèvre, S. Lidin, B. Malaman, T. Mazet, J. Tobola, V. Vernière, *Chemistry of Metals and Alloys* **2008**, *1*, 24–33.

[32] D. C. Fredrickson, S. Lidin, G. Venturini, B. Malaman, J. Christensen, *Journal of the American Chemical Society* **2008**, *130*, 8195–8214, DOI `10.1021/ja077380+`.

[33] H. Barz, *Materials Research Bulletin* **1980**, *15*, 1489–1491, DOI `10.1016/0025-5408(80)90107-5`.

[34] O. Oleksyn, H.-U. Nissen, R. Wessicken, *Philosophical Magazine Letters* **1998**, *77*, 275–278, DOI `10.1080/095008398178426`.

[35] O. Y. Oleksyn, H. Böhm, *Zeitschrift für Kristallographie - Crystalline Materials* **1998**, *213*, 270–274, DOI `10.1524/zkri.1998.213.5.270`.

[36] K. P. Hilleke, R. T. Fredrickson, A. I. Vinokur, D. C. Fredrickson, *Crystal Growth & Design* **2017**, *17*, 1610–1619, DOI `10.1021/acs.cgd.6b01606`.

[37] V. M. Berns, D. C. Fredrickson, *Inorganic chemistry* **2014**, *53*, 10762–10771, DOI `10.1021/ic5020412`.

[38] H. Yang, J. N. Hausmann, V. Hlukhyy, T. Braun, K. Laun, I. Zebger, M. Driess, P. W. Menezes, *ChemCatChem* **2022**, *14*, e202200293, DOI `10.1002/cctc.202200293`.

[39] D. Johrendt, A. Mewis, *Journal of Alloys and Compounds* **1994**, *205*, 183–189, DOI `10.1016/0925-8388(94)90787-0`.

[40] D. Johrendt, A. Mewis, *Z. Naturforsch., B (Zeitschrift für Naturforschung B)* **1996**, *51*, 655–664, DOI `10.1515/znb-1996-0506`.

[41] J. Glaser, *Zeitschrift für anorganische und allgemeine Chemie* **2002**, *628*, 1946–1950, DOI `10.1002/1521-3749(200209)628:9/10<1946::AID-ZAAC1946>3.0.CO;2-I`.

[42] V. Hlukhyy, T. F. Fässler, *Zeitschrift für anorganische und allgemeine Chemie* **2008**, *634*, 2316–2322, DOI `10.1002/zaac.200800272`.

[43] L. Siggelkow, V. Hlukhyy, T. F. Fässler, *Zeitschrift für anorganische und allgemeine Chemie* **2010**, *636*, 1870–1879, DOI `10.1002/zaac.201000083`.

[44] P. I. Krypyakevych, G. I. Oleksiv, *Dopovidi Akademii Nauk Ukrains'koi RSR, Seriya A: Fiziko-Tekhnichnita Matematichni Nauki* **1970**, *1970*, 63–65, DOI `10.1086/ahr/76.5.1574`.

[45] K. Kudo, H. Hiiragi, T. Honda, K. Fujimura, H. Idei, M. Nohara, *Journal of the Physical Society of Japan* **2020**, *89*, 013701, DOI `10.7566/JPSJ.89.013701`.

[46] S. Pyon, K. Kudo, J.-i. Matsumura, H. Ishii, G. Matsuo, M. Nohara, H. Hojo, K. Oka, M. Azuma, V. O. Garlea, K. Kodama, S.-i. Shamoto, *Journal of the Physical Society of Japan* **2014**, *83*, 093706, DOI `10.7566/JPSJ.83.093706`.

[47] D. Hirai, R. Kawakami, O. V. Magdysyuk, R. E. Dinnebier, A. Yaresko, H. Takagi, *Journal of the Physical Society of Japan* **2014**, *83*, 103703, DOI `10.7566/JPSJ.83.103703`.

[48] L. Siggelkow, V. Hlukhyy, T. F. Fässler, *Zeitschrift für anorganische und allgemeine Chemie* **2017**, *643*, 1424–1430, DOI `10.1002/zaac.201700180`.

[49] L. G. Akselrud, V. I. Yarovets, O. I. Bodak, Y. P. Yarmolyuk, E. I. Gladyshevskii, *Soviet Physics. Crystallography* **1976**, *21*, 210–211.

[50] V. G. Terziev, *Soviet Physics. Crystallography* **1978**, *23*, 531–533.

[51] L. Siggelkow, V. Hlukhyy, T. F. Fässler, *Zeitschrift für anorganische und allgemeine Chemie* **2011**, *637*, 2000–2006, DOI `10.1002/zaac.201100306`.

[52] H. Probst, A. Mewis, *Zeitschrift für anorganische und allgemeine Chemie* **1991**, *597*, 173–182, DOI `10.1002/zaac.19915970120`.

[53] A. Reich, M. Panthöfer, H. Modrow, U. Wedig, M. Jansen, *Journal of the American Chemical Society* **2004**, *126*, 14428–14434, DOI `10.1021/ja0401693`.

[54] H.-Y. Zhao, J. Wang, L.-Y. Ai, Y. Liu, *Journal of Physical Chemistry A* **2016**, *120*, 6303–6308, DOI `10.1021/acs.jpca.6b05258`.

[55] J. J. Guo, H. Y. Zhao, J. Wang, L. Y. Ai, Y. Liu, *Journal of Chemical Physics* **2017**, *146*, 064310, DOI `10.1063/1.4975988`.

[56] H.-Y. Zhao, L.-Y. Ai, H.-M. Ma, J.-J. Guo, J.-L. Qiu, J. Wang, Y. Liu, *Journal of Physical Chemistry C* **2019**, *123*, 17639–17643, DOI `10.1021/acs.jpcc.8b12141`.

[57] E. Zintl, W. Haucke, *Zeitschrift für Elektrochemie und angewandte physikalische Chemie* **1938**, *44*, 104–111.

[58] O. Moze, C. H. de Groot, F. R. de Boer, K. Buschow, *Journal of Alloys and Compounds* **1996**, *235*, 62–65, DOI `10.1016/0925-8388(95)02098-5`.

[59] M. El-Hagary, H. Michor, M. Wind, E. Bauer, G. Hilscher, P. Rogl, *Journal of Alloys and Compounds* **2004**, *367*, 239–245, DOI `10.1016/j.jallcom.2003.08.045`.

[60] H. Witte, *Zeitschrift für Angewandte Mineralogie* **1938**, *1*, 255–268.

[61] G. Bergman, J. L. T. Waugh, *Acta Crystallographica* **1956**, *9*, 214–217, DOI `10.1107/S0365110X56000632`.

[62] G. Bergman, J. L. T. Waugh, *Acta Crystallographica* **1953**, *6*, 93–94, DOI `10.1107/S0365110X53000223`.

[63] H. Nyman, S. Andersson, *Acta Crystallographica, Section A: Crystal Physics, Diffraction, Theoretical and General Crystallography* **1979**, *35*, 934–937, DOI `10.1107/S0567739479002084`.

4 Conclusion

The structural variety in ternary polar intermetallic compounds, containing alkaline earth metal, transition metal (iron, cobalt or nickel) and tetrel element (silicon or germanium), reflects within this thesis. In most cases, compounds were found with known structure types in new element combinations. Typically, high temperatures are required to react the elements, however, different reaction pathways are possible, including such with used containers. At too low temperatures, formed binary phases are not activated for further reaction and at too high temperatures, possible reactions with the container materials affect the samples and compositions. Thus it is difficult to control the exact stoichiometry, especially for small batches.

$CaFe_2Ge_2$ was found that fills the gap left by reported homologs and solid solution series. Since it decomposes at high temperatures, activation of the educts via ball milling was required to react at lower temperatures. Crystallographic and magnetic properties agreed well with trends reported for related solid solutions. Experiments using it as parent compound for substitution were challenging and no superconductivity could be achieved.

Compounds $Ca_{1-x}Co_6Ge_6$ and $CaFe_6Ge_6$ were found with and without order in channels, growing as three-component twins. Whereas the iron compounds orders readily, the cobalt homolog prefers the unordered modification. This shows how intermetallic compounds may form with different valence electron concentrations in the same parent type, but are affected in structural details.

Nickel silicide compounds proved to be special and don't follow general trends. $SrNi_2Si_2$ does not behave like well-known 122 structures and makes a complicated distortion variant, SrNiSi adopts a structure of the aliovalent pnictide system. Compared to BaPdP, it is placed at the border of intermetallic and Zintl phases. $BaNi_{16}Si_{12}$ forms a unique structure which marks two records: (i) regarding the low amount of alkaline earth metal; (ii) regarding the coordination number of a single atom in intermetallic compounds. It is the first time that a catalan pentakis dodecahedron was formed in a solid structure and confirms the stability of this hypothetical fragment.

In the investigated magnesium compounds, due to its size and electronegativity, the Mg atoms were not able to break the the polyanionic network into 2-dimensional layers. Instead octahedral clusters formed in G-phases.

For investigated compounds it was observed that aliovalent substitution of elements may or may not lead to a different crystal structure. Electronic as well as atomic size contribute to the structure formation. This is a confirmation of the trend observed when going from electronically balanced Zintl phases to intermetallic systems, such as Hume-Rothery or Laves phases.

In this work, systems and compounds were chosen close to expected structural instabilities. Whereas DOS calculations for found crystal structures seemed promising for many compounds, no superconductivity could be observed in measurements.

5 Publications and Manuscripts

5.1 $CaFe_2Ge_2$ with square-planar iron layers – Closing a gap in the row of CaT_2Ge_2 (T = Mn–Zn)

Braun, T.; Hlukhyy, V.

published in

J. of Solid State Chem. **276**, 368–375 (2019)

Reprinted with permission from Braun, T.; Hlukhyy, V.; *J. of Solid State Chem.* **276**, 368–375 (2019)

Journal of Solid State Chemistry 276 (2019) 368–375

Contents lists available at ScienceDirect

Journal of Solid State Chemistry

journal homepage: www.elsevier.com/locate/jssc

$CaFe_2Ge_2$ with square-planar iron layers – Closing a gap in the row of CaT_2Ge_2 (T = Mn–Zn)

Thomas Braun, Viktor Hlukhyy [*]

Department of Chemistry, Technische Universität München, Lichtenbergstr. 4, 85747, Garching, Germany

ARTICLE INFO

Keywords:
Iron layer
Germanide
$ThCr_2Si_2$-type structure
Ferromagnetism
Superconductivity

ABSTRACT

The intermetallic compound $CaFe_2Ge_2$ has been synthesized by ball-milling a stoichiometric mixture of pre-melted “FeGe” alloy with elemental Ca and subsequent annealing in welded niobium ampoule in a resistance furnace. Its crystal structure has been investigated by powder X-ray diffraction method: $ThCr_2Si_2$ structure type (space group $I4/mmm$, $Z = 2$), $a = b = 3.99366(4)$ Å, $c = 10.7060(1)$ Å. Like iron-based superconductors, the main structural motif in $CaFe_2Ge_2$ is a square-planar layer of Fe atoms that are tetrahedrally coordinated by Ge atoms. The (Fe_2Ge_2) layers are alternating along the c-axis with the layers of Ca^{2+} cations and are interconnected via Ge–Ge bonds, resulting in a three-dimensional $(Fe_2Ge_2)^{2-}$ polyanionic framework. The topological analysis of the Electron Localization Function (ELF) confirms 3D character of (Fe_2Ge_2) layers similar to reported 122 iron tetrelides YFe_2Ge_2 and $CaFe_2Si_2$. $CaFe_2Ge_2$ fills the gap in the row of CaT_2Ge_2 (T = Mn–Zn), being a fully-substituted variant (Ge/As) of the well-known superconducting collapsed tetragonal $CaFe_2As_2$. Magnetic measurements revealed the occurrence of ferromagnetic order in $CaFe_2Ge_2$ below 50 K.

1. Introduction

The $ThCr_2Si_2$ structure type (122) has been known for more than 50 years and up to now more than 600 representatives have been found [1–3]. This number becomes even bigger when the solid solutions of substitution are taken into account. Representatives of this structure type with the general formula AT_2X_2 (A = alkaline (earth), lanthanoid or actinoid; T = transition metal; X = group III–V element), are known for the high flexibility regarding the X–X distance and hence the c lattice parameter. The structures can be separated into collapsed (cT) and uncollapsed tetragonal (ucT), having shorter X–X distance with strong interlayer interactions or longer X–X distances with non-bonding contacts, respectively [4,5]. Some of these compounds have been reported to undergo a reversible temperature-induced phase transition [6,7]. This phase transition is often accompanied with distortion of the squared T-atomic layer and magnetic ordering or appearance of superconductivity [8–11].

The discovery of superconductivity in $Ba_{1-x}K_xFe_2As_2$ ($T_C = 38$ K) made this structural family a promising research subject [12]. The substitution in parent 122 structures can lead to various new superconducting materials, e.g. $BaFe_{2-x}Co_xAs_2$ or $BaFe_2As_{2-x}P_x$, where either the alkaline earth element, the transition metal or the main group element is partially replaced by another element of neighboring group [13,14]. However, also iron containing 122 compounds are known, which show superconductivity without the need of doping or solid solution, such as AFe_2As_2 (A = K, Rb, Cs, Ca) and YFe_2Ge_2 [15–18]. Replacement of arsenic by non-toxic elements is very important in terms of application as superconductor. The substitution of pnictide by tetrelide atom leads, as a rule, to increasing magnetism in iron-containing 122 compounds [19].

The investigations of superconductivity and magnetism have not been limited to iron-based 122 compounds, but have been extend to other transition metals like Mn, Co, or Ni. The structural phase transition in Co-based 122 compounds from ucT to cT form, induced by physical or chemical pressure, causes dramatic changes in the magnetism of these systems [20,21]. Numerous Ni-based compounds show superconductivity for the undoped 122 compositions: e.g. pnictides $SrNi_2P_2$, $SrNi_2As_2$, $BaNi_2P_2$, and $BaNi_2As_2$ [22–25], chalcogenides KNi_2S_2 and KNi_2Se_2 [26,27], and germanide $SrNi_2Ge_2$ [28]. However, the chemical substitution in these phases often causes the increase of critical temperatures: T_c of 3.2 K in $Sr(Pd_{1-x}Ni_x)_2Ge_2$ [29], T_c of 2.9 K in $BaNi_2(Ge_{1-x}P_x)_2$ [30], and T_c of 3.0 K in $SrNi_2(Ge_{1-x}P_x)_2$ [7]. In the course of our recent investigations of other $ThCr_2Si_2$-type structure representatives AeT_2X_2 (Ae = alkaline earth; T = transition metal; X = group IV–V element) $CaCo_2Si_2$, $SrCo_2Si_2$, $CaFe_2Si_2$, $CaRh_2Si_2$, $CaFe_{2-x}Rh_xSi_2$, $BaCo_2Ge_2$,

---

[*] Corresponding author.
E-mail address: viktor.hlukhyy@lrz.tum.de (V. Hlukhyy).

https://doi.org/10.1016/j.jssc.2019.05.032
Received 26 March 2019; Received in revised form 18 May 2019; Accepted 19 May 2019

$SrNi_{2-x}Sb_2$, and $BaNi_2Ge_2$ have been discovered and characterized [31–34].

Within the row of compounds CaT_2Ge_2 (T = Mn–Zn) only the iron-containing one was missing [35,36]. Welter and Malaman investigated the solid solution $CaMn_{2-x}Fe_xGe_2$ ($0 \leq x \leq 1.9$) [37], synthesized by melting the elements in an induction furnace and subsequent annealing. For $x \geq 1.2$ the obtained samples contained rising amounts of air-sensitive impurity phases and the preparation of the fully-substituted iron compound was not achieved. In the present work, we describe a new experimental approach that successfully leads to almost phase-pure air-stable $CaFe_2Ge_2$ – the ball-milling of stoichiometric mixture of pre-melted "FeGe" alloy with elemental Ca and subsequent annealing. This method can be potentially used for synthesis of other intermetallic compounds, which cannot be obtained by classical high-temperature synthetic routes. The title compound $CaFe_2Ge_2$ is homologue to recently reported $CaFe_2Si_2$ [34] and a fully-substituted variant (As/Ge) of the well-known superconductor $CaFe_2As_2$ (collapsed tetragonal modification) [18]. Preliminary results of these investigations have been briefly reported recently [38].

2. Experimental section

2.1. Synthesis

The sample of $CaFe_2Ge_2$ was prepared from the pure elements. Starting materials were commercially available elements: ingots of calcium (Alfa Aesar, 99.5%, redistilled), iron granules (Alfa Aesar, 99.98%), and germanium pieces (Evochem GmbH, 99.999%). At the first stage, the precursor with composition Fe:Ge = 1:1 was prepared by arc-melting the elements in an arc-furnace equipped with a water-cooled copper hearth (Mini Arc Melting System, MAM-1, Johanna Otto GmbH) placed in an argon filled Glovebox (MBraun 20G, argon purity 99.996%). The resulting pellet was grinded with an agate mortar. At the next stage, the "FeGe" powdered sample and chopped Ca-pieces in molar ratio 2:1.1 were ball-milled using a milling system *Pulverisette* (Fritsch GmbH) with the grinding bowl and balls made of hardened steel. The materials were enclosed in a container equipped with a gas-tight lock-system under an argon atmosphere. After milling, the powder was cold-pressed and the pellet annealed in an evacuated graphitized silica tube at 800 °C for 3 days. The polycrystalline sample is stable against air and moisture. No single crystals suitable for X-ray analysis could be obtained.

2.2. X-ray investigations

The sample was characterized with powder X-ray diffraction (PXRD) on a STOE Stadi-P with Cu-$K_{\alpha1}$ source (λ = 1.54058 Å), curved Ge(111)-monochromator and DECTRIS MYTHEN 1K detector. In order to determine the lattice parameters of $CaFe_2Ge_2$ Si-powder was used as external standard. The powder diffractogram (Fig. 1) was corrected using polynomial functions calculated from the matching mode of the experimental and standard Si-peak positions using the WinXPOW package [39]. Phase analysis was performed using structure models from database [35,40]. Rietveld analysis has been done with the Fullprof Suite [41]. Reflections of the main phase were indexed in tetragonal unit cell and the structure of $CaFe_2Si_2$ [34] was chosen as a starting model for refinement. Peak profile shape was described by a pseudo-Voigt function; background of the diffraction pattern was fitted using a linear interpolation between selected data points in non-overlapping regions. Scale factor, lattice parameters, fractional coordinates of atomic sites and their isotropic displacement parameters, profile shape parameters, and half width (Caglioti) parameters were varied during the Rietveld refinement. The sample contained only 1.9(1)% of Fe_3Ge as impurity phase. Obtained data and parameters are given in Tables 1 and 2. Interatomic distances for $CaFe_2Ge_2$ are listed in Table 3. Crystallographic data for the structure in this paper has been deposited with the Cambridge Crystallographic Data Centre, CCDC, 12 Union Road, Cambridge CB21EZ, UK (Fax:

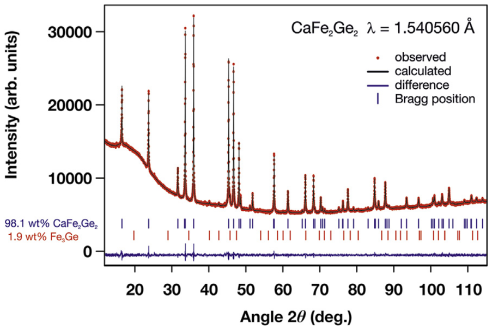

Fig. 1. Results of Rietveld refinement for powder X-ray diffraction data of $CaFe_2Ge_2$. The calculated positions of the Bragg reflections for $CaFe_2Ge_2$ and Fe_3Ge are shown by the blue (top) and red (bottom) rows of vertical tick marks, respectively. (For interpretation of the references to colour in this figure legend, the reader is referred to the Web version of this article.)

Table 1
Crystal data and structure refinement for $CaFe_2Ge_2$ (Rietveld method, powder-X-ray diffraction data, T = 298 K).

Empirical formula	$CaFe_2Ge_2$
Formula weight/g mol^{-1}	296.992
Space group, Z	*I*4/*mmm*, 2
Unit cell dimensions/Å	$a = b = 3.99366(4)$ $c = 10.7060(1)$
Unit cell volume/Å^3	$V = 170.753(3)$
Calculated density/g cm^{-3}	5.78
Step scan increment 2θ/deg	0.015
2θ range/deg	10.02 to 115.02
No. of profile points	7001
Program	*FullProf*
Shape param η	1.07624
Caglioti parameters	$U = 0.02723$ $V = -0.00830$ $W = 0.01798$
No. of reflections	52
No. of refined parameters	22
R_B	0.017
R_P	0.009
R_{exp}	0.012
R_{wp}	0.012
χ^2	1.04

Table 2
Atomic coordinates and equivalent isotropic displacement parameters for $CaFe_2Ge_2$ (space group *I*4/*mmm*).

	Wyckoff position	x	y	z	U_{iso}/Å^2 × 10^3
Ca	2*a*	0	0	0	15.2(5)
Fe	4*d*	0	1/2	1/4	13.6(3)
Ge	4*e*	0	0	0.37767(5)	14.8(3)

Table 3
Interatomic distances for $CaFe_2Ge_2$ and selected corresponding integrated crystal orbital Hamilton populations (iCOHPs) values at E_F.

		Distance/Å	-iCOHP/ eV			Distance/Å	-iCOHP/ eV
Ca	4 × Ca	3.99366(4)	–	Fe	4 × Fe	2.82394(2)	1.151
	8 × Ge	3.1129(3)	0.607		4 × Ge	2.4198(4)	2.513
	8 × Fe	3.33930(3)	0.447	Ge	1 × Ge	2.6193(8)	1.777

+44-1223-336-033; e-mail: deposit@ccdc.cam.ac.uk, http://www.ccdc.cam.ac.uk) and can be obtained free of charge on quoting the depository number CSD- 1905672.

2.3. Thermal analysis

Thermal stability was measured via differential thermal analysis (DTA) up to 900 °C using a differential scanning calorimeter (NETZSCH DSC 404C). The sample of $CaFe_2Ge_2$ was enclosed in a custom-made niobium container by crimping the niobium in the upper part of the crucible using a pipe tong and subsequent welding. Another empty niobium container was used as reference. To prevent corrosion of the containers, an argon flow rate of $50\,mL\,min^{-1}$ was used. Three heating/cooling cycles with a rate of $5\,°C\,min^{-1}$ were performed. The results of the thermograms were evaluated with the software Netzsch - Proteus Analysis [42]. After DTA experiment the container was opened. PXRD showed no phase change or decomposition of the title compound.

2.4. Magnetic measurements

Magnetic properties were measured using a MPMS XL5 SQUID magnetometer (Quantum Design). A gelatin capsule was filled with 40 mg of the sample and inserted into a plastic straw. The data were corrected for the susceptibility of the sample holder and the diamagnetic contributions of core electrons (Pascal's constants). Zero-field-cooled (ZFC) susceptibility was measured upon heating the sample from 2 to 300 K in a magnetic field of 0.1 kOe after the sample had been precooled in a zero magnetic field. The field-cooled (FC) susceptibility was taken when the sample was cooled from 300 to 2 K in a magnetic field of 0.1 kOe. Field-dependent measurements were carried out at 2 and 300 K with the field sweeping from −50 to 50 kOe.

2.5. Electronic structure calculations

Electronic structure calculations have been investigated using the experimentally determined structural data. The linear muffin-tin orbital (LMTO) method in the atomic sphere approximation (ASA) was employed using the tight-binding (TB) program TB-LMTO-ASA [43]. Radii of the muffin-tin spheres were determined after Jepsen and Andersen [44]. Total and projected density of states (DOS) and the band structure including orbital-decomposed "fat bands" were generated with no spin polarization. The basis set contained s-d orbitals for iron, s-p for germanium and s, d for calcium. Ca 3p and Ge 3d orbitals were employed using the downfolding technique [45]. Chemical bonding was investigated using the crystal orbital Hamilton populations (COHP) [46], which combines the total density of states and elements of the Hamiltonian corresponding to the overlap population. Positive values represent bonding and negative values antibonding contributions.

3. Results and discussion

$CaFe_2Ge_2$ is the second compound after $Ca_{0.5}Fe_3Ge_3$ [47] reported in the ternary system Ca–Fe-Ge. Difficulties in obtaining ternary compounds in this system via well-known arc-melting technique are likely related to the immiscibility of the components Ca and Fe in the liquid state. Up to now, the row of CaT_2Ge_2 compounds with light transition metals (T) has been reported: $CaMn_2Ge_2$, $CaCo_2Ge_2$, $CaNi_2Ge_2$, $CaCu_2Ge_2$ and $CaZn_2Ge_2$ [36]. All these compounds could be easily synthesized by arc-melting. The existence of the lighter homologue $CaFe_2Si_2$ as well as electron-richer $CaFe_2P_2$ and $CaFe_2As_2$ has also been established [34,48–50]. The most of the rare earth containing compounds with iron RFe_2Ge_2 (R = La–Nd, Sm, Gd–Yb, Th, U, Np) have been reported as well [3,18,52,66–74]. Cell parameters and selected interatomic distances of all these compounds are collected in Table 4. The 122 pseudo-ternary calcium iron germanides have been synthesized by mixing of calcium with a rare earth metal: $La_{0.59}Ca_{0.41}Fe_2Ge_2$, $Ce_{1-x}Ca_xFe_2Ge_2$ ($x = 0.12$–0.80), $Gd_{1-x}Ca_xFe_2Ge_2$ ($x = 0.04$–0.74), $Yb_{1-x}Ca_xFe_2Ge_2$ ($x = 0.25$–0.70) [51] or iron with manganese in $CaMn_{2-x}Fe_xGe_2$ ($x = 0$–1.9, while the samples with $x > 1.2$ contain increasing amounts of binary impurities). The last solid solution ends with $CaMn_{0.1}Fe_{1.9}Ge_2$, which is the iron-richest 122 calcium iron germanide reported so far [37]. The current work is the first to give experimental data for the $CaFe_2Ge_2$ ternary phase.

3.1. Crystal structure

$CaFe_2Ge_2$ crystallizes in the $ThCr_2Si_2$-type (space group $I4/mmm$, $Z = 2$). The structure along the a axis is illustrated in Fig. 2. The structure type has been previously discussed in detail for isostructural compounds [2,3,52]. The structure of $CaFe_2Ge_2$ consists of $(Fe_2Ge_2)^{2-}$ network with a square lattice of iron atoms, which are tetrahedrally coordinated by four germanium atoms. Germanium is in form of Ge_2^{6-} dumbbells linking the (Fe_2Ge_2) layers together. Calcium is situated in the cavity between these dumbbells and the iron lattices. The experimental established structural data of $CaFe_2Ge_2$ agree well with those of the isostructural relatives (Table 4). They also fit perfectly into the extrapolation of structural parameters reported for $CaMn_{2-x}Fe_xGe_2$ (Fig. 3).

The Fe–Fe-distance of 2.824(1) Å is slightly elongated compared to those in $CaFe_2Si_2$ (2.785 Å) [34] as well as in superconducting YFe_2Ge_2 (2.803 Å) [16], $CaFe_2As_2$ (2.738 Å) [53], and equiatomic MgFeGe (2.747 Å) [66], but much longer then for elemental iron (2.48 Å). This T–T distance in $CaFe_2Ge_2$ is short among the row of CaT_2Ge_2 compounds (Table 4), causing the large c/a value of 2.68. The shortest interatomic distance of 2.420(1) Å in the $CaFe_2Ge_2$ compound occurs between Fe and Ge, which is longer comparing to that of superconducting YFe_2Ge_2 (2.345 Å) [11], but shorter than in MgFeGe (2.473 Å) [66]. The value of tetrahedral angle α of 111.2(1)° (Ge-Fe-Ge, Fig. 2) is close to the value of ideal tetrahedral angle (109.4°) and lies between those of MgFeGe (103.6 Å) [66] and YFe_2Ge_2 (115.4° Å) [16]. The Ge–Ge-distance of 2.619(1) Å is somewhat shorter than in YFe_2Ge_2 (2.721 Å) and larger than in elemental germanium (2.445 Å), but fits well with Ge–Ge distances in the $CaMn_2Ge_2$, $CaCo_2Ge_2$ and $CaNi_2Ge_2$ and (2.53–2.67 Å) [1,67]. This Ge–Ge distance of 2.619(1) Å can be actually considered as a covalent Ge–Ge bond, as will be shown by electronic structure calculations (Section 3.3). The layers are therefore linked by Ge–Ge-contacts and title compound belongs to the "collapsed" tetragonal 122-compounds. A more detailed view on related 122 compounds, comparisons and trends can be found in the previous publication on $CaFe_2Si_2$ [34].

A differential thermal analysis did not show any phase transition up to 900 °C, which would be caused e.g. by breaking of Ge–Ge-bonds or distortion of the Fe-squared layers. However, as show further investigations, the compound is metastable and decomposes peritect(oid)ically at higher temperatures. This could be approved by arc melting $CaFe_2Ge_2$ pressed into a pellet in the glove box. A PXRD after the melting procedure showed a complete decomposition into secondary phases.

3.2. Magnetic properties

The close relation of $CaFe_2Ge_2$ to the superconducting $CaFe_2As_2$ (collapsed tetragonal modification) [18] and YFe_2Ge_2 gave reasons to investigate magnetic properties of the compound, which depends entirely on the magnetic interactions between the Fe atoms within or between the Fe-squared layers. As $FeGe_x$ impurities are strongly magnetic [68] and even in small quantities can prevent precise determination of the bulk physical properties of main phase, the numerous efforts were made (according to the synthetic route described in Section 2.1) in order to improve the purity of $CaFe_2Ge_2$ sample. One of the best in this sense sample (Fig. 4), containing 19.7 and 0.7 wt% of paramagnetic $CaFe_6Ge_6$ [69] and diamagnetic CaO [70], respectively, was characterized by susceptibility measurements in ZFC/FC (zero-field-cooled/field-cooled) mode at 0.1 kOe, and by magnetization isotherms at different

Table 4
Lattice parameters, selected interatomic distances and tetrahedral angles (α) in RT_2X_2 (Ae = Ca, rare-earth metal, actinoide; T = transition metal, X = Si, Ge, P. As) compounds (*I*4/*mmm* space group).

	a/Å	c/Å	V/Å^3	c/a	z	$d(T\text{–}T)$/Å	$d(X\text{–}X)$/Å	α/deg	Lit.
$CaFe_2X_2$									
$CaFe_2Si_2$	3.94	10.19	157.99	2.59	0.375	2.78	2.55	114.40	[34]
$CaFe_2P_2$	3.86	9.99	148.39	2.59	0.364	2.73	2.71	118.74	[50]
$CaFe_2As_2$	3.87	11.73	175.86	3.03	0.367	2.74	3.13	109.57	[53]
CaT_2Ge_2									
$CaMn_2Ge_2$	4.16	10.86	187.51	2.61	0.384	2.94	2.53	110.21	[52]
$CaFe_2Ge_2$	3.994(1)	10.706(1)	170.75	2.68	0.3777(1)	2.824(1)	2.620(1)	111.22(5)	this work
$CaCo_2Ge_2$	3.99	10.30	163.95	2.58	0.371	2.82	2.67	116.24	[52]
$CaNi_2Ge_2$	4.07	9.99	165.83	2.45	0.370	2.88	2.60	119.20	[52]
$CaCu_2Ge_2$	4.14	10.22	174.96	2.47	0.379	2.93	2.47	114.86	[52]
$CaZn_2Ge_2$	4.21	10.85	192.31	2.58	0.386	2.98	2.47	109.94	[54]
$CaRu_2Ge_2$	4.25	9.99	180.67	2.35	0.368	3.01	2.63	121.81	[55]
$CaRh_2Ge_2$	4.14	10.36	177.76	2.50	0.374	2.93	2.61	116.37	[55]
$CaPd_2Ge_2$	4.33	9.99	187.28	2.31	0.376	3.06	2.47	119.50	[55]
$CaAg_2Ge_2$	4.33	10.93	204.93	2.52	0.389	3.06	2.43	109.88	[54]
$CaIr_2Ge_2$	4.15	10.32	177.75	2.49	0.376	2.93	2.57	116.01	[55]
$CaAu_2Ge_2$	4.43	10.23	200.76	2.31	0.379	3.13	2.48	118.43	[56]
RFe_2Ge_2									
YFe_2Ge_2	3.96	10.46	164.31	2.64	0.370	2.80	2.72	115.37	[16]
$LaFe_2Ge_2$	4.11	10.56	178.06	2.57	0.372	2.90	2.71	115.81	[52]
$CeFe_2Ge_2$	4.07	10.48	173.31	2.58	0.377	2.88	2.58	113.61	[57]
$PrFe_2Ge_2$	4.06	10.51	173.23	2.59	0.375	2.87	2.63	114.20	[58]
$NdFe_2Ge_2$	4.04	10.49	170.84	2.60	0.375	2.85	2.62	113.88	[52]
$SmFe_2Ge_2$	4.00	10.46	167.45	2.61	0.378	2.83	2.55	112.45	[57]
$GdFe_2Ge_2$	3.99	10.49	166.84	2.63	0.375	2.82	2.62	113.38	[1]
$TbFe_2Ge_2$	3.97	10.46	164.71	2.64	0.380	2.81	2.51	111.06	[59]
$DyFe_2Ge_2$	3.96	10.45	163.61	2.64	0.38	2.80	2.51	111.06	[60]
$HoFe_2Ge_2$	3.95	10.44	162.63	2.64	0.384	2.79	2.42	109.34	[61]
$ErFe_2Ge_2$	3.96	10.43	163.72	2.63	0.374	2.80	2.63	113.72	[62]
$TmFe_2Ge_2$	3.92	10.38	159.84	2.65	0.375	2.77	2.60	113.03	[57]
$YbFe_2Ge_2$	3.92	10.50	161.72	2.68	0.38	2.77	2.52	110.33	[60]
$ThFe_2Ge_2$	4.10	10.17	171.06	2.48	0.371	2.90	2.62	118.09	[63]
UFe_2Ge_2	4.02	9.96	160.65	2.48	0.374	2.84	2.52	117.01	[64],[a]
$NpFe_2Ge_2$	3.92	9.40	144.34	2.40	0.375	2.77	2.35	118.07	[65]

[a] Disordered with 81/19 and 19/81 at.% of Fe/Ge on the 4*d* and 4*e* site, respectively.

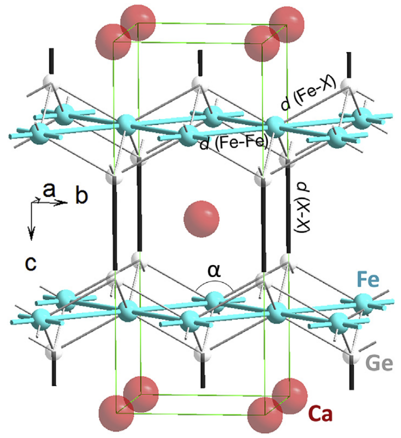

Fig. 2. Visualization of the crystal structure of $CaFe_2Ge_2$. The polyanionic $(Fe_2Ge_2)^{2-}$ network is emphasized.

temperatures (300 and 2 K) with fields up to 50 kOe (Fig. 5).

The thermal dependencies of the molar magnetic susceptibilities indicate no superconductive transition down to 1.8 K. Below 50 K susceptibility increases significantly, indicating the development of magnetic ordering, and a bifurcation between the ZFC and FC susceptibilities is observed, yielding to ferromagnetic long-range order. The effective magnetic moment of 3.63 μB/Fe atom and Weiss constant (paramagnetic Curie temperature) $\theta_p = 104$ K were obtained by fitting the data with the Curie-Weiss law in the paramagnetic temperature region between 190–300 K. The positive values of Weiss constant suggest ferromagnetic interactions in $CaFe_2Ge_2$ compound. The ferromagnetic Curie temperature $T_c \approx 44$ K was obtained from the minimum of derivative curve $d\chi/dT$ of the field-cooled magnetic susceptibilities as a function of temperature (Fig. 5a, in blue). This fits perfectly into the extrapolation of Curie temperatures reported for $CaMn_{2-x}Fe_xGe_2$ (Fig. 6). The magnetization does not achieve saturation in a field of 20 kOe, but it appears that the saturated magnetic moment is likely to be ~0.8 μ_B per formula unit. At 2 K the remanent magnetization is about 0.29 μ_B/f.u. along with a coercivity of about 263 Oe.

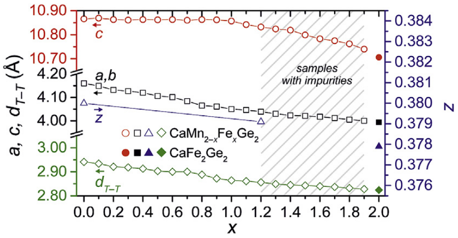

Fig. 3. Comparison of selected structural parameters of the solid solution $CaMn_{2-x}Fe_xGe_2$ reported by Welter and Malaman (hollow symbols) [37] with the values obtained for $CaFe_2Ge_2$, reported in this work (filled symbols).

3.3. *Electronic structure calculations*

The collapsed tetragonal (cT) $CaFe_2Ge_2$, containing $(Ge\text{–}Ge)^{6-}$ dimer, is electronically similar to the uncollapsed-tetragonal (ucT) $CaFe_2As_2$

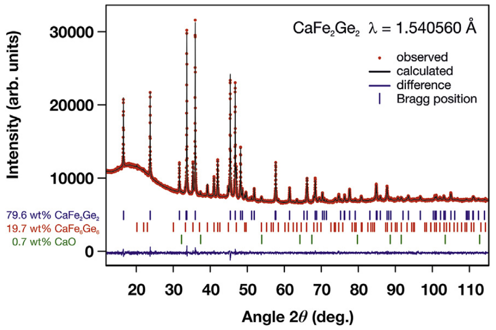

Fig. 4. Results of Rietveld refinement for powder X-ray diffraction data of CaFe$_2$Ge$_2$, used for magnetic measurements. The calculated positions of the Bragg reflections for CaFe$_2$Ge$_2$, CaFe$_6$Ge$_6$ and CaO are shown with blue (top), red (middle) or green (bottom) vertical tick marks, respectively. (For interpretation of the references to colour in this figure legend, the reader is referred to the Web version of this article.)

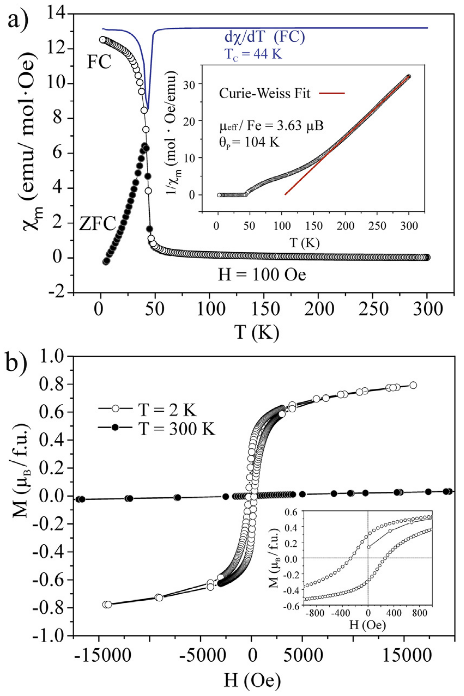

Fig. 5. Magnetic properties of CaFe$_2$Ge$_2$: a) molar magnetic susceptibility χ_m (ZFC/FC), the $d\chi/dT$ derivative (FC, blue curve) and inverse molar susceptibility $1/\chi_m$ (insert, FC) as a function of temperature; b) field-dependent magnetization measured at 300 and 2 K.

compound with non-bonded 2 × As^{3-} anions, having a similar formal charge distribution: Ca^{2+}(Fe^{2+})$_2$(Ge–Ge)$^{6-}$ *vs* Ca^{2+}(Fe^{2+})$_2$(As^{3-})$_2$. Therefore, the electronic structure has been studied with respect to the superconductivity and magnetic instability. As expected, similarities with the recently reported isostructural homologue CaFe$_2$Si$_2$ are evident [34].

Total DOS and orbital resolved pDOS for CaFe$_2$Ge$_2$ are presented in Fig. 7. The DOS is split into two blocks clearly divided by a band gap of 3 eV. The first block is located at energies between −11 and −7.5 eV.

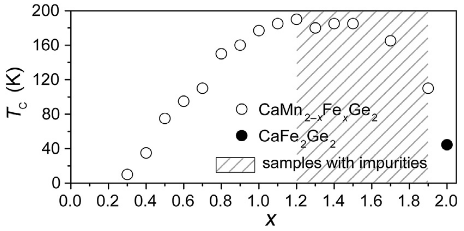

Fig. 6. Ferromagnetic Curie temperatures for CaMn$_{2-x}$Fe$_x$Ge$_2$. Hollow dots are taken from literature [37], the solid dot is for CaFe$_2$Ge$_2$, reported in this work.

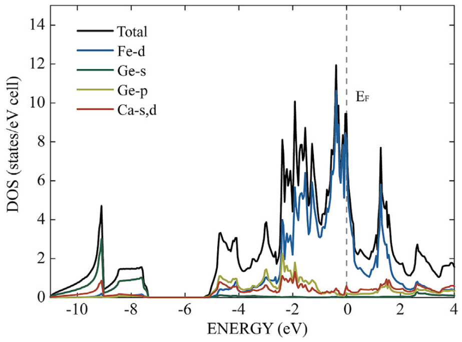

Fig. 7. Density of states (DOS) and projected DOS calculated for CaFe$_2$Ge$_2$.

Main contributions in this block come from Ge-s orbitals, with minor contributions of Ca orbitals. Above the band gap (from −5.5 eV up to energies above the Fermi level), the second DOS block is located. In the first part of the second block (between −5.5 to −1 eV) the pDOS of Fe-d, Ge-p show similar shapes, indicating a strong hybridization of these orbitals and corresponding to the covalent Fe–Ge bonds within (Fe$_2$Ge$_2$)$^{2-}$ polyanion. Here, a significant contribution of the Ca-s,d orbitals to the bonding should be noted. The DOS region between −1 and 2 eV is formed almost exclusively by Fe-d orbitals and to a lesser extent by Ge-p and Ca-s,d orbitals. There is no band gap at the Fermi level, indicating metallic character. A local DOS-maximum, which has mainly Fe-$d_{x^2-y^2}$ and $d_{xz,yz}$ character (estimated from fatband calculations, Fig. 8), is observed around the Fermi level. E_F crosses the shoulder of this sharp peak. Such DOS-peaks around the Fermi level often are correlated with a certain degree of structural or magnetic instability and in our case is confirmed by detected ferromagnetism in this compound.

In order to check interactions between the atoms, crystal orbital Hamilton population analyses (COHP) were evaluated (Fig. 9, Table 3). The strongest bonding interaction (i.e. −iCOHP value) is found for the shortest Fe–Ge contacts. This value is slightly weaker than in the recently published CaFe$_2$Si$_2$ compound [34]. Bonding orbitals for the Fe–Ge interactions are almost filled and these bonds are nearly effectively optimized at the Fermi level. The Fe–Fe COHPs show that along with the bonding also antibonding orbitals are filled at the Fermi level. The Fe–Ge bonds are stronger than Fe–Fe interactions (see iCOHPs values in Table 3), but taking into account the location of Fe-d orbitals near Fermi level, the Fe–Fe interactions play an important role for the structure stability. In contrast, the Ca–Ge and Ca–Fe interactions (iCOHP values of 0.61 and 0.45 eV/bond, respectively) are much weaker.

The bonding situation was further studied by a topological analysis of the electron density in real space using the Electron Localization Function (ELF), sketched in Fig. 10. The ELF reveals clearly a disynaptic valence basin (>0.65) between two Ge atoms of adjacent (Fe$_2$Ge$_2$) layers, indicating a localized covalent Ge–Ge bond. Similar interlayer *X*–*X* bonds

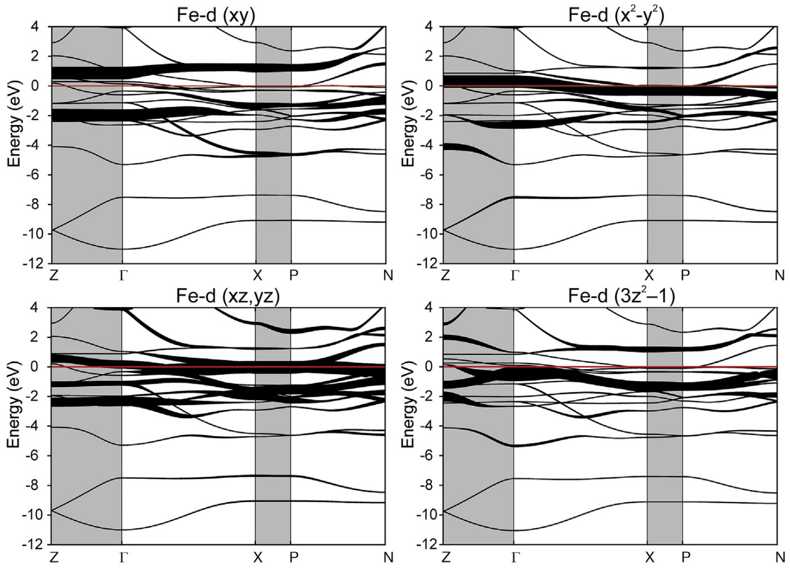

Fig. 8. Band structure of $CaFe_2Ge_2$ with fatbands (orbital resolved bands) represented for Fe(d) orbitals. The k-space paths marked with a grey background are perpendicular to the (Fe_2Ge_2) layers.

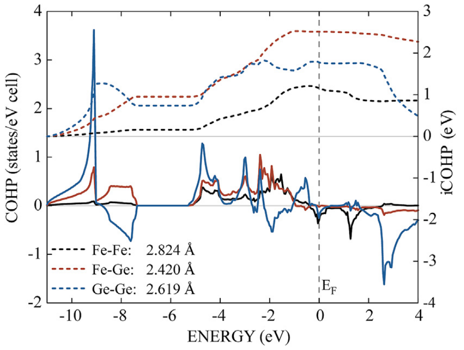

Fig. 9. Crystal orbital Hamiltonian populations (COHP) curves and integrated iCOHPs for the Fe–Fe, Fe–Ge, and Ge–Ge bonds calculated for $CaFe_2Ge_2$.

($X = $ Si, Ge) have been recently described in $CaCo_2Si_2$, $CaFe_2Si_2$ and $CaNi_2Ge_2$ [33,34,71].

4. Conclusions

Novel intermetallic compound $CaFe_2Ge_2$ has been synthesized and investigated in terms of crystal and electronic structures as well as magnetic properties. The compound fits well in the row of CaT_2Ge_2 ($T = $ Mn–Zn) regarding structural parameters. The structure can be viewed as three-dimensional $^3_\infty(Fe_2Ge_2)$ framework with encapsulated Ca-atoms. A formal electron transfer in $CaFe_2Ge_2$ may be written as $Ca^{2+}(Fe_2Ge_2)^{2-}$. The singly bonded Ge–Ge dimer in $CaFe_2Ge_2$ has a formal charge $(Ge–Ge)^{6-}$, like the two non-bonded $2 \times As^{3-}$ in uncollapsed-tetragonal (ucT) $AeFe_2As_2$ ($Ae = $ Ca, Sr, Ba). Therefore, the formal oxidation state of iron in both cases is similar – Fe^{2+}. Interestingly, for the CaT_2X_2 compounds $CaMn_2Ge_2$, $CaCo_2Si_2$, $CaNi_2Ge_2$ [33,37,71,72] with collapsed tetragonal structure corresponding $CaTX$ compounds with equiatomic isolated two-dimensional $^2_\infty(FeGe)^{2-}$ layers ($T = $ Mn, Co, Ni; $X = $ Ge, Si) exist [71,73,74]. Generally, the X–X bond formation in the polyanionic $^3_\infty(TX)^-$ network of $CaT_2X_2 = Ca(TX)_2$ can be regarded as an oxidative coupling product of $^2_\infty(TX)^{2-}$ layers of $CaTX$ compounds. Taking into account the fact that the (FeGe) layers have been already found in MgFeGe compound [66], there is a high probability of existence of

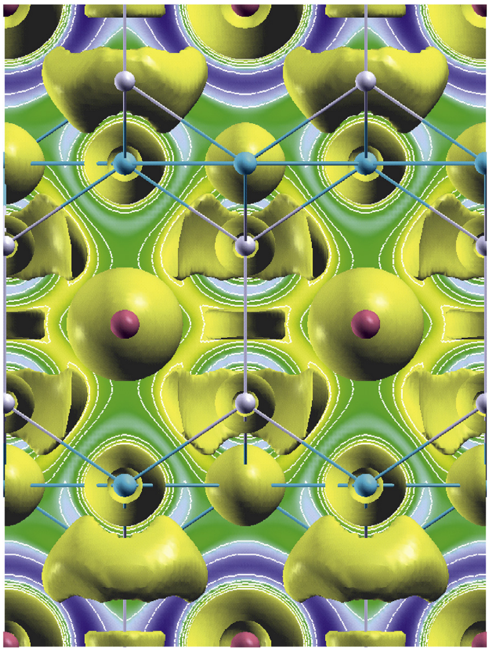

Fig. 10. Topology of the Electron Localization Function for $CaFe_2Ge_2$ calculated from the all-electron density. A 3D ELF plot with isosurface at $\eta > 0.65$ and contour line diagrams of the ELF in the *ac*-plane presents the Ge–Ge bonding.

CaFeGe compound with similar (FeGe) layers separated by Ca atoms (CeFeSi-type structure). Our efforts to synthesize CaFeGe by conventional high-temperature solid-state reaction were unsuccessful until now (like MgFeGe [66]); however, the new synthetic approach may help us to stabilize this compound. In related pnictides $AeFe_2As_2$ weak antiferromagnetic properties (SDW) have been observed, whereas the ferromagnetic ordering takes place in $CaFe_2Ge_2$. The atomic substitution in one of the positions of $CaFe_2Ge_2$ in order to suppress magnetism and induction of superconductivity should be a subject of further research.

Acknowledgments

This research was financially supported by the German Research Foundation (Deutsche Forschungsgemeinschaft, DFG, Grant HL 62/3-1) and the TUM Graduate School.

References

[1] W. Rieger, E. Parthé, Ternäre Erdalkali-und Seltene Erdmetall-Silicide und-Germanide mit $ThCr_2Si_2$-Struktur, Monatshefte Chem. 100 (1969) 444–454, https://doi.org/10.1007/BF00904086.

[2] G. Just, P. Paufler, On the coordination of $ThCr_2Si_2$ ($BaAl_4$-type compounds within the field of free parameters, J. Alloy. Comp. 232 (1996) 1–25, https://doi.org/10.1016/0925-8388(95)01939-1.

[3] Z. Ban, M. Sikirica, The crystal structure of ternary silicides ThM_2Si_2 (M = Cr, Mn, Fe, Co, Ni and Cu), Acta Crystallogr. 18 (1965) 594–599, https://doi.org/10.1107/S0365110X6500141X.

[4] S. Jia, A.J. Williams, P.W. Stephens, R.J. Cava, Lattice collapse and the magnetic phase diagram of $Sr_{1-x}Ca_xCo_2P_2$, Phys. Rev. B 80 (2009) 165107, https://doi.org/10.1103/PhysRevB.80.165107.

[5] E. Cuervo-Reyes, R. Nesper, Interlayer bonding in compounds with the $ThCr_2Si_2$ -type structure: insight on the ferromagnetism of $SrCo_2(Ge_{1-x}P_x)_2$ from electronic structure calculations, Phys. Rev. B 90 (2014) 64416, https://doi.org/10.1103/PhysRevB.90.064416.

[6] V. Keimes, A. Hellmann, D. Johrendt, A. Mewis, T. Woike, Über den Einfluß von Substitution auf die Kristallstruktur von $SrNi_2P_2$, Z. Anorg. Allg. Chem. 624 (1998) 830–836, https://doi.org/10.1002/(SICI)1521-3749(199805)624:5<830:AID-ZAAC830>3.0.CO;2–6.

[7] V. Hlukhyy, A.V. Hoffmann, V. Grinenko, J. Scheiter, F. Hummel, D. Johrendt, T.F. Fässler, Structural instability and superconductivity in the solid solution $SrNi_2(P_{1-x}Ge_x)_2$, Phys. Status Solidi B 254 (2017) 1600351, https://doi.org/10.1002/pssb.201600351.

[8] D. Johrendt, H. Hosono, R.-D. Hoffmann, R. Pöttgen, Structural chemistry of superconducting pnictides and pnictide oxides with layered structures, Z. Kristallogr. 226 (2011) 435–446, https://doi.org/10.1524/zkri.2011.1363.

[9] H. Hosono, K. Tanabe, E. Takayama-Muromachi, H. Kageyama, S. Yamanaka, H. Kumakura, M. Nohara, H. Hiramatsu, S. Fujitsu, Exploration of new superconductors and functional materials, and fabrication of superconducting tapes and wires of iron pnictides, Sci. Technol. Adv. Mater. 16 (2016) 33503, https://doi.org/10.1088/1468-6996/16/3/033503.

[10] J. Paglione, R.L. Greene, High-temperature superconductivity in iron-based materials, Nat. Phys. 6 (2010) 645–658, https://doi.org/10.1038/NPHYS1759.

[11] A.A. Kordyuk, Iron-based superconductors: magnetism, superconductivity, and electronic structure (Review Article), Low Temp. Phys. 38 (2012) 888, https://doi.org/10.1063/1.4752092.

[12] M. Rotter, M. Tegel, D. Johrendt, Superconductivity at 38 K in the iron arsenide $(Ba_{1-x}K_x)Fe_2As_2$, Phys. Rev. Lett. 101 (2008) 107006, https://doi.org/10.1103/PhysRevLett.101.107006.

[13] J.G. Analytis, J.-H. Chu, R.D. McDonald, S.C. Riggs, I.R. Fisher, Enhanced Fermi-surface nesting in superconducting $BaFe_2(As_{1-x}P_x)_2$ revealed by the de Haas-van Alphen effect, Phys. Rev. Lett. 105 (2010) 207004, https://doi.org/10.1103/PhysRevLett.105.207004.

[14] A.S. Sefat, R. Jin, M.A. McGuire, B.C. Sales, D.J. Singh, D. Mandrus, Superconductivity at 22 K in Co-doped $BaFe_2As_2$ crystals, Phys. Rev. Lett. 101 (2008) 117004, https://doi.org/10.1103/PhysRevLett.101.117004.

[15] Z. Bukowski, S. Weyeneth, R. Puzniak, J. Karpinski, B. Batlogg, Bulk superconductivity at 2.6 K in undoped $RbFe_2As_2$, Physica C 470 (2010) S328–S329, https://doi.org/10.1016/j.physc.2009.11.103.

[16] J. Chen, K. Semeniuk, Z. Feng, P. Reiss, P. Brown, Y. Zou, P.W. Logg, G.I. Lampronti, F.M. Grosche, Unconventional superconductivity in the layered iron germanide YFe_2Ge_2, Phys. Rev. Lett. 116 (2016) 127001, https://doi.org/10.1103/PhysRevLett.116.127001.

[17] K. Sasmal, B. Lv, B. Lorenz, A.M. Guloy, F. Chen, Y.-Y. Xue, C.-W. Chu, Superconducting Fe-based compounds $(A_{1-x}Sr_x)Fe_2As_2$ with A=K and Cs with transition temperatures up to 37 K, Phys. Rev. Lett. 101 (2008) 107007, https://doi.org/10.1103/PhysRevLett.101.107007.

[18] D.-Y. Chen, J. Yu, B.-B. Ruan, Q. Guo, L. Zhang, Q.-G. Mu, X.-C. Wang, B.-J. Pan, G.-F. Chen, Z.-A. Ren, Superconductivity in undoped $CaFe_2As_2$ single crystals, Chin. Phys. Lett. 33 (2016) 67402, https://doi.org/10.1088/0256-307X/33/6/067402.

[19] D. Guterding, H.O. Jeschke, I.I. Mazin, J.K. Glasbrenner, E. Bascones, R. Valentí, Nontrivial role of interlayer cation states in iron-based superconductors, Phys. Rev. Lett. 118 (2017) 17204, https://doi.org/10.1103/PhysRevLett.118.017204.

[20] K. Kovnir, W.M. Reiff, A.P. Menushenkov, A.A. Yaroslavtsev, R.V. Chernikov, M. Shatruk, "Chemical metamagnetism": from antiferromagnetic $PrCo_2P_2$ to ferromagnetic $Pr_{0.8}Eu_{0.2}Co_2P_2$ via chemical compression, Chem. Mater. 23 (2011) 3021–3024, https://doi.org/10.1021/cm200782z.

[21] S. Jia, P. Jiramongkolchai, M.R. Suchomel, B.H. Toby, J.G. Checkelsky, N.P. Ong, R.J. Cava, Ferromagnetic quantum critical point induced by dimer-breaking in $SrCo_2(Ge_{1-x}Px)_2$, Nat. Phys. 7 (2011) 207–210, https://doi.org/10.1038/nphys1868.

[22] T. Mine, H. Yanagi, T. Kamiya, Y. Kamihara, M. Hirano, H. Hosono, Nickel-based phosphide superconductor with infinite-layer structure, $BaNi_2P_2$, Solid State Commun. 147 (2008) 111–113, https://doi.org/10.1016/j.ssc.2008.05.010.

[23] F. Ronning, N. Kurita, E.D. Bauer, B.L. Scott, T. Park, T. Klimczuk, R. Movshovich, J.D. Thompson, The first order phase transition and superconductivity in $BaNi_2As_2$ single crystals, J. Phys. Condens. Matter 20 (2008) 342203, https://doi.org/10.1088/0953-8984/20/34/342203.

[24] F. Ronning, E.D. Bauer, T. Park, S.-H. Baek, H. Sakai, J.D. Thompson, Superconductivity and the effects of pressure and structure in single-crystalline $SrNi_2P_2$, Phys. Rev. B 79 (2009) 134507, https://doi.org/10.1103/PhysRevB.79.134507.

[25] E.D. Bauer, F. Ronning, B.L. Scott, J.D. Thompson, Superconductivity in $SrNi_2As_2$ single crystals, Phys. Rev. B 78 (2008) 391, https://doi.org/10.1103/PhysRevB.78.172504.

[26] J.R. Neilson, A. Llobet, A.V. Stier, L. Wu, J. Wen, J. Tao, Y. Zhu, Z.B. Tesanovic, N.P. Armitage, T.M. McQueen, Mixed-valence-driven heavy-fermion behavior and superconductivity in KNi_2Se_2, Phys. Rev. B 86 (2012) 742, https://doi.org/10.1103/PhysRevB.86.054512.

[27] J.R. Neilson, T.M. McQueen, A. Llobet, J. Wen, M.R. Suchomel, Charge density wave fluctuations, heavy electrons, and superconductivity in KNi_2S_2, Phys. Rev. B 87 (2013) 193, https://doi.org/10.1103/PhysRevB.87.045124.

[28] T.L. Hung, I.A. Chen, C.H. Huang, C.Y. Lin, C.W. Chen, Y.B. You, S.T. Jian, M.C. Yang, Y.Y. Hsu, J.C. Ho, Y.Y. Chen, H.C. Ku, Low temperature heat capacity of layered superconductors $SrNi_2Ge_2$ and $SrPd_2Ge_2$, J. Low Temp. Phys. 171 (2013) 148–155, https://doi.org/10.1007/s10909-012-0832-z.

[29] C.D. Yang, H.C. Hsu, W.Y. Tseng, H.C. Chen, H.C. Ku, M.N. Ou, Y.Y. Chen, Y.Y. Hsu, Superconductivity in $Sr(Pd_{1-x}Ni_x)_2Ge_2$, J. Phys. Conf. Ser. 273 (2011) 12089, https://doi.org/10.1088/1742-6596/273/1/012089.

[30] D. Hirai, F. von Rohr, R.J. Cava, Emergence of superconductivity in $BaNi_2(Ge_{1-x}P_x)_2$ at a structural instability, Phys. Rev. B 86 (2012) 100505, https://doi.org/10.1103/PhysRevB.86.100505.

[31] V. Gvozdetskyi, V. Hlukhyy, R. Gladyshevskii, T.F. Fässler, Crystal structure and magnetic properties of $SrNi_{2\text{-}x}Sb_2$, Z. Anorg. Allg. Chem. 641 (2015) 1859–1862, https://doi.org/10.1002/zaac.201500518.

[32] V. Hlukhyy, D. Trots, T.F. Fässler, First-order phase transition in $BaNi_2Ge_2$ and the influence of the valence electron count on distortion of the $ThCr_2Si_2$ structure type, Inorg. Chem. 56 (2017) 1173–1185, https://doi.org/10.1021/acs.inorgchem.6b02190.

[33] L. Siggelkow, V. Hlukhyy, T.F. Fässler, Synthesis, structure and chemical bonding of $CaCo_2Si_2$ and $BaCo_2Ge_2$ – two new compounds with $ThCr_2Si_2$ structure type, Z. Anorg. Allg. Chem. 636 (2010) 378–384, https://doi.org/10.1002/zaac.200900533.

[34] V. Hlukhyy, A.V. Hoffmann, T.F. Fässler, Synthesis, structure and chemical bonding of $CaFe_{2-x}Rh_xSi_2$ ($x = 0$, 1.32, and 2) and $SrCo_2Si_2$, J. Solid State Chem. 203 (2013) 232–239, https://doi.org/10.1016/j.jssc.2013.04.033.

[35] FIZ Karlsruhe, ICSD: Inorganic Crystal Structure Database, Leibniz Institute for Information Infrastructure, Karlsruhe, Germany, 2017.

[36] C. Kranenberg, D. Johrendt, A. Mewis, R. Pöttgen, G. Kotzyba, H. Trill, B.D. Mosel, New compounds of the $ThCr_2Si_2$-type and the electronic structure of CaM_2Ge_2 (M: Mn–Zn), J. Solid State Chem. 167 (2002) 107–112, https://doi.org/10.1006/jssc.2002.9626.

[37] R. Welter, B. Malaman, Magnetic behaviour of the Mn sublattice in $ThCr_2Si_2$-type $CaMn_{2-x}Fe_xGe_2$ solid solution investigated by magnetic measurements and neutron diffraction, J. Alloy. Comp. 354 (2003) 35–46, https://doi.org/10.1016/S0925-8388(02)01354-3.

[38] T. Braun, V. Hlukhyy, $CaFe_2Ge_2$ – a substitution variant of the superconducting iron arsenide $CaFe_2As_2$, in: Proc. of 19. *Vortragstagung der Anorganischen Chemie der FG Wöhler-Vereinigung und Festkörperchemie und Materialforschung*, Regensburg (Germany), 2018. P233.

[39] WinXPOW, STOE & Cie GmbH, Darmstadt, Germany, 2011.

[40] P. Villars, K. Cenzual, Pearson's Crystal Data: Crystal Structure Database for Inorganic Compounds (On DVD), ASM International, Materials Park, Ohio, USA, 2019.

[41] J. Rodriguez-Carvajal, FullProf: a program for Rietveld refinement and pattern matching analysis, in: At the Satellite Meeting on Powder Diffraction of the XV IUCr Congress, Toulouse, France, 1990.

[42] NETZSCH Proteus Thermal Analysis, NETZSCH-Gerätebau GmbH, Selb, Germany, 2016.

[43] R.W. Tank, O. Jepsen, O.K. Andersen, in: The STUTTGART TB-LMTO-ASA Program, Stuttgart, 1998.

[44] O. Jepsen, O.K. Andersen, Calculated electronic structure of the sandwich d^1 metals LaI_2 and CeI_2, Z. Phys. B: Condens. Matter 97 (1995) 35–47, https://doi.org/10.1007/BF01317585.

[45] W.R.L. Lambrecht, O.K. Andersen, Minimal basis sets in the linear muffin-tin orbital method, Phys. Rev. B 34 (1986) 2439–2449, https://doi.org/10.1103/PhysRevB.34.2439.

[46] R. Dronskowski, P.E. Blöchl, Crystal orbital Hamilton populations (COHP), J. Phys. Chem. 97 (1993) 8617–8624, https://doi.org/10.1021/j100135a014.

[47] V.Y. Gvozdetskyi, R.E. Gladyshevskii, N.V. German, Multicomponent phases with $CeAl_2Ga_2$- and $Y_{0.5}Co_3Ge_3$-type structures in the Gd–Ca–Fe–Co–Ge system, Phys. Chem. Solid State 16 (2015) 104–110, https://doi.org/10.15330/pcss.16.1.104-110.

[48] F. Ronning, T. Klimczuk, E.D. Bauer, H. Volz, J.D. Thompson, Synthesis and properties of $CaFe_2As_2$ single crystals, J. Phys. Condens. Matter 20 (2008) 322201, https://doi.org/10.1088/0953-8984/20/32/322201.

[49] N. Ni, S. Nandi, A. Kreyssig, A.I. Goldman, E.D. Mun, S.L. Bud'ko, P.C. Canfield, First-order structural phase transition in $CaFe_2As_2$, Phys. Rev. B 78 (2008) 14523, https://doi.org/10.1103/PhysRevB.78.014523.

[50] A. Mewis, Ternäre Phosphide mit $ThCr_2Si_2$-Struktur, Z. Naturforsch. B Chem. Sci.: Anorg. Chem., Org. Chem. 35 (1980) 141–145, https://doi.org/10.1515/znb-1980-0205.

[51] V. Gvozdetskyi, V. Hlukhyy, R. Gladyshevskii, Quaternary phases $R_{1\text{-}x}Ae_xT_2Ge_2$ (R = La, Ce, Gd, Yb; Ae = Ca, Sr; T = Fe, Co, Ni) with $CeAl_2Ga_2$ (122) structure type, Chem. Met. Alloy. 8 (2015) 123–128.

[52] G. Venturini, B. Malaman, X-ray single crystal refinements on some RT_2Ge_2 compounds (R = Ca, Y, La, Nd, U; T = Mn–Cu, Ru–Pd), J. Alloy. Comp. 235 (1996) 201–209, https://doi.org/10.1016/0925-8388(95)02140-X.

[53] G. Wu, H. Chen, T. Wu, Y.L. Xie, Y.J. Yan, R.H. Liu, X.F. Wang, J.J. Ying, X.H. Chen, Different resistivity response to spin-density wave and superconductivity at 20 K in $Ca_{1-x}Na_xFe_2As_2$, J. Phys. Condens. Matter 20 (2008) 422201, https://doi.org/10.1088/0953-8984/20/42/422201.

[54] B. Eisenmann, N. May, W. Müller, H. Schäfer, A. Weiss, J. Winter, G. Ziegleder, Neue Vertreter des $ThCr_2Si_2$-Typs und dessen Verwandtschaft zum Anti-PbFCl-Gitter, Z. Naturforsch. B Chem. Sci.: Anorg. Chem., Org. Chem., Biochem., Biophys., Biol. 25 (1970) 1350–1352, https://doi.org/10.1515/znb-1970-1207.

[55] G. Venturini, B. Malaman, B. Roques, Contribution à la cristallochimie des isotypes de $ThCr_2Si_2$ et $CaBe_2Ge_2$, J. Solid State Chem. 79 (1989) 136–145, https://doi.org/10.1016/0022-4596(89)90259-4.

[56] N. May, H. Schäfer, Neue Verbindungen im $ThCr_2Si_2$-Typ, Z. Naturforsch. B Chem. Sci.: Anorg. Chem., Org. Chem., Biochem., Biophys., Biol. 27 (1972) 864–865, https://doi.org/10.1515/znb-1972-0726.

[57] A.V. Morozkin, Y.D. Seropegin, A.V. Gribanov, I.A. Sviridov, J.M. Kurenbaeva, A.L. Kurenbaev, Analysis of the melting temperatures of RTX_2 ($CeNiSi_2$ structure) and RT_2X_2 ($CeGa_2Al_2$ structure) compounds [R = La,Ce,Sm,Er,Tm; T = Fe,Co,Ni; X = Si,Ge], J. Alloy. Comp. 264 (1998) 190–196, https://doi.org/10.1016/S0925-8388(97)00231-4.

[58] A. Szytuła, A. Oleś, M. Perrin, Magnetic ordering in $PrFe_2Ge_2$, J. Magn. Magn. Mater. 86 (1990) 377–382, https://doi.org/10.1016/0304-8853(90)90146-H.

[59] W. Bażela, J. Leciejewicz, H. Ptasiewicz-Bąk, A. Szytuła, Magnetic properties of $TbFe_2Si_2$ and $TbFe_2Ge_2$, J. Magn. Magn. Mater. 72 (1988) 85–87, https://doi.org/10.1016/0304-8853(88)90274-0.

[60] D. Rossi, R. Marazza, R. Ferro, Lattice parameters of some $ThCu_2Si_2$-type phases in ternary alloys of rare earths with cobalt (or iron) and silicon (or germanium), J. Less Common. Met. 58 (1978) 203–207, https://doi.org/10.1016/0022-5088(78)90201-1.

[61] J.J. Bara, H.U. Hrynkiewicz, A. Miłoś, A. Szytuła, Investigation of the crystal properties of RFe_2Si_2 and RFe_2Ge_2 by X-ray diffraction and mössbauer spectroscopy, J. Less Common. Met. 161 (1990) 185–192, https://doi.org/10.1016/0022-5088(90)90026-G.

[62] A. Szytuła, D. Kaczorowski, S. Baran, B. Penc, A. Gil, A. Hoser, Magnetic ordering and low-temperature thermodynamic properties of $ErFe_2Ge_2$, J. Magn. Magn. Mater. 322 (2010) 2973–2977, https://doi.org/10.1016/j.jmmm.2010.05.016.

[63] S.K. Malik, S.G. Sankar, V.U.S. Rao, R. Obermyer, Magnetic behavior of some rare earth germanides of the type RFe_2Ge_2, AIP Conf. Proc. 29 (1976) 585–586, https://doi.org/10.1063/1.30463.

[64] A. Szytuka, S. Siek, J. Leciejewicz, A. Zygmunt, Z. Ban, Neutron diffraction study of UT_2X_2 (T = Mn, Fe, X = Si, Ge) intermetallic systems, J. Phys. Chem. Solids 49 (1988) 1113–1118, https://doi.org/10.1016/0022-3697(88)90162-X.

[65] J. Gal, M. Kroupp, Z. Hadari, I. Nowik, Mössbauer and magnetization studies of the NpM_2Ge_2(M = Cr, Fe, Co, Ni, Cu) intermetallic compounds, Solid State Commun. 20 (1976) 515–517, https://doi.org/10.1016/0038-1098(76)90159-9.

[66] X. Liu, S. Matsuishi, S. Fujitsu, H. Hosono, MgFeGe as an isoelectronic and isostructural analog of the superconductor LiFeAs, Phys. Rev. B 85 (2012) 469, https://doi.org/10.1103/PhysRevB.85.104403.

[67] W. Dörrscheidt, N. Niess, H. Schäfer, Neue Verbindungen AB_2X_2 (A = Erdalkalimetall, B = Übergangselement, X = Element(IV)) im $ThCr_2Si_2$-Typ, Z. Naturforsch. B Chem. Sci.: Anorg. Chem., Org. Chem. 31 (1976) 890–891, https://doi.org/10.1515/znb-1976-0634.

[68] K. Kanematsu, T. Ohoyama, Magnetic and X-ray studies of iron-germanium system II. Phase diagram and magnetism of each phase, J. Phys. Soc. Jpn. 20 (1965) 236–242, https://doi.org/10.1143/JPSJ.20.236.

[69] T. Braun, V. Hlukhyy (in preparation).

[70] Calcium oxide (CaO) magnetic properties, in: W. Martienssen, H. Landolt, R. Börnstein (Eds.), Numerical Data and Functional Relationships in Science and Technology: New Series, Springer, Berlin, 1999, pp. 1–2 [u.a.].

[71] V. Hlukhyy, N. Chumalo, V.' Zaremba, T.F. Fässler, Syntheses and structures of the germanides CaNiGe and MgCoGe as well as chemical bonding in CaNiGe and $CaNi_2Ge_2$, Z. Anorg. Allg. Chem. 634 (2008) 1249–1255, https://doi.org/10.1002/zaac.200700534.

[72] R. Welter, I. Ijjaali, G. Venturini, E. Ressouche, B. Malaman, Investigations of the $La_{1-x}CaxMn_2Ge_2$ ($0 \leq x \leq 1$) solid solution by magnetic measurements and neutron diffraction, J. Magn. Magn. Mater. 187 (1998) 278–292, https://doi.org/10.1016/S0304-8853(98)00147-4.

[73] A.V. Hoffmann, V. Hlukhyy, T.F. Fässler, Synthesis, structure, and chemical bonding in CaCoSi, Z. Anorg. Allg. Chem. 640 (2014) 2882–2888, https://doi.org/10.1002/zaac.201400356.

[74] W. Dörrscheidt, H. Schäfer, Neue intermetallische Verbindungen im anti-PbFCl-Strukturtyp, Z. Naturforsch. B Chem. Sci.: J. Chem. Sci. 31 (1976) 1050–1052, https://doi.org/10.1515/znb-1976-0810.

5.2 Trends in $ThCr_2Si_2$-Type Tetrelides with Iron, Cobalt or Nickel—Disorder and Distortion

Braun, T.; Hlukhyy, V.

Manuscript for publication

Trends in $ThCr_2Si_2$-Type Tetrelides with Iron, Cobalt or Nickel—Disorder and Distortion

Thomas Braun, Viktor Hlukhyy[1]

Department of Chemistry, Technische Universität München, Lichtenbergstr. 4, 85747, Garching, Germany

Abstract

Compounds of $ThCr_2Si_2$-type or derived structures with alkaline earth metal (Ca, Sr, Ba), transition metal (Mn, Fe, Co, Ni, Cu) and tetrel element (Si, Ge) have been compared and investigated. $SrNi_2Si_2$ was identified by powder and single crystal X-ray diffraction methods. It resembles a distortion variant of $ThrCr_2Si_2$-type with highly distorted squared Ni-layers and broken interlayer-Si–Si-bonds. In addition, solid solutions have been prepared and investigated: $Y_{1-x}Ca_xFe_2Ge_2$, $CaFe_{2-x}Co_xGe_2$ and $CaFe_2Ge_{2-x}P_x$ as well as $Sr_{1-x}Ca_xCo_2Ge_2$ and $Sr_{1-x}Ba_xCo_2Ge_2$. Magnetic properties were measured for selected samples.

Keywords: Intermetallics, $ThCr_2Si_2$-type, magnetic properties

1. Introduction

$ThCr_2Si_2$ structural type is common among intermetallic compounds. It is a colored variant of $BaAl_4$ with general formula AT_2X_2 and space group $I4/mmm$ with more than 700 ternary representatives, containing a combination of electropositive metal A (alkaline, alkaline earth or rare earth, Sc, Y, Zr, Hf), a transition metal T of group 6 to 11 and a main group element X of group 13 to 16. Considering also solid solutions, more than 2500 entries are found in the ICSD data base [1]. Derived from $BaAl_4$-type, different color variants are possible with different order and symmetry, such as $ThCr_2Si_2$, $CaBe_2Ge_2$ and more complicated substitution variants [2]. The structure combines metallic, covalent and ionic features, which makes it very versatile. For that reason it has been called “the ‘perovskite’ of intermetallics” [3]. Atomic arrangement is illustrated in Figure 1, where transition metal atoms form a planar square net. Each atom is tetrahedrally coordinated by X-atoms, resulting in a checkerboard-patterned layer where T-square are capped alternatingly from top or bottom. Metal–metal-contacts create an infinite 2-dimensional layer that allows for various interesting properties of this structure class. Some

---

[1] Corresponding author.

E-mail address: viktor.hlukhyy@tum.de (V. Hlukhyy)

compounds make distortion variants: In $SrNi_2P_2$ a superstructure is formed with short and long inter-layer P–P-contacts [4,5]; in orthorhombically distorted $BaNi_2Si_2$ and $BaNi_2Ge_2$ deformation of Ni-substructure due to intralayer atomic interaction is observed. The 4^4-net of Ni-atoms is transformed into distorted 6^3 variant. Interlayer Si–Si- or Ge–Ge-contacts are broken by moving closer to the nickel net. They approach each other within the layer which is accompanied by enlarging the Ni–Ni-distance interjacent to these two atoms [6]. In $SrNi_2P_2$ and $BaNi_2Ge_2$ also the undistorted $ThCr_2Si_2$-type has been observed as high temperature modification [4,5,7].

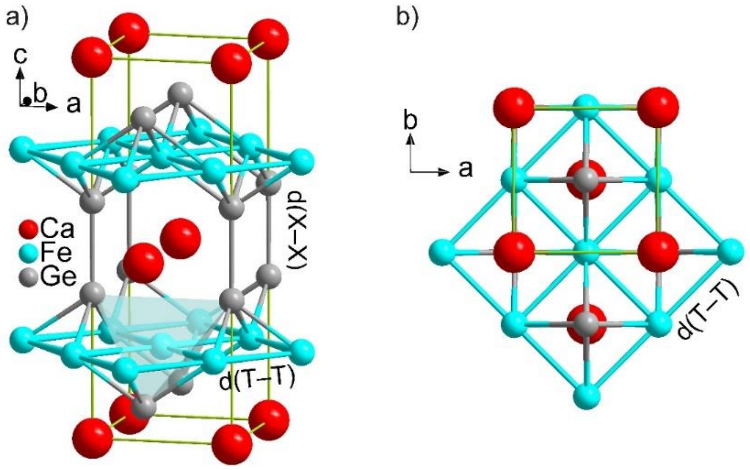

Figure 1 $CaFe_2Ge_2$ as example of $ThCr_2Si_2$-type crystal structure in tetragonal space group *I*4/*mmm*: a) side view and b) top view.

Extensive research has been performed on rare earth metal (*RE*) containing compounds due to their magnetic properties. The rare earth atoms as well as host lattice can carry magnetic moments, form magnetic sub-lattices and interact with each other [8,9]. Systems are known which exhibit e.g. different types of anti-ferromagnetism [10], spin-density [11] or charge density waves [12], heavy fermions [13] or superconductivity [14,15]. Magnetic properties are sensible to foreign atoms, partial substitution in solid solutions can have strong influence on the behavior. Magnetic and structural phase transitions may vary based on the degree of substitution. Regions close to concentration of structural instabilities, where a transition occurs, can result in superconductivity [16–18]. Hence, many experiments have been performed on solid solutions, introducing electron- or hole-doping or chemical pressure. In many cases, phase transitions can be observed that result either in magnetic superstructures or significant structural distortion [19–21].

Aside from *RE* compounds, also alkaline earth metal tetrelides have been investigated. For example the following nickel-based compounds were found to be superconducting: $SrNi_2Ge_2$ (T_C = 0.87 K) [22], $BaNi_2Ge_{2-x}P_x$ ($T_{C,max}$ = 2.9 K) [18], $SrNi_2P_{2-x}Ge_x$ ($T_{C,max}$ = 3.0 K) [17] and $SrPd_{2-x}Ni_xGe_2$ ($T_{C,max}$ = 2.9 K) [22]. Limiting the view on AeT_2X_2 compounds with alkaline earth metal, manganese, iron, cobalt, nickel, copper and tetrel elements, a handful of compounds and solid solutions have been reported. AT_2Sn_2 compounds with tin are only formed with rare earth or copper. In addition, based on the iron, cobalt and nickel compounds, following solid solutions have been reported: $La_{1-x}Ca_xFe_2Ge_2$, $La_{1-x}Sr_xFe_2Ge_2$, $Ce_{1-x}Ca_xCo_2Ge_2$, $Gd_{1-x}Ca_xCo_2Ge_2$, $Yb_{1-x}Ca_xCo_2Ge_2$ [23], $CaFe_{2-x}Rh_xSi_2$ [24], $CaMn_{2-x}Fe_xGe_2$ [25], $SrCo_2Ge_{2-x}P_x$ [19], $SrPd_{2-x}Ni_xGe_2$ [22], $SrNi_2P_{2-x}Ge_x$ [17], $BaNi_2Ge_{2-x}P_x$ [18] and $Gd_{1-x}Ca_xFe_{2-y}Co_yGe_2$ [26].

2. Experimental

2.1. Synthesis

Starting material for synthesis were pure elements: ingots of calcium (Alfa Aesar, 99.5%, redistilled), strontium (ChemPur, 98%, redistilled prior to use) or barium (ChemPur, 99.5%), yttrium chips (99.9%, Chempur), iron granules (1–2 mm, 99.98%, Alfa Aesar) or iron powder (99.9%, Chempur), cobalt pieces (≥ 99.9%, Alfa Aesar), nickel wire (Alfa Aesar, 99.98%), silicon pieces (Alfa Aesar, 99.999%), germanium pieces (< 3 cm, Evochem GmbH, 99.999%), red phosphorus powder (≥ 97.0%, Sigma-Aldrich).

Single crystals of $SrNi_2Si_2$ were found after melting the elements with ratio 1.06:2:1 in an arc furnace and subsequent annealing in an induction furnace (sealed Ta-ampule, 5 minutes at 1000 °C, cooling to 700 °C within 30 minutes, 75 min dwell time, cooling down to room temperature). For phase analysis, a stoichiometric mixture of strontium pieces, nickel powder and silicon powder was sealed in a niobium ampoule and heated in an induction furnace. After 30 minutes at 950 °C the power was reduced by 1% per minute until 800 °C were reached. After dwelling for 60 minutes the furnace was cooled down with the same rate until 20% heating power and then quickly cooled to room temperature. In a second step the sample was ground and pressed into a pellet. After sealing into graphitized silica, it was annealed in a muffle furnace at 600 °C for 6 days and cooled to room temperature with −1 °C/min.

Solid solutions $Sr_{1-x}Ca_xCo_2Ge_2$ and $Sr_{1-x}Ba_xCo_2Ge_2$ have been prepared by arc-melting from elements with 3% and 5% excess for calcium and barium, respectively. In a first step CoGe was formed and in a second step alkaline earth metals were added. To ensure homogeneity, pellets were turned over and remelted two additional times. In case of calcium-strontium solid solutions, phase purity could be improved by annealing in graphitized silica ampoules at 800 °C for one week.

For $Y_{1-x}Ca_xFe_2Ge_2$, Y, Ca, Fe and Ge (ratio 0.2:0.8:2:2) were arc melted and remelted several times in an argon filled glovebox. Yttrium and iron were first melted together to avoid formation of highly stable YGe. Then, germanium and calcium were added. A product piece was sealed in graphitized silica and annealed at 800 °C for 58 h before turning off the oven to cool to room temperature.

Several steps were performed to synthesize $CaFe_{2-x}Co_xGe_2$, depending on x. First iron and cobalt were arc-melted together, then germanium was added and at last calcium (10% excess). $x = 1.9 – 1.8$: Ca, Fe, Co and Ge were arc melted without further annealing. $x = 1.5 – 0.6$: analogue to above, additional annealing in graphitized silica at 800 °C for 3 days. $x = 0.4, 0.2$: Co, Fe and Ge were arc melted all at once, grinded at sealed into a niobium ampoule together with calcium. The samples were heated to 1000 °C for 2 h, slowly cooled to 800 °C for 72 and cooled to room temperature. Resulting products were homogenized, pressed to pellets, sealed into niobium ampoules and further annealed at 800 °C for 2.5 days.

$CaFe_2Ge_{1.91}P_{0.09}$ and $CaFe_2Ge_{0.27}P_{1.73}$ were synthesized by reacting calcium with $FeGe_{1-x}P_x$ ($x = 0.4$ and 1.6, respectively). $FeGe_{1-x}P_x$ was prepared using a modified procedure described by Mills and Mar [27]. Powders of iron an phosphorous (10% excess of P) were mixed and sealed in silica ampoules. They were heated to 400 °C and then slowly to 800 °C with 0.33 °C/min to allow reaction of vaporized phosphorous with the iron, minimizing the formation of high pressure within the ampoule. After dwelling at 800 °C for 20 h, it was cooled quickly to 700 °C and kept another 3 hours before taking the samples out of the oven. The products were given into a ball mill jar (hardened steel, 15 ml, 3 ball with $d = 1$ cm) together with calcium (10% excess) and milled at 600 rpm for 18 h (10 min + 5 min break, reverse mode). The resulting powder was pelletized, sealed into graphitized silica and annealed. It was heated to 400 °C, kept there one hour and slowly heated to 800 °C. After 60 h dwelling time, the oven was turned off to let the sample cool to room temperature.

2.2. X-ray investigations

Phase analysis and structural investigations have been performed with powder X-ray diffraction method (PXRD). A STOE Stadi-P equipped with Cu-$K_{\alpha1}$ source ($\lambda = 1.54060$ Å), monochromator (curved Ge(111)) and DECTRIS MYTHEN 1K detector, calibrated to external silicon standard. Rietveld refinement has been performed with Bruker Topas [28] or Fullprof Suite [29], using structural models and pseudo-Voigt function. Single crystals or $SrNi_2Si_2$ where selected under air with a microscope and fixed on a glass fiber using nail polish. Crystals were very small (about 20 µm size length) and measured with a STOE STADIVARI single crystal X-Ray diffractometer. It is equipped with with Mo-K_α Genix 3D High Flux microfocus (λ = 0.71073 Å), graded multilayer mirror monochromator and DECTRIS Pilatus 300K detector. Cell indexing and integration has been performed with the diffractometer' software X-Area [30]. A structural working model has been established with ShelXS [31] and refined with ShelXL [32–34]. Superstructure reflections/satellites were too weak to describe modulation and refine the structure.

2.3. Magnetic measurements

A MPMS-XL5 magnetometer by Quantum Design was used to investigate magnetic properties. Powdered samples have been filled into a gelatin capsule and been fixed into a plastic straw. Data have been corrected for diamagnetic contribution of the sample holder and the sample's core electrons. Field-dependent magnetization was recorded between −50 and +50 kOe, $M(T)$-scans were recorded between 1.8 and 300 K, either after cooling with zero-field (ZFC) or while cooling in applied field (FC).

3. Results

3.1. $SrNi_2Si_2$

The compound was detected while analyzing single crystals of a multi-phase sample containing unidentified reflections in the powder diffractogram. Using the 1:2:2 composition, a sample showing $SrNi_2Si_2$ as main phase (Figure 2) could be prepared. The crystal structure was refined with monoclinic space group *C2/m* and lattice parameters a = 17.836(4) Å, b = 10.287(2) Å, c = 16.601(3) Å, β = 122.41(3)°, V = 2572(1)Å³. Data are given in Table 1 and illustrated in Figure 3. Indexing the cell does suggest a 30× orthorhombic supercell of tetragonal $ThCr_2Si_2$-type. However, the refinement gives better results for a monoclinic model. Figure 4 shows construction section of the reciprocal space. In the layer perpendicular to reciprocal axis a*, two sets of reflections can be seen. Some of them do have non-integer h and l values that mark them as satellites. The structure appears to be affected by modulation, as can be seen by the zig-zag-pattern in the bottom part of the image that does not agree with the length of the unit cell vector. Due to small size of the obtained crystal, intensities of some observed satellites, e.g. $(0.8, 2k, -6.\overline{6})$ were very weak and others such as $(-0.\overline{3}, 2k, -4.5)$ are very close to main reflections, as can be seen in the $hk2$-layer. As a result only an averaged structure model could be refined with some displacement ellipsoids kept isotropic, these appear as spheres in Figure 3.

Table 1 Crystal data and structure refinement of $SrNi_2Si_2$. The lattice parameter was taken from powder Rietveld analysis

empirical formula	SrN_2Si_2
formula weight (g mol^{-1})	261.22
temperature (K)	298
crystal system	*monoclinic*
space group	$C2/m$
pearson code	$mC150$
unit cell dimensions	
a (Å)	17.836(4)
b (Å)	10.287(2)
c (Å)	16.601(3)
beta (°)	122.41(3)
volume (Å^3)	2572(1)
Z	30
ρ_{calcd} (g cm^{-3})	5.06
μ (mm^{-1})	26.785
$F(000)$	3660
crystal size (mm^3)	0.1×0.05×0.025
theta range for data collection (°)	3.96 – 35.5
index ranges in *hkl*	$-25 \le h \le 23$, $-14 \le k \le 13$, $-13 \le k \le 11$
reflections collected	16727
independent reflections	3934 ($R_{\text{int}} = 0.0885$)
Reflections with $I \ge 2\sigma(I)$	1479 ($R_{\text{sigma}} = 0.0845$)
data/restraints/parameters	3934/0/153
goodness-of-fit on F^2	0.738
final R indices ($I > 2\sigma(I)$)	$R_1 = 0.0337$, $wR_2 = 0.0524$
R indices (all data)	$R_1 = 0.1314$, $wR_2 = 0.0663$
Extinction coefficient	–
largest diff. peak and hole (e·Å^{-3})	1.655, −1.360

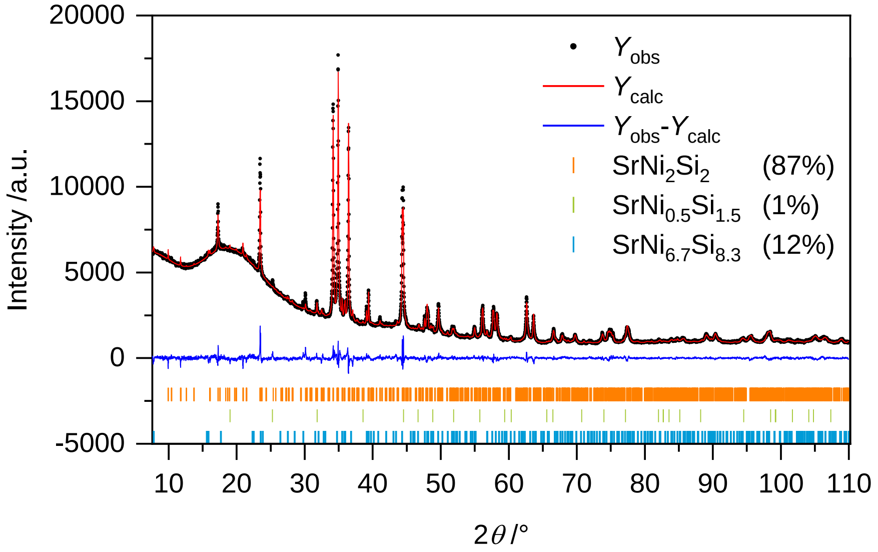

Figure 2 X-ray diffraction data with main phase in agreement with an averaged model of $SrNi_2Si_2$. Rietveld method with fixed atomic displacement parameter has been performed.

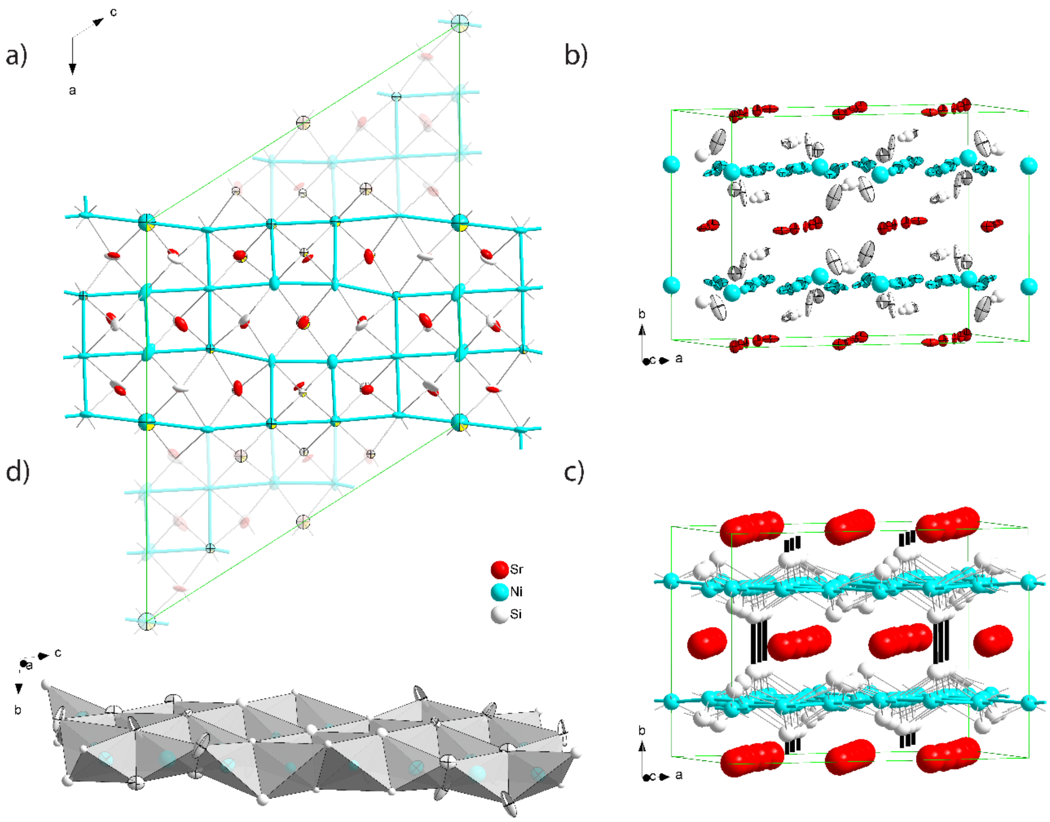

Figure 3 Approximate model of $SrNi_2Si_2$. a) Top view with emphasize on Ni–Ni-contacts. Repetitive parts of the pattern have been greyed out. b) Side view with displacement ellipsoids. c) Ball and Stick model with bonds drawn for short contacts. d) Corrugated layer of distorted edge-sharing Ni@Si_4-tetrahedra. Atoms are drawn as displacement ellipsoids at 90%. Anisotropic ellipsoids are drawn as octant. Ni–Ni, Ni–Si and Si–Si shortest distances are shown in blue, grey and black, respectively.

The structure represents a strongly deformed $ThCr_2Si_2$-type with irregular Ni-layers and Ni–Ni-distances from 2.632(7)–2.928(7) Å. Even the shortest contact is larger than the sum of atomic radii with 2.49 Å [35]. Si–Si-contacts are divided in three groups. Short dumbbells (2.55(2)–2.57(2) Å) are formed between Si-atoms that are centered above closed Ni-quadrangles. Above partially opened Ni-mesh with one elongated Ni–Ni-distance of 3.115(6) Å, Si–Si-contacts also show elongated length of 2.70(2) Å. Silicon atoms situated above Ni–Ni-meshes opened on two sides are shifted even closer to the layer. Thus some dumbbells are formed between layers and others are broken where silicon atoms are shifted towards the layer, as can be seen in Figure 3c and compared to Figure 1. Also all Si-contacts are larger than the sum of atomic radii of 2.35 Å [35]. Ni–Si-distances vary from 2.23 to 2.38 Å, which are typical values for intermetallics. They are shorter than the sum of atomic radii with 2.42 Å and can be considered covalent [35]. While the Ni atoms form a flat plane, the layer of edge-sharing Ni@Si_4-tetrahedra is corrugated with some Si-atoms being pulled towards the Ni-plane (Figure 3d). As a consequence also different Si-Ni-Si-angles are found in the structure between 76.0(4)° and 136.7(7)°, some being close to the value for regular tetrahedra. Opening of Ni-squares and Si-dumbbell formation within the layer is similar to low-temperature modification of $BaNi_2Ge_2$ [7]. A corrugated tetrahedral layer is also known for low-temperature $SrNi_2P_2$ [4], however, in this compound the square planar Ni-layer is less distorted. Since $SrNi_2P_2$ is superconducting at T_C = 1.4 K and T_C can be increased via doping with tetrel element germanium [17], magnetic measurements have been performed on a polycrystalline sample containing $SrNi_2Si_2$. The mixture didn't show any sign of superconductivity.

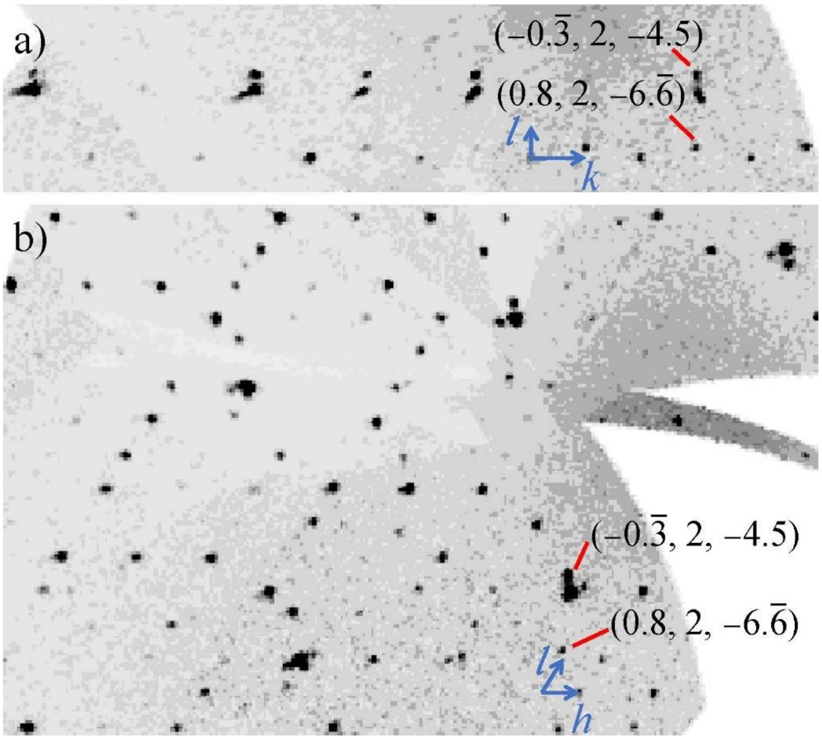

Figure 4 Constructed sections of the reciprocal lattice showing a) the plane perpendicular to a^* crossing (0 0 −3) and b) the $h2l$-layer. There are two sets of reflections indicating modulation.

3.2. *Solid solutions based on AT_2X_2 compounds*

Superconductivity could be created or enhanced in many compounds by applying external pressure or by partial substitution of an atom species [36]. Solid solutions have been reported for all three crystallographic positions in AT_2X_2 (A = alkaline, alkaline earth or rare earth, Sc, Y, Zr, Hf; T = transition metal form group 6 to 11, X = main group element of group 13 to 16). $Ba_{1.6}K_{0.4}Fe_2As_2$ (T_C = 38 K) [37] is an example where the cationic site has been modified, in $BaFe_{1.86}Co_{0.14}As_2$ (T_C = 23 K) [38] the transition metal was altered and in $BaFe_2As_{1.4}P_{0.6}$ (T_C = 30 K) [39] the p-element was targeted. These solid solutions are typically accompanied with structural changes and higher critical temperature is found near the structural transition, indicating a correlation between instability and superconductivity. Similar to $BaFe_2As_2$ containing a Fe-square layer [40], $CaFe_2Ge_2$ [41] could be a parent compound for superconductors. The substitution of iron with manganese in $CaMn_{2-x}Fe_xGe_2$ leads to the transition from ferro- to antiferromagnetic behavior with no superconductivity at the border [25]. Also the substitution of iron with rhodium in isovalent silicide $CaFe_{2-x}Rh_xSi_2$ did not create superconductivity [24]. In this work, new solid solutions have been tested: $Y_{1-x}Ca_xFe_2Ge_2$, $CaFe_{2-x}Co_xGe_2$, $CaFe_2Ge_{2-x}P_x$, $Sr_{1-x}Ca_xCo_2Ge_2$ and $Sr_{1-x}Ba_xCo_2Ge_2$.

Table 2 Refined values of lattice parameters and atomic position for prepared solid solutions with different *x*.

Compound	*x*	*a*,*b* [Å]	*c* [Å]	*V* [Å]	*z* [Å]
$Y_{1-x}Ca_xFe_2Ge_2$	0.06(1)	3.96332(5)	10.4614(2)	164.326 (5)	0.3781(1)
$CaFe_{2-x}Co_xGe_2$ [a]	1.86	3.99985(5)	10.3201(2)	165.109(6)	0.3709(1)
	1.78	3.99839(5)	10.3422(5)	165.342(5)	0.3711(2)
	1.72	4.00268(6)	10.3329(2)	165.548(6)	0.3706(2)
	1.38	4.00504(9)	10.3836(3)	166.557(9)	0.3709(2)
	0.94	4.0074(2)	10.4561(7)	167.92(2)	0.3722(3)
	0.88	4.00094(6)	10.5019(2)	168.11(6)	0.3738(2)
	0.60	4.00716(9)	10.5204(3)	168.93(9)	0.3737(2)
	0.58	3.9985(2)	10.5721(5)	169.03(2)	0.375(3)
	0.32	3.9954(2)	10.6366(8)	169.79(2)	0.3752(5)
$CaFe_2Ge_{2-x}P_x$	0.09(1)	3.98825(6)	10.6577(2)	169.522(6)	0.37661(6)
	1.73(4)	3.87740(9)	10.0937(4)	151.751(9)	0.3651(3)
$Sr_{1-x}Ca_xCo_2Ge_2$	0.00	4.0755(1)	10.6806(2)	177.400(5)	0.36283(1)
	0.07(1)	4.0644(1)	10.6302(2)	175.607(5)	0.36378(1)
	0.22(1)	4.0603(5)	10.5811(2)	174.443(4)	0.36485(1)
	0.33(1)	4.0432(1)	10.4968(3)	171.594(8)	0.36624(1)
	0.55(1)	4.0307(1)	10.4467(5)	169.72(1)	0.36698(1)
	0.72(1)	4.0141(1)	10.3849(4)	167.331(8)	0.36788(1)
	0.83(1)	4.0069(1)	10.3611(3)	166.353(8)	0.36933(1)
$Sr_{1-x}Ba_xCo_2Ge_2$	0.25(5)	4.0787(2)	10.813(1)	179.88(3)	0.3602(5)
	0.50(2)	4.08536(7)	11.0533(4)	184.48(2)	0.3584(4)
	0.7(2)	4.084(2)	11.288(2)	188.28(4)	0.354(1)

[a] Degree of substitution has been estimated from volume assuming Vegard's law

3.2.1. $Ca_xY_{1-x}Fe_2Ge_2$

YFe_2Ge_2 is known to be superconducting below 1.8 K [42,43]. To investigate if partial substitution of yttrium with calcium increases the transition temperature, $Ca_{0.06}Y_{0.94}Fe_2Ge_2$ has been prepared. Since the substitution is challenging without significant amount of secondary phases, only one composition was analyzed. Powder X-ray diffraction data contain the 122-phase as main phase with additional $CaFe_6Ge_6$ as side phase and some unindexed reflections.

Rietveld refinement (Figure 5 and Figure 6) has been performed to determine the degree of substitution. Calcium occupancy of 10% and lattice parameter with $a = 3.96342(6)$ Å, $c = 10.4623(3)$ Å are in agreement with Vegard's law, as shown in Figure 6a. Magnetic measurements on this multicomponent sample exhibit paramagnetism at 300 K and 2 K (Figure 6b) with some saturation caused by ferromagnetic secondary phases. No superconductivity has been observed over 1.8 K by cooling in a weak magnetic field, which cannot, however, exclude the superconductivity below 1.8 K.

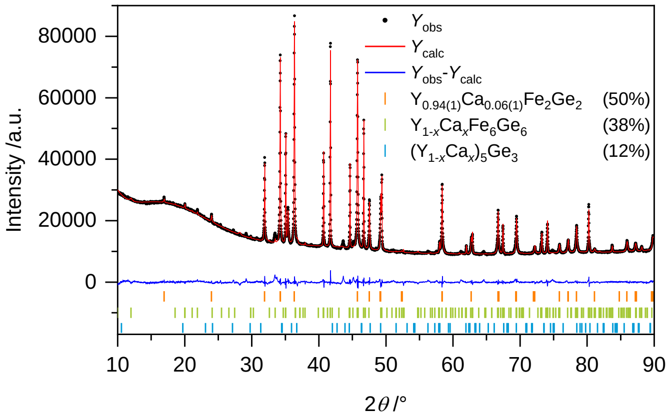

Figure 5 Rietveld refinement of $Y_{0.94}Ca_{0.06}Fe_2Ge_2$ with $ThCr_2Si_2$-type.

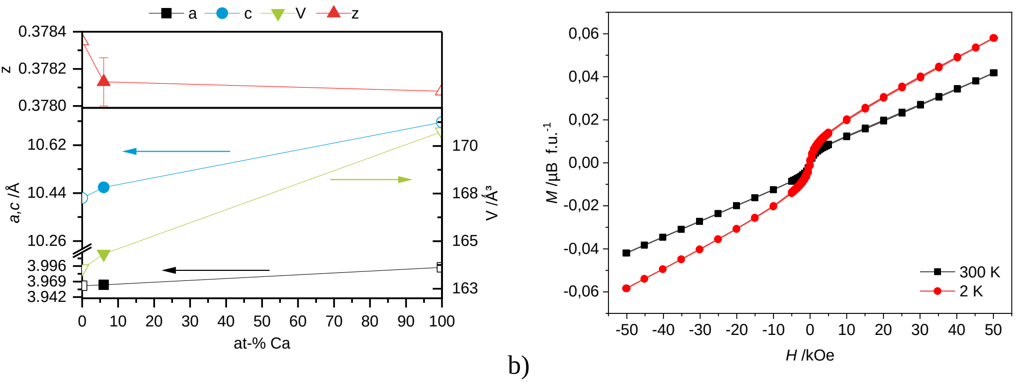

a) b)

Figure 6 a) Vegard plot, arrows highlight corresponding axes, literature values are marked with open symbols, lines are guide to the eyes, error bars are smaller than symbol size. b) $M(H)$ measurement of $Y_{0.94}Ca_{0.06}Fe_2Ge_2$ between −50000 and 50000 Oe, showing paramagnetic behavior with minor ferromagnetic impurities.

3.2.2. *$CaFe_{2-x}Co_xGe_2$*

As $CaFe_2Ge_2$ forms a solid solution with $CaMn_2Ge_2$ over the full range [25], we examined the solubility with the electron richer homologue $CaCo_2Ge_2$. Figure 7 contains powder XRD data of $CaFe_{2-x}Co_xGe_2$ where solubility from $x = 0$ to $x = 1.56$ has been observed. Substitution over the full range might be possible but as given in Figure 8a, determined compositions contain less iron than used for synthesis, especially for $x \leq 0.4$ and $x = 0.9$. Because of similar number of electrons, iron and cobalt occupation could not be distinguished by Rietveld refinement. It was assumed that Vegard's law applies for solid solution of d-metals, and the volume converted into at.-% of iron, since Vegard-behavior has been observed for $CaMn_{2-x}Fe_xGe_2$ [25], $SrPd_{2-x}Ni_xGe_2$ [22], $LaMn_{2-x}V_xSi_2$, $YMn_{2-x}V_xSi_2$, $LaFe_{2-x}V_xSi_2$ [44]. Non-Vegard behavior has been observed for compounds where breaking of the inter-layer bond occurs at transition from collapsed to uncollapsed structures. That is not the case for $CaCo_2Ge_2$ und $CaFe_2Ge_2$. (Table 3). Phase purity was not achieved for all samples and secondary phases Fe_3Ge, $Fe_{0.9}Ge_{0.1}$ and CaO could be identified.

Figure 8b shows magnetization measurements for $CaFe_{2-x}Co_xGe_2$. All samples are ferromagnetic with saturation magnetization per formula unit increasing with increasing iron content for $x \leq 0.64$. Increasing x further lead to decreasing saturation. However, as samples are not phase pure, this can also be influenced by secondary phases. No superconductivity was observed upon cooling to 1.8 K.

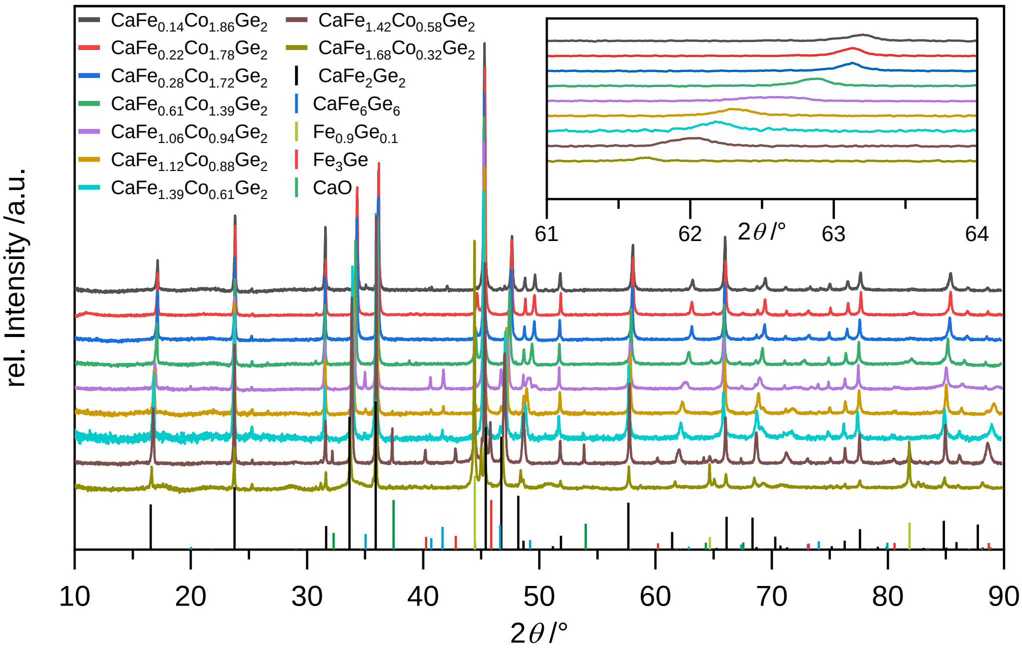

Figure 7 Powder X-ray diffraction data of solid solution $CaFe_{2-x}Co_xGe_2$. Left inset shows the 116 reflection which is shifted with increasing x. Right inset indicates the change of cell parameter, at-% of Fe has been estimated on the cell volume assuming Vegard's law.

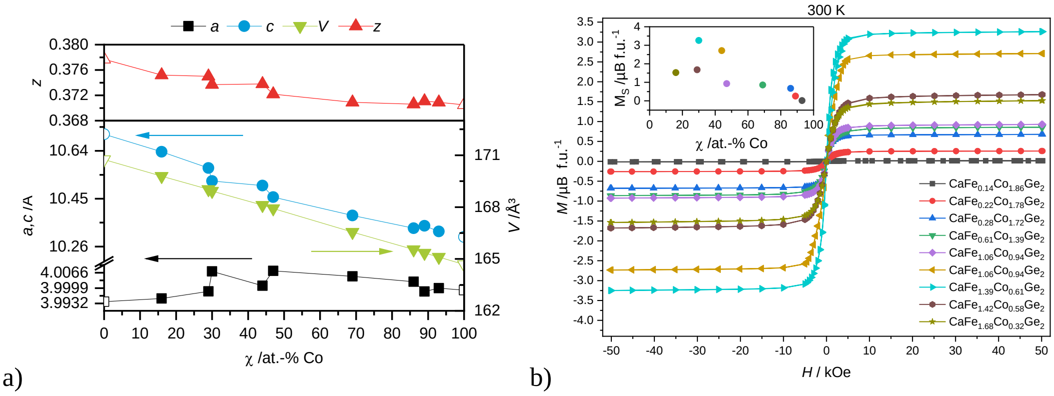

a) b)

Figure 8 a) Evolution of structural parameters upon substitution in $CaFe_{2-x}Co_xGe_2$. χ has been derived from volume assuming Vegard's law, with χ = 100% for x = 2. Arrows highlight corresponding axes, literature values are marked with open symbols, lines are guide to the eyes, error bars are smaller than symbol size. b) Magnetization at 300 K, the inset shows saturation magnetization M_S.

3.2.3. $CaFe_2Ge_{2-x}P_x$

Inspired by superconducting solid solutions such as $SrNi_2P_{2-x}Ge_x$ [17], $BaNi_2Ge_{2-x}P_x$ [18] and $BaFe_2As_{2-x}P_x$ [39], substitution of germanium by phosphorus has been investigated for $CaFe_2Ge_{2-x}P_x$ (x = 0.09, 1.73). Refined values for x differ slightly from 0.4 and 0.6 that were used for synthesis, solid solution was achieved but only with presence of Fe_3Ge as secondary phases (Figure 9). Magnetic measurements shows paramagnetism for $CaFe_2Ge_{0.27}P_{1.73}$ at 300 K and 2 K with little saturation caused by ferromagnetic Fe_3Ge [45]. $CaFe_2Ge_{1.91}P_{0.09}$ appears ferromagnetic at both temperatures, which is in contrast to $CaFe_2Ge_2$ [41], probably caused by Fe_3Ge.

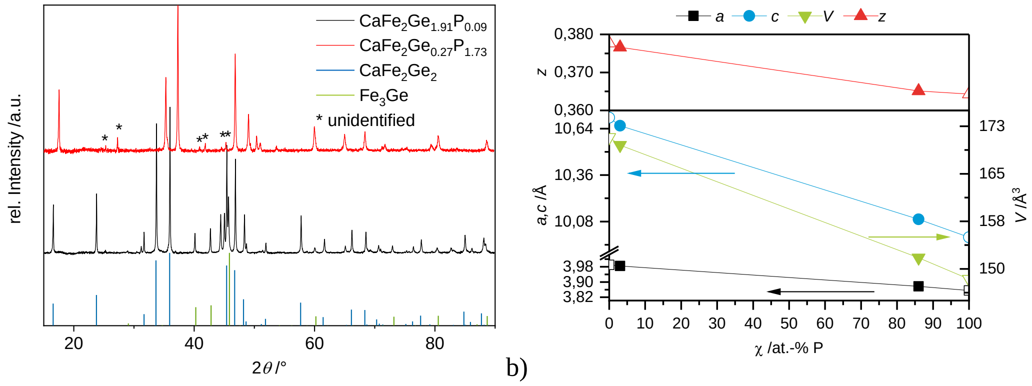

a) b)

Figure 9 a) Powder X-Ray diffraction data of $CaFe_2Ge_{1.91}P_{0.09}$ and $CaFe_2Ge_{0.27}P_{1.73}$. b) Evolution of structural parameters upon substitution. Arrows highlight corresponding axes, literature values are marked with open symbols, lines are guide to the eyes, error bars are smaller than symbol size.

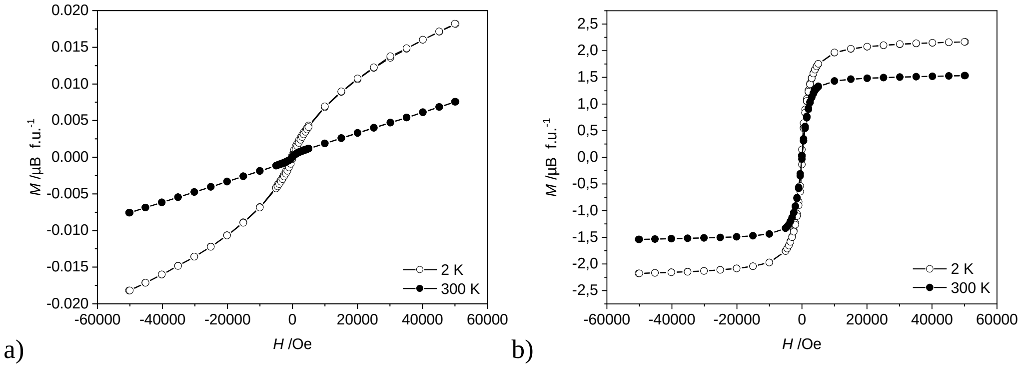

Figure 10 Magnetization of a) $CaFe_2Ge_{0.27}P_{1.73}$ and b) $CaFe_2Ge_{1.91}P_{0.09}$ at 300 K and 2 K. Ferromagnetism of germanium-rich compound might be caused by ferromagnetic secondary phases.

3.2.4. $Sr_{1-x}Ca_xCo_2Ge_2$ and $Sr_{1-x}Ba_xCo_2Ge_2$

$CaCo_2Ge_2$, $SrCo_2Ge_2$ and $BaCo_2Ge_2$ all crystalize with $ThCr_2Si_2$-type [46–48]. With increasing size of alkaline earth atoms, also the lattice parameter increase, as can be seen in Table 3. Co–Co-distances remain almost constant whereas the Ge–Ge-distance increases significantly, which also represents in the c-parameter. While in $CaCo_2Ge_2$, a collapsed structure with Ge–Ge-bonds ($d_{\mathrm{Ge-Ge}}$ = 2.67 Å) is formed, these bonds are broken in uncollapsed structure of $BaCo_2Ge_2$ ($d_{\mathrm{Ge-Ge}}$ = 3.55 Å). $SrCo_2Ge_2$ shows an intermediate distance of $d_{\mathrm{Ge-Ge}}$ = 2.90 Å that is an edge case between collapsed and uncollapsed case [49]. This compound can be regarded as structurally instable and substitution lead to interesting magnetic properties. This has been done e.g. by mixing germanium with phosphorous which resulted in a transition from collapsed to uncollapsed modification accompanied with dimer-breaking [19]. To investigate the influence of different alkaline earth atoms on this structure, solid solution with calcium or barium has been done. For $Sr_{1-x}Ca_xCo_2Ge_2$, calcium substitutes strontium over the full range (Figure 11a), as can be seen clearly for reflections with 2θ above 50°, where reflections are shifted to lower angles with increasing strontium content. Since no deviation from Vegard's law (Figure 11b) could be observed that would indicate a structural instability, magnetic measurements (Figure 13a) have been performed on a sample in the middle of the row. Rietveld refinement provided the composition $Sr_{0.46}Ca_{0.54}Co_2Ge_2$ and paramagnetism was measured at 2 K and 300 K. Little saturation was observed that is attributed to secondary phases. No superconductivity has been observed down to 1.8 K. Solid solution with x = 0.54 as well as $SrCo_2Ge_2$ are paramagnetic [19]. Since $CaCo_2Ge_2$ is reported to be ferromagnetic with T_C around 55 K [50], a magnetic transition is expected within this solid solution for $0 \leq x \leq 0.5$.

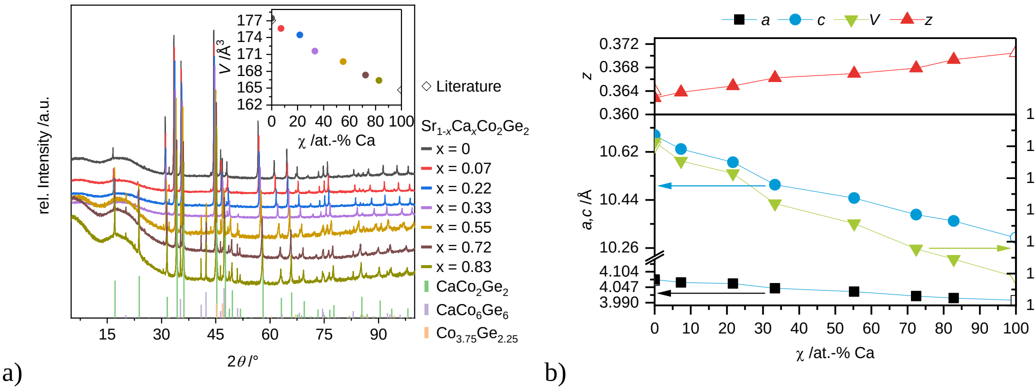

Figure 11 a) Powder X-ray diffraction data of $Sr_{1-x}Ca_xCo_2Ge_2$, reflections are shifted to lower angles with increasing x. b) Evolution of structural parameters upon substitution. Arrows highlight corresponding axes, literature values are marked with open symbols, lines are guide to the eyes, error bars are smaller than the symbol size.

No simple solid solution does form for $Sr_{1-x}Ba_xCo_2Ge_2$. Samples with nominal $x = 0.25$, 0.5 and 0.75 have been prepared (Figure 12a). Reflections are shifted and indicate partial substitution, but hk3- and hk6-reflections appear very broad whereas hk0-reflections are quite sharp. This is typical for structural strain and potential modulation. Figure 13b shows magnetic measurements of these three solid solutions, all appear paramagnetic at 2 K and 300 K. Saturation for samples with higher strontium content were attributed to presence of secondary phases. Cooling down to 1.8 K in weak magnetic field did not exhibit superconductivity.

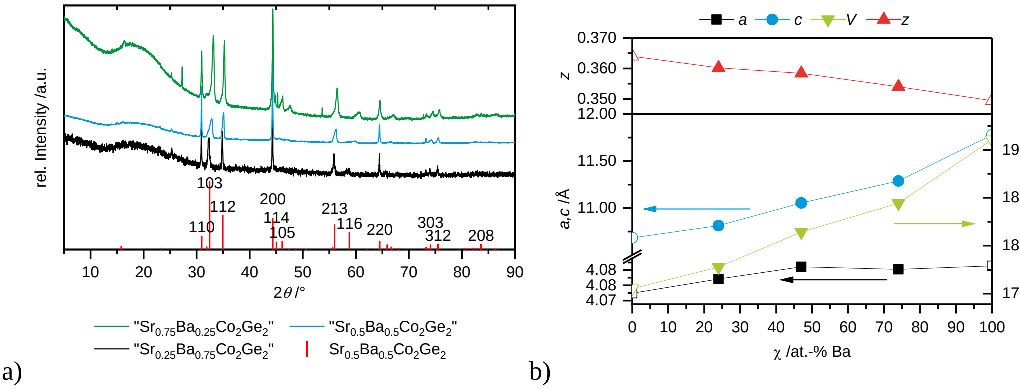

Figure 12 a) PXRD of solid solution $Sr_{1-x}Ba_xCo_2Ge_2$ with some remarkably sharp reflections of type (*hk*0) and some very broad (*hk*3 and *hk*6). As reference reflections for $Sr_{0.5}Ba_{0.5}Co_2Ge_2$ have been simulated by fitting to the lattice parameter, error bars are smaller than the symbol size. b) Evolution of structural parameters upon substitution with $\chi = 100\%$ for $x = 2$. Arrows highlight corresponding axes, literature values are marked with open symbols, lines are guide to the eyes.

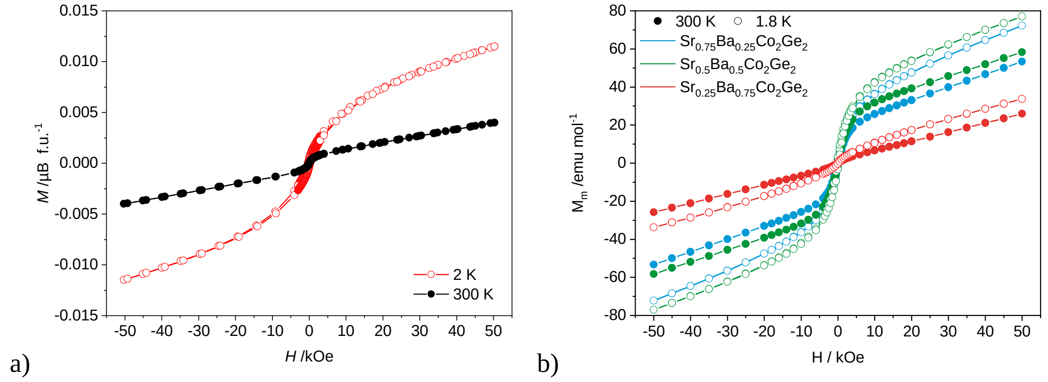

Figure 13 Magnetization measurement of a) $Sr_{0.46}Ca_{0.54}Co_2Ge_2$ and b) $Sr_{1-x}Ba_xCo_2Ge_2$ at 2 K and 300 K.

4. Discussion

An overview of relevant structural parameters of AeT_2X_2-compounds (Ae = Ca, Sr, Ba; T = Mn–Ni; X = Si, Ge) compounds is presented in Table 3 and Figure 14. As $SrNi_2Si_2$, $BaNi_2Si_2$ [6] and $BaNi_2Ge_2$ [7] are distortion variants of $ThCr_2Si_2$ with lower symmetry, layers are not always stacked in *c*-direction. With respect to the overview in the table, values corresponding to *c* of the parent 122-type have been given in the *c* column, regardless of the lattice parameter name in their structure. Cell volume has been normalized to cell content of $Z = 2$ and pseudo-*a*-values have been calculated from volume using $a = \sqrt{V/c}$. Exact metal–metal-distances for tetragonal structure were obtained from the a value using $d(T-T) = a/\sqrt{2}$ and an effective averaged value (pseudo-122) for distorted variants with the pseudo-*a*-value. Due to distortion if for some parameters more than one value exist, the range is shown in the affected subfigures by error bars.

The substitution of transition metal from manganese to copper shows a minimum of volume for cobalt compounds. This observation may be related to the discussion by Zheng and Hoffmann [51], where the stability of $BaAl_4$-type and related compounds and their electronic structure has been analyzed in dependence of the total number of valence electrons. In addition, *a*- and *c*-parameter increase with increasing size of alkaline earth or tetrel atoms, as has been discussed e.g. by A. Mewis [52] or Hlukhyy *et al.* [24]. No general trend is observed for development of *c*-parameter, which is a measure of distance between layers that are separated by alkaline earth atoms.

Table 3 Comparison of structural data for various alkaline earth – transition metal – tetrel element compounds with stoichiometry 1:2:2. For $SrNi_2Si_2$ the effective volume has been derived by normalizing the monoclinic cell volume to the unit cell content of $ThCr_2Si_2$-type. Because of distortion, some values are irregular. Pseudo-a- and c-values have been calculated to compare with $ThCr_2Si_2$-parent type. For clarity see Figure 1 and Figure 14. *VE* gives the sum of valence electrons. Type of magnetism reported in literature is shown as Magn.

Compound	Mag.	*VE*	*a,b* [Å]	*c* [Å]	*V* [Å]	*c/a* [Å]	*z* [Å]	$d_{(T\text{–}T)}$ [Å]	$d_{(X\text{–}X)}$ [Å]	$d_{(X\text{–}X)'}$ [Å]	$\angle_{(X\text{-}T\text{-}X)}$ [°]	Ref.
$CaMn_2Ge_2$	AFM	24	4.16	10.87	189.19	2.61	0.387	2.949	2.456	4.071	108.8	[1,53]
$SrMn_2Ge_2$		24	4.3	10.91	201.73	2.54	0.38	3.041	2.618	4.158	113.2	[1]
$BaMn_2Ge_2$	AFM	24	4.47	10.99	219.59	2.46	0.375	3.161	2.748	4.188	116.8	[1,53]
$CaFe_2Si_2$		26	3.94	10.19	157.99	2.59	0.375	2.785	2.554	3.768	114.4	[1]
$CaFe_2Ge_2$	FM	26	3.99	10.71	170.75	2.68	0.378	2.824	2.619	3.930	111.2	[1,41]
$CaCo_2Si_2$		28	3.92	9.92	152.11	2.53	0.370	2.769	2.579	3.651	117.4	[1]
$SrCo_2Si_2$		28	3.97	10.40	164.16	2.62	0.361	2.810	2.898	3.631	119.9	[1]
$CaCo_2Ge_2$		28	4.00	10.33	165.28	2.58	0.371	2.828	2.675	3.768	116.2	[1]
$SrCo_2Ge_2$	PM	28	4.08	10.65	177.28	2.61	0.364	2.885	2.897	3.771	118.5	[1,19]
$BaCo_2Ge_2$		28	4.09	11.78	196.65	2.88	0.350	2.889	3.548	3.719	120.4	[1]
$CaNi_2Si_2$	PM	30	3.99	9.71	154.88	2.43	0.371	2.823	2.504	3.675	119.0	[1,54]
$SrNi_2Si_2$		**30**	***4.08***	***10.27***	***171.3***	***2.52***	**Irreg.**	***2.885***	**Irreg.**	**Irreg.**	**Irreg.**	*****
$BaNi_2Si_2$		30	*4.17*	11.33	197.02	2.72	0.318	2.949	4.124	*2.537*	Irreg.	[1]
$CaNi_2Ge_2$		30	4.08	10.01	166.91	2.45	0.370	2.888	2.608	3.752	119.2	[1]
$SrNi_2Ge_2$	PM	30	4.18	10.24	178.94	2.45	0.362	2.956	2.833	3.737	122.6	[1,22,55]
HT-$BaNi_2Ge_2$		30	4.27	11.25	204.86	2.64	0.338	3.017	3.637	3.614	123.0	[1]
LT-$BaNi_2Ge_2$	PM	30	*4.24*	11.32	204.05	*2.67*	0.331	*3.001*	3.835	*2.855*	Irreg.	[1,7]
$CaCu_2Si_2$		32	4.05	9.92	162.6	2.449	0.364	2.863	2.697	3.648	121.7	[1]
$SrCu_2Si_2$		32	4.2	10.0	176.4	2.381	0.379	2.970	2.420	3.934	116.9	[1]
$CaCu_2Ge_2$		32	4.14	10.22	175.0	2.470	0.379	2.926	2.467	3.943	114.9	[1]
$SrCu_2Ge_2$		32	4.27	10.26	187.0	2.402	0.369	3.019	2.688	3.883	120.5	[1]

* this work

Depending on the interlayer-distance, *X*–*X*-interactions can be found in so-called collapsed or be absent in uncollapsed compounds. Interestingly, while the *a*-parameter and thus averaged *T*–*T*-distance are increasing in direction of late transition metals, *c*-parameter, *X*–*X*-distances and *XTX*-angles don't follow a global trend. This can be explained by distortion of $SrNi_2Si_2$, $BaNi_2Si_2$ and LT-$BaNi_2Ge_2$ from parent tetragonal compound. Ni–Ni-interactions between short contacts are weakened, creating a hexagonal opening that allows for shorter intralayer contacts *d*(*X*–*X*)', whereas interlayer contacts *d*(*X*–*X*) grow. For *d*(*T*–*T*), *d*(*X*–*X*), *d*(*X*–*X*)' and ∠(*X*-*T*-*X*) several distances are present due to distortion and reduced symmetry. The barium compounds have large interlayer distances and in the distorted variants short intralayer bonds, due to weakened *T*–*T*-interactions. In the strontium nickel silicide both situations coexist. This reminds of the structure of $SrNi_2P_2$ [4]. Here a supercell with $b = 3 \cdot a$ describes a structure where every third subcell is uncollapsed with no interlayer-bond. However, in case of silicon-compounds $SrNi_2Si_2$, disorder has been found, most likely due to modulation. It remains unclear whether only short and long Ni–Ni- and Si–Si-distances occur with a peculiar ordering scheme. Or if also intermediate states are present and not just a result of averaging over different positions. As can be seen in Figure 14, angles and distances found in the working model (see below) of this compound span over a range of all distances found for the homologues and adopt very small and very large values, depending on the regarded section.

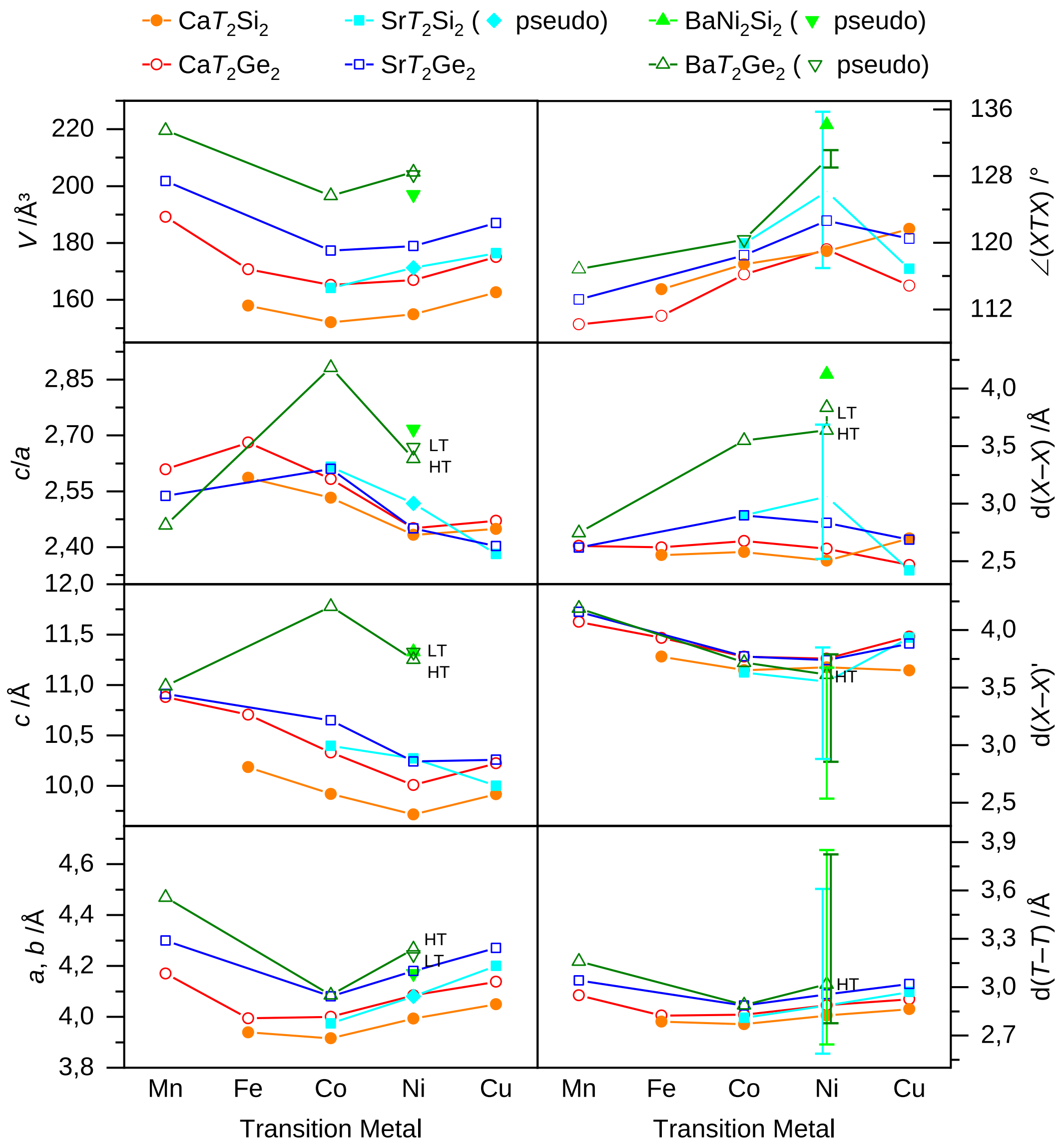

Figure 14 Visualized structural parameter of AeT_2X_2-compounds (Ae = Ca, Sr, Ba; T = Mn–Ni; X = Si, Ge). $d(X–X)$ measures shortest inter-layer distance and $d(X–X)$' distance within a layer. In case of distortion from $ThCr_2Si_2$-type, pseudo-values have been calculated for cell parameters. Values that span a range within a structure are shown as vertical bars that are vertically spread for better distinguishability. For $BaNi_2Ge_2$ points are shown according to high- and low-temperature phase and labeled respectively. Lines between points are guides to the eye.

Remarkably is the absence of some combinations within AeT_2X_2-family. With manganese only germanides $CaMn_2Ge_2$, $SrMn_2Ge_2$ and $BaFe_2Ge_2$ exist and no silicides have been reported. With iron only calcium compounds $CaFe_2Ge_2$ and $CaFe_2Si_2$, no strontium or barium compound are known. For nickel and cobalt all three alkaline earth metals are possible with both tetrel elements. Compared to other compounds of the structure type the synthesis of $CaFe_2Ge_2$ is not straightforward [41]. It does not form from melt and decomposes into binaries in the arc furnace. $CaFe_2Si_2$ is easier to form, but no phase pure sample was accomplished so far [24]. It is obvious that iron marks a point of instability in this system. With cobalt all combinations except $BaCo_2Si_2$ exist, with nickel, (as shown in this work,) all combinations are possible. However, $BaNi_2Si_2$ and LT-$BaNi_2Ge_2$ are distorted, with selective Ni–Ni-contacts elongated and X–X-dumbbell formation in the plane instead between the planes.

Pseudo c^*-parameter of $SrNi_2Si_2$ is considerable larger than in $CaNi_2Si_2$, $CaNi_2Ge_2$ and even slightly larger than $SrNi_2Ge_2$. Such an increase of c-parameter is also observed for the neighboring cobalt system, where $CaCo_2Si_2$ shows a small cell, $SrCo_2Si_2$, $CaCo_2Ge_2$ and $SrCo_2Ge_2$ larger ones. It is not inherent by the interlayer-distance $d(X–X)$, which can vary between covalent to non-bonding. Also, the tetrahedra angle $\measuredangle(X\text{-}T\text{-}X)$ contributes as it determines “layer thickness” in combination with $d(T–T)$. The last variable is directly linked to the a-parameter, so the c/a-ratio is a good indicator to differentiate between collapsed and uncollapsed structure. Via solid solution, an intermediate bonding situation can be created which might lead to structural instability and superconducting behavior. This bond breaking is on the one hand attributed to the size of atomic radii, which becomes to large when substituting calcium with strontium. On the other hand, also the number of electrons has an influence, which can be seen for the calcium compounds. Small unit cells are found in $CaNi_2Si_2$, $CaNi_2Ge_2$ and large unit cells for both cobalt representatives. This behavior has been discussed by Pobel et al. for $CaFe_{2-x}Ni_xAs_2$ [56]. It was concluded that with less electrons also the interlayer-bonds are weakened due to stronger metal-metal interactions and dumbbells formation is diminished.

In $SrNi_2Si_2$ distortion of regular nickel-layer affects the shape of $Ni@Si_4$-tetrahedra, as can be seen in Figure 3c. The interlayer-distance is even larger than for $SrNi_2Ge_2$, which indicates that strontium atoms don’t penetrate that deep into the nickel-silicon-layer or the layer itself becomes thicker due to corrugation. Substitution of calcium with strontium has only minor effect on the Ni–Ni-interactions and thus breaks some interlayer-Si–Si-bonds to open some space. This behavior has been observed for $SrNi_2P_2$ low temperature modification, a $ThCr_2Si_2$-related compound with both, broken and formed dumbbells between layers. With even larger barium atoms, all interlayer Si–Si-bonds are broken in $BaNi_2Si_2$ and LT-$BaNi_2Ge_2$, leading to elongated

Ni–Ni-contacts and intra-layer dumbbell-formation. In $BaNi_2P_2$ however, no distortion of the Ni-layer occurs and uncollapsed $ThCr_2Si_2$-type is formed. Strontium thus is not able to completely separate layers and thus weakens bonds. To check, if this might lead to superconductivity, magnetic measurements on $SrNi_2Si_2$ have been performed. Phase purity was not good enough to determine type of magnetism, so only a low-field low-temperature was recorded that did not show superconductivity.

Solid solution formed for $Y_{0.94}Ca_{0.06}Fe_2Ge_2$, $CaFe_{2-x}Co_xGe_2$ (x = 0.32–1.86) and $CaFe_2Ge_{2-x}P_x$ (x = 0.09, 1.73). The first is paramagnetic down to 2 K, which was also observed for the pure yttrium compound that is a superconductor below 1.8 K. Miscibility of iron with cobalt is possible over the whole range but the occupation cannot be refined due to close electron number of both elements. The deviation of nominal composition to calculated one using Vegard’s law is most likely caused by formation of side products, which changed the stoichiometry. Magnetic measurements show ferromagnetic behavior at 300 K for all $CaFe_{2-x}Co_xGe_2$ compounds, saturation magnetization has a maximum for $CaCo_{0.61}Fe_{1.39}Ge_2$. DOS calculated for parent $CaFe_2Ge_2$ shows a sharp peak close to Fermi level, this specific solid solution might match the valence electron concentration passing this peak. Substitution of germanium with phosphorus in $CaFe_2Ge_{2-x}P_x$ did not create superconductivity. Germanium-rich side is ferromagnetic, even at room temperature [41]; the phosphorus rich side is paramagnetic over the whole temperature range, just as it is known for pure $CaFe_2P_2$ [57]. Interesting properties are expected for the composition, where the transition from ferro- to paramagnetism occurs. As $AeCo_2Ge_2$ (Ae = Ca, Sr, Ba) exists with all three heavier earth alkaline metals, solid solution of Ca/Sr and Sr/Ba have been prepared. Miscibility could be obtained over the whole range. However magnetic measurements showed paramagnetism for all tested compounds and no superconductivity.

5. Conclusion

A summary of alkaline earth transition metal tetrelide compounds with stoichiometry 1:2:2 has been developed and new ternary compounds and pseudo-ternary solid solutions were found. All compounds crystallize within $ThCr_2Si_2$-type or structurally related modifications. Properties are affected by the number of valence electrons and the structure appears to be most stable for cobalt compounds. Nickel compounds with additional electrons show weakened transition metal interactions and distortion with larger cations. Many of these samples do not form in high purity and little is known of their magnetic properties. However, a transition from antiferromagnetism over ferromagnetism towards pauli-paramagnetism seems to become apparent going from Mn to Ni. None of these compounds showed superconductivity down to 1.8 K.

6. Acknowledgments

This research was financially supported by the German Research Foundation (Deutsche Forschungsgemeinschaft, DFG, Grant HL 62/3-1) and the TUM Graduate School.

7. References

[1] FIZ Karlsruhe, ICSD: Inorganic Crystal Structure Database, Leibniz Institute for Information Infrastructure, Karlsruhe, Germany, 2022.

[2] E. Parthé, B. Chabot, H.F. Braun, N. Engel, *Acta Crystallogr. B Struct. Sci.* **1983**, *39*, 588–595, https://doi.org/10.1107/S010876818300302X.

[3] M. Shatruk, *J. Solid State Chem.* **2019**, *272*, 198–209, https://doi.org/10.1016/j.jssc.2019.02.012.

[4] V. Keimes, D. Johrendt, A. Mewis, C. Huhnt, W. Schlabitz, *Z. Anorg. Allg. Chem.* **1997**, *623*, 1699–1704, https://doi.org/10.1002/zaac.19976231104.

[5] V. Keimes, A. Hellmann, D. Johrendt, A. Mewis, T. Woike, *Z. Anorg. Allg. Chem.* **1998**, *624*, 830–836, https://doi.org/10.1002/(SICI)1521-3749(199805)624:5<830:AID-ZAAC830>3.0.CO;2-6.

[6] W. Dörrscheidt, H. Schäfer, *Z. Naturforsch., B: Anorg. Chem., Org. Chem.* **1980**, *35*, 297–299, https://doi.org/10.1515/znb-1980-0307.

[7] V. Hlukhyy, D. Trots, T.F. Fässler, *Inorg. Chem.* **2017**, *56*, 1173–1185, https://doi.org/10.1021/acs.inorgchem.6b02190.

[8] E.G. Gerasimov, N.V. Mushnikov, *Phys. Metals Metallogr.* **2018**, *119*, 1309–1312, https://doi.org/10.1134/S0031918X18130069.

[9] G. Venturini, R. Welter, E. Ressouche, B. Malaman, *J. Alloys Compd.* **1994**, *210*, 213–220, https://doi.org/10.1016/0925-8388(94)90141-4.

[10] N.V. Baranov, E.G. Gerasimov, N.V. Mushnikov, *Phys. Met. Metallogr.* **2011**, *112*, 711–744, https://doi.org/10.1134/S0031918X11070039.

[11] G. Wu, H. Chen, T. Wu, Y.L. Xie, Y.J. Yan, R.H. Liu, X.F. Wang, J.J. Ying, X.H. Chen, *J. Phys.: Condens. Matter* **2008**, *20*, 422201, https://doi.org/10.1088/0953-8984/20/42/422201.

[12] J.R. Neilson, T.M. McQueen, A. Llobet, J. Wen, M.R. Suchomel, *Phys. Rev. B* **2013**, *87*, 193, https://doi.org/10.1103/PhysRevB.87.045124.

[13] B.D. White, J.D. Thompson, M.B. Maple, *Phys. C* **2015**, *514*, 246–278, https://doi.org/10.1016/j.physc.2015.02.044.

[14] P. Zhang, H. Zhai, *Condens. Matter* **2017**, *2*, 28, https://doi.org/10.3390/condmat2030028.

[15] T. Terashima, M. Kimata, H. Satsukawa, A. Harada, K. Hazama, S. Uji, H. S. Suzuki, T. Matsumoto, K. Murata, *J. Phys. Soc. Jpn.* **2009**, *78*, 83701, https://doi.org/10.1143/JPSJ.78.083701.

[16] K. Kudo, Y. Kitahama, K. Iba, M. Takasuga, M. Nohara, *J. Phys. Soc. Jpn.* **2017**, *86*, 35001, https://doi.org/10.7566/JPSJ.86.035001.

[17] V. Hlukhyy, A.V. Hoffmann, V. Grinenko, J. Scheiter, F. Hummel, D. Johrendt, T.F. Fässler, *Phys. Status Solidi B* **2017**, *254*, 1600351, https://doi.org/10.1002/pssb.201600351.

[18] D. Hirai, F. von Rohr, R.J. Cava, *Phys. Rev. B* **2012**, *86*, 100505, https://doi.org/10.1103/PhysRevB.86.100505.

[19] S. Jia, P. Jiramongkolchai, M.R. Suchomel, B.H. Toby, J.G. Checkelsky, N.P. Ong, R.J. Cava, *Nat. Phys.* **2011**, *7*, 207–210, https://doi.org/10.1038/nphys1868.

[20] K. Kovnir, W.M. Reiff, A.P. Menushenkov, A.A. Yaroslavtsev, R.V. Chernikov, M. Shatruk, *Chem. Mater.* **2011**, *23*, 3021–3024, https://doi.org/10.1021/cm200782z.

[21] D. Johrendt, H. Hosono, R.-D. Hoffmann, R. Pöttgen, *Z. Kristallogr.* **2011**, *226*, 435–446, https://doi.org/10.1524/zkri.2011.1363.

[22] C.D. Yang, H.C. Hsu, W.Y. Tseng, H.C. Chen, H.C. Ku, M.N. Ou, Y.Y. Chen, Y.Y. Hsu, *J. Phys.: Conf. Ser.* **2011**, *273*, 12089, https://doi.org/10.1088/1742-6596/273/1/012089.

[23] V. Gvozdetskyi, V. Hlukhyy, R. Gladyshevskii, *Chem. Met. Alloys* **2015**, *8*, 123–128.

[24] V. Hlukhyy, A.V. Hoffmann, T.F. Fässler, *J. Solid State Chem.* **2013**, *203*, 232–239, https://doi.org/10.1016/j.jssc.2013.04.033.

[25] R. Welter, B. Malaman, *J. Alloys Compd.* **2003**, *354*, 35–46, https://doi.org/10.1016/S0925-8388(02)01354-3.

[26] V.Y. Gvozdetskyi, R.E. Gladyshevskii, N.V. German, *Phys. Chem. Solid State* **2015**, *16*, 104–110, https://doi.org/10.15330/pcss.16.1.104-110.

[27] A.M. Mills, A. Mar, *J. Alloys Compd.* **2000**, *298*, 82–92, https://doi.org/10.1016/S0925-8388(99)00653-2.

[28] Bruker, TOPAS, Bruker AXS inc., Karlsruhe, Germany, 2017.

[29] J. Rodriguez-Carvajal, FullProf: A Program for Rietveld Refinement and Pattern Matching Analysis. At the Satellite Meeting on Powder Diffraction of the XV IUCr Congress, Toulouse, France, 1990.

[30] X-Area, STOE & Cie GmbH, Darmstadt, Germany, 2015.

[31] G.M. Sheldrick, SHELXS-2014: Program for the Determination of Crystal Structure, University of Göttingen, Göttingen, Germany, 2014.

[32] G.M. Sheldrick, SHELXL-2014: Program for Crystal Structure Refinement, University of Göttingen, Göttingen, Germany, 2014.

[33] G.M. Sheldrick, *Acta Crystallogr., Sect. C: Struct. Chem.* **2015**, *71*, 3–8, https://doi.org/10.1107/S2053229614024218.

[34] G.M. Sheldrick, *Acta Crystallogr., Sect. A: Found. Crystallogr.* **2008**, *64*, 112–122, https://doi.org/10.1107/S0108767307043930.

[35] J. Emsley, The elements, 3rd ed., Clarendon Press; Oxford University Press, Oxford, New York, 2000.

[36] H. Hosono, A. Yamamoto, H. Hiramatsu, Y. Ma, *Mater. Today (Oxford, U. K.)* **2018**, *21*, 278–302, https://doi.org/10.1016/j.mattod.2017.09.006.

[37] M. Rotter, M. Tegel, D. Johrendt, *Phys. Rev. Lett.* **2008**, *101*, 107006, https://doi.org/10.1103/PhysRevLett.101.107006.

[38] N. Ni, M.E. Tillman, J.-Q. Yan, A. Kracher, S.T. Hannahs, S.L. Bud’ko, P.C. Canfield, *Phys. Rev. B* **2008**, *78*, https://doi.org/10.1103/PhysRevB.78.214515.

[39] J.G. Analytis, J.-H. Chu, R.D. McDonald, S.C. Riggs, I.R. Fisher, *Phys. Rev. Lett.* **2010**, *105*, 207004, https://doi.org/10.1103/PhysRevLett.105.207004.

[40] A.S. Sefat, R. Jin, M.A. McGuire, B.C. Sales, D.J. Singh, D. Mandrus, *Phys. Rev. Lett.* **2008**, *101*, 117004, https://doi.org/10.1103/PhysRevLett.101.117004.

[41] T. Braun, V. Hlukhyy, *J. Solid State Chem.* **2019**, *276*, 368–375, https://doi.org/10.1016/j.jssc.2019.05.032.

[42] Y. Zou, Z. Feng, P.W. Logg, J. Chen, G. Lampronti, F.M. Grosche, *Phys. Status Solidi RRL* **2014**, *8*, 928–930, https://doi.org/10.1002/pssr.201409418.

[43] J. Chen, K. Semeniuk, Z. Feng, P. Reiss, P. Brown, Y. Zou, P.W. Logg, G.I. Lampronti, F.M. Grosche, *Phys. Rev. Lett.* **2016**, *116*, 127001, https://doi.org/10.1103/PhysRevLett.116.127001.

[44] E.G. Gerasimov, Y.A. Dorofeev, J.-G. Pak, A.N. Pirogov, V.S. Gaviko, V.A. Kazantsev, A.E. Teplykh, *Phys. Met. Metallogr.* **2004**, *97*, 244–252.

[45] J.W. Drijver, S.G. Sinnema, F. van der Woude, *J. Phys. F: Met. Phys.* **1976**, *6*, 2165–2177, https://doi.org/10.1088/0305-4608/6/11/015.

[46] G. Venturini, B. Malaman, *J. Alloys Compd.* **1996**, *235*, 201–209, https://doi.org/10.1016/0925-8388(95)02140-X.

[47] W. Dörrscheidt, N. Niess, H. Schäfer, *Z. Naturforsch., B: Anorg. Chem., Org. Chem.* **1976**, *31*, 890–891, https://doi.org/10.1515/znb-1976-0634.

[48] L. Siggelkow, V. Hlukhyy, T.F. Fässler, *Z. Anorg. Allg. Chem.* **2010**, *636*, 378–384, https://doi.org/10.1002/zaac.200900533.

[49] E. Cuervo-Reyes, R. Nesper, *Phys. Rev. B* **2014**, *90*, 64416, https://doi.org/10.1103/PhysRevB.90.064416.

[50] L.R. Aryal, Synthesis, Structure and Some Properties of $ThCr_2Si_2$ Type Compounds: $\mathit{Ae}Co_2Ge_2$ (Ae=Ca,Sr) and $\mathit{A}Co_2As_2$ (A=K,Ba). Master's Thesis, Houston, 2013.

[51] C. Zheng, R. Hoffmann, *Z. Naturforsch., B: J. Chem. Sci.* **1986**, *41*, 292–320, https://doi.org/10.1515/znb-1986-0304.

[52] A. Mewis, *Z. Naturforsch., B: Anorg. Chem., Org. Chem.* **1980**, *35*, 141–145, https://doi.org/10.1515/znb-1980-0205.

[53] B. Malaman, G. Venturini, R. Welter, E. Ressouche, *J. Alloys Compd.* **1994**, *210*, 209–212, https://doi.org/10.1016/0925-8388(94)90140-6.

[54] G. Gavoille, N.K. Hansen, R. Welter, B. Malaman, P. Herzig, H.-G. Krane, *J. Phys. Condens. Matter* **2000**, *12*, 2667–2679, https://doi.org/10.1088/0953-8984/12/12/308.

[55] T.L. Hung, I.A. Chen, C.H. Huang, C.Y. Lin, C.W. Chen, Y.B. You, S.T. Jian, M.C. Yang, Y.Y. Hsu, J.C. Ho, Y.Y. Chen, H.C. Ku, *J. Low. Temp. Phys.* **2013**, *171*, 148–155, https://doi.org/10.1007/s10909-012-0832-z.

[56] R. Pobel, R. Frankovsky, D. Johrendt, *Z. Naturforsch., B: J. Chem. Sci.* **2013**, *68*, 581–586, https://doi.org/10.5560/znb.2013-3045.

[57] S. Jia, S. Chi, J.W. Lynn, R.J. Cava, *Phys. Rev. B* **2010**, *81*, https://doi.org/10.1103/PhysRevB.81.214446.

5.3 Structural Order-Disorder in $CaFe_6Ge_6$ and $Ca_{1-x}Co_6Ge_6$

Braun, T.; Hlukhyy, V.

published in

J. of Solid State Chem. **in press**, 123742 (2022)

Reprinted with permission from Braun, T.; Hlukhyy, V.; *J. of Solid State Chem.* **in press**, 123742 (2022)

Structural Order-Disorder in $CaFe_6Ge_6$ and $Ca_{1-x}Co_6Ge_6$

Thomas Braun, Viktor Hlukhyy*

Department of Chemistry, Technische Universität München, Lichtenbergstr. 4, 85747, Garching, Germany

Keywords: Intermetallic compounds, Iron, Cobalt, Kagomé layer, Germanides

Abstract

Ternary alkaline earth transition metal germanides $CaFe_6Ge_6$ and $Ca_{1-x}Co_6Ge_6$ have been synthesized and investigated. Depending on synthesis paths, different modifications have been found, all ordering variants of stuffed CoSn-type: $CaFe_6Ge_6$ with $Y_{0.5}Co_3Ge_3$-type ($P6/mmm$, a = 5.1077(1) Å, c = 4.0636(2) Å), $MgCo_6Ge_6$-type ($P6/mmm$, a = 5.1017(1) Å, c = 8.1080(5) Å) or $TbFe_6Sn_6$-type ($Cmcm$, a = 8.150(2) Å, b = 17.698(4) Å, c = 5.116(1) Å) and $Ca_{1-x}Co_6Ge_6$ with $Y_{0.5}Co_3Ge_3$-type ($P6/mmm$, a = 5.1016(2) Å, c = 3.9286(3) Å) or $ScFe_6Ga_6$-type ($Immm$, a = 8.830(2) Å, b = 5.100(1) Å, c = 7.855(2) Å). The main structural motif in $Ca(Fe/Co)_6Ge_6$ is Kagomé layers of Fe/Co atoms alternating with honeycomb layers of Ge atoms, where the hexagonal channels are filled with Ca atoms and Ge-Ge dumbbells. Up to date, calcium is the largest guest atom in this 166 structural family. The crystal chemistry and chemical bonding are discussed in terms of linear muffin-tin orbital band structure calculations and a topological analysis using the electron localization function.

1. Introduction

Various polar intermetallic compounds consisting of rare/alkaline earth elements (*Re/Ae*), transition metals (*T*) and p-block elements (*X*) have been found to be superconducting under appropriate conditions. Famous are iron-based systems of different compositions: Fe*Ch* (*Ch* = chalcogen), *A*FeAs (*A* = alkali metal), *RE*FeAsO, $AeFe_2As_2$ (*Ae* = alkaline earth metal), $Sr_2VFeAsO_3$, $A_2Fe_4Se_5$ (*A* = K, Rb, Cs, Tl) [1,2]. All contain square planar layers of iron atoms tetrahedrally coordinated by four pnictide or chalcogenide atoms. By stacking these layers and intercalating with atoms or oxide layers the different structural families are formed. Recently,

---

* Corresponding author.
E-mail address: viktor.hlukhyy@lrz.tum.de (V. Hlukhyy)

some iron tetrelides have also been reported, showing, however, lower superconducting transition temperatures: YFe_2Ge_2 (T_C ~ 1.8 K) and LaFeSiH (T_C ~ 11 K) [3,4]. It has been found that also isostructural compounds with other transition metals can feature superconductivity, e.g. $SrNi_2Ge_2$ (T_C ~ 1.4 K), $SrNi_2(P_{1-x}Ge_x)_2$ (T_C ~ 3.0 K) and LaCoSi (4 K) [5–7].

Beside iron-containing superconductors with the square-planar (4^4) d-metal-layers, also compounds with other planar lattice arrangement of transition metal atoms are fascinating by their physical properties. In particular, compounds containing honeycomb- (6^3) or Kagomé- (3.6.3.6) layers, such as CsV_3Sb_5 [8], or Laves phase Mg_2Ir_3Si [9]. Other layered superconductors are $CeRu_3Si_2$ (T_C ~ 1 K) and $LaRu_3Si_2$ (T_C ~ 7.8 K), containing planar layers of transition metal, with the structure derived from $CaCu_5$ [10,11].

The $CaCu_5$ and CoSn structures as well as related $ThMn_{12}$ and Zr_4Al_3 are all based on a common structural motif: alternately stacked Kagomé and graphene-like honeycomb layers (Figure S1, Supporting Information). They form an edge-sharing trigonal-bipyramidal framework with hexagonal channels. In the different structure types, the remaining atoms can be situated in hexagonal channels along z direction in plane with the Kagomé-net (CoSn-type), in plane with the honeycomb ($CaCu_5$-type) or at an intermediate position (closer to the Kagomé-net), forming dumbbells with the center of gravity in plane with the honeycomb (Zr_4Al_3-type). $ThMn_{12}$ structural type represents an intergrowth of $CaCu_5$- and Zr_4Al_3-types, where the channels are filled alternately with isolated atoms and dumbbells and the Kagomé-net is slightly corrugated.

Via atom substitution and combination of these four structure types many ternary intergrowth variants with general formula MT_6X_6 (M = Li, Mg, group IIIA, IVA elements, lanthanides, U; T = transition metal; X = Si, Ge, Ga, In, Sn) can be obtained [12–15]. The host framework ("T_6X_4") consists of T-atoms building the Kagomé-net and X-atoms forming the honeycomb. The channels are filled with M atoms and X_2-dumbbells, with sequence $M–X_2–M–X_2$. If the hexagonal voids are occupied by statistical mixture of 50% metal atoms and 50% dumbbells the $Y_{0.5}Co_3Ge_3$-type is formed. Depending on the arrangements of channels starting with M or with X_2, various different superstructures have been found and compared [12,13,16,17]. Fredrickson *et al.* [17] investigated the 166-compounds and solid solutions with respect to find an explanation of favored orders. And why it might become structurally advantageous to change the order upon substitution. The work beautifully illustrates how the electropositive guest atoms lead to dumbbell-formation and distortion of the surrounding honeycomb.

Magnetic properties have also been investigated in this family of compounds since the coupling between transition metal (*T*) in Kagomé layer and rare-earth metal (*M*) in channels results in complex magnetic interactions [14,18–21]. However, in some cases it has been shown that the *M* and *T* sublattices can order independently from each other [22]. With non-magnetic *M* atoms the structures show antiferromagnetism with Néel temperatures around 460 to 560 K [18,23–25]. The magnetic spin is oriented parallel to the (pseudo)hexagonal axis or in some cases slightly canted [26–28].

In the present work, we describe the synthesis, crystal structure and magnetism of $CaFe_6Ge_6$ and $Ca_{1-x}Co_6Ge_6$ compounds, whose existence was recently briefly reported by Gvozdetskyi *et al.*[29] $CaFe_6Ge_6$ has been successfully used as precatalyst for alkaline oxygen evolution reaction [30].

2. Experimental Section

2.1. Syntheses

All samples were prepared using commercially available elements of high purity: calcium (ChemPur, 99.5%, ingots), cobalt (Alfa Aesar, 99.9+%, shots), germanium (ChemPur, 99.999%, pieces) and iron (Alfa Aesar, 99.9%, granules). Arc melting has been performed using a modified Mini Arc Melting system (MAM-1, Johanna Otto GmbH) with a water-cooled copper-hearth in an argon filled glovebox (MBraun 20G, argon purity 99.996%). To avoid excessive evaporation of alkaline earth metal, melting was performed carefully and the sample turned several times. For annealing the samples were sealed either in welded niobium tubes and heated with an induction furnace or in graphitized silica tubes and annealed in a muffle furnace. Details for the preparation of single crystals can be found in the Supporting Information. Bulk samples were synthesized by pre-melting the transition metal and germanium in a stoichiometric ratio of 1:1. Then 1.02 eq. of calcium were added. The resulting piece was sealed under vacuum in graphitized silica and annealed in a muffle furnace (Nabertherm GmbH, Controller P330) at 800 °C for several days. The samples are air-stable grey solids with metallic luster at the broken edges.

2.2. X-ray Investigations

Phase analysis of the samples has been performed via powder X-ray diffraction (PXRD) on a STOE Stadi P equipped a Cu $K_{\alpha1}$ source (λ = 1.54060 Å), a curved Ge(111)-monochromator and a MYTHEN 1K PSD detector. The samples were homogenized and placed between two Scotch tapes. The corrections has been done versus external Si-standard by polynomial functions calculated from the matching mode of the experimental and standard Si-peak positions using the WinXPOW package [31]. The iron compounds show high phase purity after the heat treatment, the cobalt compounds show little amounts of $CaCo_2Ge_2$ (Figures 1 and 2). Rietveld refinement data were performed using the FullProf Suite [32].

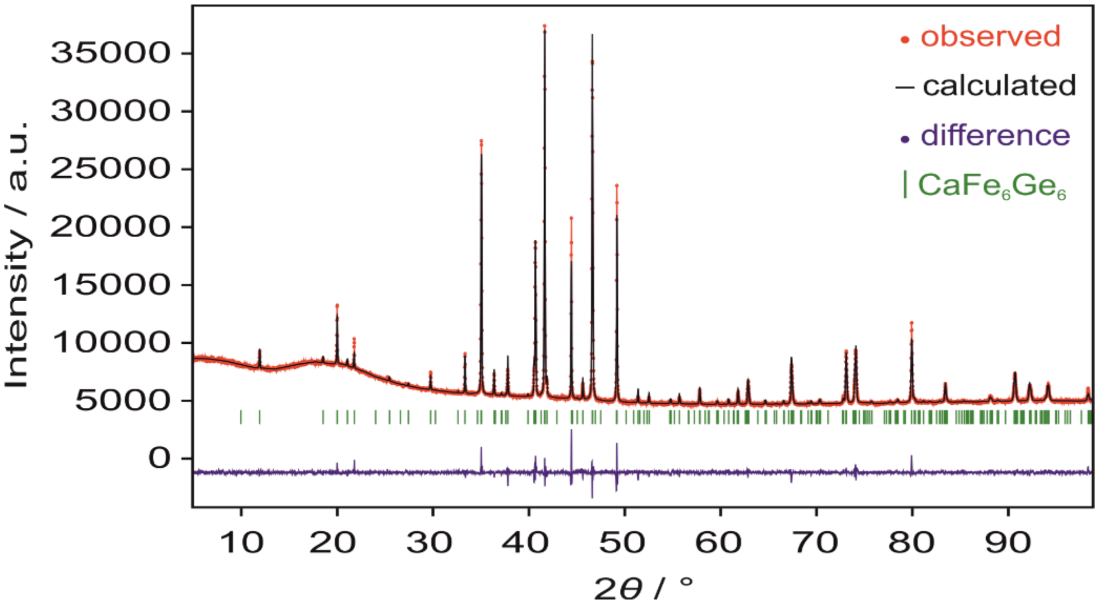

Figure 1. Rietveld refinement of powder X-ray diffraction data: $CaFe_6Ge_6$ annealed at 800 °C (space group *Cmcm*, Pearson code *oC*52).

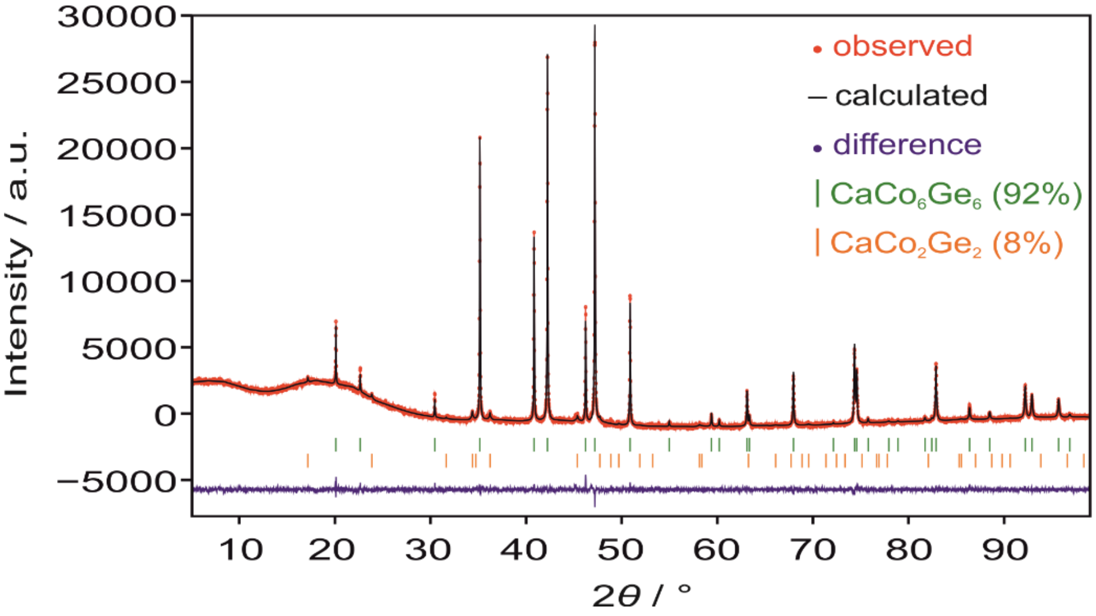

Figure 2. Rietveld refinement of powder X-ray diffraction data: $Ca_{1-x}Co_6Ge_6$ annealed at 800 °C, using *hP*7 structural model.

Single crystal data were collected with different diffractometers (for assignment of each reported crystal see Supporting Information and Table 1, Table **2**): a Bruker APEX-II with CCD detector (APEX II, κ-CCD), a rotating anode FR591 (Mo-K_α radiation, $\lambda = 0.71073$ Å) and a MONTEL optic monochomator; data set was collected with diffractometer software [33] and processed with SAINT [34] and SADABS [35], including an empirical absorption correction; a STOE IPDS 2T (rotating anode FR591, Mo-K_α radiation, $\lambda = 0.71073$ Å) with image plate detector; data were collected and analyzed with X-Area software package [36] and absorption was corrected numerically [37,38]; a STOE Stadivari (Genix 3D High Flux microfocus with Mo-K_α, graded multilayer mirror monochomator, DECTRIS Pilatus 300K detector); data were collected and analyzed using the X-Area software suite [36] including scaling with Laue Analyzer [39] und numerical absorption correction [37,38]; an Oxford-Xcalibur3 diffractometer (CCD area detector) with graphite monochromatized Mo-K_α ($\lambda = 0.71073$ Å) radiation; the Oxford CrysAlis RED software was used for data processing, including an empirical absorption correction with ABSPACK [40,41].

Structure solution was obtained with direct methods in SHELXS-2014 [42] and refined with SHELXL-2014 (full-matrix least-squares on F_0^2) [43,44]. To ensure the right composition, all occupation parameter were refined in separate least-square cycles. In the final cycles, not-affected positions were set back to ideal full occupation. All relevant details of the measurements and the structure refinements are listed in Table 1 and 2, the atomic positions and equivalent isotropic displacement parameters are given in Table 3 and 4. Observed electron density Fourier maps (bitmap and 3D-relief plot) were created with WinGX package [45]. Crystallographic data for structures in this paper have been deposited with the Cambridge Crystallographic Data Centre, CCDC, 12 Union Road, Cambridge CB21EZ, UK (Fax: +44-1223-336-033; e-mail: deposit@ccdc.cam.ac.uk, http://www.ccdc.cam.ac.uk) and can be obtained free of charge on quoting the depository numbers: CSD-2209484 for $CaFe_6Ge_6$ (crystal I), CSD-2209479 for $CaFe_6Ge_6$ (II), CSD-2209480 for $CaFe_6Ge_6$ (IIIa), CSD-2209481 for $CaFe_6Ge_6$ (IIIb), CSD-2209485 for $CaFe_6Ge_6$ (IV), CSD-2209486 for $Ca_{0.86}Co_6Ge_6$ (I), CSD-2209483 for $Ca_{0.90}Co_6Ge_6$ (II), CSD-2209477 for $Ca_{0.74}Co_6Ge_6$ (III), CSD-2209482 for $Ca_{0.89}Co_6Ge_6$ (IVa), CSD-2209478 for $Ca_{0.91}Co_6Ge_6$ (IVb).

Table 1 Crystal data and structure refinement of several crystals of $CaFe_6Ge_6$ with $Y_{0.5}Co_3Ge_3$-type (I), $MgFe_6Ge_6$-type (II), $TbFe_6Sn_6$-type structure (III, IV).

crystal	I	II	III		IV
empirical formula	$Ca_{0.5}Fe_3Ge_3$	$CaFe_6Ge_6$	$CaFe_6Ge_6$		$CaFe_6Ge_6$
formula weight (g mol^{-1})	405.76	810.72	810.72		810.72
temperature (K)	293	293	293		293
crystal system	hexagonal	hexagonal	orthorhombic		orthorhombic
space group	$P6/mmm$	$P6/mmm$	$Cmcm$		$Cmcm$
pearson code	$hP7$	$hP16$	$oC52$		$oC52$
structure type	$Y_{0.5}Co_3Ge_3$	$MgCo_6Ge_6$	$TbFe_6Sn_6$		$TbFe_6Sn_6$
unit cell dimensions					
a (Å)	5.1077 (1)	5.1017(1)	8.140(2)		8.150(2)
b (Å)	$= a$	$= a$	17.661(4)		17.698(4)
c (Å)	4.0636(2)	8.1080(5)	5.104(1)		5.116(1)
volume (Å^3)	91.810(6)	182.76(1)	733.7(3)		737.9(3)
Z	1	1	4		4
ρ_{calcd} (g cm^{-3})	7.73	7.366	7.34		7.30
μ (mm^{-1})	36.22	36.393	36.26		36.05
$F(000)$	184	368	1472		1472
crystal size (mm^3)	0.12×0.07×0.05	0.15x0.10.0.02	0.1×0.1×0.06		0.05×0.04×0.02
theta range for data collection (°)	4.6 – 50	4.6 – 32.42	2.3 – 32.5		2.3 – 32.5
index ranges in hkl	±10 , ±10, $-4 \le l \le 8$	±7 , ±7, $-12 \le l \le 7$	$-12 \le h \le 11$, $-26 \le k \le 24$, ±7		±12 , ±26 , ±7 ,
reflections collected	4986	3480	6146		7564
independent reflections	229 ($R_{int} = 0.013$)	174 ($R_{int} = 0.031$)	776 ($R_{int} = 0.044$)		779 ($R_{int} = 0.037$)
Reflections with $I \ge 2\sigma(I)$	228 ($R_{sigma} = 0.030$)	141 ($R_{sigma} = 0.011$)	591 (R_{sigma} 0.030)		437 (R_{sigma} 0.022)
data/restraints/parameters	229/0/13	174/0/22	776/0/46 (twin)	776/0/56 (disordered)	779/0/45 (twin)
goodness-of-fit on F^2	1.200	1.212	1.074	1.065	1.074
final R indices ($I > 2\sigma(I)$)	$R_1 = 0.033$, $wR_2 = 0.075$	$R_1 = 0.028$, $wR_2 = 0.080$	$R_1 = 0.020$, $wR_2 = 0.046$	$R_1 = 0.019$, $wR_2 = 0.044$	$R_1 = 0.024$, $wR_2 = 0.051$
R indices (all data)	$R_1 = 0.033$, $wR_2 = 0.075$	$R_1 = 0.033$, $wR_2 = 0.077$	$R_1 = 0.026$, $wR_2 = 0.051$	$R_1 = 0.025$, $wR_2 = 0.049$	$R_1 = 0.055$, $wR_2 = 0.057$
Extinction coefficient	—	0.038(5)	0.0025(1)	0.0025(1)	0.0025(1)
largest diff. peak and hole (e Å^{-3})	2.55, −1.09	1.89, −0.95	1.23, −1.51	0.96, −1.52	1.23, −1.51

Table 2 Crystal data and structure refinement of several crystals of $Ca_{1-x}Co_6Ge_6$ with $Y_{0.5}Co_3Ge_3$ type (I,II,III) and $ScFe_6Ga_6$ type structure (IV).

crystal	I	II	III	IV	
empirical formula	$Ca_{0.43(1)}Co_3Ge_3$	$Ca_{0.45(1)}Co_3Ge_3$	$Ca_{0.37(1)}Co_3Ge_3$	$Ca_{0.89(1)}Co_6Ge_6$	$Ca_{0.91(1)}Co_6Ge_6$
formula weight (g mol^{-1})	411.83	412.60	818.70	824.79	825.59
temperature (K)	293	293	293	293	
crystal system	hexagonal	Hexagonal	hexagonal	orthorhombic	
space group	$P6/mmm$	$P6/mmm$	$P6/mmm$	$Immm$	
pearson code	$hP7$	$hP7$	$hP7$	$oI26$	
structure type	$Y_{0.5}Co_3Ge_3$	$Y_{0.5}Co_3Ge_3$	$Y_{0.5}Co_3Ge_3$	$ScFe_6Ga_6$	
unit cell dimensions					
a (Å)	5.1018(1)	5.1016(2)	5.0746(7)	8.830(2)	
b (Å)	$= a$	$= a$	$= a$	5.100(1)	
c (Å)	3.9262(2)	3.9286(3)	3.8870(8)	7.855(2)	
volume (Å^3)	88.501(6)	88.55(1)	86.69(3)	353.7(1)	
Z	1	1	1	2	
ρ_{calcd} (g cm^{-3})	7.73	7.74	7.84	7.74	7.75
μ (mm^{-1})	36.24	39.245	39.967	39.29	39.31
$F(000)$	186	186	184	744	
crystal size (mm^3)	0.12×0.07×0.05	0.05×0.04×0.015	0.09×0.07×0.06	0.1×0.1×0.06	
theta range for data collection (°)	2.3 – 89.9	4.6 – 45	5 – 45	3.5 – 37.5	
index ranges in hkl	$-6 \le h \le 10$, $-7 \le k \le 9$, $-6 \le l \le 7$	$-9 \le h \le 10$, ±10, ±7	$-9 \le h \le 6$, $-8 \le k \le 10$, ±7	±15 , ±8, $-13 \le l \le 11$	
reflections collected	1946	3652	2825	13252	
independent reflections	180 ($R_{int} = 0.032$)	182 ($R_{int} = 0.022$)	178 ($R_{int} = 0.0475$)	556 ($R_{int} = 0.0411$)	
Reflections with $I \geq 2\sigma(I)$	161 ($R_{sigma} = 0.057$)	163 ($R_{sigma} = 0.091$)	130 ($R_{sigma} = 0.0767$)	482 ($R_{sigma} = 0.0118$)	
data/restraints/parameters	180/1/16	182/1/16	178/1/16	556/0/33 (twin)	556/1/41 (disordered)
goodness-of-fit on F^2	1.096	1.124	0.764	1.072	1.102
final R indices ($I > 2\sigma(I)$)	$R_1 = 0.031$, $wR_2 = 0.068$	$R_1 = 0.023$, $wR_2 = 0.043$	$R_1 = 0.0223$, $wR_2 = 0.0199$	$R_1 = 0.025$, $wR_2 = 0.070$	$R_1 = 0.021$, $wR_2 = 0.056$
R indices (all data)	$R_1 = 0.036$, $wR_2 = 0.071$	$R_1 = 0.031$, $wR_2 = 0.046$	$R_1 = 0.0430$, $wR_2 = 0.0216$	$R_1 = 0.027$, $wR_2 = 0.073$	$R_1 = 0.024$, $wR_2 = 0.058$
Extinction coefficient	0.11(1)	0.042(6)	0.044(3)	0.0035(6)	0.0043(5)
largest diff. peak and hole (e Å^{-3})	2.53, −1.86	1.032, −1.129	1.356, −1.347	1.23, −1.51	1.68, −1.24

Table 3 Atomic coordinates and equivalent isotropic displacement parameters of the $CaFe_6Ge_6$ compounds investigated in this report.

Atom	Site	Occupancy	*x*/*a*	*y*/*b*	*z*/*c*	$U_{eq}/10^{-3}\cdot$Å^{2} a)
I: $Ca_{0.5}Fe_3Ge_3$ (*P*6/*mmm*)						
Ca1	1a	0.505(3)	0	0	0	12.4(2)
Fe1	3g	1	½	0	½	12.8(1)
Ge1	2e	0.495(3)	0	0	0.3075(2)	13.6(2)
Ge2	2c	1	⅓	⅔	0	13.8(1)
II: $CaFe_6Ge_6$ (*P*6/*mmm*)						
Ca	1a	0.783(8)	0	0	0	3(7)
Ca*	1a	0.217(8)	0	0	½	4(3)
Fe	3g	1	½	0	0.25033(8)	8.7(4)
Ge1	2e	0.766(5)	0	0	0.3460(2)	10.8(4)
Ge1*	2e	0.234(5)	0	0	0.1521(6)	7(1)
Ge2	2c	1	⅓	⅔	0	10.0(4)
Ge3	1b	1	⅓	⅔	½	9.7(4)
III: $CaFe_6Ge_6$ (*Cmcm*, solved as twin)						
Ca1	4c	1	0	0.12627(5)	¼	4.9(1)
Ge1	4c	1	0	0.04203(3)	¾	4.4(2)
Ge2	4c	1	½	0.04103(3)	¾	4.1(2)
Ge3	4c	1	0	0.21000(3)	¾	3.7(2)
Ge4	4c	1	½	0.20606(3)	¾	3.6(2)
Ge5	8g	1	0.34662(3)	0.12485(2)	¼	4.1(1)
Fe1	8d	1	¼	¼	0	3.2(2)
Fe2	8e	1	0.25075(4)	0	0	3.0(2)
Fe3	8g	1	0.25125(4)	0.12497(3)	¾	3.2(1)
III: $CaFe_6Ge_6$ (*Cmcm*, solved with disorder)						
Ca1	4c	0.927(2)	0	0.12605(7)	¼	5.1(2)
Ca1*	4c	0.073(2)	½	0.1230(9)	¼	10(2)
Ge1	4c	1	0	0.04191(2)	¾	4.7(2)
Ge2	4c	1	½	0.04104(3)	¾	4.4(2)
Ge3	4c	1	0	0.20977(2)	¾	3.8(2)
Ge4	4c	1	½	0.20639(3)	¾	3.8(2)
Ge5	8g	0.927(2)	0.34656(4)	0.12487(2)	¼	4.2(2)
Ge5*	8g	0.073(2)	0.1551(7)	0.1250(3)	¼	7(1)
Fe1	8d	1	¼	½	0	3.3(2)
Fe2	8e	1	0.25065(3)	0	0	3.2(2)
Fe3	8g	1	0.25108(3)	0.12499(3)	¾	3.3(1)
IV: $CaFe_6Ge_6$ (*Cmcm*, solved as twin)						
Ca1	4c	1	½	0.1264(2)	¼	7.6(3)
Fe1	8g	1	0.2488(1)	0.8740(3)	¼	5.8(2)
Fe2	8e	1	0.2493(1)	0	0	6.9(7)
Fe3	8d	1	¼	¼	0	5.2(7)
Ge1	8g	1	0.15355(7)	0.12477(5)	¼	7.2(1)
Ge2	4c	1	0	0.2896(1)	¼	6.4(5)
Ge3	4c	1	0	0.9587(1)	¼	6.9(5)
Ge4	4c	1	½	0.9577(1)	¼	6.6(5)
Ge5	4c	1	½	0.2937(1)	¼	6.9(5)

a) U_{eq} is defined as one third of the trace of the orthogonalized *Uij* tensor.

Table 4 Atomic coordinates and equivalent isotropic displacement parameters of the $Ca_{1-x}Co_6Ge_6$ compounds investigated in this report.

Atom	Site	Occupancy	*x*/*a*	*y*/*b*	*z*/*c*	$U_{eq}/10^{-3}\cdot Å^2$ [a]
I: $Ca_{0.43(1)}Co_3Ge_3$ (*P*6/*mmm*)						
Ca1	1a	0.431(7)	0	0	0	7.5(7)
Co1	3g	1	½	0	½	8.6(2)
Ge1	2e	0.431(7)	0	0	0.3091(5)	8.4(5)
Ge2	2c	1	⅓	⅔	0	7.8(2)
Ge3	1b	0.14(2)	0	0	½	120(30) [b]
II: $Ca_{0.45(1)}Co_3Ge_3$ (*P*6/*mmm*)						
Ca1	1a	0.450(7)	0	0	½	8.(6)
Co1	3g	1	½	0	½	8.5(1)
Ge1	2e	0.450(7)	0	0	0.3091(3)	8.8(4)
Ge2	2c	1	⅓	⅔	0	7.6(2)
Ge3	1b	0.10(2)	0	0	½	100(40) [b]
III: $Ca_{0.37(1)}Co_3Ge_3$ (*P*6/*mmm*)						
Ca1	1a	0.369(7)	0	0	0	8(1)
Co1	3g	1	½	0	½	8.3(1)
Ge1	2e	0.369(7)	0	0	0.3071(5)	9.5(5)
Ge2	2c	1	½	⅔	0	8.6(1)
Ge3	1b	0.26(2)	0	0	½	80(1) [b]
IV: $Ca_{0.89(1)}Co_6Ge_6$ (*Immm*, solved as twin)						
Ca1	2a	0.89(1)	0	0	0	10.4(4)
Co1	4j	1	½	0	0.2472(1)	10.4(2)
Co2	8k	1	¼	¼	¼	10.4(1)
Ge1	4e	1	0.33489(7)	0	0	9.4(2)
Ge2	4f	1	0.16869(7)	½	0	9.7(2)
Ge3	4i	0.89(1)	0	0	0.3455(1)	10.7(2)
Ge4	4i	0.11(1)	0	0	0.278(7)	70(13) [b]
IV: $Ca_{0.91(1)}Co_6Ge_6$ (*Immm*, solved with disorder)						
Ca1	2a	0.61(1)	0	0	0	10.2(3)
Ca1*	2c	0.30(1)	½	½	0	12.6(6)
Co1	4j	1	½	0	0.24894(4)	11.0(1)
Co2	8k	1	¼	¼	¼	10.9(1)
Ge1	4e	1	0.33406(3)	0	0	10.0(1)
Ge2	4f	1	0.16733(3)	½	0	10.2(1)
Ge3	4i	0.61(1)	0	0	0.34553(9)	10.6(5)
Ge3*	4i	0.30(1)	0	0	0.1549(2)	12.5(4)
Ge4	4i	0.09(1)	0	0	0.270(4)	70(13) [b]

[a] U_{eq} is defined as one third of the trace of the orthogonalized U_{ij} tensor. [b] Large cigar-like ellipsoids resulting from statisctical Ca-deficiency, indicating high disorder of Ge within channels (see Figure 6).

2.3. Energy Dispersive X-ray Analysis (EDX)

Single crystal compositions have been validated with an Hitachi TM-1000 scanning electron microscope (SEM) equipped with an EDX analyzer (SWIFT-ED-TM). In the measured range (heavier than sodium) no impurities have been observed. Measurements have been performed without internal standard in a semi-quantitative way, images of crystals and EDX results are given in Supporting Information (Figure S2).

2.4. Thermal analysis

A scanning calorimeter (NETZSCH DSC 404C) was used for differential thermal analysis (DTA). About 50 - 100 mg of homogenized sample was sealed in custom-made niobium crucibles. Two to three heating/cooling cycles were run under argon atmosphere up to 900 °C (Figure S3, Supp. Inf.).

2.5. Magnetic measurements

With a MPMS XL5 SQUID magnetometer powdered samples (ca. 40 mg in a gelatin capsule fixed within a plastic straw) were investigated. Data were corrected for diamagnetic contributions of core electrons (Pascal's constants) and the sample holder. Field-dependent magnetization was measured between −50 and 50 kOe at 2 and 300 K respectively. For magnetic susceptibility, the samples have been precooled down to 2 K in zero magnetic field. Zero-field-cooled (ZFC) and subsequent field-cooled (FC) measurements were run at 20 Oe to check for superconductivity and at 5000 or 1000 Oe for $CaFe_6Ge_6$ or $Ca_{1-x}Co_6Ge_6$ respectively, to saturate magnetic impurities.

2.6. Electronic Structure Calculations

DFT-calculations using the TB-LMTO-ASA Method have been performed [46,47]. Exchange correlation terms were treated within the local density approximation with parameterization according to von Barth and Hedin [48]. Spherical atom radii were set automatically after Jepsen and Andersen [49]. As basis set the follwoing short-ranged atom-centered TB-LMTOs were used: s-d orbital for iron and cobalt, s-p for germanium and s, d for calcium. Downfolding technique was used for Ca 3p and Ge 3d orbitals [50]. Electron localization function has been calculated to visualize topographical surface of electron density within transition metal Kagomé-nets, germanium-nets and Ge_2-dumbbells. Values range from 0 to 1: large values refer to large degree of electron localization such as bonding and non-bonding states, medium values may arise from delocalized (metallic) states and low values show nodes and spatial minima [51].

Since disorder cannot be calculated with LMTO, only fully-ordered models have been used. In case of hexagonal *P*6*/mmm* space group, for $CaFe_6Ge_6$ only the larger supercell with $MgFe_6Ge_6$-type has been used and in case of $Ca_{0.5}Co_3Ge_3$ a model isotructural to the iron compound has been created, doubling the *c*-parameter.

3. Results and Discussion

CaT_6Ge$_6$ (T = Fe, Co) have been recently reported to crystallize in the hexagonal $Y_{0.5}Co_3Ge_3$ structure type (space group $P6/mmm$) with atomic disorder within hexagonal channels, with only lattice parameters established from powder X-ray diffraction [29]. CaT_6Ge$_6$ (T = Fe, Co) are the second ternary compounds after $CaFe_2Ge_2$ [52] and $CaCo_2Ge_2$ [53] reported in corresponding systems. Our detailed research shows that besides the highly disordered hexagonal structures with $Y_{0.5}Co_3Ge_3$-type also the ordered orthorhombic variants with slightly deformed Kagomé layers can be obtained.

Fredrickson *et al.* [17] described $MgFe_6Ge_6$-type as modification with highest possible electrostatic stabilization with all cations and negatively polarized germanium atoms in one layer. At the other hand, with maximal sterical stabilization lies $ScFe_6Ga_6$. These and other possible types of order are given in Figure S4 (Supp. Inf.). In the first case, all channels have the electropositive "guest" atom occupy all hexagonal voids of the same layer and no free void where the atoms of a honeycomb could retreat. The highest possible arrangement to reduce this "chemical pressure" is alternating rows of occupied and empty segments, which is the case for $ScFe_6Ga_6$. By filling a segment with a large cation, the atom above and below are pushed in the the adjaced segments, forming dumbbells there. Intermediate between these two are patterns with several rows occupied by an atom followed by a number of empty rows. One of these is the $TbFe_6Sn_6$-type, where two rows with calcium atoms are followed by two rows with Ge-dumbbells. This clearly shows that in contrast to $MgFe_6Ge_6$, where electronic contribution predominates, the substitution with larger calcium requires an intermediate order to balance between electronic and steric factors.

3.1. Crystal structure of $CaFe_6Ge_6$

$CaFe_6Ge_6$ can be formed directly via arc melting (Figure S5, Supp. Inf.) and occurs also as secondary phase in the synthesis of $CaFe_2Ge_2$ [52]. In order to obtain phase purity, additional annealing procedure was necessary. Afterwards, the powder diffractogram (Figure 1) shows some additional reflections, which were assigned to superstructure peaks of ordered $TbFe_6Sn_6$-type. A refinement with co-existence of disordered $Y_{0.5}Co_3Ge_3$-type and ordered $TbFe_6Sn_6$-type is given in Figure S6 (Supp. Inf.). However, since all reflections of the minor phase are overlapping with those from the main phase, some parameters could not be refined simultaneously and these values are not reliable.

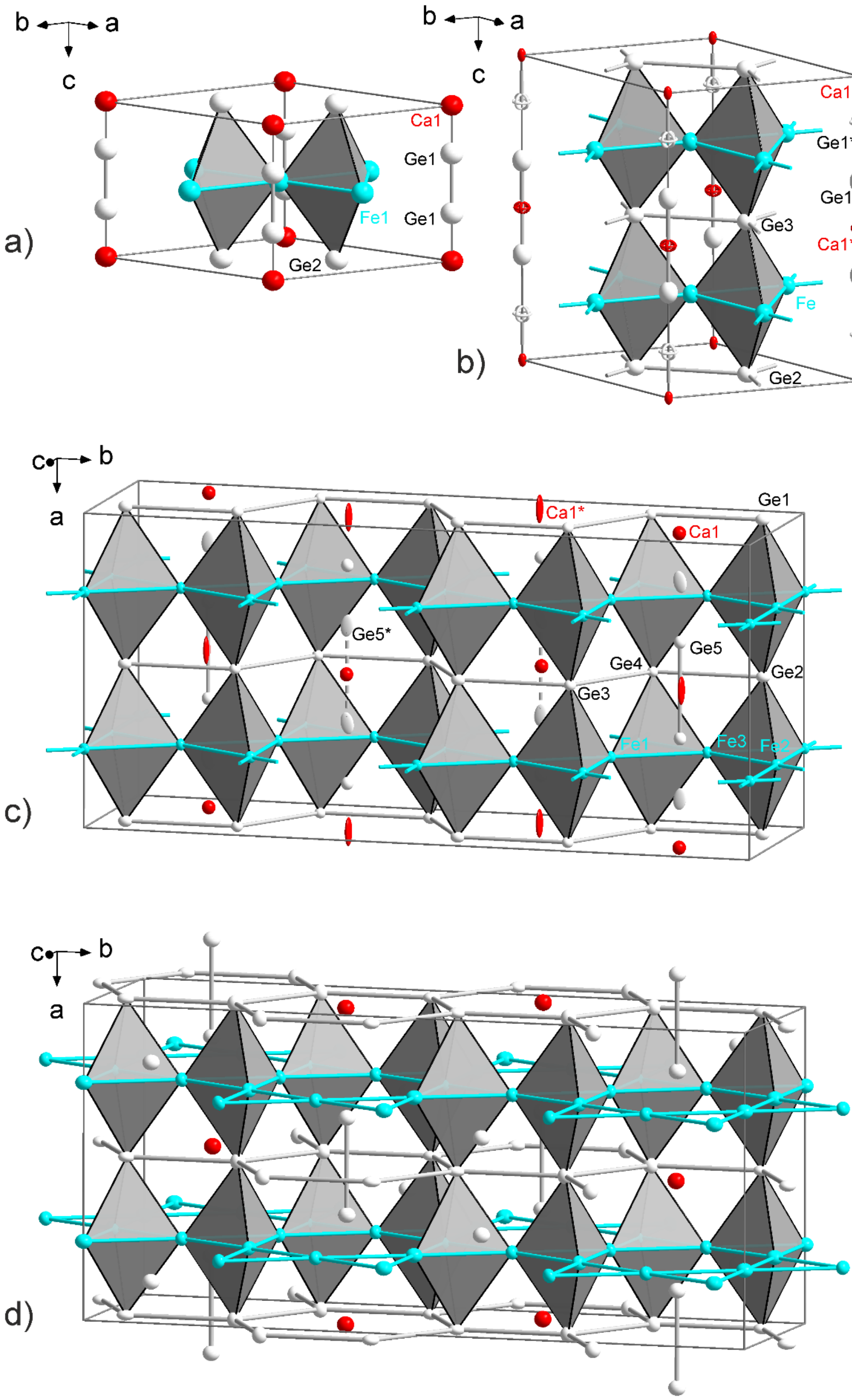

Figure 3. Crystal structure of $CaFe_6Ge_6$. a) $Y_{0.5}Co_3Ge_3$-type (crystal I), with random distribution of Ca-atoms and Ge–Ge-dumbbells (occupation Ca1 = 50.5(3)%, Ge1 = 49.5(3)%), b) $MgFe_6Ge_6$-type (II) (occ. Ca1 = 78.3(8)%, Ca1* = 21.7(8)%, Ge1 = 76.6(5)%, Ge1* = 23.4(5)%) and c) $TbFe_6Sn_6$-type (III, IV) with alternating Ca and Ge–Ge in the cannels, refined with positional disorder, less occupied split position drawn as principal ellipsoids (occ. Ca1 ≙ Ge5 = 92.7(2)%, Ca1* ≙ Ge5* = 7.3(2)%), d) similar to c), but refined as twin with no disorder.

To investigate the structural transition $Y_{0.5}Co_3Ge_3$-type ↔ $TbFe_6Sn_6$-type into detail (Figure 3), single crystals were grown by heating to 1000 °C, cooling down to different temperatures and annealing the samples for different time. No reversible order-disorder transition could be observed and all samples show the presence of the $TbFe_6Sn_6$-type. The single crystals (III and IV) show a large unit cell that can be indexed as hexagonal or orthorhombic, but no satisfying structural model could be found at first. Using the smaller orthorhombic unit cell of $TbFe_6Sn_6$ – type (*Cmcm*) with split position to refine fractional disorder, gives reasonable reliability factors, but some reflections are ignored (see Figure S7b-ii, Supp. Inf.). Another approach was used for the structure refinements of $HoFe_6Ge_6$, $DyFe_6Sn_6$ and HfPdGe, where a large unit cell indicates to be in fact a result of three pseudomerohedrally twinned micro-domains [54–56]. This can be explained by starting with the long-ranging hexagonal Fe_6Ge_4 host lattice. Due to the 6-fold rotational axis in the center of channel, three symmetry related orientations of the orthorhombic subcell are possible. The possible reciprocal cells are illustrated in the constructed reciprocal sections in Figure S7 (Supp. Inf.). When ordering takes place in different directions within the same crystal, multiple domains might remain. To estimate if the $CaFe_6Ge_6$ crystals are twinned or the structure has a certain disorder, both possibilities have been refined and are given in Table 1 and Table 3. The model using (1 0 0) (0 ½ 3) (0 ¼ −½) as twinning matrix successfully describes the structure without any disorder. Looking at the 3*kl*-section of the reciprocal lattice, all superstructure reflections are clear and no diffuse scattering can be seen.

Crystals grown in an induction furnace with faster cooling don’t show superstructure reflections and the structure can be described with hexagonal cell of $Y_{0.5}Co_3Ge_3$-type (crystal I) or $MgFe_6Ge_6$-type (crystal II) listed in Table 1 and Table 3. The reciprocal 0*kl*-section of crystal I (Figure S7-iii, Supp. Inf.) contains some diffusive scattering, but regarding the *hk*1.5 plane (Figure S7a-ii) no distinct reflections like to the ones shown in Figure S7b-ii (Supp. Inf.) have been seen yet, only vague spots are present. It is evident that slow cooling or tempering is necessary to develop an order. Differential thermal analysis of annealed samples did not show evidence of reversible phase change between 150 and 900 °C (Figure S3, Supp. Inf.).

In the following, interatomic distances of the ordered modification (*oC*52) are examined and listed in Table 5 together with those of related Ca-Fe-Ge ternary and Ca-Ge/Fe-Ge binary compounds as well as pure elements. The Fe–Fe-distances in the Kagomé-net have a very close range, indicating only a very slight distortion. These are larger compared to CoSn-type FeGe, whose distances are identical to elemental iron, and similar to $MgFe_6Ge_6$. Insertion of alkaline earth atoms increases the hexagonal voids, a large Ca-excess leads to the formation of $CaFe_2Ge_2$

compound with square planar iron lattice and considerably larger Fe–Fe -distance. Germanium positions in $CaFe_6Ge_6$ can be distinguished between Ge_d in dumbbells and Ge_f in hexagonal framework. Within the framework range of Ge–Ge-distances is similar to that of $MgFe_6Ge_6$ and larger than in FeGe. Figure 4 illustrates a slight distortion of the hexagonal network, where Ge_f–Ge_f-distances are shorter with dumbells in both adjacent channels, largest with two adjacent calcium atoms and intermediate in mixed environment. The length of the dumbbells is a bit shorter than within the framework, which agrees with the picture of bigger calcium forcing the Ge atoms within chanels to move closer to each other. It is almost as short as in elemental germanium and considerably shorter than the Ge–Ge-contacts in $CaFe_2Ge_2$. The Fe–Ge-distances are shorter within the framework than to the dumbbells, so the last can be regarded as isolated Ge_2^{2-}-fragmtents. All Fe–Fe, Ge–Ge and Fe–Ge-distances are within the range found for binary M_xGe_y (M = Ca, Fe) compounds. The Ca–Fe distance of 3.2472(7) Å is the shortest up to date. The Ca–Ge distance is shorter between calcium atoms and Ge-dumbbell (2.8217(6) Å) than between calcium and the framework Ge-atoms (2.949(1) – 2.972(1) Å).

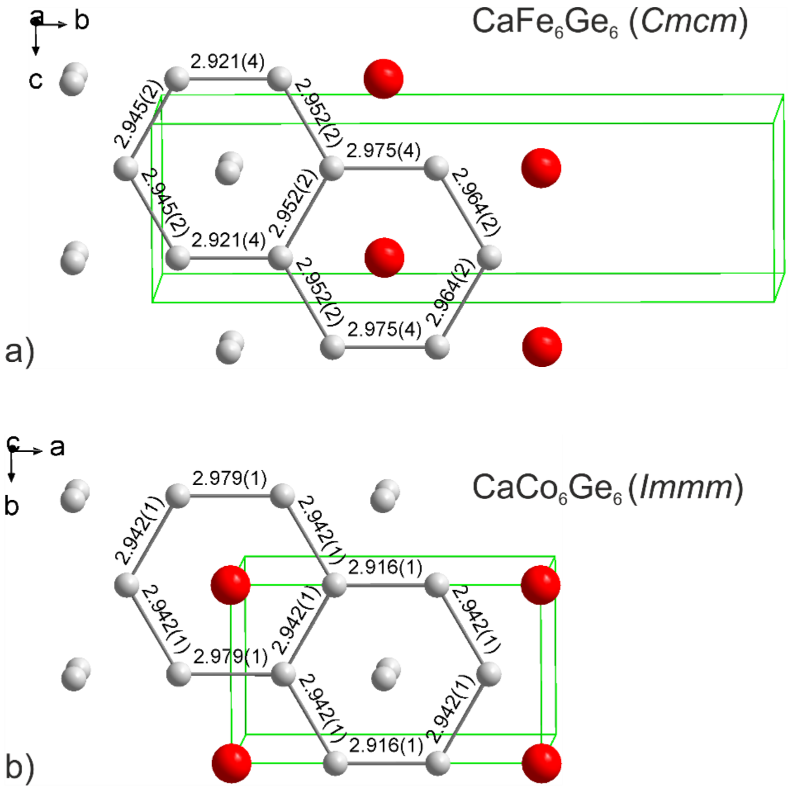

Figure 4. Ge–Ge distances within the honeycomb-layer of (a) $CaFe_6Ge_6$ (crystal III) and (b) $Ca_{1-x}Co_6Ge_6$ (crystal IV). Distances situated between two calcium atoms are generally elongated compared to those between two adjacent dumbbells. The layer contains alternatingly rows (from bottom left to top right) of calcium and rows of Ge_2-dumbbells. All numbers are given in Å, calcium atoms in red and germanium-atoms in white.

Table 5 Comparison of interatomic distances in the ternary compounds $CaFe_6Ge_6$, $MgFe_6Ge_6$ and $CaFe_2Ge_2$, in the Ca-Ge and Fe-Ge binary compounds and pure elements. The shortest distance between two types of atoms is highlighted in bold, not considering numbers in brackets. Ge_f and Ge_d corresponds to the atoms in the Fe_6Ge_4-framework or Ge_2-dumbbell respectively.

d / Å	$Ca_{0.5}Fe_3Ge_3$ *P*6/*mmm* (I)	$CaFe_6Ge_6$ *P*6/*mmm* (II)	$CaFe_6Ge_6$ *Cmcm* (III)	$MgFe_6Ge_6$	$CaFe_2Ge_2$	FeGe [1]	M_xGe_y (M = Ca, Fe)	Element
d(Fe–Fe)	2.5539(1)	2.5508(1)	2.5493(7) – 2.5517(5)	2.53	2.82	2.48	**2.46** – 2.86	2.48
$d(Ge_f–Ge_f)$	2.9490(1)	2.9455(1)	2.915(1) – 2.9666(6)	2.93	2.62	**2.87**	2.51 – 3.38	**2.45**
$d(Ge_d–Ge_d)$	2.499(1)	2.498(2)	2.4971(7)	2.56		—		
$d(Ge_f–Ge_d)$	3.2027(3)	3.1992(6)	**3.1725(9)** – 3.2036(5)	3.19		[3.51]		
$d(Fe–Ge_f)$	2.5103(1)	2.5033(5) – 2.5077(4)	2.4801(7) – 2.5374(7)	2.48 – 2.49	2.42	2.48	**2.04** – 3.09	—
$d(Fe–Ge_d)$	2.6710(2)	2.6661(5)	2.6644(5) – 2.6705(5)	2.64		2.48		
$d(Ae–Ae)$	5.1017(1)	5.107(1)	5.104(1)	[5.067]	3.994	—	**3.34** – 3.75	3.948
$d(Ae–Fe)$	3.2634(1)	3.2598(4)	**3.2472(7)** – 3.2814(8)	[3.23]	3.34	—	—	—
$d(Ae–Ge_f)$	2.9490(1)	**2.9455(1)**	2.949(1) – 2.972(1)	[2.93]	3.11	—	2.97 – 3.56	—
$d(Ae–Ge_d)$	2.8142(8)	**2.805(2)**	2.8217(6)	[2.74]				

[1] CoSn-type with Fe_6Ge_4-subunit that also occurs in $CaFe_6Ge_6$ and $MgFe_6Ge_6$.

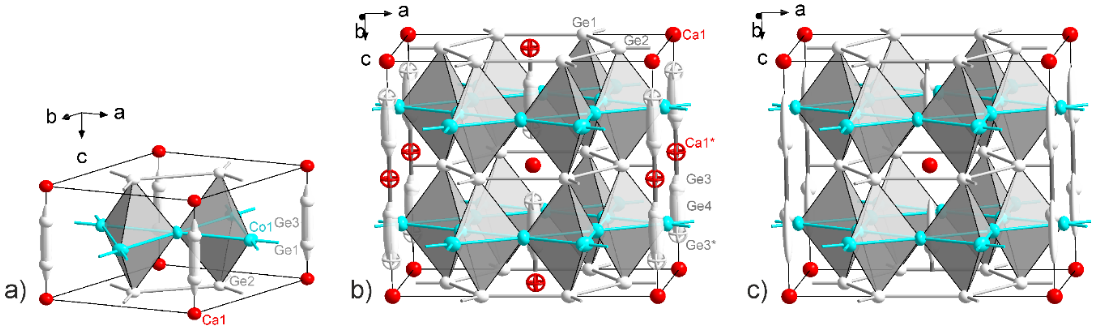

Figure 5. Crystal structure of $Ca_{1-x}Co_6Ge_6$. a) $Y_{0.5}Co_3Ge_3$ / CoSn types intergrowth (crystal I, II, III) with randomly distributed Ca-atoms, Ge–Ge-dumbbells and single Ge-atoms with elongated displacement ellipsoid along c-direction (occupation Ca1 ≙ Ge1 = 43.1(7)%, Ge3 = 14(2)%), b) $ScFe_6Ga_6$ / CoSn types intergrowth (crystal IV) with alternating Ca and Ge–Ge in the channels, refined with positional disorder, less occupied positions drawn as principal ellipsoids (occ. Ca1 ≙ Ge3 = 61(1)%, Ca1* ≙ Ge3* = 30(1)%, Ge4 = 9(1)%), c) similar to b), but refined as twin (occ. Ca1 ≙ Ge3 = 89(1)%, Ge4 = 11(1)%).

3.2. Crystal structure of $Ca_{1-x}Co_6Ge_6$

Similar to $CaFe_6Ge_6$, the $Ca_{1-x}Co_6Ge_6$ compound can be obtained directly by arc melting a stoichiometric mixture of the elements. Subsequent annealing results in the removal of most secondary phases. The powder XRD (Figure 2) can be fitted with “*hP*7” ($Y_{0.5}Co_3Ge_3$-type) model. Various different temperature treatments have been tested but no superstructure reflections have been found that would indicate ordering within the channels. Single crystals always showed the $Y_{0.5}Co_3Ge_3$-type with additional electron density (Figure 5a, Table **2** and Table 4). However, after annealing the sample contains the crystals (IV) with a larger pseudohexagonal unit cell, that could be indexed with orthorhombic lattice. Similar to iron-compound described above, the crystal structure can be solved using a smaller orthorhombic unit cell with disorder on split positions or $(\frac{1}{2}\ {-\frac{3}{2}}\ 0)\ ({-\frac{1}{2}}\ {-\frac{1}{2}}\ 0)\ (0\ 0\ 1)$ as twinning matrix. However, the cobalt compound adopts the $ScFe_6Ga_6$-type (*Immm*) with deficient calcium, which allows some germanium in plane with cobalt Kagomé net, similar to the CoSn-type.

Usually in 166-family the channels are filled by alternating rare earth / alkaline earth atoms with dumbbells. The structure can be derived from CoSn, where Ca atoms occupy the void in the channels, pushing the p-element apart and forcing it to form the dumbbells. This is illustrated in Figure 6, where “Ge3” describes the atomic position analogue to Sn position in CoSn-type, when no calcium would be present. With short-range order, calcium and the dumbbell’s center of gravity can be at each top or bottom corner of the unit cell, respectively. But in case of Ca-deficiency the germanium atoms move back to the “equilibrium position” of CoSn-type, which results in a large cigar-like displacement ellipsoid. Unlike the $CaFe_6Ge_6$

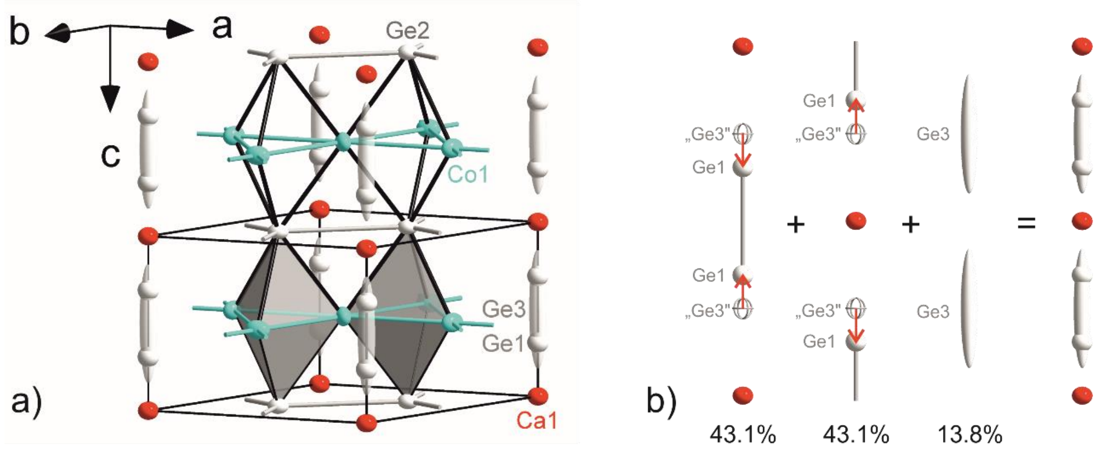

Figure 6. a) Structure of $Ca_{1-x}Co_6Ge_6$ with disorder in channels. Co1 and Ge2 form the framework, Ca1, Ge1 and Ge3 fill the channels. The different locations within the channels are projected into an averaged unit cell with split positions whose occupancies sum up to 100%. b) Possible arrangements of the atoms. Calcium atoms force germanium atoms from Ge3 position (shown as principal ellipsoids) to Ge1 position, creating dumbbells. Ca vacancy leads to positional disorder with cigar-like ellipsoids (Ge3).

compound with highly disordered structure (small hexagonal cell, crystal I), where in the channels the calcium atoms overlaps/coexists with the germanium dumbbells in a 50:50 ratio, for $Ca_{1-x}Co_6Ge_6$ compound one additional germanium position Ge3 with occupancy of 13.8 at.% is found as a result of calcium deficiency. Samples being annealed for longer time (crystal III) show less calcium and more Ge3 atoms. Thus the structures of $Ca_{1-x}Co_6Ge_6$ compound can be described as an intergrowth of the $Y_{0.5}Co_3Ge_3$ (crystals I, II, III) or $ScFe_6Sn_6$ (crystal IV) and CoSn structure types. This is remarkable since no modification of CoGe is known to form this type. $CaFe_6Ge_6$, for which the binary FeGe with CoSn-type is known, does not show any calcium deficiency or electron density between the germanium positions. Fourier maps of observed electron density are given in Figure 7 for $Ca_{1-x}Co_6Ge_6$ with ordered and disordered modification and ordered $CaFe_6Ge_6$. To collect the electron density of all possible domains, the split-models have been used for both cobalt compounds instead of a twinning matrix. Between end-positions of Ge–Ge-dumbbells the contributions of Ge3 are visible. There is no distinct maximum which agrees with the large, cigar-like displacement ellipsoid. For the iron compound, no significant electron density is observered between atoms.

As described recently, the $ScFe_6Ga_6$-type is an ordered structure with minimized strain caused by the insertion of guest atoms into the hexagonal voids of T_3X_2 host substructure and substitution with larger atoms eventually can result in an unordered $Y_{0.5}Co_3Ge_3$-type structure [17]. Calcium is the largest reported guest atom that has been successfully introduced to the T_3X_2 host substructure. The substitution of iron with slightly larger cobalt leads to most sterically-dominated arrangement. The difficulty to obtain the single crystals, which show any superstructure reflections, whereas most attempts resulted in the disordered modification, demonstrates that calcium barely fits into $Ca_{1-x}Co_6Ge_6$. The electronic factor may also play a role in the stability of the structure: $CaCo_6Ge_6$ is 6 electrons richer compared to $CaFe_6Ge_6$. This might explain why some calcium gets lost during annealing leaving up to 26% of the voids unoccupied. No indication for reversible phase transition upon heating/cooling could be detected with differential thermal analysis between 150 and 900 °C.

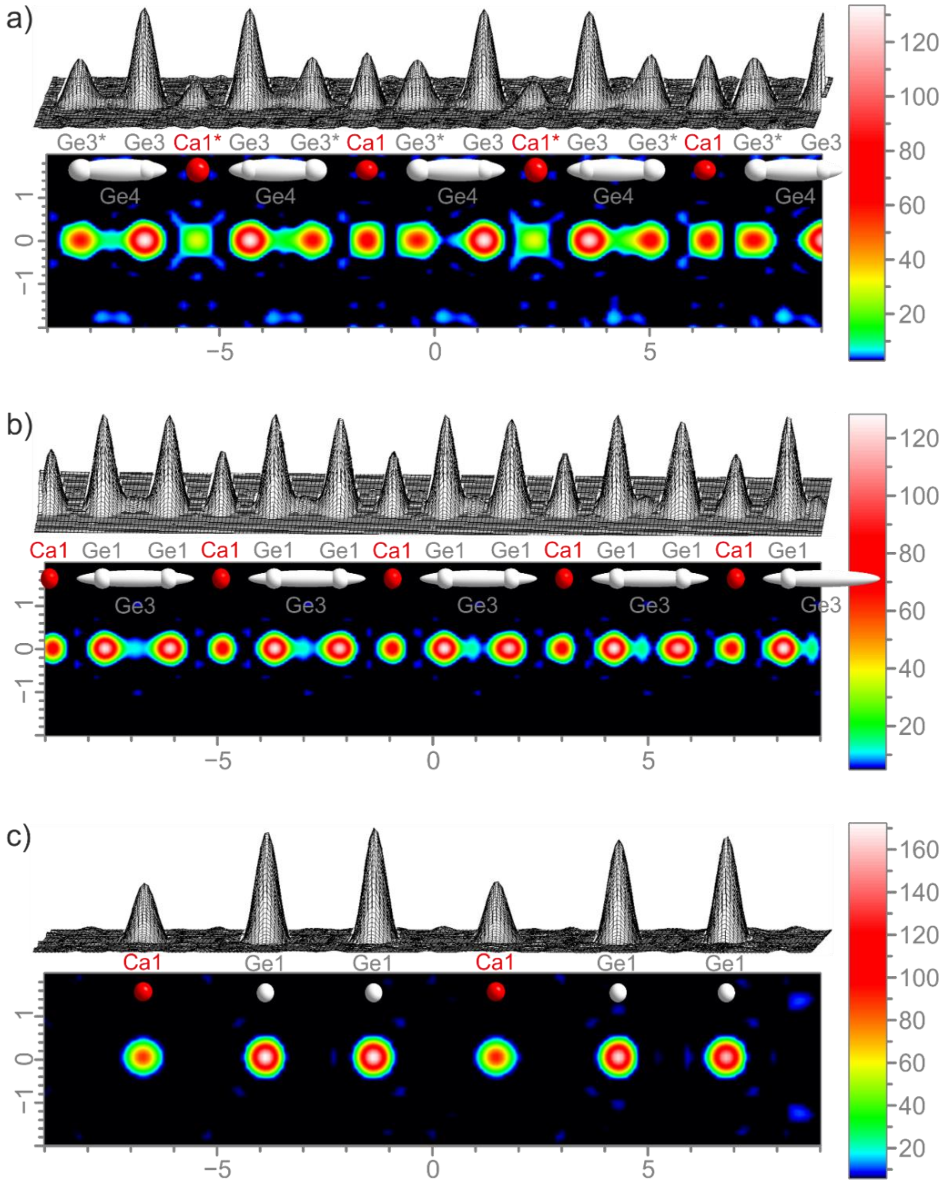

Figure 7. Observed electron density Fourier map (bitmap and 3D-relief plot) as well as the corresponding ADP ellipsoids of a) $Ca_{1-x}Co_6Ge_6$ with $GaFe_6Sn_6$-type (crystal IV), b) $Ca_{1-x}Co_6Ge_6$ with $Y_{0.5}Co_3Ge_3$-type (crystal I) and c) $CaFe_6Ge_6$ with $TbFe_6Sn_6$-type structure (crystal IV). The large ellipsoids of Ge3 or Ge4, respectively, can be seen as smeared electron density between the well-defined Ge-atoms.

Table 6 Comparison of bonding distances found for elemental and binary compounds in the Ca–Co–Ge-system and the ternary compounds $CaCo_6Ge_6$, $MgCo_6Ge_6$ and $CaCo_2Ge_2$. The shortest interatomic distance between two types of atoms is highlighted in bold, not considering numbers in brackets. Ge_f and Ge_d corresponds to the atoms in the Fe_6Ge_4-framework or Ge_2-dumbbell respectively; Ge_a refers to the additional Ge-position that is created by the deficiency of calcium.

d / Å	$Ca_{0.37(1)}Co_3Ge_3$	$Ca_{0.45(1)}Co_3Ge_3$	$Ca_{0.89(1)}Co_6Ge_6$	$MgCo_6Ge_6$	$CaCo_2Ge_2$	M_xGe_y (M = Ca, Co)	element
	*P*6/*mmm* (III)	*P*6/*mmm* (II)	*Immm* (IV)				
d(Co–Co)	2.5373(2)	2.5507(1)	2.5492(4) – 2.5498(5)	2.54	2.82	**2.38** – 2.84	2.51
d(Ge_f–Ge_f)	2.9302(3)	2.9452(1)	2.916(1) – 2.979(1)	2.93	2.67	2.43 – 3.27	2.45
d(Ge_d–Ge_d)	**2.388(3)**	2.429(2)	2.428(2)	2.50			
d(Ge_f–Ge_d)	3.1637(8)	3.1859(5)	3.1670(9) – 3.1782(6)	3.18			
d(Ge_f–Ge_a)	[3.5158(3)]	[3.5403(1)]	[3.405(3) – 3.416(3)]				
d(Co–Ge_f)	2.4337(3)	2.4549(1)	2.4283(9) – 2.4823(9)	2.43	2.35	**2.24** – 2.79	—
d(Co–Ge_d)	2.6458(6)	2.6586(3)	2.6517(6) – 2.6571(5)	2.63			
d(Co–Ge_a)	2.5372(3)	2.5508(1)	2.558(4) – 2.559(5)				
d(*Ae*–*Ae*)	5.075(1)	5.102(1)	5.100(1)		4.00	**3.34**–3.75	3.948
d(Ca–Co)	**3.1962(3)**	3.2193(1)	3.2178(4)	[3.19][1]	3.26		—
d(Ca–Ge_f)	**2.9297(4)**	2.9453(1)	2.9530(5) – 2.9569(9)	[2.93][1]	3.12	2.97 – 3.56	—
d(Ca–Ge_d)	**2.693(2)**	2.714(1)	2.714(1)	[2.62][1]			

[1] corresponding distances to Mg are given.

Table 6 lists relevant interatomic distances in $Ca_{1-x}Co_6Ge_6$ (*oI*26), other Ca-Co-Ge ternary and Ca-Ge/Co-Ge binary compounds as well as in the elements. Germanium atoms are divided into Ge_f as part of the host structure, Ge_d in dumbbells and additional Ge_a atom within the channel.

Cobalt-sublattice is a slightly distorted Kagomé lattice in *Immm* structure, almost as short as in the element. Honeycomb germanium sublattice is also slightly distorted with largest Ge_f–Ge_f-distance between two calcium-filled channels and shortest distance between two channels filled by germanium dumbbells (Figure 4). These Ge–Ge-distances in $Ca_{1-x}Co_6Ge_6$ are slightly larger than in $MgCo_6Ge_6$ and $CaFe_6Ge_6$ due to larger atomic size of calcium atoms compared to magnesium and cobalt atoms compared to iron, respectively. The length of the dumbbells is significantly shorter and matches with the shortest Ge–Ge-distance found in binary Ca-Ge/Co-Ge compounds. The additional germanium atoms only fit in the channel with no calcium or dumbbell next to it. Its distance to the honeycomb-layer is too large to consider as bonding, the only meaningful distance is to the cobalt Kagomé layer. These Ge atoms are closer to the metal atoms than the Ge–Ge dumbbell but at larger distance than the germanium atoms of the framework. Other Co–Ge distances are intermediate between those of $MgCo_6Ge_6$ and $CaFe_6Ge_6$ compounds. The Ca–Ge distance is shorter between calcium and dumbbell-atoms than between calcium and the framework-atoms. The Ca–Co and Ca–Ge contacts in $Ca_{1-x}Co_6Ge_6$ are the shortest up to date with 3.1962(3) and 2.693(2) Å, respectively. The last is remarkably shorter than for any binary compound (−8.6%) and even shorter than in the iron analogon (−3.8%). This might explain the deficiency of Ca position as well as the difficulty to obtain an ordered structure.

3.3. Magnetic properties

$CaFe_6Ge_6$. Magnetic measurements of bulk sample with $TbFe_6Sn_6$-type exhibit a small hysteresis and saturation is attributed to ferromagnetic impurities (Figure 8). Magnetic susceptibility was measured at 5000 Oe to obtain saturation of impurities. The resulting Field-cooled susceptibility follows the Curie-Weiss-law with an asymptotic Curie-Temperature of −1065 K. This indicates antiferromagnetic order, which is often discussed in relation of Kagomé-lattices [21,25,57,58]. However, no antiferromagnetic order was observed down to 2 K. In contrast, for $MgFe_6Ge_6$ Matzet *et al.* [23] reported a Néel-Temperature of 501 K. It seems that the large calcium atoms prevents the formation of magnetic order. The effective magnetic moment is 2.72 μ_B per iron atom.

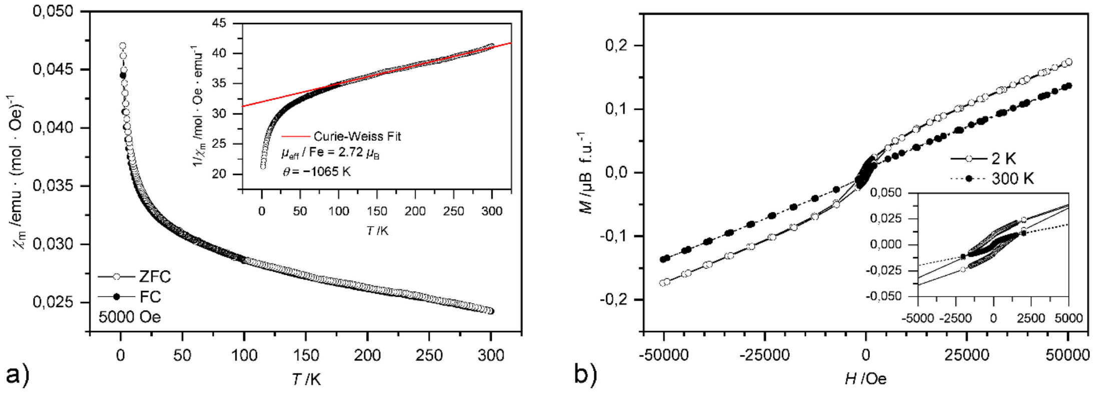

Figure 8. Magnetic properties of $CaFe_6Ge_6$: a) molar magnetic susceptibility χ_m (ZFC/FC) and inverse molar susceptibility $1/\chi_m$ (insert, FC) as function of temperature; b) field-dependent magnetization measured at 300 and 2 K.

$Ca_{1-x}Co_6Ge_6$. Magnetic properties of $Ca_{1-x}Co_6Ge_6$ bulk sample with $Y_{0.5}Co_3Ge_3$-type structure (Figure 9) are similar to that of $CaFe_6Ge_6$. Some small hysteresis with saturation might be attributed to ferromagnetic impurities. Essentially, magnetization and susceptibility show paramagnetism, following the Curie-Weiss law. Asymptotic Curie temperature is −1880 K but no Néel temperature could be found below which the phase becomes antiferromagnetic. Effective magnetization of 0.79 μ_B per cobalt atom is lower than for the iron compound and is in agreement with the fact that the cobalt compound is reluctant to form an ordered structure.

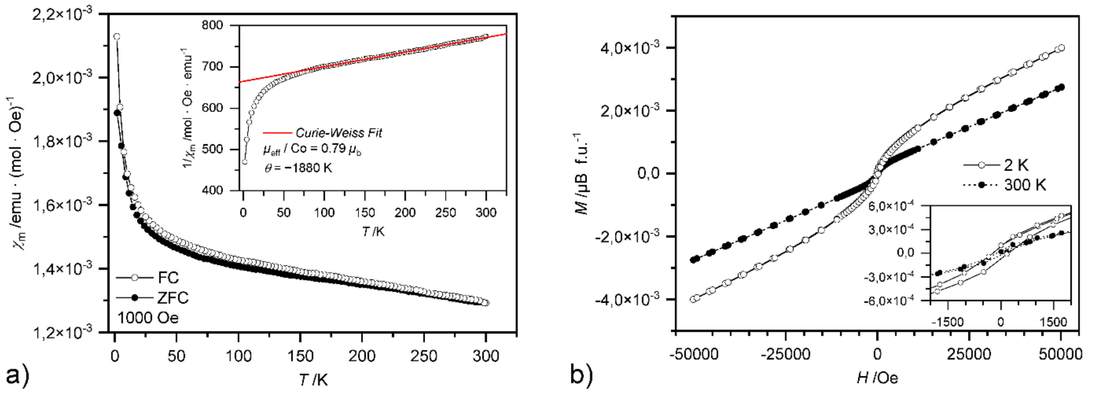

Figure 9. Magnetic properties of $Ca_{1-x}Co_6Ge_6$: a) molar magnetic susceptibility χ_m (ZFC/FC) and inverse molar susceptibility $1/\chi_m$ (insert, FC) as function of temperature; b) field-dependent magnetization measured at 300 and 2 K.

3.4. Electronic structure calculations

To investigate the influence of the type of order on the electronic structure, the LMTO-calculations have been performed for different modifications. The resulting density of states (DOS) and orbital-projected DOS for the fully ordered orthorhombic modifications are given in Figure 10. They are very similar to the calculations using the hexagonal $MgFe_6Ge_6$-type as a structural model (Figures S8 and S9, Supp. Inf.). All structures feature a block between −13 and −7 eV that contains mainly Ge–s states. Followed by a small pseudogap, a large block of bands dominated by Ge–p and Ni–d states is found with two groups of large peaks below and one closely above the Fermi level. While the rough shape is similar for iron- and cobalt-compound, which is in agreement with the rigid-band-model, the location of the Fermi-level is different due to the addition electrons in $CaCo_6Ge_6$. In the iron-compound (Figure 10a) it is located on the shoulder of the large peak, whereas in cobalt compound (Figure 10b) it is shifted to the pseudo gap. As single crystals show some calcium-deficiency, the integrated DOS has been considered and correspondingly adapted. It seems that the Fermi level is attracted to a small local minimum, however, the calculation gets imprecise as an additional Ge position and the disorder may change the electronic structure. Both compounds have states at the Fermi-level, which means these should have metallic properties.

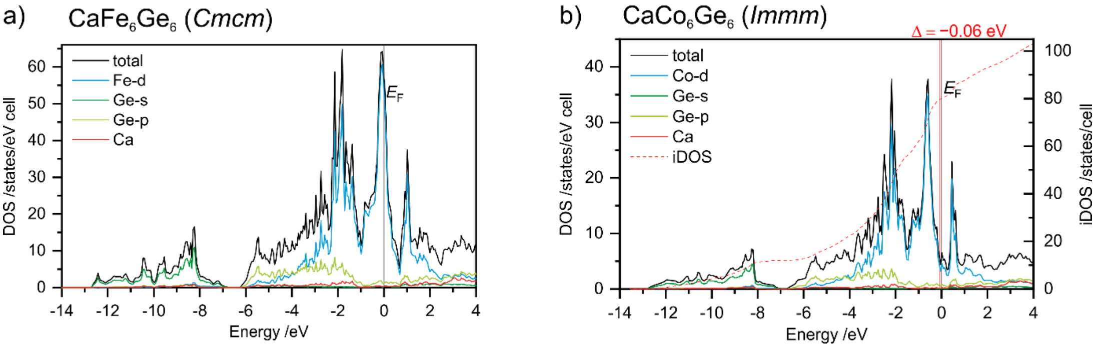

Figure 10. Density of states (DOS) for $CaFe_6Ge_6$ with space group *Cmcm* and $CaCo_6Ge_6$ with space group *Immm*. Projected DOS are given for selected orbitals and integrated DOS has been used to look for effects caused by calcium-deficiency in $CaCo_6Ge_6$.

Figure 11 shows topographical sections of electron density based on the electron localization function (ELF). As the cobalt compound prefers an disordered type, which cannot be used for calculations, a hexagonal model with doubled *c*-axis ($MgFe_6Ge_6$-type) has been used. For both compounds, short Ge–Ge-contacts are found in Ge_2-dumbbells and longer in the hexagonal germanium sublattice, as can be seen in Table 5 and Table 6. The ELF shows a distinct maximum in the middle of dumbbells ①, which clearly demonstrates covalent character. Additionally, each dumbbell-atom has weaker maxima opposite to the bond ② similar as observed for $MgCo_6Ge_6$ [59]. These are also visible in the *T*-layer (Figure 11c,g), showing a polarized covalent bond between Ge_2-dumbbells and *T*-atoms of the host structure. The graphite-like Ge-nets (Figure 11b, e, f) contain both, voids centered by calcium atoms and voids containng the midle of dumbbells. The electron density within this layer is mainly determined by Ge–Ge non-bonding contacts ③,④ and the polar covalent bonds to the *T* atoms above and below, forming trigonal bipyramids shown in Figure 3 and Figure 5. Thus the ELF around germanium looks quite similar independent of the atoms in the channels. A minor difference between bonds surrounded by calcium ③ and those surrounded by dumbbells ④ can be seen though. The latter have a slightly more enhance maximum, more significant with the iron compound. This difference also shows in different bond lengths given in Figure 4. The *T*-Kagomé-nets always face a dumbbell on the one and calcium atom on the other side, independent of the type of order between channels (Figure 11c,g). Electron density is delocalized between the metal atoms ⑤ and polarized towards Ge_2-dumbbells ② as discussed above. Hence the dumbbells are not pure ionic Ge_2^{2-}-fragments but interact with the cobalt lattice. This interaction is more pronounced in $CaCo_6Ge_6$, where a local minium ⑤ is found within the cobalt triangle.

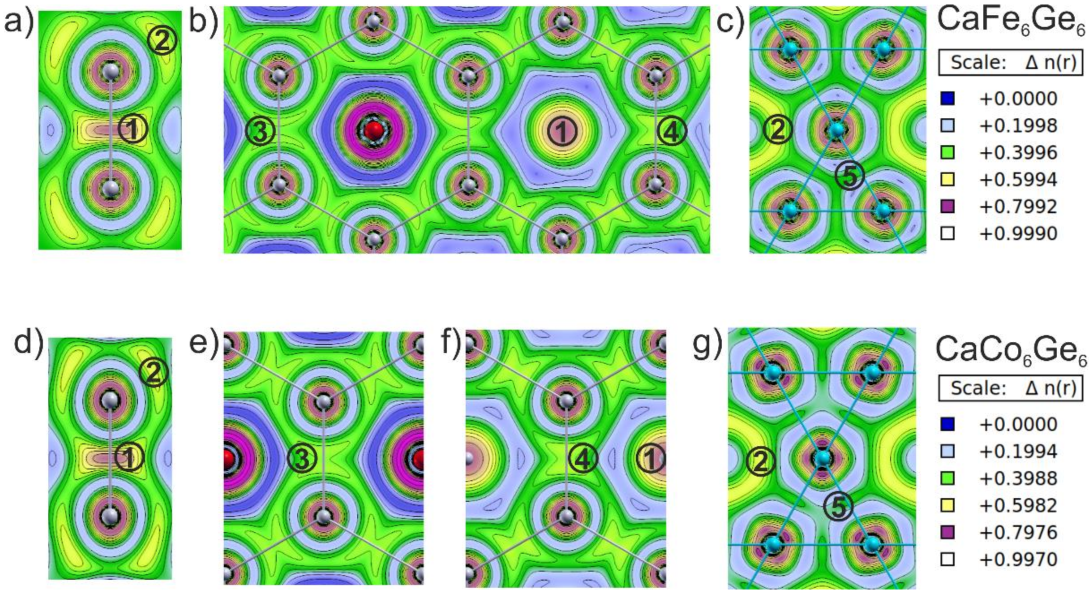

Figure 11 Electron localization function (ELF) representation at Ge_2-dumbbells (a,d), in the layer containing honeybomb-Ge-lattice (b,e,f) or the transition metal Kagomé-net (c,g) at 0.25% cell height. $CaFe_6Ge_6$ (a-c) orders preferably with *Cmcm* modification and contains calcium atoms and Ge_2-dumbbells within the same layer. $CaCo_6Ge_6$ (d-g) with hexagonal modification contains layers with either only calcium atoms at $z = 0$ (d) or Ge_2-dumbbells at $z = 0.5$ (f). Selected ELF maxima have been numbered for discussion.

4. Conclusion

Ternary compounds $CaFe_6Ge_6$ and $Ca_{1-x}Co_6Ge_6$ have been synthesized and their crystal structure and magnetic properties were investigated. The host structure T_3Ge_2 (T = Fe, Co) is filled with calcium and Ge_2-dumbbells. Both compounds have been found in $Y_{0.5}Co_3Ge_3$-type (*P*6/*mmm*, *hP*7) with small hexagonal unit cell and the disorder of calcium and dumbbells. Cobalt compound, however, is rather an $Y_{0.5}Co_3Ge_3$ / CoSn-types intergrowth as some calcium is deficient and allows for the dumbbells to separate into the single Ge-atoms that shift in plane with cobalt-layer. Via annealing the long-range order has been found as $TbFe_6Sn_6$-type (*Cmcm*, *oC*52) and $ScFe_6Ga_6$ / CoSn intergrowth (*Immm*, *oI*26) for the iron and cobalt compound respectively. Annealing a longer period led to decreasing calcium content in $Ca_{1-x}Co_6Ge_6$. Both compounds show Curie-Weiss-paramagnetism with the large asymptotic Curie temperatures, however, no antiferromagnetic order is found down to 2 K. The weak effective magnetic moments indicate some attenuation of the magnetic spin which is situated in frustrated Kagomé-arrangement. The effect is stronger for the cobalt compound. Electronic structure calculations confirm a covalent character within the Ge_2-dumbbells and delocalized bonds within Ge-honeycomb layers and Co-Kagomé nets.

5. Acknowledgments

This research was financially supported by the German Research Foundation (Deutsche Forschungsgemeinschaft, DFG, Grant HL 62/3-1) and the TUM Graduate School.

6. References

[1] H. Hosono, A. Yamamoto, H. Hiramatsu, Y. Ma, Recent advances in iron-based superconductors toward applications, Mater. Today (Oxford, U. K.) 21 (2018) 278–302. https://doi.org/10.1016/j.mattod.2017.09.006.

[2] P.D. Johnson, G. Xu, W.-G. Yin, Iron-Based Superconductivity, Springer International Publishing, Cham, 2015.

[3] J. Chen, K. Semeniuk, Z. Feng, P. Reiss, P. Brown, Y. Zou, P.W. Logg, G.I. Lampronti, F.M. Grosche, Unconventional Superconductivity in the Layered Iron Germanide YFe_2Ge_2, Phys. Rev. Lett. 116 (2016) 127001. https://doi.org/10.1103/PhysRevLett.116.127001.

[4] F. Bernardini, G. Garbarino, A. Sulpice, M. Núñez-Regueiro, E. Gaudin, B. Chevalier, M.-A. Méasson, A. Cano, S. Tencé, Iron-based superconductivity extended to the novel silicide LaFeSiH, Phys. Rev. B 97 (2018). https://doi.org/10.1103/PhysRevB.97.100504.

[5] C.D. Yang, H.C. Hsu, W.Y. Tseng, H.C. Chen, H.C. Ku, M.N. Ou, Y.Y. Chen, Y.Y. Hsu, Superconductivity in $Sr(Pd_{1-x}Ni_x)_2Ge_2$, J. Phys.: Conf. Ser. 273 (2011) 12089. https://doi.org/10.1088/1742-6596/273/1/012089.

[6] V. Hlukhyy, A.V. Hoffmann, V. Grinenko, J. Scheiter, F. Hummel, D. Johrendt, T.F. Fässler, Structural instability and superconductivity in the solid solution $SrNi_2(P_{1-x}Ge_x)_2$, Phys. Status Solidi B 254 (2017) 1600351. https://doi.org/10.1002/pssb.201600351.

[7] Z. He, R. Huang, K. Zhou, Y. Liu, S. Guo, Y. Song, Z. Guo, S. Hu, L. He, Q. Huang, L. Li, J. Zhang, S. Wang, J. Guo, X. Xing, J. Chen, Superconductivity in Co-Layered LaCoSi, Inorg. Chem. 60 (2021) 6157–6161. https://doi.org/10.1021/acs.inorgchem.1c00699.

[8] B.R. Ortiz, S.M.L. Teicher, Y. Hu, J.L. Zuo, P.M. Sarte, E.C. Schueller, A.M.M. Abeykoon, M.J. Krogstad, S. Rosenkranz, R. Osborn, R. Seshadri, L. Balents, J. He, S.D. Wilson, CsV_3Sb_5: A Z_2 Topological Kagome Metal with a Superconducting Ground State, Phys. Rev. Lett. 125 (2020) 247002. https://doi.org/10.1103/PhysRevLett.125.247002.

[9] K. Kudo, H. Hiiragi, T. Honda, K. Fujimura, H. Idei, M. Nohara, Superconductivity in Mg_2Ir_3Si: A Fully Ordered Laves Phase, J. Phys. Soc. Jpn. 89 (2020) 13701. https://doi.org/10.7566/JPSJ.89.013701.

[10] S. Li, B. Zeng, X. Wan, J. Tao, F. Han, H. Yang, Z. Wang, H.-H. Wen, Anomalous properties in the normal and superconducting states of $LaRu_3Si_2$, Phys. Rev. B 84 (2011) 214527. https://doi.org/10.1103/PhysRevB.84.214527.

[11] U. Rauchschwalbe, W. Lieke, F. Steglich, C. Godart, L. C. Gupta, and R. D. Parks, Superconductivity in a Mixed-valent System: $CeRu_3Si_2$.

[12] G. Venturini, H. Ihou-mouko, C. Lefèvre, S. Lidin, B. Malaman, T. Mazet, J. Tobola, V. Vernière, Structures and crystal chemistry of MT_6X_6 phases, filled derivatives of the CoSn-B35 structure, Chem. Met. Alloys 1 (2008) 24–33.

[13] G. Venturini, Filling the CoSn host-cell: the $HfFe_6Ge_6$-type and the related structures, Z. Kristallogr. 221 (2006). https://doi.org/10.1524/zkri.2006.221.5-7.511.

[14] G. Venturini, R. Welter, B. Malaman, Crystallographic data and magnetic properties of RT_6Ge_6 compounds (R=Sc, Y, Nd, Sm, Gd–Lu; T=Mn, Fe), J. Alloys Compd. 185 (1992) 99–107. https://doi.org/10.1016/0925-8388(92)90558-Q.

[15] FIZ Karlsruhe, ICSD: Inorganic Crystal Structure Database, Leibniz Institute for Information Infrastructure, Karlsruhe, Germany, 2022.

[16] W. Buchholz, H.-U. Schuster, Intermetallische Phasen mit B35-Überstruktur und Verwandtschaftsbeziehung zu $LiFe_6Ge_6$, Z. Anorg. Allg. Chem. 482 (1981) 40–48. https://doi.org/10.1002/zaac.19814821105.

[17] D.C. Fredrickson, S. Lidin, G. Venturini, B. Malaman, J. Christensen, Origins of superstructure ordering and incommensurability in stuffed CoSn-type phases, J. Am. Chem. Soc. 130 (2008) 8195–8214. https://doi.org/10.1021/ja077380+.

[18] P. Schobinger-Papamantellos, K. Buschow, F. de Boer, C. Ritter, O. Isnard, F. Fauth, The Fe ordering in RFe_6Ge_6 compounds with non-magnetic R (R=Y, Lu, Hf) studied by

neutron diffraction and magnetic measurements, J. Alloys Compd. 267 (1998) 59–65. https://doi.org/10.1016/S0925-8388(97)00548-3.

[19] T. Mazet, B. Malaman, Macroscopic magnetic properties of the $HfFe_6Ge_6$-type RFe6X6 (X=Ge or Sn) compounds involving a non-magnetic R metal, J. Alloys Compd. 325 (2001) 67–72. https://doi.org/10.1016/S0925-8388(01)01378-0.

[20] G.K. Marasinghe, J. Han, W.J. James, W.B. Yelon, N. Ali, The relationship between magnetic interactions and near neighbor interatomic distances in the transition metal sublattice of $R(Mn/Fe)_6A_6$ (R=Nd or Sm, A=Ge or Sn), J. Appl. Phys. 91 (2002) 7863. https://doi.org/10.1063/1.1451305.

[21] N.V. Baranov, E.G. Gerasimov, N.V. Mushnikov, Magnetism of compounds with a layered crystal structure, Phys. Met. Metallogr. 112 (2011) 711–744. https://doi.org/10.1134/S0031918X11070039.

[22] J.M. Cadogan, D.H. Ryan, A study on the magnetic behaviour of polymorphic $YbFe_6Ge_6$, J. Phys. Condens. Matter 22 (2010) 16009. https://doi.org/10.1088/0953-8984/22/1/016009.

[23] T. Mazet, V. Ban, R. Sibille, S. Capelli, B. Malaman, Magnetic properties of $MgFe_6Ge_6$, Solid State Commun. 159 (2013) 79–83. https://doi.org/10.1016/j.ssc.2013.01.027.

[24] A. Szytuła, E. Wawrzyńska, A. Zygmunt, Crystal structure and magnetic properties of $GdCo_6X_6$ (X=Ge, Sn) and $TbCo_6Ge_6$, J. Alloys Compd. 366 (2004) L16–L18. https://doi.org/10.1016/S0925-8388(03)00752-7.

[25] J. Cadogan, D. Ryan, Independent magnetic ordering of the rare-earth (R) and Fe sublattices in the RFe_6Ge_6 and RFe_6Sn_6 series, J. Alloys Compd. 326 (2001) 166–173. https://doi.org/10.1016/S0925-8388(01)01242-7.

[26] T. Mazet, B. Malaman, Evidence of spin reorientation in $YbFe_6Ge_6$ from neutron diffraction and ^{57}Fe Mössbauer experiments, J. Phys.: Condens. Matter 12 (2000) 1085–1095. https://doi.org/10.1088/0953-8984/12/6/325.

[27] O. Zaharko, P. Schobinger-Papamantellos, C. Ritter, J. Rodríguez-Carvajal, K. Buschow, Influence of thermal history on crystal structure, microstructure and magnetic properties of $TbFe_6Ge_6$ (II), J. Magn. Magn. Mater. 187 (1998) 293–308. https://doi.org/10.1016/S0304-8853(98)00148-6.

[28] T. Mazet, O. Isnard, B. Malaman, Neutron diffraction and ^{57}Fe Mössbauer study of the $HfFe_6Ge_6$-type RFe_6Ge_6 compounds (R=Sc, Ti, Zr, Hf, Nb), Solid State Commun. 114 (2000) 91–96. https://doi.org/10.1016/S0038-1098(00)00003-X.

[29] V.Y. Gvozdetskyi, R.E. Gladyshevskii, N.V. German, Multicomponent Phases with $CeAl_2Ga_2$- and $Y_{0.5}Co_3Ge_3$-Type Structures in the Gd–Ca–Fe–Co–Ge System, Phys. Chem. Solid State 16 (2015) 104–110. https://doi.org/10.15330/pcss.16.1.104-110.

[30] H. Yang, J.N. Hausmann, V. Hlukhyy, T. Braun, K. Laun, I. Zebger, M. Driess, P.W. Menezes, An Intermetallic $CaFe_6Ge_6$ Approach to Unprecedented Ca−Fe−O Electrocatalyst for Efficient Alkaline Oxygen Evolution Reaction, ChemCatChem 14 (2022) e202200293. https://doi.org/10.1002/cctc.202200293.

[31] WinXPOW, STOE & Cie GmbH, Darmstadt, Germany, 2011.

[32] J. Rodriguez-Carvajal, FullProf: A Program for Rietveld Refinement and Pattern Matching Analysis. At the Satellite Meeting on Powder Diffraction of the XV IUCr Congress, Toulouse, France, 1990.

[33] Bruker, APEX Suite of Crystallographic Software, Bruker AXS inc., Madison, Wisconsin (USA), 2008.

[34] SAINT, Bruker AXS inc., Madison, Wisconsin (USA), 2001.

[35] SADABS, Bruker AXS inc., Madison, Wisconsin (USA), 2001.

[36] X-Area, STOE & Cie GmbH, Darmstadt, Germany, 2015.

[37] X-RED32, STOE & Cie GmbH, Darmstadt, Germany, 2016.

[38] X-SHAPE, STOE & Cie GmbH, Darmstadt, Germany, 2015.

[39] LANA, STOE & Cie GmbH, Darmstadt, Germany, 2016.

[40] CrysAlis RED, Oxford Diffraction Ltd., Abingdon, Oxfordshire, England, 2009.

[41] SCALE3 ABSPACK: CrysAlis Software Package, Oxford Diffraction Ltd., Abingdon, Oxfordshire, England, 2015.

[42] G.M. Sheldrick, SHELXS-2014: Program for the Determination of Crystal Structure, University of Göttingen, Göttingen, Germany, 2014.

[43] G.M. Sheldrick, SHELXL-2014: Program for Crystal Structure Refinement, University of Göttingen, Göttingen, Germany, 2014.

[44] G.M. Sheldrick, Crystal structure refinement with SHELXL, Acta Crystallogr., Sect. C: Struct. Chem. 71 (2015) 3–8. https://doi.org/10.1107/S2053229614024218.

[45] L.J. Farrugia, WinGX and ORTEP for Windows: an update, J. Appl. Crystallogr. 45 (2012) 849–854. https://doi.org/10.1107/S0021889812029111.

[46] M. van Schilfgarde, T.A. Paxton, O. Jepsen, O.K. Andersen, TB-LMTO-ASA, Stuttgart, Germany, 1994.

[47] R.W. Tank, O. Jepsen, O.K. Andersen, The STUTTGART TB-LMTO-ASA program, Stuttgart, 1998.

[48] U.v. Barth, L. Hedin, A local exchange-correlation potential for the spin polarized case: I, J. Phys. C: Solid State Phys. 5 (1972) 1629–1642. https://doi.org/10.1088/0022-3719/5/13/012.

[49] O. Jepsen, O.K. Andersen, Calculated electronic structure of the sandwich d^1 metals LaI_2 and CeI_2, Z. Phys. B: Condens. Matter 97 (1995) 35–47. https://doi.org/10.1007/BF01317585.

[50] W.R.L. Lambrecht, O.K. Andersen, Minimal basis sets in the linear muffin-tin orbital method, Phys. Rev. B 34 (1986) 2439–2449. https://doi.org/10.1103/PhysRevB.34.2439.

[51] A. Savin, R. Nesper, S. Wengert, T.F. Fässler, ELF, Angew. Chem. Int. Ed. Engl. 36 (1997) 1808–1832. https://doi.org/10.1002/anie.199718081.

[52] T. Braun, V. Hlukhyy, $CaFe_2Ge_2$ with square-planar iron layers – Closing a gap in the row of CaT_2Ge_2 (T = Mn–Zn), J. Solid State Chem. 276 (2019) 368–375. https://doi.org/10.1016/j.jssc.2019.05.032.

[53] W. Dörrscheidt, N. Niess, H. Schäfer, Neue Verbindungen AB_2X_2 (A = Erdalkalimetall, B = Übergangselement, X = Element(IV)) im $ThCr_2Si_2$-Typ, Z. Naturforsch., B: Anorg. Chem., Org. Chem. 31 (1976) 890–891. https://doi.org/10.1515/znb-1976-0634.

[54] O. Oleksyn, H.-U. Nissen, R. Wessicken, Microtwinning in $HoFe_6Ge_6$ studied by high-resolution electron microscopy and electron diffraction, Philos. Mag. Lett. 77 (1998) 275–278. https://doi.org/10.1080/095008398178426.

[55] O.Y. Oleksyn, H. Böhm, Ordering in $DyFe_6Sn_6$ studied by conventional X-ray single crystal diffraction, Z. Kristallogr. 213 (1998) 270–274. https://doi.org/10.1524/zkri.1998.213.5.270.

[56] Y. Prots, R. Demchyna, U. Burkhardt, U. Schwarz, Crystal structure and twinning of HfPdGe, Z. Kristallogr. 222 (2007) 513–520. https://doi.org/10.1524/zkri.2007.222.10.513.

[57] W.-S. Wang, Y.-C. Liu, Y.-Y. Xiang, Q.-H. Wang, Antiferromagnetism, *f*-wave and chiral *p*-wave superconductivity in a Kagome lattice with possible application to sd^2-graphenes, 2015, http://arxiv.org/pdf/1511.08001v1.

[58] M.V. Gvozdikova, P.-E. Melchy, M.E. Zhitomirsky, Magnetic phase diagrams of classical triangular and kagome antiferromagnets, J. Phys. Condens. Matter 23 (2011) 164209. https://doi.org/10.1088/0953-8984/23/16/164209.

[59] C. Gieck, M. Schreyer, T.F. Fässler, S. Cavet, P. Claus, Synthesis, crystal structure, and catalytic properties of $MgCo_6Ge_6$, Chem. Eur. J. 12 (2006) 1924–1930. https://doi.org/10.1002/chem.200500411.

Supporting Information:

Structural Order-Disorder in $CaFe_6Ge_6$ and $Ca_{1-x}Co_6Ge_6$

Thomas Braun, Viktor Hlukhyy

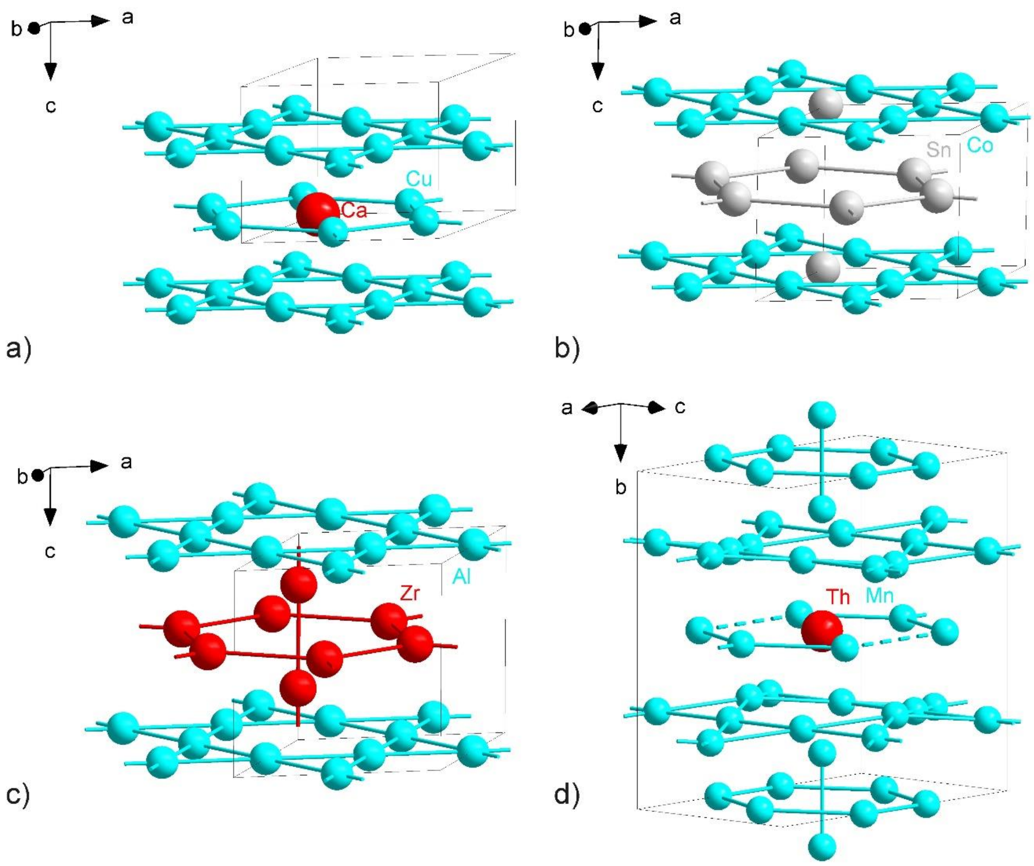

Figure S1 a) $CaCu_5$-type, b) CoSn-type, c) Zr_4Al_3-type and d) $ThMn_{12}$-type. Atoms forming layers with Kagomé or honeycomb nets have been connected to highlight structural relationship.

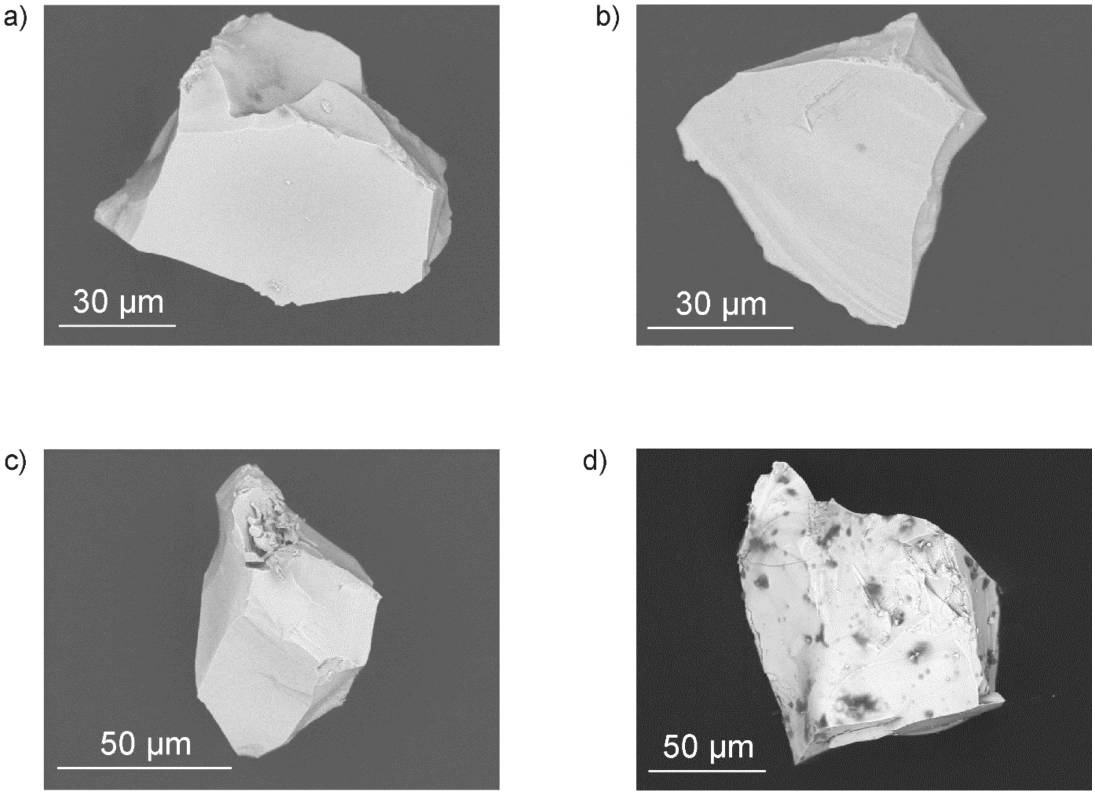

Figure S2 Electron microscope image of a) $CaFe_6Ge_6$ single crystal III, atomic ratio of Ca:Fe:Ge = 1.1:6.1:5.8, b) $CaFe_6Ge_6$ single crystal IV, atomic ratio of Ca:Fe:Ge = 1.0:5.6:6.4, c) $CaCo_6Ge_6$ single crystal III, atomic ratio of Ca:Co:Ge = 0.7:5.9:6.5 and d) $Ca_{1-x}Co_6Ge_6$ single crystal IV, atomic ratio of Ca:Co:Ge = 0.9:6.0:6.1. Compositions were measured by EDX and are given in atom-%.

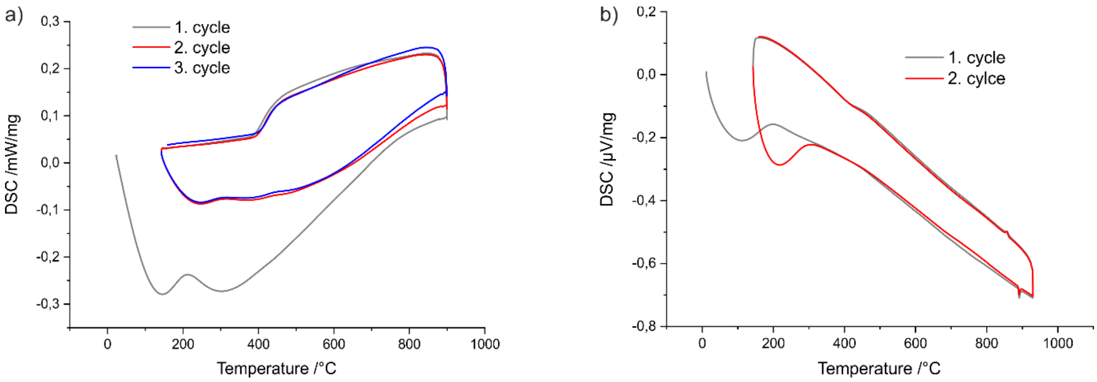

Figure S3 Differential thermal analysis (DTA) of $CaFe_6Ge_6$ (left). No signals have been found that would be a sign of phase transition from unordered to ordered modification. $Ca_{1-x}Co_6Ge_6$ (right) only show very weak signals around 870 °C.

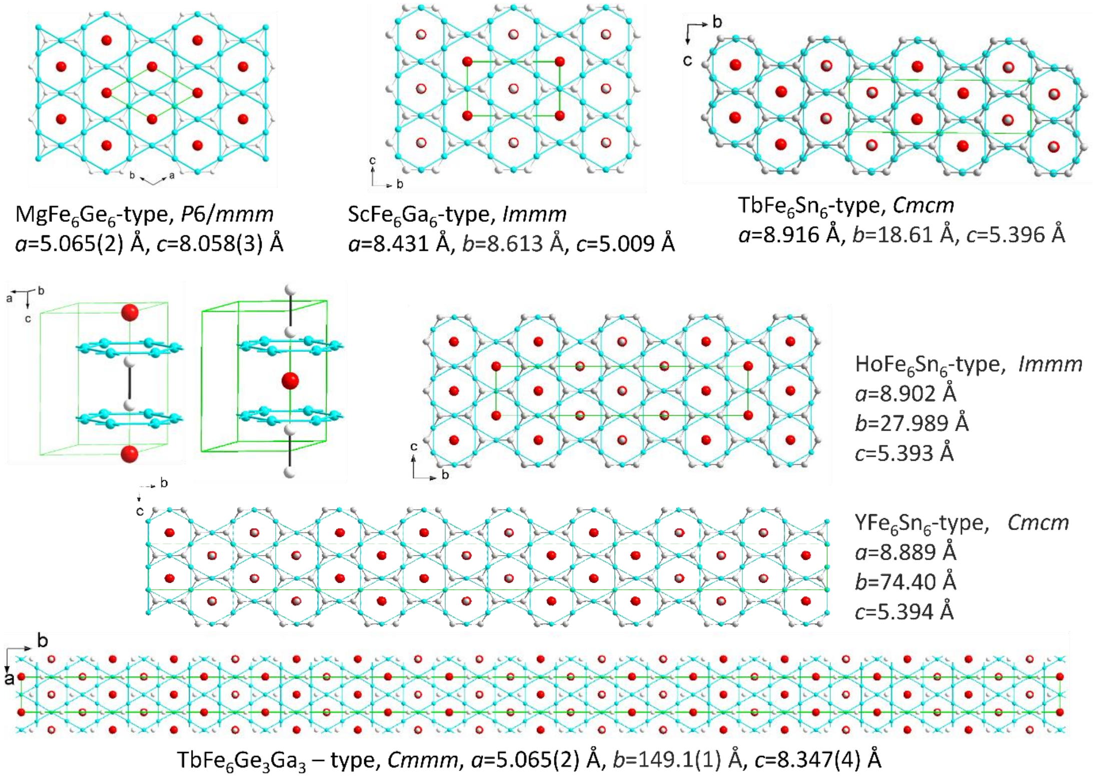

Figure S4 Different types of order within the family of 166-comounds demonstrating that various supercells of different size allows for simple to very complex ordered variants.

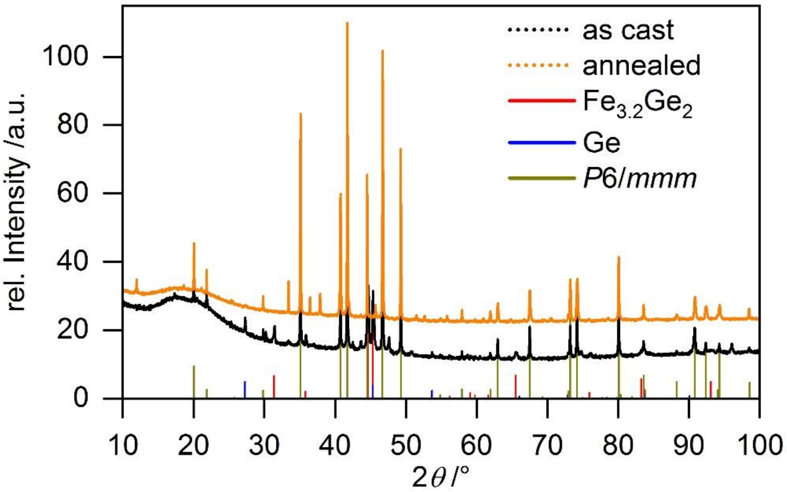

Figure S5 Powder pattern of $CaFe_6Ge_6$ as cast and after annealing at 800 °C. Annealing removed secondary phases, whereas additional reflections appeared, that are not described by disordered $Y_{0.5}Co_3Ge_3$-type (space group *P*6/*mmm*) structure model.

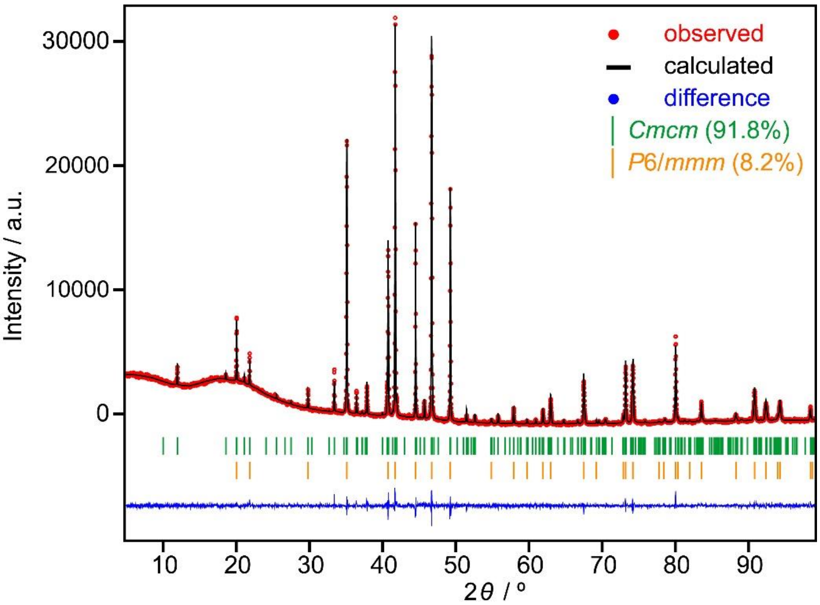

Figure S6 Rietveld refinement of $CaFe_6Ge_6$ annealed at 800 °C with co-existence of disordered $Y_{0.5}Co_3Ge_3$-type (space group *P*6/*mmm*) and ordered $TbFe_6Sn_6$-type (space group *Cmcm*) phases.

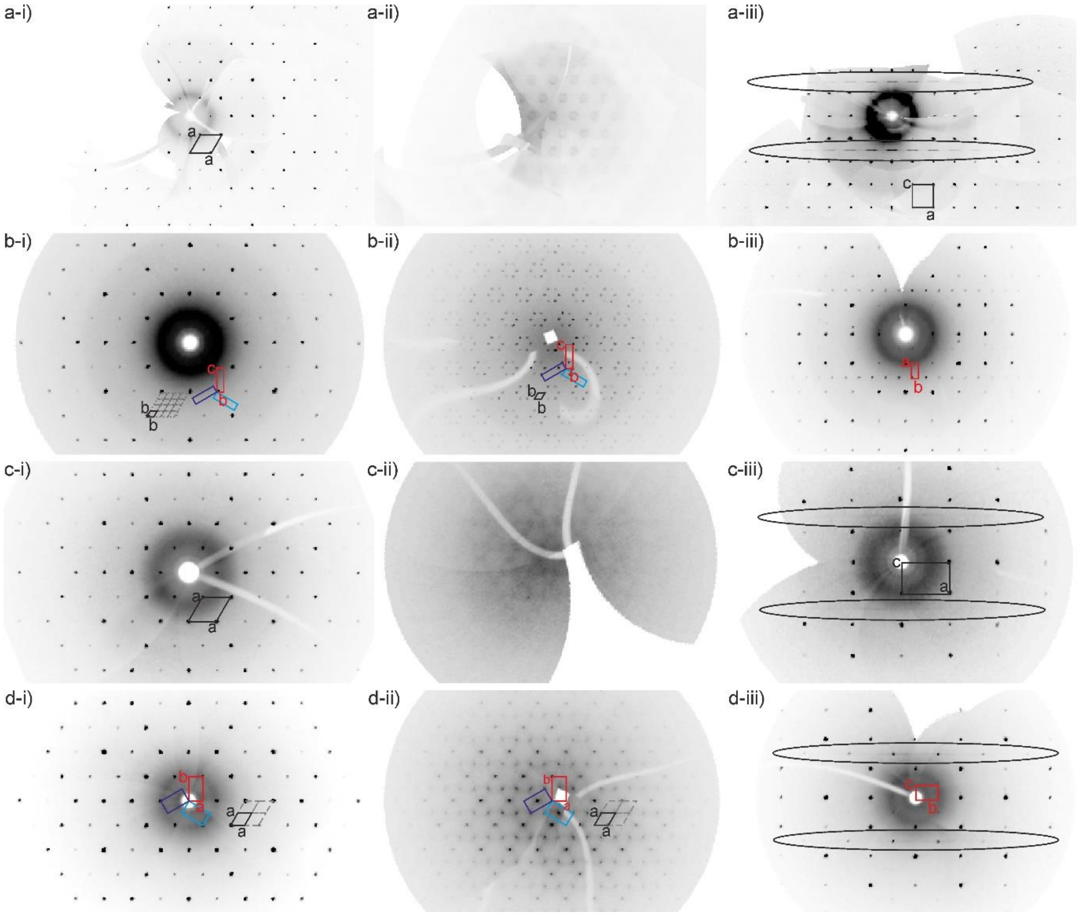

Figure S7 Constructed reciprocal lattice sections of the single crystal XRD measurements of a) CaFe$_6$Ge$_6$ (*hP*7), b) CaFe$_6$Ge$_6$ (*oC*52), c) Ca$_{0.9}$Co$_6$Ge$_6$ (*hP*7) and d) Ca$_{0.9}$Co$_6$Ge$_6$ (*oI*26). Figures i) show the section through the origin, perpendicular to the (pseudo)hexagonal axis, ii) the same direction but with a distance of 1.5 (a,c) or 3 (b,d), iii) shows a section parallel to the (pseudo)hexagonal axis. In the images, the three possible domains of orthorhombic as well as the (pseudo)hexagonal unit cells are given. In the images on the right, regions are emphasized that contain diffusive scattering. Images were recorded with STOE IPDS 2T (rotating anode FR591, Mo-K_α radiation, λ = 0.71073 Å) with image plate detector.

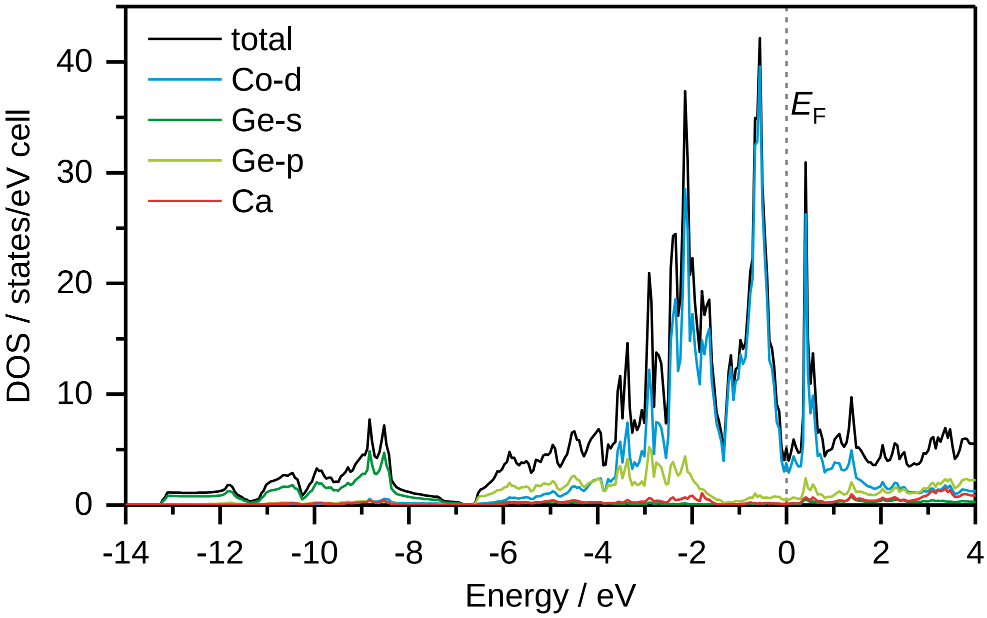

Figure S8 DOS of “hypotetical” $CaCo_6Ge_6$ with $MgFe_6Ge_6$-type (*P*6/*mmm*). Projected DOS are given for selected orbitals.

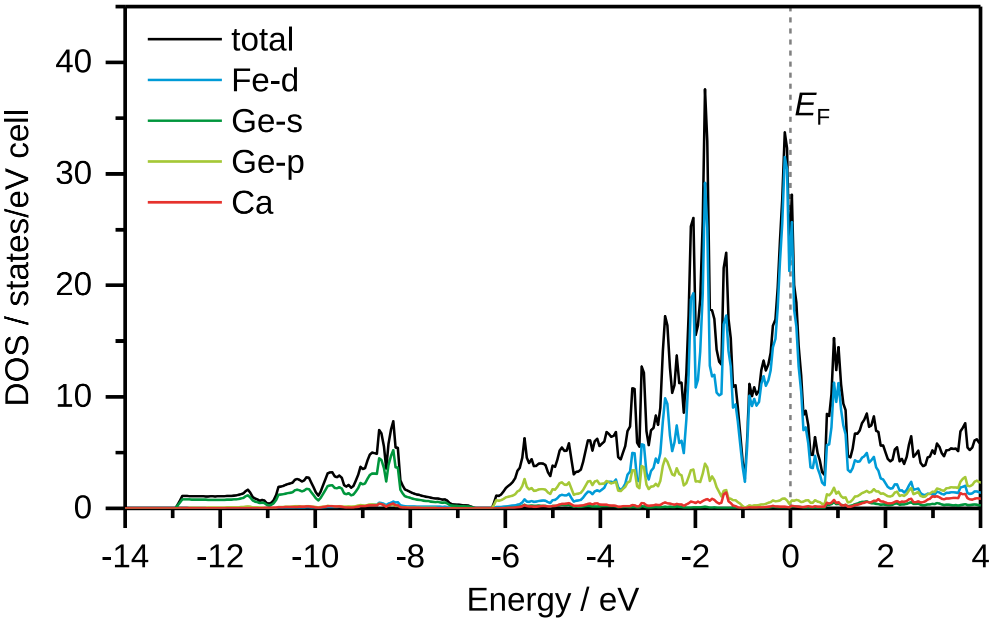

Figure S9 DOS for $CaFe_6Ge_6$ with $MgFe_6Ge_6$-type (*P*6/*mmm*). Projected DOS are given for selected orbitals.

Single Crystal preparation details

$CaFe_6Ge_6$:

I: Ca, Fe, Ge with ratio 1:1:3 in welded Nb-crucible, heated via induction furnace to 1050 °C, dwelled for 15 minutes, cooled to about 700 °C with −1% power/minute, cooling to room temperature within minutes. Measured with Bruker APEX-II with CCD detector (APEX II, κ-CCD), a rotating anode FR591 (Mo-K_α radiation, λ = 0.71073 Å) and a MONTEL optic monochomator.

II: Ca, Fe, Ge with ratio 1:1:3 in welded Nb-crucible, heated via induction furnace to 1050 °C, dwelled for 15 minutes, cooled quickly to room temperature. Measured with Oxford-Xcalibur3 CCD area detector diffractometer (EDX: Ca:Fe:Ge = 1:6.1:7.1 atom-%)

III: Fe + Ge arc-melted, then arc melted with 1.02 eq. calcium. Sealed into graphitizes silica and then annealed to 800 °C for three days. Reannealing to 1000 °C for 2 hours, cooling to 800 °C with −6 °C/h, dwelling 3 days, turning off the oven and quickly quenching the sample at ca. 700 °C. Measured with Bruker APEX-II with CCD detector (APEX II, κ-CCD), a rotating anode FR591 (Mo-K_α radiation, λ = 0.71073 Å) and a MONTEL optic monochomator. (SEM + EDX in Figure S2a)

IV: Fe + Ge arc-melted, then arc melted with 1.02 eq. calcium. Sealed into graphitizes silica and then annealed to 1000 °C for 2 hours, cooled to 930 °C with −12 °C/h and dwelled for 16 days. Measured with STOE Stadivari (Genix 3D High Flux microfocus with Mo-K_α, graded multilayer mirror monochomator, DECTRIS Pilatus 300K detector) (SEM + EDX in Figure S2b)

$Ca_{1-x}Co_6Ge_6$:

I: Co + Ge arc-melted, then arc melted with 1.02 eq. calcium. Sealed into graphitizes silica and then annealed to 1000 °C for 2 hours, cooled to 800 °C with −6 °C/h and dwelled for 5 days. Measured with Bruker APEX-II with CCD detector (APEX II, κ-CCD), a rotating anode FR591 (Mo-K_α radiation, λ = 0.71073 Å) and a MONTEL optic monochomator.

II Co + Ge arc-melted, then arc melted with 1.02 eq. calcium. Sealed into graphitizes silica and then annealed to 1000 °C for 2 hours, cooled to 700 °C with −6 °C/h and dwelled for 1 day. Measured with Bruker APEX-II with CCD detector (APEX II, κ-CCD), a rotating anode FR591 (Mo-K_α radiation, λ = 0.71073 Å) and a MONTEL optic monochomator.

III: Co + Ge arc-melted, then arc melted with 1.02 eq. calcium. Sealed into graphitizes silica and then annealed to 1000 °C for 2 hours, cooled to 700 °C with −6 °C/h and dwelled for 15 day. Measured with STOE Stadivari (Genix 3D High Flux microfocus with Mo-K_α, graded multilayer mirror monochomator, DECTRIS Pilatus 300K detector) (SEM + EDX in Figure S2c)

IV: Co + Ge arc-melted, then arc melted with 1.02 eq. calcium. Sealed into graphitizes silica and then annealed to 800 °C for three days. Reannealing to 1000 °C for 2 hours, cooling to 800 °C with −6 °C/h, dwelling 3 days, turning off the oven and quickly quenching the sample at ca. 700 °C. Measured with STOE Stadivari (Genix 3D High Flux microfocus with Mo-K_α, graded multilayer mirror monochomator, DECTRIS Pilatus 300K detector) (SEM + EDX in Figure S2d)

5.4 SrNiSi with Two Different Stacking Variants — An Electron Deficient Zintl-Phase

Braun, T.; Hlukhyy, V.

Manuscript for publication

SrNiSi with two different stacking variants — An electron deficient Zintl-Phase

Thomas Braun, Viktor Hlukhyy[1]

Department of Chemistry, Technische Universität München, Lichtenbergstr. 4, 85747, Garching, Germany

Abstract

Two polymorphic modifications of new ternary polar intermetallic SrNiSi compound have been synthesized and been investigated with X-ray diffraction and TB-LMTO-ASA methods. They are closely related to BaPdP with planar ($3^2.8^2$)(3.8^2)-nets. α-SrNiSi crystallizes with space group *Cmca*, (a = 9.431(2) Å, b = 7.511(2) Å, c = 7.508(2) Å), the structure is similar to BaPdP-type but with ordered Si-position in SrNiSi instead of a split P-position in BaPdP. β-SrNiSi crystallizes in $I4_1/acd$ space group (a = 7.5491(6) Å, c = 18.918(2) Å) and comprises of blocks of the alpha phase, turned by 90°. Both modifications can be regarded as metallic, electron deficient Zintl-variants of BaPdP.

Keywords: Intermetallics, Silicide, Single Crystal, Stacking, Layers

1. Introduction

Among intermetallic compounds is a variety with general formula *RTX* consisting of a rare earth or alkaline metal (*R*), a (late) transition metal (*T*) and a p-block element from group 13–15 (*X*) [1]. The structures, albeit with very simple stoichiometry, are manifold. The range from very simple AlB_2-type or Laves Phases with mixed occupied sites over color ordered variants with separate Wyckoff positions and/or superstructures and deformation variants of the above to complex arrangements with large unit cells [2–4]. Besides structural features, these compounds exhibit interesting physical properties, such as magnetic, thermal, electrical properties as well as they can be considered as potential hydrogen storage materials [5,6].

Limiting the scope to alkaline earth metals containing *RTX* compounds, 234 entries are found in Inorganic Crystal Structure Database (ICSD) from 2022 [7]. Close to 30 different structure types are formed of which some are closely related to each other and derived from the

---

[1] Corresponding author.

E-mail address: viktor.hlukhyy@tum.de (V. Hlukhyy)

same aristotype. Most common is ZrBeSi-type, a colored AlB_2-variant next to SrPtSb with 2D-layers. Dividing the layers into ribbons and tilting every second by 90° leads to a 3D-linked network of LaPtSi- or CaPtAs-type, the first being a colored variant of $ThSi_2$ [8]. Corrugation of hexagonal layers of ZrBeSi-type similar to grey arsenic and linking them in diamond or lonsdaleite arrangement results in AlLiSi- (half-Heusler) or LiGaGe-type respectively [2,3,9].

Another way of deforming AlB_2-type layers gives $CeCu_2$-type. This aristotype is related to various colored superstructures: EuAuGe, SrAgGe, TiNiSi-MgSrSi, HoPdGe and CaAuSn that are prevalent with rare earth element compounds [3,10]. Derived from $SrSi_2$, a structure with only 3-connected framework atoms that form loops of 10 atoms, LaIrSi is obtained [11–13]. Another structure family found in the system of *RTX* compounds are Laves phases. Simple $MgZn_2$ and $MgNi_2$ as well as larger supercells with elaborate stacking sequences such as $Mg(Al_{0.5}Cu_{0.5})_2$ or MgCuAl were found [5,14]. Yet another type is found for ZrNiAl that is derived from $InMg_2$ (= Fe_2P) [1,5]. The last prominent Type is PbClF with 2-dimensional polyanionic layers of square planar transition metal atoms [15]. It is called CeFeSi-type or “111-type” in the context of superconducting iron pnictides, but does also form with alkaline earth, transition metal and tetrel elements, e.g. CaCoSi [16], CaNiGe and MgCoGe [17]. Interestingly, going from smaller Mg^{2+} to larger Ba^{2+} cations, polyanionic substructures change dimensionality. Equiatomic MgNiGe forms a 3-dimensional structure, SrNiGe and BaNiGe a 1-dimensional one with $^{1}_{\infty}[TX]^{-}$polyanions [18]. MgCuAs- and MgAgSb types can be constructed from PbClF fragments to 3-dimensional linked networks [19].

Other equiatomic compounds with peculiar structures are CaPdAl, CaPdAs, CaPtP and BaPdP that show $^{2}_{\infty}[TX]^{-}$-polyanions. Last three are made of (almost) flat planes [8,20–22]. Moreover, there are some compounds with EuNiGe-type, consisting of corrugated $^{2}_{\infty}[TX]^{-}$ layers. Their configuration is strongly related to BaPdP.

In this work, we will present two modification of SrNiSi that are structurally close to BaPdP, but quite different from homologue SrNiGe.

2. Experimental Section

2.1. Syntheses

Element pieces have been used for synthesis: ingots of strontium (ingots, ChemPur, 98%, redistilled prior to use), nickel (wire, Alfa Aesar, 99.98%) and silicon (granules, Alfa Aesar, 99.999%). Single crystals have been found as secondary phases in different samples. The sample containing α-SrNiSi (singe crystals suitable for X-ray investigation) was obtained by melting the elements in an arc furnace with ratio 1:2:1, sealing in a niobium ampoule and subsequent annealing in an induction furnace. The sample was heated to 1050 °C and after five minutes of dwelling cooled by decreasing the power output with −1%/min to 750 °C, dwelled for 75 minutes and cooled to room temperature with −5%/min. β-SrNiSi was found in a sample with composition 1:2:2, produced by arc melting nickel and silicon and annealing the grinded solid with 10 percent excessive strontium in a resistance furnace. The sample was heated to 1000 °C, dwelled for one hour, cooled to 700 °C within 50 hours, dwelled 77 hours and cooled to room temperature. To get SrNiSi as main phase, several steps were necessary. First, Ni_2Si and SrSi were produced via arc melting. Then both binary phases were mixed with strontium, sealed in a niobium ampoule and kept at 800 °C for one hour in the induction furnace. The product was grinded, pressed to a pellet and heated for another hour at 900 °C. Besides SrNiSi the powder diffractogram shows mainly $SrNi_{0.5}Si_{1.5}$ and $SrNi_5Si_3$ [23]. However, the powder data (Figure S1 of the supporting information) do not allow determining which modification has been formed.

2.2. X-ray Investigations

Phase composition and purity of the synthesized samples were was inspected with a STOE Stadi-P X-ray powder diffractometer. It is equipped with a Cu-$K_{\alpha1}$-source (λ = 1.54058 Å), a curved Ge(111)-monochromator and DECTRIS MYTHEN 1K detector. Samples were grinded and powder fixed on Scotch magic tape and corrected using silicon as external standard. Expected diffraction patterns of α- and β-SrNiSi were calculated on basis of single crystal data resolved models. α-SrNiSi was measured on a STOE IPDS 2T with Mo-K_α-source (λ = 0.71073 Å), graphite monochromator and image plate detector. β-SrNiSi was measured on a STOE STADIVARI with Genix 3D High Flux microfocus source (Mo-K_α, λ = 0.71073 Å), graded multilayer mirror monochromator and DECTRIS Pilatus 300K detector. All single crystal data have been processed with the diffractometer software package X-Area [24]. Absorption correction has been performed numerically following LANA [25], using a crystal model generated with X-Shape [26] on basis of 500 reflection pairs selected by X-RED32 [27]. A structural model was created with direct methods using SHELXS-2014 and atomic parameter refined with SHELXL-2014 [28–31]. The final structure data are given in Table 1 and Table 2. SEM-EDX data show a composition of Sr:Ni:Si = 1.1:1:0.9 at-% which is in well agreement to the ideal values for SrNiSi of 1:1:1.

Table 1 Crystal data and structure refinement of SrNiSi. The lattice parameter was taken from powder Rietveld analysis

empirical formula	α-SrNiSi	β-SrNiSi
formula weight (g mol^{-1})	174.42	174.42
temperature (K)	293	293
crystal system	orthorhombic *)	tetragonal
space group	*Cmca*	$I4_1/acd$
unit cell dimensions		
a (Å)	9.431(2)	7.5491(6)
b (Å)	7.511 (2)	7.5491(6)
c (Å)	7.508(2)	18.918(2)
volume (Å^3)	531.8(2)	1078.1(2)
Z	8	16
ρ_{calcd} (g cm^{-3})	4.357	4.298
μ (mm^{-1})	27.197	26.832
F(000)	640	1280
crystal size (mm^3)	0.04 × 0.04 × 0.02	0.09 × 0.08 × 0.07
theta range for data collection (°)	2.7 – 26.0	4.3 – 35.0
index ranges in *hkl*	±11, ±9, ±9	−12<h<11, −11<k<12, ±30
reflections collected	2755	6741
independent reflections	281 (R_{int} = 0.0547)	597 (R_{int} = 0.0267)
Reflections with $I \geq 2\sigma(I)$	256 (R_{sigma} = 0.0222)	423 (R_{sigma} = 0.0127)
data/restraints/parameters	281/19/0	597/17/0
goodness-of-fit on F^2	1.129	1.027
final *R* indices ($I > 2\sigma(I)$)	R_1 = 0.0315, wR_2 = 0.0814	R_1 = 0.0173, wR_2 = 0.0410
R indices (all data)	R_1 = 0.0357, wR_2 = 0.0838	R_1 = 0.0302, wR_2 = 0.0441
Extinction coefficient	–	0.00050(7)
largest diff. peak and hole (e·Å^{-3})	0.814, −0.857	0.981, −0.578

*) Refined as a 2-component inversion twin.

Table 2 Atomic coordinates and equivalent isotropic displacement parameter.

Atom	Site	*x/a*	*y/b*	*z/c*	U_{eq} [a] /10^{-3} · Å^2
α-SrNiSi (*Cmca*)					
Sr	8d	0.30868(9)	0	0	16.9(4)
Ni	8f	0	0.1199(2)	0.1199(2)	14.7(4)
Si	8f	0	0.3258(3)	0.3251(4)	16.6(6)
β-SrNiSi ($I4_1/acd$)					
Sr	16d	0	¼	0.27935(2)	11.26(8)
Ni	16f	0.11987(3)	0.36987(3)	⅛	9.08(9)
Si	16f	0.32516(7)	0.57516(7)	⅛	10.0(1)

[a] U_{eq} is defined as one third of the trace of the orthogonalized *Uij* tensor.

Table 3 Atomic distances, corresponding sums of atomic radii and value of integrated COHP at the Fermi level E_F

	$\Sigma_{\text{atomic radii}}$ / Å	α-SrNiSi (*Cmca*) / Å		−ICOHP / eV	β-SrNiSi (*I*4$_1$/*acd*) / Å		−ICOHP / eV
d(Ni–Ni)	2.49	2.547(2)	*1x*	0.993	2.5595(7)	*1x*	0.993
d(Ni–Si)	2.42	2.183(3)	*1x*	3.634	2.1916(8) (1x)	*1x*	3.674
		2.247(3)	*1x*	2.882	2.2632(6) (1x)	*1x*	2.876
		2.251(3)	*1x*	2.852		*1x*	
d(Sr–Ni)	3.40	3.178(1)	*2x*	0.410	3.1881(4) (2x)	*2x*	0.412
		3.494(1)	*2x*	0.254	3.5111(3) (4x)	*4x*	0.254
		3.495(1)	*2x*	0.254			
d(Sr–Si)	3.33	3.305(2)	*2x*	0.417	3.3229(3) (4x)	*4x*	0.422
		3.312(2)	*2x*	0.413			
		3.451(2)	*2x*	0.302	3.4657(5) (2x)	*2x*	0.305
d(Sr–Sr)	4.30	3.609(2)	*1x*	0.093	3.6190(7) (1x)	*1x*	0.092
		3.9153(8)	*4x*	0.082	3.9345(4) (4x)	*4x*	0.084

2.3. Computational Methods

Self-consistent field calculations have been performed with Stuttgart-TB-LMTO-ASA software package, using the local density approximation (LDA) [32,33]. Linear muffin-tin orbitals (LMTOs) created with the atomic sphere approximation (ASA) including empty spheres. Radii of the spheres were determined after Jepsen and Andersen by blowing up spheres until volume filling is reached within limited allowed overlap [34,35]. Tight-binding model was used, constructing wave functions by superposition of wave functions from isolated atoms [36]. Inner shells are treated as soft-cores, higher quantum numbers down-folded [34] and all relativistic effects except spin-orbit coupling were included. The exchange-correlation term was parametrized after von Barth and Hedin [37]. Density of States (DOS) were calculated with the tetrahedron method [38] and bond character investigated via crystal orbital Hamilton population (COHP) [39,40]. Visualization of the calculated electron distribution was performed using electron localization function (ELF) [41] and plotted with XCrysDen [42,43].

For BaPdP input parameters from literature have been used, however, the phosphorus split position was replaced by a full occupied atom on the higher-symmetrical orbit. Results are in agreement with reported density of states (DOS) [22,44]. As basis set, following orbitals have been used: Sr: s, d and down-folded p, f; Ni: s, p, d; Si: s, p and down-folded d; Ba: s, d, f and down-folded p; Pd: s, p, d and down-folded f; P: s, p and down-folded d.

3. Results

3.1. Crystal Structure of SrNiSi

Single crystal investigations indicate two different modifications of SrNiSi, shown in Figure 1. They consist of flat $(3^2.8^2)(3.8^2)$-nets of Ni and Si atoms that are stacked in two different manners. In α-SrNiSi all layers are parallel to the *bc*-plane and shifted by *b*/2 in *b*-direction with respect to each other. Resulting stacking sequence is AB. In β-SrNiSi the layers are parallel to the *ab*-plane. Layers are alternatingly shifted by *a*/2 along *a* and *b*/2 along *b axis*, giving the sequence AB(AB)'. It can be regarded as two units of the α-phase that are rotated by 90° to each other. The configuration of a single layer is identical in both modifications and strontium has similar arrangement. With an interlayer distance of about 4.7 Å the stacking has no impact on the bonding situation and coordination of nickel and silicon. Figure S2 (Supporting Information) shows strontium coordination polyhedra for both phases. Strontium atom rest on octagonal Ni_4Si_4-rings and are capped by a Ni_2Si_2-units. These units are identical in both structures. The only difference arises regarding $Sr_2@Ni_8Si_8$-units formed by sharing octagonal faces. In α-SrNiSi both apical sections are ecliptical, resulting in D_{2h}-symmetry. In β-SrNiSi the resulting unit has D_{2d}-symmetry with staggered apical sections. Considering all polyhedra, the "more complex" arrangement in the beta phase leads to a transition from D_{2h} to D_{4h} symmetry when going from *Cmca* to $I4_1/acd$.

α-SrNiSi can be regarded as isostructural to BaPdP [22]. However while in this compound phosphor atoms occupy a split position (16 *g*), in the present compound silicon occupies the special position (8 *f*) and makes flat $^2_\infty[\mathrm{NiSi}]^-$ layers (Figure 1). Silicon binds to three nickel atoms with slightly distorted sp^2-hybrid geometry. Nickel shows similar geometry with an additional Ni–Ni contact. This arrangement can be derived from an ideal 4.8^2-net by distorting the four-membered ring into a rhomb. Nickel atoms come closer to form a bond and push the silicon towards the next rhomb, resulting in $(3^2.8^2)(3.8^2)$-nets.

This explains why Ni–Si-bonds between rhombs are shorter than within the rhomb. All bond distances for both modifications and sum of elemental radii are given in Table 3. Values of the beta phase are slightly larger because of increased lattice parameters. Ni–Ni-contacts (2.55–2.56 Å) are slightly larger than in the Ni-element. Ni–Si (2.18–2.26 Å) and Sr–Sr-distances (3.61–3.93 Å) are shorter than the sum of elemental radii [45], Sr–Ni and Sr–Si lie in a small range around it. The distance between strontium atoms that share an octagonal void, is remarkably short, especially for cations of same charge. This has already been observed for BaPdP [22].

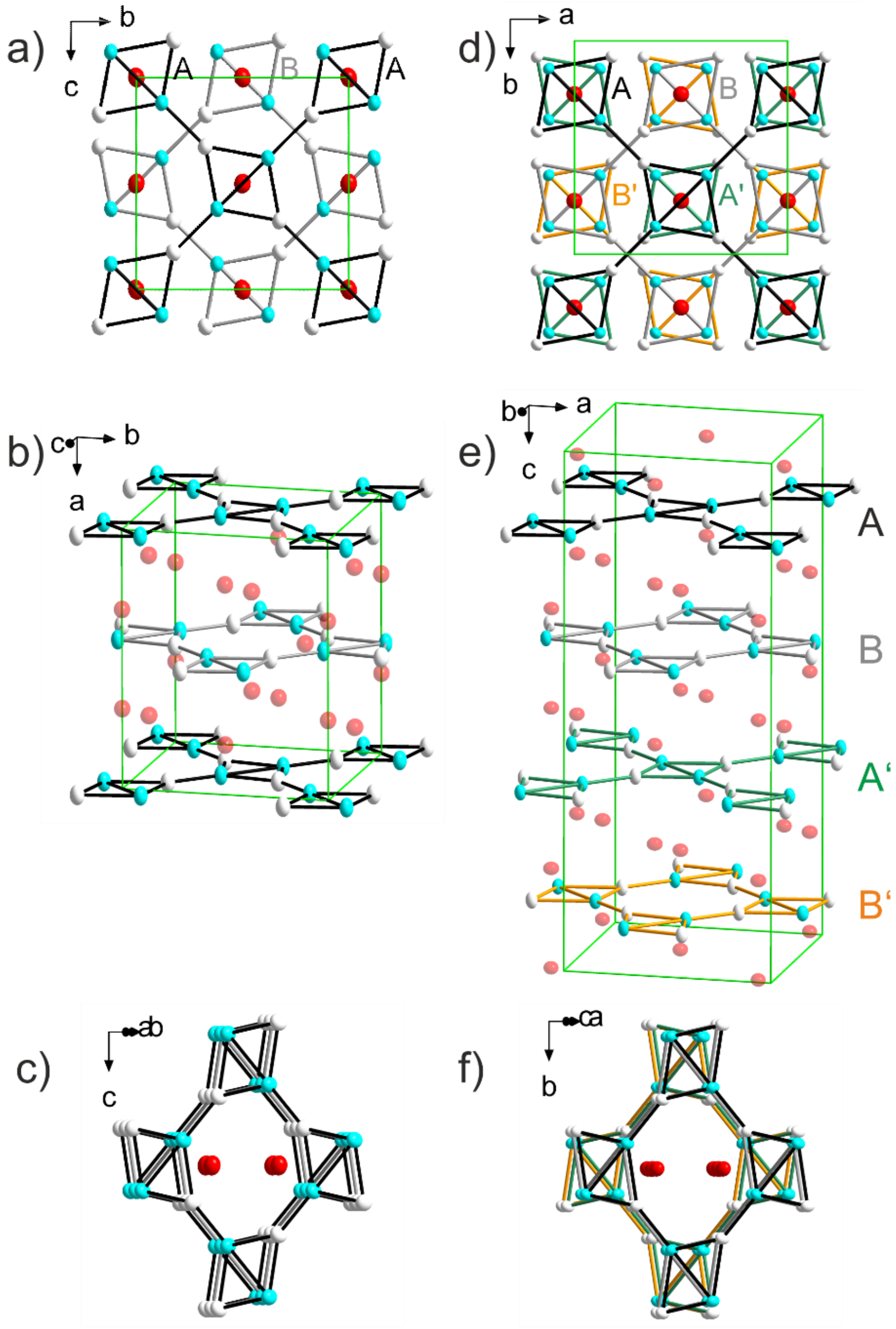

Figure 1 Representation of SrNiSi structure. a)-c): α-phase with orthorhombic *Cmca* space group, d)-f): β-phase with tetragonal *I*4$_1$/*acd* space group. The front view shown in the middle (b, e) exhibits the layered structure. Different orientation of the layers are highlighted in black, grey, green and orange. The top view (a, d) demonstrates how the layers are shifted with respect the each other. To keep track, a Ni_2Si_2-unit has been emphasized and labeled. On the bottom (c, f) a tilted view demonstrates that in the α-phase all layers are stacked with identical orientation whereas the β-phase can be regarded as two α-units that are turned by 90° to each other. Nickel atoms are represented in blue, silicon in white and strontium in red as ellipsoids with 90% probability.

For further comparison, close homologues SrNiGe [18] and SrPdSi [13] are of interest as well as members of Sr–Ni–Si family $SrNiSi_3$ [46], $SrNi_2Si$ [47] and $SrNi_5Si_3$ [23]. CaNiSi, BaNiSi or SrCoSi have not yet been reported. The Ni–Ni-distances of SrNiSi (2.55–2.56 Å) are larger than shortest distances in the mentioned silicides (2.25–2.43 Å) and almost as large as for SrNiGe (2.59 Å). In contrast one of the three Ni–Si bonds of SrNiSi (2.18–2.19 Å) is remarkably shorter than for other compounds (2.25–2.36 Å), the −iCOHP value 1.2 eV larger compared to $SrNi_2Si$, indicating a strong covalent bond. SrNiSi has a different structure than the other equiatomic nickel silicides. However, also isoelectronic SrNiGe and SrPdSi crystallize each in another structure. Larger Pd leads to LaIrSi-type, which is common for 1:1:1 compounds and described in the next section. SrNiGe makes an untypical structure with 2-dimensional NiGe-ribbons. These ribbons remind of condensed NiSi-rhombs found in SrNiSi, with weaker Ni–*X*-bonds (*X* = Si, Ge) and an additional Ni–Ni-bond. The fact that the silicide does not adopt the isoelectronic structure but that of Zintl-phase BaPdP, lets argue that SrNiSi is an edge case between intermetallic and alectron-deficient Zintl compound.

The structural and electronical relationship of selected *RTX* compounds (*R* = alkaline earth, *T* = transition metal, *X* = P, As, Sb) SrPdAs (ZrBeSi-type), CaPdAs and BaPdP has been investigated and discussed by Johrend and Mewis in detail [44]. All of them have planar $(TX)^{2-}$-nets with 6^3 or 4.8^2-nets, which are (distorted) variants of AlB_2-type. The *T* and *X*-atoms are each linked to three atoms of the other kind and in case of BaPdP a weak *T*–*T*-bond is established. The bonding is derived from trigonal planar crystal field with anti-binding e”(π*) and e’(σ*) states. The first pair is d_{xz}, d_{yz} and the second is $d_{x^2-y^2}$, d_{xy}. In case of 17 valence electrons, Peierls distortion occurs between the e’-states and the top bands are separated by a small band gap. This explains the deviation from ideal 4.8^2-net configuration and a weak *T*–*T*-bonding, resulting in $(3^2.8^2)(3.8^2)$-net. The flat geometry of the layers is explained with the fact that all affected bands are fully occupied and no energy is gained by deforming and splitting these states. However the argumentation is not consistent with present results. SrNiSi has 16 valence electrons, being isoelectronic to CaPdSi and CaPtSi. Nevertheless, the first crystalizes isostructural to BaPdP while the second adopts EuNiGe-type structure with strongly corrugated layers. The third crystallizes with LaIrSi-type structure, however, under 4 GPa pressure it can also adopt EuNiGe-type at 800 °C; a transition into TiNiSi-type is possible at 1100 °C, resulting in a four-connected 3D-network [13]. Hence not only electronic but other factors contribute to the flat planar arrangement.

3.2. Electronic Structure Calculation

BaPdP, which has been discussed as metallic Zintl compound, has one electron more than isostructural SrNiSi. To compare both structures, LMTO calculations have been performed. Figure 2 shows band structure, density of states (DOS) and projected DOS for both modifications of SrNiSi. Total DOS of both modification, normalized to formula units, is plotted together with integrated DOS in Figure S3. Wigner-Seitz-cells, Brilloin zones and used k-paths are given in Figure S4 (Supporting Information). As expected they are quite identical and iDOS difference between Fermi level and pseudogap at 0.8 eV is exactly one electron. Two blocks are present separated by a gap of about 2 eV. Between −10 and −7 eV are mainly Si-s contributions. Above −5 eV many states merge, with large contribution by Ni-d orbitals between −4 and −2 eV. SrNiSi shows anisotropic behavior with many bands crossing the Fermi level along directions within the Sr–Si-layer (marked in grey in Figure 2a) and c) and few in other directions. The Fermi level is located at a local maximum, which often is referred to interesting magnetic properties and instabilities. However, measurements on a sample containing large amount of SrNiSi did not show superconductivity. No band gap is observed and metallic properties are expected. This is in contrast to BaPdP that has a distinct band gap with the Fermi level exactly at the border [44]. This can be explained by the extra electron of phosphorous that fills the states up to the pseudogap at 0.8 eV and the Si-s stated shifted to relative energies between −10 and −12 eV.

Three-valent phosphorous can be easily stated by sp^2-configuraton with a free electron pair. To accomplish the same structure with silicon, an additional electron has to be introduced according to the Zintl Klemm concept. While ELF plot and isosections are topologically very similar for both SrNiSi-variants, remarkable differences can be found compared to BaPdP. Electron densitiy is found between adjacent nickel atoms indicating metallic Ni–Ni-interactions (Figure 3b,e), whereas the region between palladium atoms is electron-poor. Also the interstitial region within Ni–Si-layers appears more delocalized with $\eta > 0.4$. Likelyhood of electrons between atoms in the layer is thus enhanced compared to Pd–P-layers that is about $\eta = 0.3$. Viewing the ELF isosurface at $\eta = 0.72$, a large basin is located around phosphor atoms with attractors above and below. The cusps are connected by necks directed towards the space between adjacent alkaline earth atoms (Figure 3g,h). This fits well the image of a polyanionic network with excessive negative charge being attracted by cations. The cusps are not present for electron poorer semimetallic silicon (Figure 3a,b,d,e). Available electron density is pronounced in the layer and in necks around silicon to compensate adjacent cationic charge. COHP was calculated and integrated up to the Fermi level (Table 3) for SrNiSi, estimating bonding interactions. Values are proportional to distances and show weaker Ni–Si-bonds in the rhomb and a slightly stronger covalent bond to the next rhomb. Ni–Ni-bonds are of metallic character, as expected. Sr–Ni- and Sr–Si-interactions are in the range for typical ionic contacts within intermetallic coumpounds.

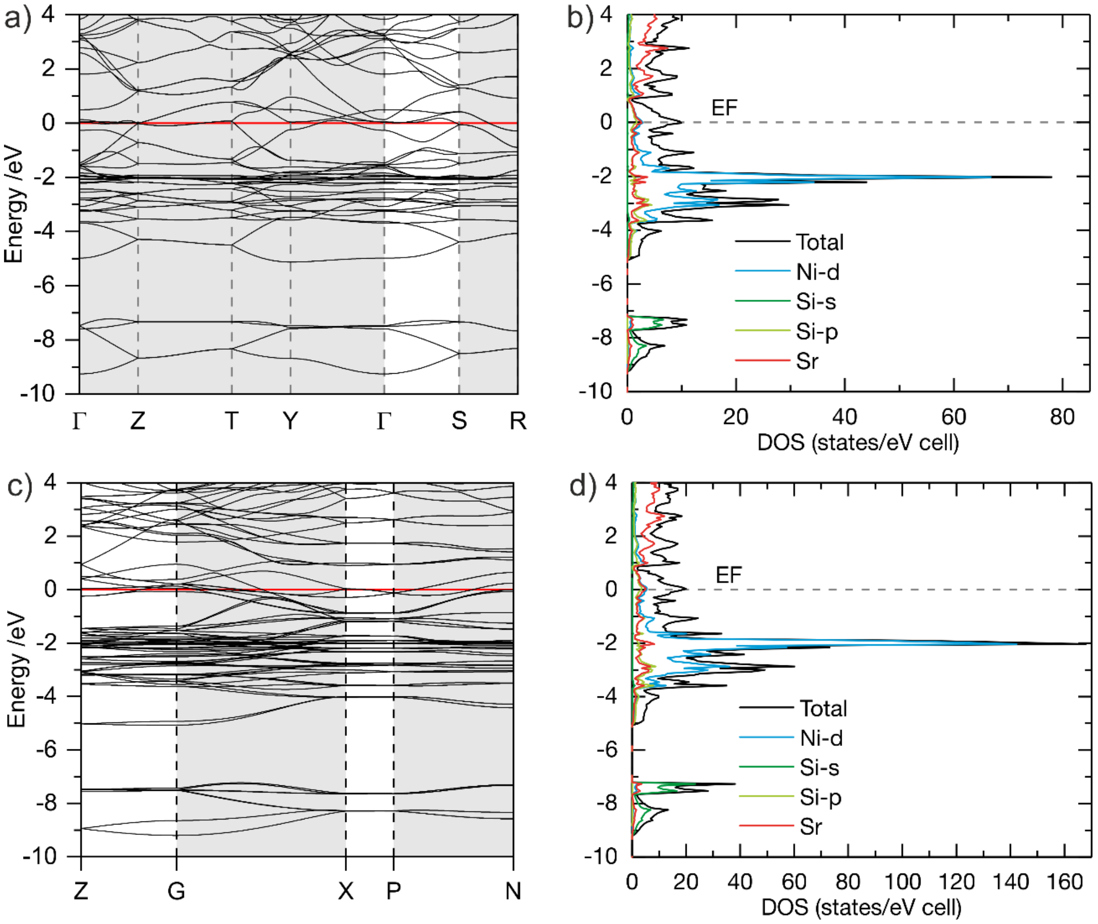

Figure 2 a), c) Band structure, b, d) density of states (DOS) and projected DOS for selected atomic orbitals of SrNiSi with *Cmca* space group (a, b) or $I4_1/acd$ space group (c, d), respectively. k-path directions within the Ni–Si-layer are highlighted in grey. Data were calculated with TB-LMTO-ASA method, Brillouin-zones and k-paths are visualized in Figure S4 in the supporting information.

Comparison of SrNiSi with isostructural BaPdP and isoelectronic CaPdSi with EuNiGe-type shows, that the planar assembly of the first two cannot only be explained simply by Peierl’s distortion of occupied and unoccupied electronic states, as described by Johrendt et al. [44]. Steric effects may contribute to the stability of this structure type as well. The high symmetry of nets in SrNiSi allows different stacking variants that are very similar in energy and configuration. Surprisingly, the more complex stacking in the β-phase creates not only a larger unit cell but also a higher symmetry compared to the α-phase.

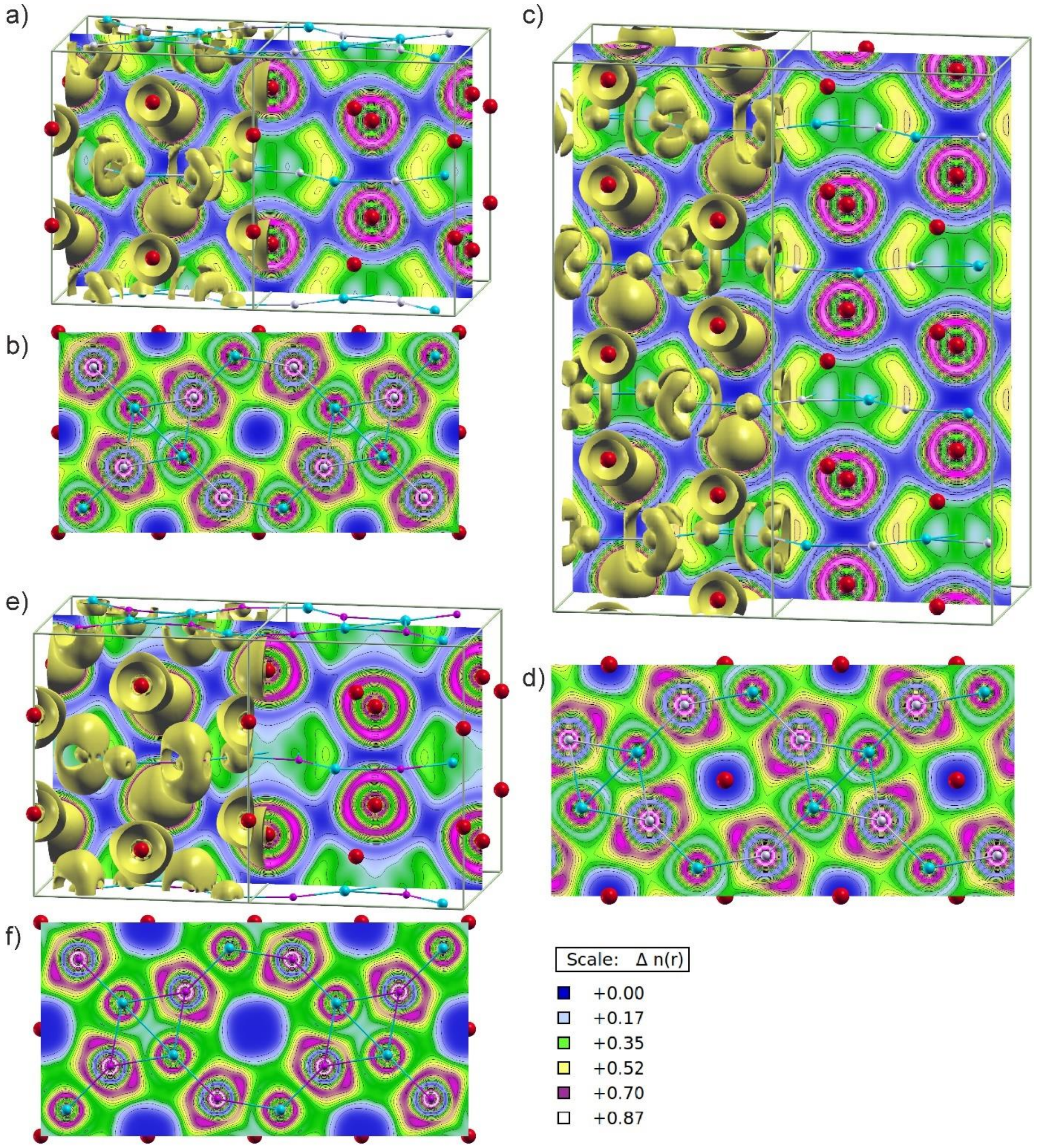

Figure 3 ELF topology and isosection calculated for a), b) SrNiSi (red = Sr, cyan = Ni, white = Si) with space group *Cmca*, c), d) space group $I4_1/acd$ and e), f) BaPdP (red = Ba, cyan = Pd, violet = P) with space group *Cmca*. TB-LMTO-ASA method was used to plot all-electron density; 3-dimensional representation of the isosurface is shown for $\eta = 0.72$. For a), c), e) an isosection parallel to *ab*-plane or *bc*-plane for space groups *Cmca*- or $I4_1/acd$ at c or $a = 0.5$, respectively, is shown, b), d), f) the isosections parallel *bc* or *ab* in plane with Ni–*X*-layers (*X* = Si, P).

4. Conclusion

Stoichiomeric intermetallic compound SrNiSi has been synthesized and structurally characterized. Two-dimensional $(3^2.8^2)(3.8^2)$-layers are stacked in two different sequences, giving two modifications: α-SrNiSi (*Cmca*) and β-SrNiSi ($I4_1/acd$). The first ist closely related to BaPdP but has no split position on the P-site. In contrast to the phosphide, which is a Zintl phase with distinct band gap, isostructural silicide is considered as electron deficient Zintl phase with metallic properties. ELF-topology demonstrates polyanionic nature of Ni–Si-layers, but electron density in Si-lone pairs is reduced and the layer stronger polarized. Shortest Ni–Si-distance up to date has been observed and bonding interactions have been confirmed with COHP-calculations.

5. Acknowledgments

This research was financially supported by the German Research Foundation (Deutsche Forschungsgemeinschaft, DFG, Grant HL 62/3-1) and the TUM Graduate School.

6. References

[1] Andrzej Szytula, *Croat. Chem. Acta* **1999**, *72*, 171–186.

[2] M.D. Bojin, R. Hoffmann, *HCA* **2003**, *86*, 1653–1682, https://doi.org/10.1002/hlca.200390140.

[3] M.L. Fornasini, F. Merlo, *J. Alloys Compd.* **1995**, *219*, 63–68, https://doi.org/10.1016/0925-8388(94)05010-4.

[4] R.-D. Hoffmann, R. Pöttgen, *Z. Kristallogr.* **2001**, *216*, https://doi.org/10.1524/zkri.216.3.127.20327.

[5] S. Gupta, K.G. Suresh, *J. Alloys Compd.* **2015**, *618*, 562–606, https://doi.org/10.1016/j.jallcom.2014.08.079.

[6] J. Evers, G. Oehlinger, A. Weiss, C. Probst, *Solid State Commun.* **1984**, *50*, 61–62, https://doi.org/10.1016/0038-1098(84)90060-7.

[7] FIZ Karlsruhe, ICSD: Inorganic Crystal Structure Database, Leibniz Institute for Information Infrastructure, Karlsruhe, Germany, 2022.

[8] G. Wenski, A. Mewis, *Z. Anorg. Allg. Chem.* **1986**, *543*, 49–62, https://doi.org/10.1002/zaac.19865431206.

[9] R. Pöttgen, H. Borrmann, C. Felser, O. Jepsen, R. Henn, R.K. Kremer, A. Simon, *J. Alloys Compd.* **1996**, *235*, 170–175, https://doi.org/10.1016/0925-8388(95)02069-1.

[10] J. Evers, G. Oehlinger, *J. Solid State Chem.* **1986**, *62*, 133–137, https://doi.org/10.1016/0022-4596(86)90223-9.

[11] K. Klepp, E. Parthé, *Acta Crystallogr., Sect. B: Struct. Crystallogr. Cryst. Chem.* **1982**, *38*, 1541–1544, https://doi.org/10.1107/S056774088200630X.

[12] S.F. Matar, R. Pöttgen, M. Nakhl, *Z. Naturforsch., B: J. Chem. Sci.* **2017**, *72*, 207–213, https://doi.org/10.1515/znb-2016-0230.

[13] J. Evers, G. Oehlinger, K. Polborn, B. Sendlinger, *J. Solid State Chem.* **1991**, *91*, 250–263, https://doi.org/10.1016/0022-4596(91)90079-W.

[14] Y. Komura, *Acta Crystallogr.* **1962**, *15*, 770–778, https://doi.org/10.1107/S0365110X62002017.

[15] W. Dörrscheidt, H. Schäfer, *Z. Naturforsch., B: J. Chem. Sci.* **1976**, *31*, 1050–1052, https://doi.org/10.1515/znb-1976-0810.

[16] A.V. Hoffmann, V. Hlukhyy, T.F. Fässler, *Z. Anorg. Allg. Chem.* **2014**, *640*, 2882–2888, https://doi.org/10.1002/zaac.201400356.

[17] V. Hlukhyy, N. Chumalo, V. Zaremba, T.F. Fässler, *Z. Anorg. Allg. Chem.* **2008**, *634*, 1249–1255, https://doi.org/10.1002/zaac.200700534.

[18] V. Hlukhyy, L. Siggelkow, T.F. Fässler, *Inorg. Chem.* **2013**, *52*, 6905–6915, https://doi.org/10.1021/ic302681t.

[19] J. Nuss, M. Jansen, *Z. Anorg. Allg. Chem.* **2002**, *628*, 1152, https://doi.org/10.1002/1521-3749(200206)628:5<1152:AID-ZAAC1152>3.0.CO;2-1.

[20] G. Cordier, T. Friedrich, *Z. Kristallogr.* **1993**, *205*, https://doi.org/10.1524/zkri.1993.205.12.135.

[21] D. Johrendt, A. Mewis, *Z. Anorg. Allg. Chem.* **1992**, *618*, 30–34, https://doi.org/10.1002/zaac.19926180106.

[22] D. Johrendt, A. Mewis, *J. Alloys Compd.* **1994**, *205*, 183–189, https://doi.org/10.1016/0925-8388(94)90787-0.

[23] T. Braun, V. Hlukhyy, in preparation.

[24] X-Area, STOE & Cie GmbH, Darmstadt, Germany, 2015.

[25] LANA, STOE & Cie GmbH, Darmstadt, Germany, 2016.

[26] X-SHAPE, STOE & Cie GmbH, Darmstadt, Germany, 2015.

[27] X-RED32, STOE & Cie GmbH, Darmstadt, Germany, 2016.

[28] G.M. Sheldrick, SHELXS-2014: Program for the Determination of Crystal Structure, University of Göttingen, Göttingen, Germany, 2014.

[29] G.M. Sheldrick, SHELXL-2014: Program for Crystal Structure Refinement, University of Göttingen, Göttingen, Germany, 2014.

[30] G.M. Sheldrick, *Acta Crystallogr., Sect. C: Struct. Chem.* **2015**, *71*, 3–8, https://doi.org/10.1107/S2053229614024218.

[31] G.M. Sheldrick, *Acta Crystallogr., Sect. A: Found. Crystallogr.* **2008**, *64*, 112–122, https://doi.org/10.1107/S0108767307043930.

[32] R.W. Tank, O. Jepsen, O.K. Andersen, The STUTTGART TB-LMTO-ASA program, Stuttgart, 1998.

[33] M. van Schilfgarde, T.A. Paxton, O. Jepsen, O.K. Andersen, TB-LMTO-ASA, Stuttgart, Germany, 1994.

[34] O. Jepsen, O.K. Andersen, *Z. Phys. B: Condens. Matter* **1995**, *97*, 35–47, https://doi.org/10.1007/BF01317585.

[35] O.K. Andersen, O. Jepsen, *Phys. Rev. Lett.* **1984**, *53*, 2571–2574, https://doi.org/10.1103/PhysRevLett.53.2571.

[36] W.R.L. Lambrecht, O.K. Andersen, *Phys. Rev. B* **1986**, *34*, 2439–2449, https://doi.org/10.1103/PhysRevB.34.2439.

[37] U.v. Barth, L. Hedin, *J. Phys. C: Solid State Phys.* **1972**, *5*, 1629–1642, https://doi.org/10.1088/0022-3719/5/13/012.

[38] P.E. Blöchl, O. Jepsen, O.K. Andersen, *Phys. Rev. B, Condens. Matter* **1994**, *49*, 16223–16233, https://doi.org/10.1103/physrevb.49.16223.

[39] R. Dronskowski, P.E. Blöchl, *J. Phys. Chem.* **1993**, *97*, 8617–8624, https://doi.org/10.1021/j100135a014.

[40] F. Boucher, O. Jepsen, O.K. Andersen, Supplement to the TB-LMTO-ASA (version 47) program, Stuttgart, 1997.

[41] A. Savin, R. Nesper, S. Wengert, T.F. Fässler, *Angew. Chem. Int. Ed. Engl.* **1997**, *36*, 1808–1832, https://doi.org/10.1002/anie.199718081.

[42] A. Kokalj, *J. Mol. Graphics Modell.* **1999**, *17*, 176–179, https://doi.org/10.1016/S1093-3263(99)00028-5.

[43] Code available from http://www.xcrysden.org/.

[44] D. Johrendt, A. Mewis, *Z. Naturforsch., B (Zeitschrift für Naturforschung B)* **1996**, *51*, 655–664, https://doi.org/10.1515/znb-1996-0506.

[45] J.C. Slater, *J. Chem. Phys.* **1964**, *41*, 3199–3204, https://doi.org/10.1063/1.1725697.

[46] N. Nasir, N. Melnychenko-Koblyuk, A. Grytsiv, P. Rogl, G. Giester, J. Wosik, G.E. Nauer, *J. Solid State Chem.* **2010**, *183*, 565–574, https://doi.org/10.1016/j.jssc.2009.12.023.

[47] T. Braun, S. Zeitz, V. Hlukhyy, *Z. Anorg. Allg. Chem.* **2019**, *645*, 388–395, https://doi.org/10.1002/zaac.201800500.

Supporting Information

SrNiSi With Two Different Stacking Variants — An Electron Deficient Zintl-Phase

Thomas Braun, Annika Schulz, Viktor Hlukhyy

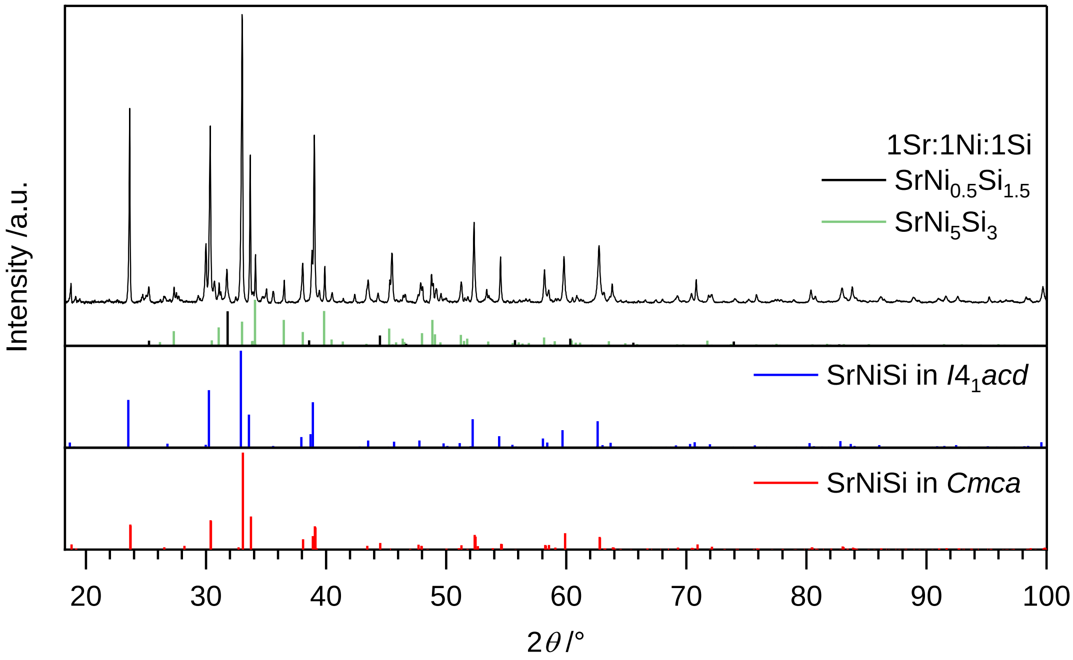

Figure S1 Powder X-Ray diffraction data of SrNiSi. It can be assigned as main phase, however both modification (shown in red and blue) show very similar patterns and are hard to distinguish. Minor reflections are difficult to assign because of secondary phases.

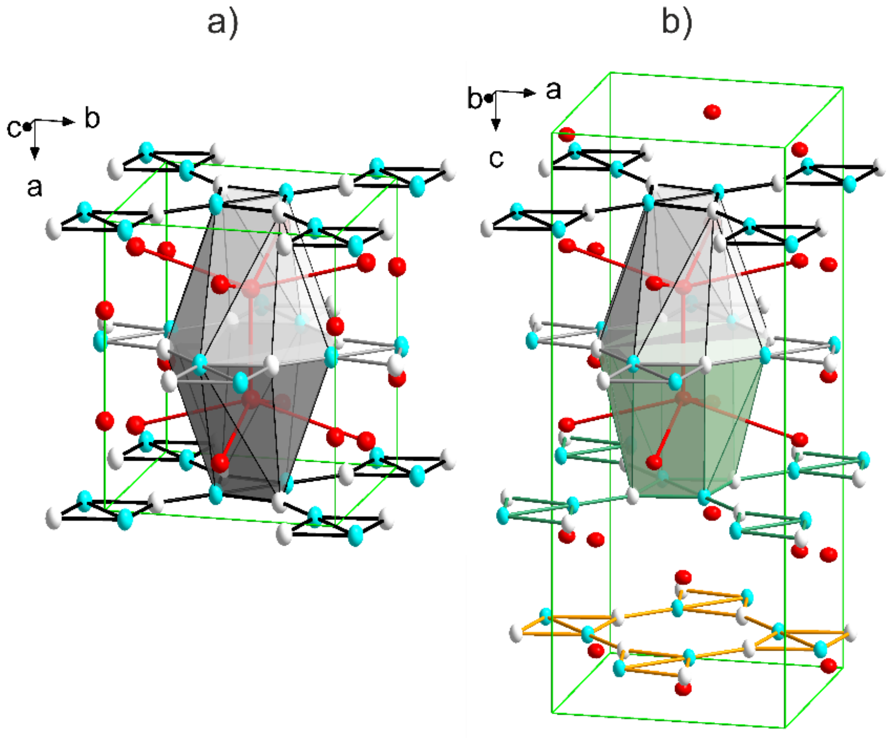

Figure S2 Coordination of strontium in a) α-SrNiSi and b) β-SrNiSi. In the left picture, the two Sr atoms sharing an octagonal face form a $Sr_2@Ni_8Si_8$-unit with D_{2h}-symmetry. In the right picture, the coordination environment of a single strontium atom is identical; however, a unit of two atoms whose polyhedra share an octagonal face has D_{2d}-symmetry. Nickel atoms are represented in blue, silicon in white and strontium in red as ellipsoids with 90% probability.

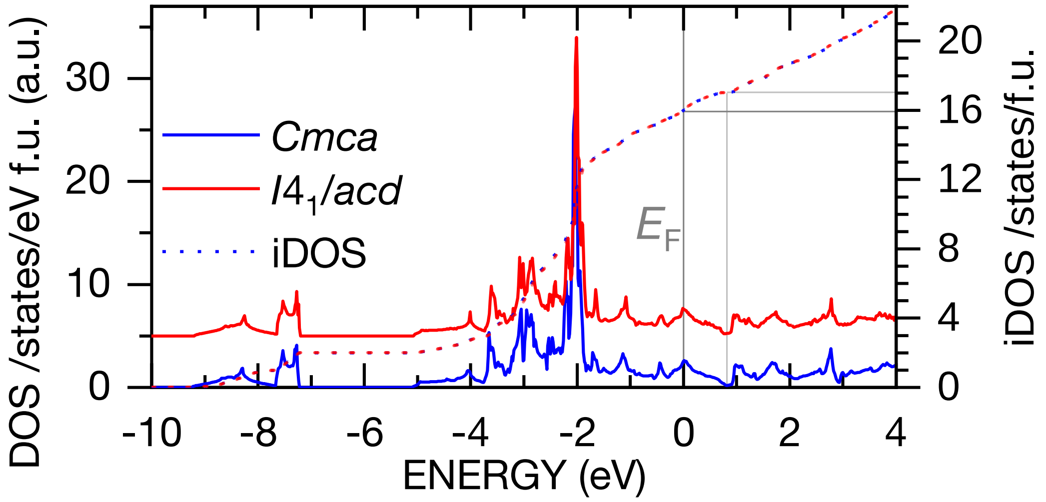

Figure S3 Comparison of density of states (DOS) and integrated DOS calculated for SrNiSi with *Cmca* and *I*4$_1$/*acd* symmetry. Values are normalized to numer of formula units. Grey lines are guides to the eye and show the difference to BaPdP, which has one additional electron.

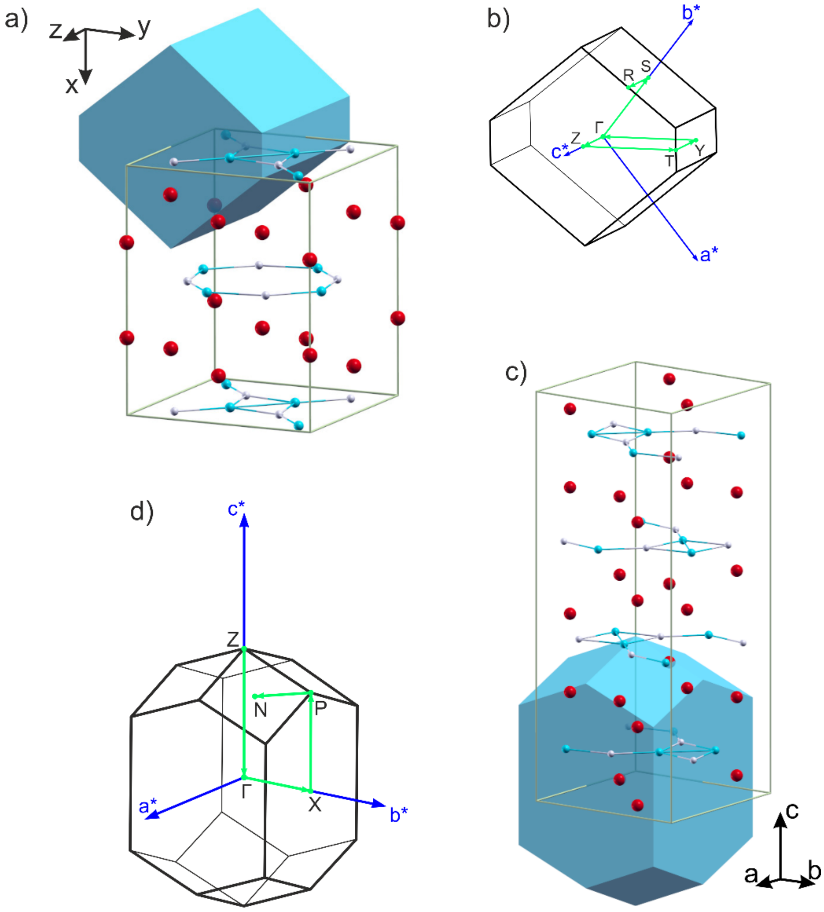

Figure S4 a, c) Structure and Wigner-Seitz-cell, drawn in blue and b, d) corresponding first brillouin zone with k-path used for Band structure calculations of of SrNiSi with *Cmca*-symmetry (a,b) or *I*4_1*/acd*-symmetry (c, d). Nickel is drawn as blue, silicon as white and strontium as red balls.S

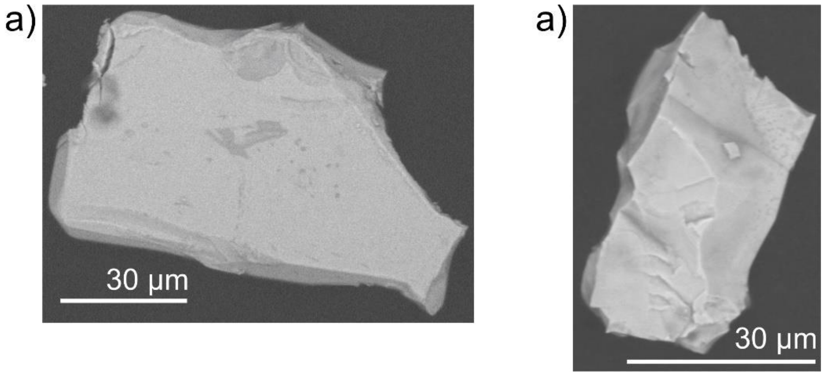

Figure S5 Electron images of the single cystals of a) α-SrNiSi and b) β-SrNiSi, used for X-Ray diffraction and EDX-analysis.

5.5 $SrNi_2Si$ and $BaNi_2Si$ – New Layered Silicides with Fused Nickel Six-membered Rings in a Boat Conformation

Braun, T.; Zeitz, S.; Hlukhyy, V.

published in

Z. Anorg. Allg. Chem. **645**, 388–395 (2019)

Journal of Inorganic and General Chemistry
ZAAC
Zeitschrift für anorganische und allgemeine Chemie

DOI: 10.1002/zaac.201800500

ARTICLE

$SrNi_2Si$ and $BaNi_2Si$ – New Layered Silicides with Fused Nickel Six-membered Rings in a Boat Conformation

Thomas Braun,[a] Sabine Zeitz,[a] and Viktor Hlukhyy*[a]

Dedicated to Prof. Dr. Thomas Fässler on the Occasion of his 60th Birthday

Abstract. Intermetallic compounds $SrNi_2Si$ and $BaNi_2Si$ were prepared by arc-melting of stoichiometric mixture of the elements and subsequent annealing in welded niobium ampoules. Both compounds were investigated by X-ray diffraction on powder as well as single crystal methods. The title compounds both crystallize in the $BaNi_2Ge$ structure type (space group *Pmmn*, $Z = 2$), a ternary ordered variant of $TiCu_3$: $a = 4.0296(9)$ Å, $b = 6.5121(14)$ Å, $c = 5.6839(21)$ Å, $R_1 = 0.040$ for $SrNi_2Si$ and $a = 4.0681(9)$ Å, $b = 6.580(4)$ Å, $c = 5.976(5)$ Å, $R_1 = 0.031$ for $BaNi_2Si$. The structure contains corrugated polyanionic $[Ni_2Si]^{2-}$ layers, stacked according to the primitive sequence *AA* along the *c* axis. Six-membered Ni rings adopt a boat conformation, silicon atoms are in the plane with nickel, and the alkaline earth cations sit between the layers. These two compounds extend the family $AeNi_2X$ (Ae = Ca, Sr, Ba; X = Si, Ge), where up to date $CaNi_2Si$, $SrNi_2Ge$, and $BaNi_2Ge$ are known. LMTO band structure calculations, including DOS, COHP, and ELF were performed to gain more insight into the electronic situation of $SrNi_2Si$ and $BaNi_2Si$.

Introduction

Polar intermetallic compounds are known for their structural diversity and variety of physical properties. They can be characterized by a remarkable complexity due to the interplay between covalent, metallic, and ionic interactions. In recent years, special attention has been drawn to compounds with flat d-metal layers, especially after the discovery of superconductivity in iron-pnictides/chalcogenides, containing square-planar Fe layers.[1] However, the interest has not been limited only to Fe-based compounds, but has been extended to similar structures with other transition metals like Co and Ni. For example, the appearance of a ferromagnetic quantum critical point is accompanied with the breaking of bonds in Ge–Ge dimers in $SrCo_2(Ge_{1-x}P_x)_2$.[2] In the Ni analogue solid solution $SrNi_2(Ge_{1-x}P_x)_2$ the breaking of interlayer bonds in Ge–Ge dimers leads to a twofold increase in superconducting critical temperature (compared with $SrNi_2P_2$).[3] Beside the square-planar (4^4) d-metal layers present in iron-pnictide superconductors, also compounds containing other planar lattice arrangement of transition metal atoms, such as honeycomb (6^3), or Kagomé (3.6.3.6) layers, should be widely investigated with respect to their physical properties.

Due to its filled d^{10} orbitals, tolerating diverse coordination patterns, nickel forms a huge number of polar intermetallic compounds in the *Ae*-Ni-*E* systems (*Ae* = alkaline-earth metal, *E* = Si, Ge) with various different structures.[4–23] Here the electropositive *Ae* atom is embedded within a polyanionic $[Ni_xE_y]^{z-}$ substructure. Such polyanions can be found for instance in Ba_2NiSi_3 as $[NiSi_3]^{4-}$ strings or as $[NiGe]^{2-}$ ribbons in (Sr/Ba)NiGe, which penetrate in one dimension.[4,5] With decreasing cation size such $[NiGe]^{2-}$ ribbons condense into a two- or three-dimensional substructure by forming layers or framework reported for CaNiGe or MgNiGe, respectively.[6,5]

Only few ternary strontium or barium nickel silicides have been reported so far: $SrNiSi_3$ ($BaNiSn_3$-type),[7] $Sr(Ni_xSi_{1-x})_2$ (AlB_2-type),[8] $SrNi_{6+x}Si_{7-x}$ ($BaAu_6Zn_7$-type)[8] as well as $BaNi_2Si_2$, Ba_2NiSi_3, and the type-I clathrate $Ba_8Ni_xSi_{46-x-y}$ (K_4Si_{23}-type).[9–12] The superconductivity in the nickel silicides $Sr(Ni_xSi_{1-x})_2$ and $Ba_8Ni_xSi_{46-x-y}$ has been recently reported,[13,9] prompting us to further detailed investigations of these systems.

In this paper, we report synthesis and characterization of new layered nickel silicides $SrNi_2Si$ and $BaNi_2Si$. Homologous compounds $CaNi_2Si$ and $SrNi_2Ge$ crystallize in the $LiCu_2Sn$-structure type, where the Ni atomic layers adopt a chair-conformation similar to grey arsenic.[14–16] The heavier homologue $BaNi_2Ge$, an ordered variant of $TiCu_3$-type, has a different structure with a boat conformation of Ni atoms.[17] The title compounds $SrNi_2Si$ and $BaNi_2Si$, which adopt the $BaNi_2Ge$-type, extend this $AeNi_2E$ family.

Experimental Section

Syntheses: Samples were prepared from the pure elements. Starting materials have been ingots of strontium (ChemPur, 98 %, redistilled prior to use), barium (ChemPur, 99.5 %), nickel wire (Alfa Aesar, 99.98 %), and silicon pieces (Alfa Aesar, 99.999 %). At the first stage, the samples with composition *Ae*:Ni:Si = 1:2:1 (*Ae* = Sr, Ba) were prepared by arc-melting of the elements in a furnace equipped with a

---

* Dr. V. Hlukhyy
E-Mail: viktor.hlukhyy@lrz.tu-muenchen.de
[a] Department of Chemistry
Technische Universität München
Lichtenbergstr. 4
85747 Garching, Germany

Supporting information for this article is available on the WWW under **http://dx.doi.org/10.1002/zaac.201800500** or from the author.

water-cooled copper hearth (Mini Arc Melting System, MAM-1, Johanna Otto GmbH) placed in an argon filled Glovebox (MBraun 20G, argon purity 99.996 %). For compensation of evaporation losses, an excess of 6 % *Ae* was provided. The resulting reguli were turned three times in order to ensure homogenization. Only polycrystalline samples were obtained by this method. At the next stage, in order to obtain suitable single crystals, the samples were sealed in cleaned Nb tubes and heated in a resistance furnace. After annealing 12 h at 960 °C the samples were cooled with 6 K per hour to 600 °C, kept there for 48 h and cooled to room temperature with 18 K per hour. The $SrNi_2Si$ and $BaNi_2Si$ compounds were found to be stable against air and moisture. Single crystals with irregular shape and metallic luster (Figure S1, Supporting Information) were isolated from the sample for further examinations. Both compounds can be easily reproduced by arc melting technique or by reactions of pure elements in a high-frequency furnace.

Powder X-ray Diffraction: A STOE Stadi P powder X-ray diffractometer equipped with a DECTRIS MYTHEN 1K detector, Cu-$K_{\alpha 1}$ source, and curved Ge(111) monochromator was used to investigate the phase purity. The $SrNi_2Si$ sample contains $Ni_{31}Si_{12}$[18] and a small amount of an unknown phase, whereas in the $BaNi_2Si$ sample only $Ni_{31}Si_{12}$ was present as impurity (Figure S2, Supporting Information). The measurements on powders were calibrated to external silicon standard. Lattice parameters of the title compounds were determined with Werner's TREOR algorithm,[19] using the diffractometer software WinXPOW.[20] They agree well with the single crystal refinements. All attempts to prepare single phase samples using different temperature programs were unsuccessful. The excess of earth alkaline metal might have been too low, leading to remaining binary nickel silicides after all leftover Sr/Ba has reacted.

Single Crystal X-ray Diffraction: The air stable single crystals were selected under a microscope and fixed at the tip of glass fibers with nail polish and measured at room temperature with a STOE IPDS 2T (Mo-K_{α}, 0.71073 Å, graphite monochromator) X-ray diffractometer. The data were corrected for absorption numerically,[21,22] A starting model of the structures was created running direct methods with the program SHELXS-2014/7[23,24] and the subsequent structure refinement was performed with the programm SHELXL-2014/7 (full-matrix least-squares on $F_0{}^2$).[25,26] To ensure the right composition, a series of separate least-squares cycles with varying refinable occupation parameter, was run. In the final cycles, all atomic positions were set to ideal full occupation again. All relevant details of the structure refinements are listed in Table 1, atomic positions and equivalent isotropic displacement parameters are given in Table 2. In Table 3, the shortest interatomic distances are summarized.

Table 1. Crystal data und structure refinement for $SrNi_2Si$ and $BaNi_2Si$.

	$SrNi_2Si$	$BaNi_2Si$
Formula weight /g·mol^{-1}	233.13	282.85
Space group	*Pmmn* (no. 59)	
Z	2	
Unit cell dimensions (powder data):		
a /Å	4.0296(9)	4.0681(9)
b /Å	6.512(1)	6.580(4)
c /Å	5.684(2)	5.976(5)
V /Å^3	149.15(7)	159.97(17)
Calculated density / g·cm^{-3}	5.19	5.89
Absorption coefficient / mm^{-1}	30.4	23.9
F(000)	216	252
Crystal size /mm^3	0.12 × 0.05 × 0.02	0.13 × 0.08 × 0.03
θ range /°	3.585 –27.488	4.612 – 29.152
Range in *hkl*	$\pm 5, -7 \leq k \leq 8, \pm 7$	$\pm 5, \pm 8, \pm 8$
Reflections collected	1137	2891
Independent reflections	212 (R_{int} = 0.0695)	264 (R_{int} = 0.0234)
Reflections with $I \geq 2\sigma(I)$	172 (R_{sigma} = 0.0898)	254 (R_{sigma} = 0.0579)
Data / parameters	212 / 15	264 / 16
GOF on F^2	1.021	1.157
Final *R* indices [$I \geq 2\sigma(I)$]	R_1 = 0.0387 wR_2 = 0.0875	R_1 = 0.0281 wR_2 = 0.0719
R indices (all data)	R_1 = 0.0459 wR_2 = 0.0898	R_1 = 0.0297 wR_2 = 0.0733
Larg. diff peak and hole /e·Å^{-3}	2.45 / –0.92	1.31 / –1.56

Crystallographic data for the structures in this paper have been deposited with the Cambridge Crystallographic Data Centre, CCDC, 12 Union Road, Cambridge CB21EZ, UK. Copies of the data can be obtained free of charge on quoting the depository numbers CSD-1881820 for $SrNi_2Si$ and CSD-1881821 for $BaNi_2Si$ (Fax: +44-1223-336-033; E-Mail: deposit@ccdc.cam.ac.uk, http://www.ccdc.cam.ac.uk).

Energy Dispersive X-ray Analysis (EDX): After single crystal XRD measurements, the crystals were analyzed with a JEOL 5900LV scanning electron microscope, equipped with an energy dispersive X-ray detector. Within the measured energy range, no impurity elements heavier than sodium were observed. The semi-quantitative EDX analysis (without internal standard) of the crystals revealed following elemental compositions in atomic percentages: Sr - 25(2), Ni - 53(6),

Table 2. Atomic coordinates and equivalent isotropic displacement parameters for $SrNi_2Si$ and $BaNi_2Si$ (space group *Pmmn*).

Atom	Site	x/a	y/b	z/c	U_{eq} a) × 10^3 /Å^2
$SrNi_2Si$					
Sr	2a	1/4	1/4	0.1183(2)	22.1(4)
Ni	4e	1/4	0.0633(1)	0.6041(2)	18.8(4)
Si	2b	1/4	3/4	0.3972(5)	19.0(8)
$BaNi_2Si$					
Ba	2a	1/4	1/4	0.11806(7)	18.3(3)
Ni	4e	1/4	0.0647(1)	0.5967(1)	13.9(3)
Si	2b	1/4	3/4	0.4047(4)	13.8(5)

a) U_{eq} is defined as one third of the trace of the orthogonalized U_{ij} tensor.

Table 3. Interatomic distances /Å for $SrNi_2Si$ and $BaNi_2Si$ calculated with the lattice parameters taken from powder X-ray data and corresponding –iCOHPs (eV per bond cell).

		Distance	–iCOHP /eV			Distance	–iCOHP /eV
$SrNi_2Si$				$BaNi_2Si$			
Sr	–Ni	3.017(2) (2 ×)	0.347	Ba	–Ni	3.109(2) (2 ×)	0.310
	–Ni	3.165(2) (2 ×)	0.448		–Ni	3.346(3) (2 ×)	0.451
	–Ni	3.273(1) (4 ×)	0.354		–Ni	3.366(1) (4 ×)	0.421
	–Si	3.412(3) (2 ×)	0.262		–Si	3.503(3) (2 ×)	0.369
	–Si	3.556(3) (2 ×)	0.280		–Si	3.709(2) (2 ×)	0.340
	–Si	3.622(2) (2 ×)	0.209		–Si	3.728(3) (2 ×)	0.418
Ni	–Si	2.3530(6) (4 ×)	2.416	Ni	–Si	2.3715(7) (4 ×)	2.270
	–Si	2.355(2) (2 ×)	2.318		–Si	2.367(2) (2 ×)	2.252
	–Ni	2.431(2) (1 ×)	1.401		–Ni	2.438(2) (1 ×)	1.225
	–Ni	2.478(1) (2 ×)	1.343		–Ni	2.4896(8) (2 ×)	1.167

Si - 23(2), and Ba - 27(3), Ni - 50(6), Si - 23(2) for $SrNi_2Si$ and $BaNi_2Si$, respectively. These values, within standard deviations, are in agreement with compositions obtained by the X-ray single crystal structure refinements.

Thermal Analysis: Differential thermal analysis (DTA) was carried out with a differential scanning calorimeter (NETZSCH DSC 404C). The samples were homogenized and about 50–100 mg filled in custom-made niobium crucibles. Containers were sealed by crimping the upper end with a pipe tong and subsequent arc-welding. Another sealed empty container was used as reference. An argon flow of 50 mL·min^{-1} was used to prevent any corrosion. Two to three heating/cooling cycles up to 960 °C with a rate of 5 K·min^{-1} were performed. The recorded data were processed with the software NETZSCH – Proteus Analysis.[27] Powder diffraction data of the samples before and after DTA can be found in Figure S3 (Supporting Information).

Electronic Structure Calculations: Density functional theory (DFT) band structure calculations of $SrNi_2Si$ and $BaNi_2Si$ were performed with the linear muffin-tin orbital (LMTO) method in the atomic spheres approximation (ASA) using the tight-binding (TB) program TB-LMTO-ASA 4.7.[28,29] These calculations were carried out by using the structures determined from single-crystal X-ray measurements. The exchange and correlation terms were treated within the local density approximation (LDA) and parameterized according to *von Barth and Hedin*.[30] Automatically determined values were used for the radii of the atomic spheres, whereas the positions and radii of the empty spheres were determined after *Jepsen* and *Andersen*.[31] The basis set of short-ranged atom-centered TB-LMTOs contained s-d valence function for Sr and Ba; s-d valence functions for Ni, and s, p valence functions for Si. Sr-5p, and Ba-6p orbitals were included using a downfolding technique.[32] The Brillouin zone integrations were performed with a 24 × 16 × 16 special k-point grid. To calculate the band structure, following k-path was used: $\Gamma = (0,0,0) \rightarrow Z = (0,0,½) \rightarrow T = (0,½,½) \rightarrow Y = (0,½,0) \rightarrow \Gamma = (0,0,0) \rightarrow X = (½,0,0) \rightarrow S = (½,½,0) \rightarrow R = (½,½,½) \rightarrow U = (½,0, ½)$.

The analysis of the chemical bonding is based upon theoretical projected (integrated) and full density of states (DOS / iDOS) curves, plots of the (integrated) crystal orbital Hamilton populations (COHP / iCOHP),[33,34] band structures with fatband representations, and contour line diagrams of the Electron Localization Function (ELF).[35] To estimate the bonding strength between adjacent atoms the –iCOHP values at the Fermi level were taken, which represented covalent interaction between these atoms: positive values were considered as bonding, negative as anti-bonding. The results are given in Table 3.

Supporting Information (see footnote on the first page of this article): SEM images of $SrNi_2Si$ and $BaNi_2Si$ single crystals, PXRD of $SrNi_2Si$ and $BaNi_2Si$, DTA curves and corresponding PXRD of $AeNi_2E$ compounds (Ae = Ca, Sr, Ba; E = Si, Ge), COHP and −iCOHP curves for SrNi2Si and $BaNi_2Si$.

Results and Discussion

Crystal Structure of $SrNi_2Si$ and $BaNi_2Si$

$SrNi_2Si$ and $BaNi_2Si$ crystallize in the $BaNi_2Ge$-type[17] (space group *Pmmn*), an ordered variant of $TiCu_3$.[36] The structure (see Figure 1) consists of infinite in the *ab* plane corrugated polyanionic $[Ni_2Si]$ layers with Ni hexagons in a boat conformation and Si atoms centering these hexagons. These layers are stacked according to the primitive sequence *AA* along the *c* axis and separated by alkaline earth atoms. Lattice parameters for $SrNi_2Si$ and $BaNi_2Si$ are close to that of $BaNi_2Ge$ (Table 4). The *a* and *b* parameters are mainly influenced by covalent interactions within the $[Ni_2Si]$ layers and change only slightly (about 0.9 %) when substituting Sr with Ba. In turn, the substitution of Si by Ge (comparing $BaNi_2Si$

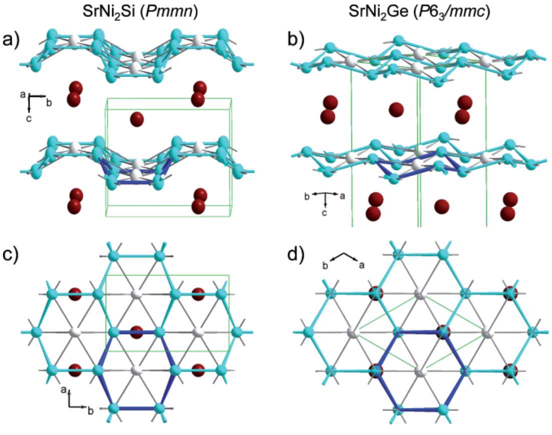

Figure 1. Crystal structures of $SrNi_2Si$ and $SrNi_2Ge$ [15]: (a) and (b) site view; (c) and (d) top view, respectively. Strontium, nickel, and silicon/germanium atoms are drawn in red, cyan blue, and white, respectively. The displacement ellipsoids for $SrNi_2Si$ (a, c) are shown at 90 % probability level. The Ni–Ni and Ni–Si bonds are emphasized in cyan blue and grey colors, respectively. One nickel hexagon is drawn in dark blue to emphasize the boat or chair conformation.

Table 4. Latice parameters and selected interatomic distances for $SrNi_2Si$, $BaNi_2Si$, and $BaNi_2Ge$[17] (space group *Pmmn*, $Z = 2$).

	a /Å	b /Å	c /Å	V /Å^3	d(Ni–Ni) /Å	d(Ni–E) /Å
$SrNi_2Si$	4.030	6.512	5.684	149.15	2.43–2.48	2.35–2.36
$BaNi_2Si$	4.068	6.580	5.976	159.97	2.44–2.49	2.37
$BaNi_2Ge$	4.157	6.694	5.950	165.56	2.48–2.52	2.42–2.43

with $BaNi_2Ge$) leads to an increase of the *a* and *b* parameters of about 1.9 % and 2.4 %, respectively. This is expected, since the size of the atoms and, respective, the lengths of Ni–Si bonds within the network are altered. On the other hand, the *c* parameter is more sensitive to the substitution of Sr by Ba (+5.2 %), whereas exchanging Si with Ge has almost no effect (+0.4 %).

To compare different structures in the $AeNi_2E$ family (Ae = Sr, Ba; E = Si, Ge) with boat conformation, the following bond lengths will be given as set of three, corresponding to $SrNi_2Si$/$BaNi_2Si$/$BaNi_2Ge$,[17] respectively. The structure contains two different Ni–Ni and Ni–E distances. Nickel hexagons have two pairs of nickel atoms in the boat deck plane with d_1(Ni–Ni) = 2.431(2)/2.438(2)/2.482 Å, linked by the two bridging nickel atoms above the deck plane, forming the "bow" and "stern" of the boat, with d_2(Ni–Ni) = 2.478(1)/2.489(1)/2.522 Å. The distances of the E to the deck Ni atoms are d_1(Ni–E) = 2.3530(6)/2.367(2)/2.422 Å and d_2(Ni–E) = 2.355(2)/2.3714(7)/2.428 Å to the bow or stern Ni atoms. In all three cases, the shortest distances occur between four nickel and the silicon/germanium atoms that are almost in the boat deck plane. They are shorter than the sum of the atomic radii of the elements (2.49, 2.42, and 2.47 Å for Ni–Ni, Ni–Si, and Ni–Ge, respectively),[37] suggesting that Ni–Ni and Ni–Si/Ge interactions play an important role in stabilizing the structure.

As already noticed, when discussing the lattice parameters, substitution of the p-element has a higher impact on the bonding situation within the Ni–E layers than substitution of the alkaline earth metal. However, the substitution of Sr by Ca[14] as well as the substitution of Si by Ge[15] in $SrNi_2Si$ leads to a different structure type with nickel atoms in a chair conformation.

The homologues $CaNi_2Si$[14] and $SrNi_2Ge$[15] (Figure 3) crystallize in the hexagonal $LiCu_2Sn$ type (space group $P6_3/mmc$),[16] Their structures contain polyanionic Ni_2E layers (E = Si, Ge), structurally closely related to that of the above discussed $BaNi_2Ge$-type, but with a chair conformation of corrugated Ni-6^3 net. It should be noted that in the $LiCu_2Sn$-type structure as well as in its representatives, such as $ErPt_2Sn$, $GdPt_2Sn$, $TbPt_2Sn$, $TmPt_2Sn$, YPt_2Sn, $DyPt_2In$, $GdPt_2In$, $HoPt_2In$, $TbPt_2In$, YPt_2In, $CePd_2In$, $LaPd_2In$, YPd_2Al, and YPd_2Zn,[38–40] the bonding pattern differs strongly: the T_2E layers (T = transition metals, E = p-elements) are interconnected into a 3D network, whereas in $CaNi_2Si$ and $SrNi_2Ge$ such layers have a very pronounced two-dimensional character.

The numbers of Ni and Si/Ge atoms coordinating the *Ae* atom are equal for both structures; the arrangement however differs, as shown in Figure 2. In the hexagonal $LiCu_2Sn$-type with chair conformation of Ni-6^3 nets, the *Ae* atom sits between the vertices (concave side) of two Ni nets. It is coordinated by six Si/Ge and eight Ni atoms. In the orthorhombic $BaNi_2Ge$-type with boat conformation, total number of coordinating atoms is the same, but only two E and two Ni atoms are above the *Ae* atom, remaining six nickel and four E atoms coordinate the *Ae* atoms below. In both modifications, nickel is linked to the three other nickel atoms, with almost similar angle values, and to three E atoms and four *Ae* atoms. Si/Ge atom is coordinated by six equidistant nickel atoms and by six *Ae* atoms.

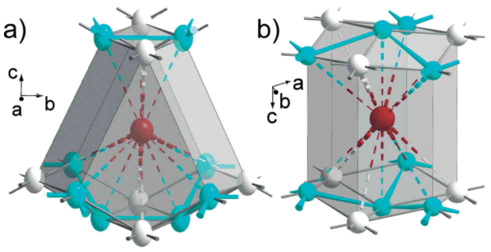

Figure 2. Coordination polyhedra of Sr atoms by Ni and Si or Ge in $SrNi_2Si$ (a) or $SrNi_2Ge$[15] (b) respectively. Strontium, nickel, and silicon/germanium atoms are drawn in red, cyan blue, and white, respectively. The displacement ellipsoids for $SrNi_2Si$ (a) are shown at 90 % probability level. The Ni–Ni and Ni–Si contacts are emphasized in cyan blue and grey colors, respectively, Sr–Ni and Sr–Ge/Si bonds are dashed and two-colored.

The tilting angle within the Ni net, which indicates the level of puckering, differs slightly between the chair and boat conformations: 126.38(5)/124.88(1)/127.27° for $SrNi_2Si$/$BaNi_2Si$/$BaNi_2Ge$ (*Pmmn*), whereas for $CaNi_2Si$ and $SrNi_2Ge$ ($P6_3/mmc$) these values are 127.29° and 133.54°, respectively. This indicates that nickel boats are slightly more corrugated than the nickel chairs.

Silicides and germanides start with the hexagonal modification and change to the orthorhombic one when going to the heavier homologues. This transition is found between Ca and Sr for the silicides and between Sr and Ba for the germanides and can be explained as following: The smaller *Ae* atoms in the $P6_3/mmc$ structure form planar 3^6 nets between the [Ni_2Si] layers, whereas bigger *Ae* in the *Pmmn* structure form puckered 3^6 nets. Obviously, the bigger cations in the planar close-packed 3^6 net require larger space, causing a stretching of the [Ni_2E] net in the *ab* plane. To a certain extent, such stretching can be compensated by the replacement of smaller Si by bigger Ge atoms in the center of the Ni^6 hexagons ($SrNi_2Ge$ crystallizes in hexagonal structure). However, since no further stretching is possible due to the strong interactions within the polyanionic Ni–E layers, the cationic 3^6 net become puckered, thereby causing boat conformation of the polyanions. Interestingly, the boundary between the two structure types can be defined as the ratio of the atomic radii $r(Ae)/r(E)$ of about 1.8 (Table 5). Numerous attempts to obtain $CaNi_2Ge$ have failed, most probably due to the small ratio $r(Ca)/r(Ge) = 1.61$, which cannot fulfill the necessary conditions of space filling.

Table 5. Ratio of the atomic radii $r(Ae)/r(E)$ (Ae = Ca, Sr, Ba; E = Si, Ge) [37] in $AeNi_2E$ (Ae = Ca, Sr, Ba, E = Si, Ge) and the space group of the corresponding compounds.

	Si	Ge
Ca	1.68 ($P6_3/mmc$)	(1.61)
Sr	1.83 ($Pmmn$)	1.76 ($P6_3/mmc$)
Ba	1.90 ($Pmmn$)	1.82 ($Pmmn$)

Well-known organic analogue of the Ni-6^3 net both conformations is cyclohexane. The chair conformation in cyclohexane is found, however, to be more energetically favorable than the boat conformation. The boat-corrugated layers in inorganic chemistry are rare, but can be found e.g. in semiconducting β-GeSe,[41] done by high-pressure high-temperature synthesis that is stable under ambient condition, whereas the α-GeSe with chair-corrugated layers can easily be obtained by heating of pure elements. Nice examples of the chair- and boat-corrugated layers are present in transition metal diborides.[42] The $AeNi_2E$ structures can be viewed as the filled (by E atoms) variants of corresponding diborides with the chair (ReB_2-type) or boat (RuB_2-type) conformations of boron-six-membered rings. Interestingly, in aluminum diboride (AlB_2-type) the boron six-membered rings are planar, that gives us hope for corresponding compounds with 2D planar Ni-6^3 layers, which like MgB_2 should be promising candidates as superconductors. Moreover, it cannot be excluded that Ni-6^3 corrugated layers of both conformations can exist as polymorphs in the $AeNi_2E$ compounds.

Thermal Analysis

In order to investigate the structural stability of all known compounds of the $AeNi_2E$ family, the title compounds $SrNi_2Si$ and $BaNi_2Si$ as well as $CaNi_2Si$, $SrNi_2Ge$, and $BaNi_2Ge$ were synthesized and investigated by differential thermal analysis (DTA). Powder X-ray diffractograms were measured before and after thermal analysis to investigate the changes in the composition of the samples (Figure S3, Supporting Information). Due to possible reactions of silicon or germanium with niobium container at higher temperatures, the upper limit was set to 960 °C. No melting temperature could be observed within this range. Samples in the hexagonal $LiCu_2Sn$-type (see Table 5) do not show any reversible signals. $CaNi_2Si$ does not show any significant peaks, whereas weak events around 710 °C (heating) and 450 °C (cooling) for $SrNi_2Ge$ are visible, which diminish however within the first cycles and may be caused by the presence of the small amounts of impurity. $BaNi_2Ge$ shows one exothermic signal at 554 °C, exclusively in the first heating cycle, and in the cooling cycles the weak signal at the same temperature as for $SrNi_2Ge$ (at 450 °C) can be seen, supporting the existence of impurity phases.

In contrast, both title silicides $SrNi_2Si$ and $BaNi_2Si$ ($BaNi_2Ge$-type structure) show endothermic (at 744 °C and 613 °C) and exothermic (at 737 °C and 531 °C) events upon heating and cooling, respectively (Figure S3d, f, Supporting Information). Since both compounds contain the same $Ni_{31}Si_{12}$ secondary phase, but the signals are at different temperatures, these peaks hint most probably to reversible structural phase transitions. Several attempts to obtain the high-temperature phases for both compounds by thermal quenching in water or liquid nitrogen were unsuccessful. Therefore, in situ temperature dependent powder X-ray diffraction experiments are highly required.

Electronic Structure Calculations

To understand the chemical bonding and the electronic structures of the two novel compounds $SrNi_2Si$ and $BaNi_2Si$, band-structure calculations were performed using the TB-LMTO-ASA method. As expected, similarities with the recently reported isostructural homologue $BaNi_2Ge$ are evident.[17] The band structures show pronounced anisotropic features with the bands crossing Fermi level only in the *ab* plane, as expected for two-dimensional structures (Figure 3).

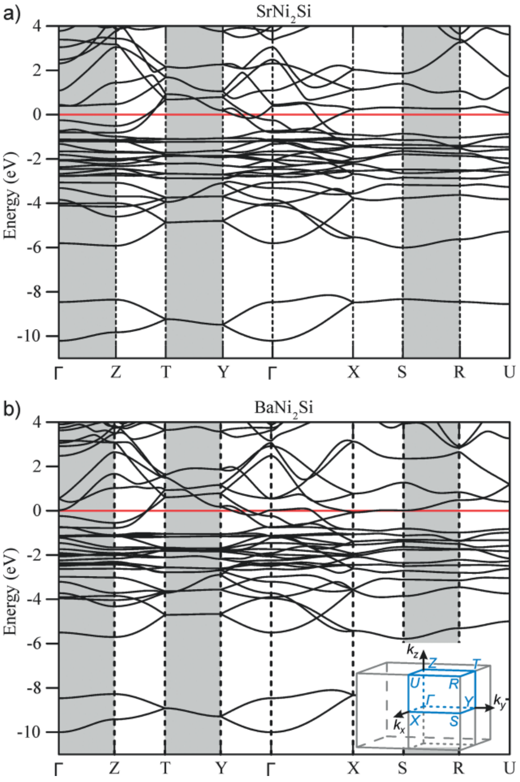

Figure 3. Band structure of (a) $SrNi_2Si$ and (b) $BaNi_2Si$. Directions perpendicular to the $[Ni_2Si]$ net (see Figure 1) are highlighted in grey. The inset shows the location of the special *k*-vector points of the asymmetric unit in reciprocal space. Bands are only crossing the Fermi level in the *ab* plane of the $[Ni_2Si]$ layer.

The DOS-plots and the contributions of the pDOS in both compounds (Figure 4) are remarkably similar and are split into two blocks clearly separated by a bandgap of 2 eV in both cases. The low-lying bands between –10 and –8 eV are predominantly Si-s states, with only minor contributions of the Ni-d and Sr/Ba-s,d orbitals. The sharp peak of the DOS indicates the presence of lone pairs at the Si atoms similar to the recently published *Ae*-Ni-*E* compounds (*Ae* = Ca, Sr, Ba; *E* = Si, Ge) with 2D polyanionic layers.[6,17,43–46] The first pseudogap for both compounds is observed at –3 eV. In the region from –6 to –3 eV the Si-p orbitals hybridize strongly with Ni-d and to a lesser extend with Sr/Ba-s,d orbitals, whereas the bands from –3 eV to Fermi level are predominantly Ni-d states. As seen from the plots of the band structure and total density of states (DOS), there is no bandgap at the Fermi level for both title compounds (Figure 3 and Figure 4). There is, however, a local minimum (pseudo-gap), which is more pronounced for $SrNi_2Si$. Because many bands still cross the Fermi level, the compounds are metallic.

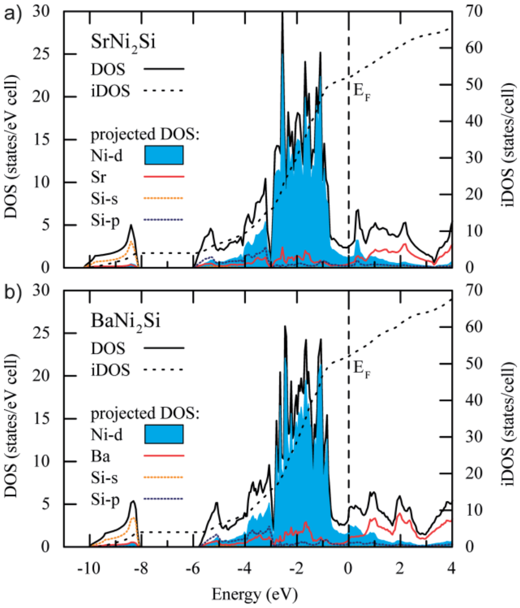

Figure 4. Total, projected, and integrated density of states (DOS, pDOS, and iDOS) plot of (a) $SrNi_2Si$ and (b) $BaNi_2Si$. The energy zero is taken at the Fermi level.

To check interactions between the atoms, crystal orbital Hamilton population analyses (COHP) were also evaluated (Figures S4 and S5, Supporting Information). The strongest bonding interactions (i.e. –iCOHP values) are found for the shortest Ni–Si contacts of both $SrNi_2Si$ and $BaNi_2Si$ compounds (Figure 5, Table 3). These values are in good accordance with those of the recently published $BaNi_2Ge$ compound; however, it is worth noting that for $SrNi_2Si$ the intralayer interactions are slightly stronger than in Ba compounds. Bonding orbitals of the Ni–Si interactions are almost filled and these bonds are nearly effectively optimized at the Fermi level. The Ni–Ni COHPs show that due to short interatomic distances along with the bonding also antibonding orbitals are filled at the Fermi level. The Ni–Ni interactions are weaker than Ni–Si bonds (see iCOHPs values in Table 3), but taking into account the location of the Ni-d orbitals near Fermi level, they play an important role for the structure stability. In contrast, the *Ae*–Ni and *Ae*–Si interactions (iCOHP values up to 0.45 eV per bond) are much weaker.

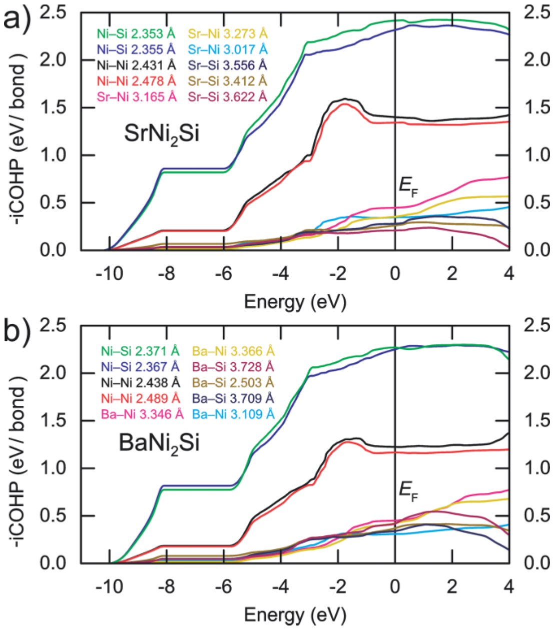

Figure 5. iCOHP curves for the different bonds in (a) $SrNi_2Si$ and (b) $BaNi_2Si$.

The bonding situation in $BaNi_2Si$ was further studied by a topological analysis of the electron density using the Electron Localization Function (ELF), as shown in Figure 6. The polyanionic layers are well separated in *c* direction by a low-electron density region (shown in dark blue), confirming two-dimensional character of the structure. There is one ELF attractor (1) with $\eta > 0.72$ oriented along the *z* axis towards the neighboring barium cations, which is associated with an electron lone pair on the Si atom. No ELF bisynaptic maxima were observed for the Ni–Si or Ni–Ni bonds directly between the respective atoms, even though relatively high –iCOHP values have been calculated. However, the second ELF maximum on the opposite side of the Si atom is split into two domains (2), which can be associated with polarized covalent Ni–Si bonds. Obviously, these ELF maxima are shifted towards the silicon atom as more electronegative element. The ELF maximum (3) between two neighboring Ni atoms, however, cannot be assigned to Ni–Ni bonds, since this slightly higher electronic density in *ab* plane is actually the remnant of two lone pairs (1) of Si atoms situated at the top and bottom of this section.

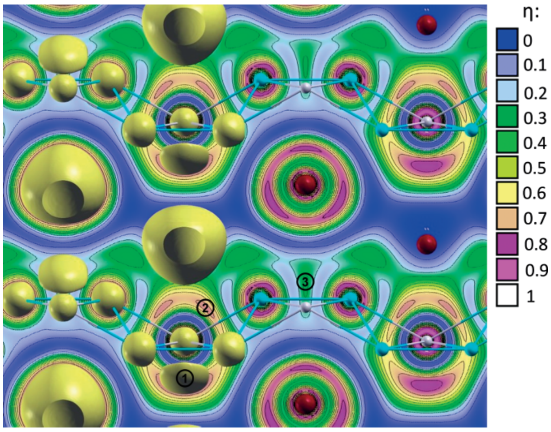

Figure 6. Topology of the ELF for $BaNi_2Si$ structure calculated from the all-electron density (TB-LMTO-ASA). 3D isosurface at $\eta > 0.72$ (left part) and 2D contour plots of the ELF in the *bc* plane (at $x = 0.25$) are shown. Barium, nickel, and silicon atoms are drawn in red, cyan blue, and white, respectively (right part).

Conclusions

Novel ternary intermetallic compounds $SrNi_2Si$ and $BaNi_2Si$ were synthesized and structurally characterized. The crystal structure contains $[Ni_2Si]$ polyanions with a pronounced two-dimensional character. Nickel-6^3 corrugated layers within the polyanions in $SrNi_2Si$, $BaNi_2Si$, and $BaNi_2Ge$ exhibit an uncommon boat conformation, whereas in the other two representatives of $AeNi_2E$ family $CaNi_2Si$ and $SrNi_2Ge$ a chair conformation of Ni-6^3 layers occurs. The dependence of the conformation of Ni layers on the ratio of the atomic radii $r(Ae)/r(E)$ can be traced in the family $AeNi_2E$ (Ae = Ca, Sr, Ba; E = Si, Ge). As shown by DTA investigations, the $SrNi_2Si$ and $BaNi_2Si$ compounds undergo most probably a reversible structural phase transition. However, future work should be devoted to the study of possible phase transitions by in-situ temperature dependent powder X-ray diffraction experiments and to a detailed description of the mechanism of chair-boat transformation within the Ni-6^3 net in $AeNi_2Si$ (Ae = Sr, Ba).

Acknowledgements

This research was financially supported by the German Research Foundation (Deutsche Forschungsgemeinschaft, DFG, Grant HL 62/3–1) and the TUM graduate school.

Keywords: Nickel silicide; Intermetallic compound; Nickel; Crystal structure; Boat conformation; Chemical bonding

References

[1] H. Hosono, A. Yamamoto, H. Hiramatsu, Y. Ma, *Mater. Today (Oxford, U.K.)* **2018**, *21*, 278–302.
[2] S. Jia, P. Jiramongkolchai, M. R. Suchomel, B. H. Toby, J. G. Checkelsky, N. P. Ong, R. J. Cava, *Nat. Phys.* **2011**, *7*, 207–210.
[3] V. Hlukhyy, A. V. Hoffmann, V. Grinenko, J. Scheiter, F. Hummel, D. Johrendt, T. F. Fässler, *Phys. Status Solidi B* **2017**, *254*, 1600351.
[4] J. Goodey, J. Mao, A. M. Guloy, *J. Am. Chem. Soc.* **2000**, *122*, 10478–10479.
[5] V. Hlukhyy, L. Siggelkow, T. F. Fässler, *Inorg. Chem.* **2013**, *52*, 6905–6915.
[6] V. Hlukhyy, N. Chumalo, V. Zaremba, T. F. Fässler, *Z. Anorg. Allg. Chem.* **2008**, *634*, 1249–1255.
[7] O. T. Bodak, E. I. Gladyshevskii, *Dopov. Akad. Nauk Ukr. RSR Ser. A: Fiz.-Tekh. Mater. Nauki* **1968**, *30*, 944–947.
[8] N. Nasir, N. Melnychenko-Koblyuk, A. Grytsiv, P. Rogl, G. Giester, J. Wosik, G. E. Nauer, *J. Solid State Chem.* **2010**, *183*, 565–574.
[9] U. Aydemir, C. Candolfi, A. Ormeci, H. Borrmann, U. Burkhardt, Y. Oztan, N. Oeschler, M. Baitinger, F. Steglich, Y. Grin, *Inorg. Chem.* **2012**, *51*, 4730–4741.
[10] M. Falmbigl, M. X. Chen, A. Grytsiv, P. Rogl, E. Royanian, H. Michor, E. Bauer, R. Podloucky, G. Giester, *Dalton Trans.* **2012**, *41*, 8839–8849.
[11] J. H. Roudebush, M. Orellana, S. Bux, T. Yi, S. M. Kauzlarich, *J. Solid State Chem.* **2012**, *192*, 102–108.
[12] G. Cordier, P. Woll, *J. Less-Common Met.* **1991**, *169*, 291–302.
[13] S. Pyon, K. Kudo, M. Nohara, *J. Phys. Soc. Jpn.* **2012**, *81*, 23702.
[14] J. Glaser, *Z. Anorg. Allg. Chem.* **2002**, *628*, 1946–1950.
[15] V. Hlukhyy, T. F. Fässler, *Z. Anorg. Allg. Chem.* **2008**, *634*, 2316–2322.
[16] P. I. Krypyakevych, G. I. Oleksiv, *Dopov. Akad. Nauk Ukr. RSR Ser. A: Fiz.-Tekh. Mater. Nauki* **1970**, 63–65.
[17] L. Siggelkow, V. Hlukhyy, T. F. Fässler, *Z. Anorg. Allg. Chem.* **2010**, *636*, 1870–1879.
[18] K. Frank, K. Schubert, *Acta Crystallogr., Sect. B: Struct. Crystallogr. Cryst. Chem.* **1971**, *27*, 916–920.
[19] P. E. Werner, L. Eriksson, M. Westdahl, *J. Appl. Crystallogr.* **1985**, *18*, 367–370.
[20] *WinXPOW*, Version 3.05, STOE & Cie GmbH, Darmstadt, Germany **2011**.
[21] *X-RED32*, Version 1.63.1, STOE & Cie GmbH, Darmstadt, Germany **2016**.
[22] *X-SHAPE*, Version 2.18, STOE & Cie GmbH, Darmstadt, Germany **2015**.
[23] G. M. Sheldrick, *SHELXS-2014*, Program for the Determination of Crystal Structure, University of Göttingen, Göttingen, Germany **2014**.
[24] G. M. Sheldrick, *Acta Crystallogr., Sect. A: Found. Crystallogr.* **2008**, *64*, 112–122.
[25] G. M. Sheldrick, *SHELXL-2014*, Program for Crystal Structure Refinement, University of Göttingen, Göttingen, Germany **2014**.
[26] G. M. Sheldrick, *Acta Crystallogr., Sect. C: Struct. Chem.* **2015**, *71*, 3–8.
[27] *NETZSCH Proteus Thermal Analysis*, Version 6.1.0, NETZSCH-Gerätebau GmbH, Selb, Germany **2016**.
[28] M. van Schilfgarde, T. A. Paxton, O. Jepsen, O. K. Andersen, *TB-LMTO-ASA*, Version 4.7, Stuttgart, Germany **1994**.
[29] R. W. Tank, O. Jepsen, O. K. Andersen, *The STUTTGART TB-LMTO-ASA program*, Stuttgart **1998**.
[30] U. v. Barth, L. Hedin, *J. Phys. C: Solid State Phys.* **1972**, *5*, 1629–1642.
[31] O. Jepsen, O. K. Andersen, *Z. Phys. B: Condens. Matter* **1995**, *97*, 35–47.
[32] W. R. L. Lambrecht, O. K. Andersen, *Phys. Rev. B* **1986**, *34*, 2439–2449.
[33] R. Dronskowski, P. E. Blöchl, *J. Phys. Chem.* **1993**, *97*, 8617–8624.
[34] F. Boucher, O. Jepsen, O. K. Andersen, *Supplement to the TB-LMTO-ASA (version 47) Program*, Stuttgart **1997**.
[35] A. Savin, R. Nesper, S. Wengert, T. F. Fässler, *Angew. Chem. Int. Ed. Engl.* **1997**, *36*, 1808–1832.

[36] N. Karlsson, *J. Inst. Met.* **1951**, *79*, 391–405.
[37] J. Emsley, *The Elements*, 3rd ed., Clarendon Press; Oxford University Press, Oxford, New York **2000**.
[38] D. B. de Mooij, K. H. J. Buschow, *J. Less-Common Met.* **1984**, *102*, 113–117.
[39] A. E. Dwight, *Mater. Res. Bull.* **1987**, *22*, 201–204.
[40] B. Gerke, U. C. Rodewald, R. Pöttgen, *Z. Anorg. Allg. Chem.* **2016**, *642*, 627–630.
[41] F. O. von Rohr, H. Ji, F. A. Cevallos, T. Gao, N. P. Ong, R. J. Cava, *J. Am. Chem. Soc.* **2017**, *139*, 2771–2777.
[42] M. Frotscher, M. Hoelzel, B. Albert, *ChemInform* **2010**, *41*.
[43] A. V. Hoffmann, V. Hlukhyy, T. F. Fässler, *Z. Anorg. Allg. Chem.* **2014**, *640*, 2882–2888.
[44] V. Hlukhyy, T. F. Fässler, *Z. Anorg. Allg. Chem.* **2010**, *636*, 100–107.
[45] L. Siggelkow, V. Hlukhyy, T. F. Fässler, *Z. Anorg. Allg. Chem.* **2011**, *637*, 2000–2006.
[46] V. Hlukhyy, D. Trots, T. F. Fässler, *Inorg. Chem.* **2017**, *56*, 1173–1185.

Received: December 7, 2018

Z. Anorg. Allg. Chem. **2018** · ISSN 0044–2313

SUPPORTING INFORMATION

Title: $SrNi_2Si$ and $BaNi_2Si$ – New Layered Silicides with Fused Nickel Six-membered Rings in a Boat Conformation
Author(s): T. Braun, S. Zeitz, V. Hlukhyy*
Ref. No.: z201800500

Supporting Information

$SrNi_2Si$ and $BaNi_2Si$ – new layered silicides with fused nickel six-membered-rings in a boat conformation

Thomas Braun, Sabine Zeitz, Viktor Hlukhyy

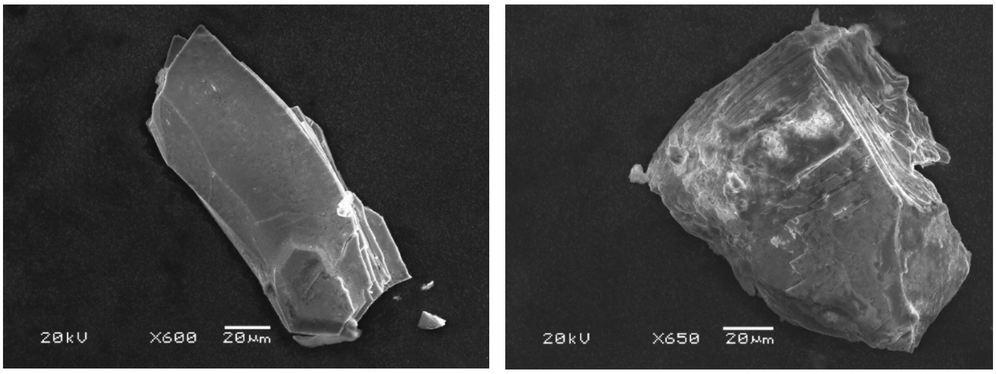

Figure S1. SEM images of the single crystals used for XRD and EDX measurements. Left: $SrNi_2Si$, right: $BaNi_2Si$.

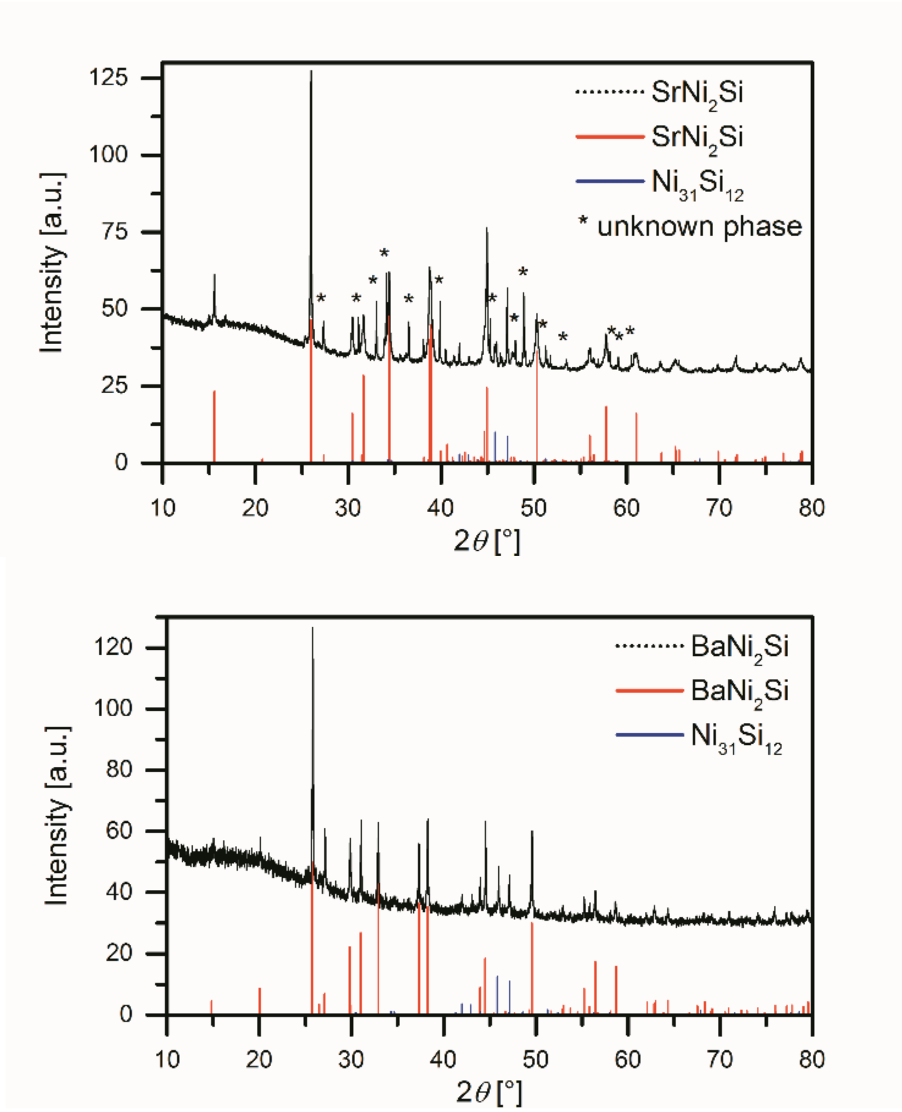

Figure S2: PXRD of $SrNi_2Si$ (top) and $BaNi_2Si$ (bottom). Diffraction patterns of the main and identified secondary phases were calculated and are drawn as bars.

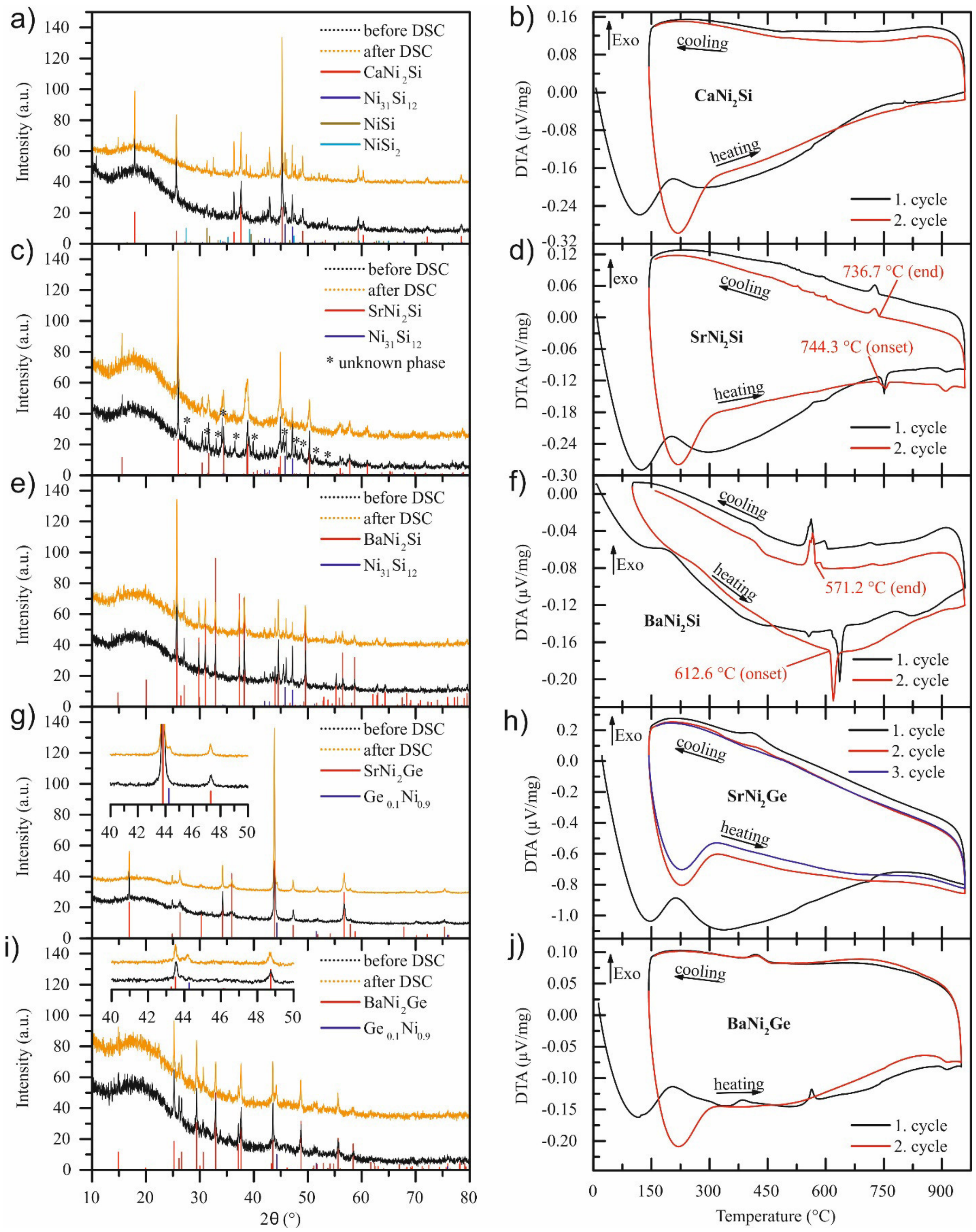

Figure S3. Left: PXRD before and after DTA measurements. Right: DTA measurement of the compounds in the *Ae*Ni$_2$Si compounds (*Ae* = Ca, Sr, Ba; *E* = Si, Ge)

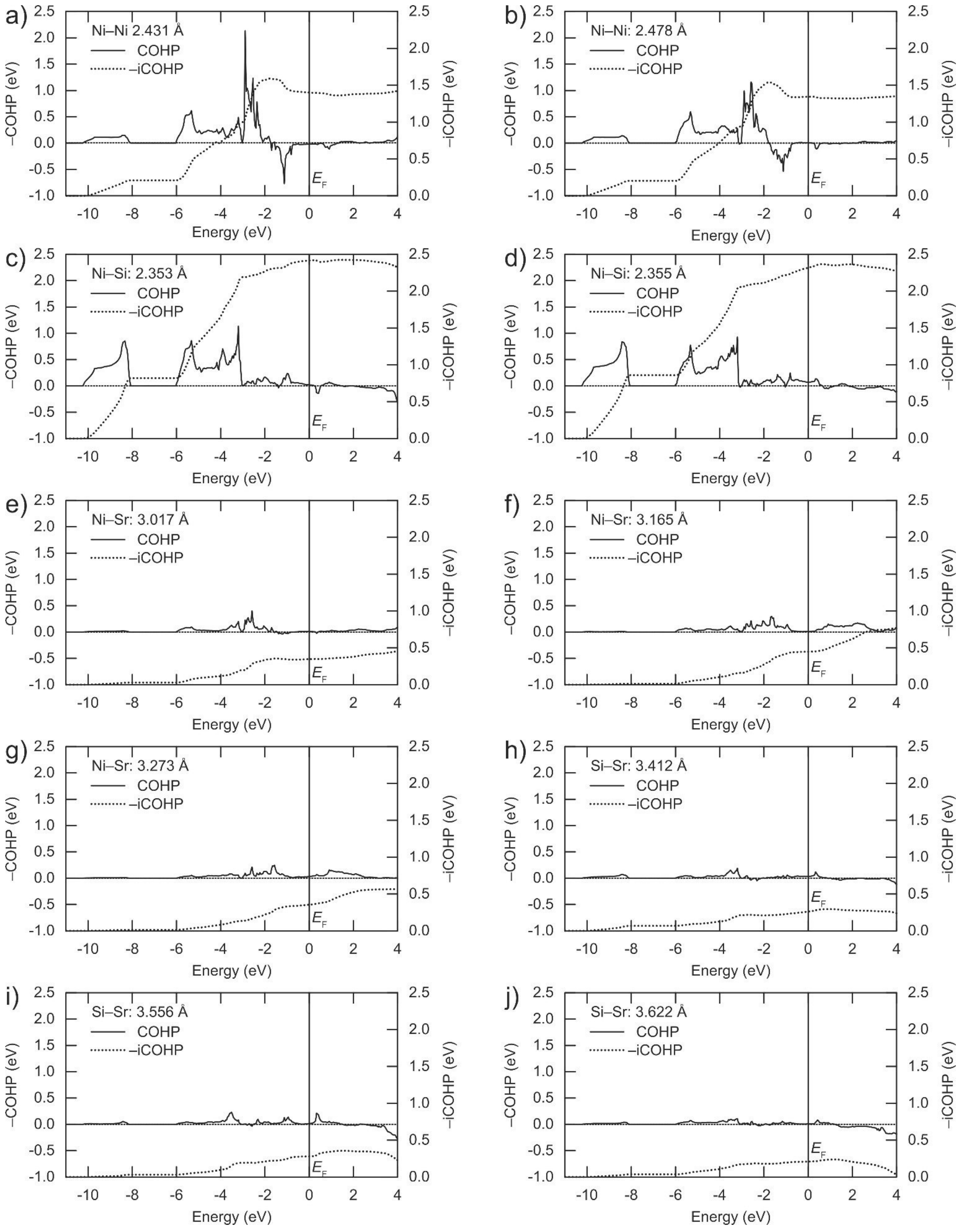

Figure S4. COHP and −iCOHP curves for the different bonds in the structures of $SrNi_2Si$

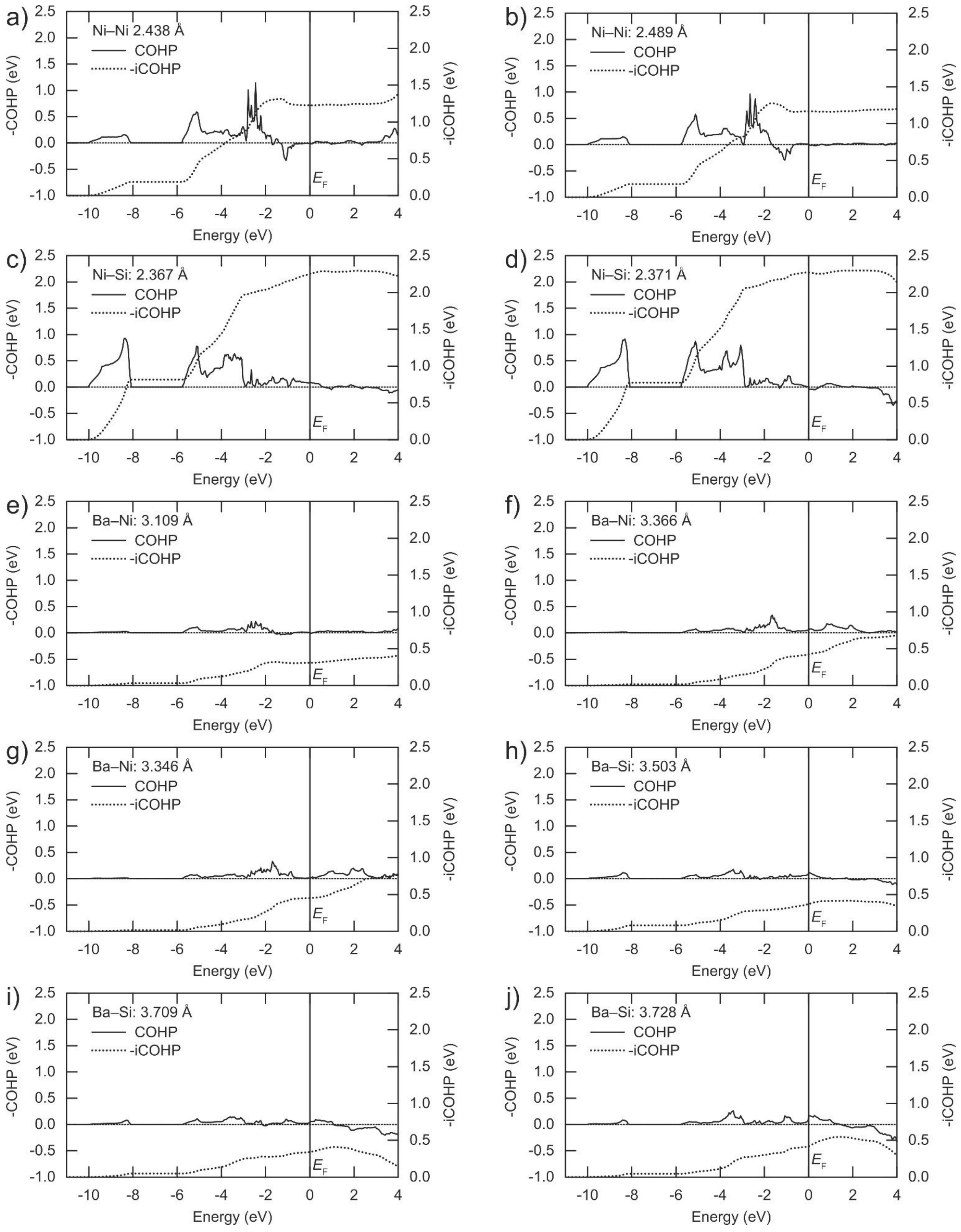

Figure S5. COHP and −iCOHP curves for the different bonds in the structures of $BaNi_2Si$

5.6 $SrNi_5Si_3$ – First Tetrelide with $LaCo_5P_3$-Type Structure

Braun, T.; Hlukhyy, V.

Manuscript for publication

$SrNi_5Si_3$ – First Tetrelide with $LaCo_5P_3$ -Type Structure

Thomas Braun, Viktor Hlukhyy[1]

Department of Chemistry, Technische Universität München, Lichtenbergstr. 4, 85747, Garching, Germany

Abstract

$SrNi_5Si_3$ has been prepared by arc-melting of stoichiometric mixture of the elements and subsequent annealing in induction furnace. It crystallizes with $LaCo_5P_3$-type, $Cmcm$, $Z = 4$, $a = 3.7251(1)$ Å, $b = 11.8705(2)$ Å and $c = 11.7177(2)$ Å, $V = 518.14(2)$ Å^3, $R_1 = 0.0109$, 412 F^2 values, 32 refineable parameters. Structural parameters have been investigated by single crystal and powder X-ray diffraction methods. Band structure and DOS were calculated with LMTO method. The structure contains polyanionic nickel-silicon framework with channels occupied by strontium. Framework itself can be constructed of distorted $Ni@Ni_6Si_6$ hexagonal prisms. It belongs to a larger compound family with metal:nonmetal ratio equal or close to 2:1.

Keywords: Polar Intermetallic Compound, Silicide, Ni-Si Prism

1. Introduction

Polar intermetallic compounds with nickel as d-metal are known for their structural variety. For example, more than 20 compounds with various structures have been found in the *Ae*-Ni-Ge systems, about half of them crystallize with own structural types: Mg_2Ni_3Ge [1], $Ca_2Ni_3Ge_2$ [2], $CaNi_5Ge_3$ [3], $Ca_7Ni_{49}Ge_{22}$ [3], $Ca_{15}Ni_{68}Ge_{37}$ [3], $Ca_5Ni_{17}Ge_8$ [4], SrNiGe [5], $BaNi_2Ge_2$ [6], $Ba_2Ni_5Ge_4$ [7]. In the case of equiatomic *Ae*NiGe (*Ae* = Mg, Ca, Sr, Ba) it has been shown that nickel and p-block elements form polyanionic substructures of one, two or three-dimensional character, depending on the size of earth alkali cations [5]. Generally, intermetallic systems R–T–X (R = alkaline or rare earth element, T = transition metal, X = Si, P, Ge, As) are characterized by a variety of compounds, especially in the region rich in transition metal with a ratio of metal ($R + T$):X, close to 2:1, the main structural motif of which is $X@T_6$ triangular trigonal prisms. As noted for example in [8], especially many such intermetallics are found in

---

[1] Corresponding author.

E-mail address: viktor.hlukhyy@tum.de (V. Hlukhyy)

the nickel based systems: $La_6Ni_2Si_3$, $La_5Ni_2Si_3$, $La_{15}Ni_7Si_{10}$ and $La_{21}Ni_{11}Si_{15}$, or $Th_2Ni_{12}P_7$, $Th_6Ni_{20}P_{13}$ and $Th_{12}Ni_{30}P_{21}$ [9,10].

Among strontium nickel silicides, $SrNi_{5.5}Si_{6.5}$, $SrNi_{9-x}Si_{4+x}$, (x = 2.5, 2.7), $SrNiSi_3$ and $SrNi_xSi_{2-x}$ ($0.1 \leq x \leq 0.7$) are known so far [11,12]. The last compound shows superconductivity up to T_C = 2.8 K for $0.1 \leq x \leq 0.3$ [13]. The search for new strontium nickel silicides as potential superconductors, lead to discovery of $SrNi_5Si_3$ ($LaCo_5P_3$-type). This compound is a new member of the RT_5X_3 family (R = rare-earth metal or U, T = transition metal, X = P, As, Ge, Si) [9]. Eight different structure types have been found within this 1:5:3 family: UCr_5P_3 ($P2_1/m$, $mP18$) [14], $LaCo_5P_3$ ($Cmcm$, $oS36$) [15], YCo_5P_3 ($Pnma$, $oP36$) [16], YNi_5Si_3 ($Pnma$, $oP36$) [17], UCo_5Si_3 ($P6_3/m$, $hP54$) [18], $CeNi_{5-x}P_3$ ($C2/m$, $mS71$) [19], $LaNi_5As_3$ ($Pnma$, $oP72$) [20], $SmRh_5Ge_3$ ($P6_3/m$, $hP108$) [21]. Most common are YCo_5P_3-type for pnictides and YNi_5Si_3 or UCu_5Si_3-type for tetrelides.

2. Experimental Section

2.1. Syntheses

A single crystal, which was used to identify title compound, was found in a polycrystalline sample with composition Sr:Ni:Si of 1:2:1 during the investigation of $SrNi_2Si$ [22] compound. A modified arc furnace (Mini Arc Melting System, MAM-1, Johanna Otto GmbH) with water-cooled copper hearth was used inside an argon-filled glove box. Pieces of strontium (ChemPur, 98%,), nickel wire (Alfa Aesar, 99.98%) and silicon (Alfa Aesar, 99.999%) were arc melted together and sealed in a welded tantalum ampoule. Subsequent annealing was performed via induction furnace (Hüttinger TIG 2.5/300) in water cooled sample space under dynamic argon atmosphere, heating to 1000 °C for 5 minutes, cooling down to circa 700 °C within 20 minutes, dwelling for 75 minutes and cooling to room temperature within 10 minutes. After identifying the novel phase, adjusted synthetic route has been performed in order to get bulk material. Elements were arc-melted with ratio Sr:Ni:Si of 1.02:5:3 to obtain $SrNi_5Si_3$ as main phase. To enhance homogeneity, the melting regulus was turned over and remelted two more times. The solid is hard and brittle with grey color and metallic luster. Obtained samples were stable under air.

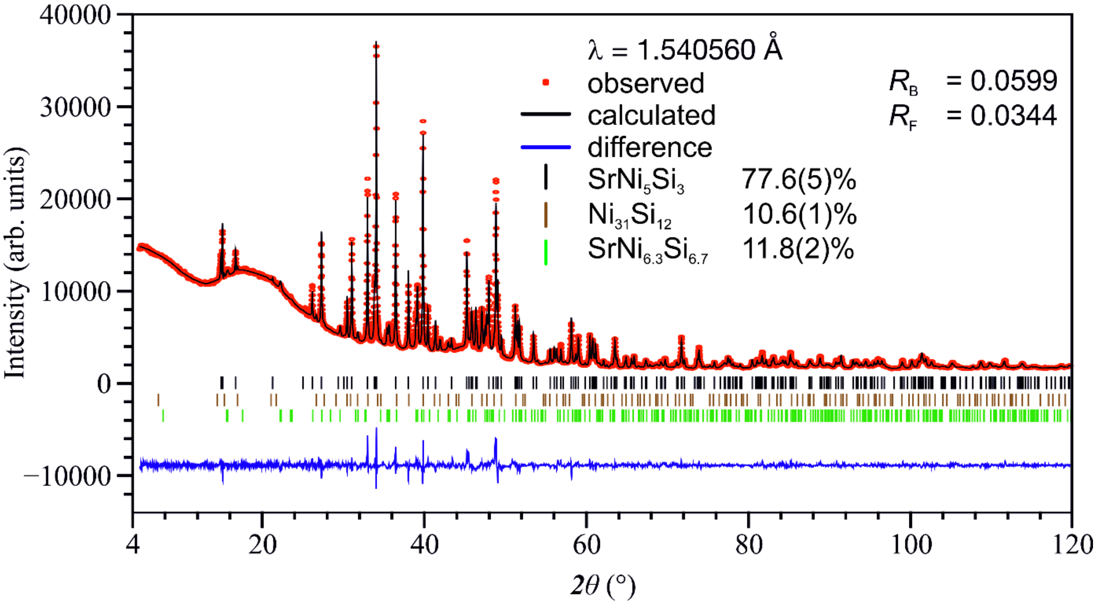

Figure 1 Powder X-Ray diffraction data measured with Cu-$K_{\alpha1}$ radiation. Rietveld refinement verifies $SrNi_5Si_3$ with $LaCo_5P_3$-structure as main phase.

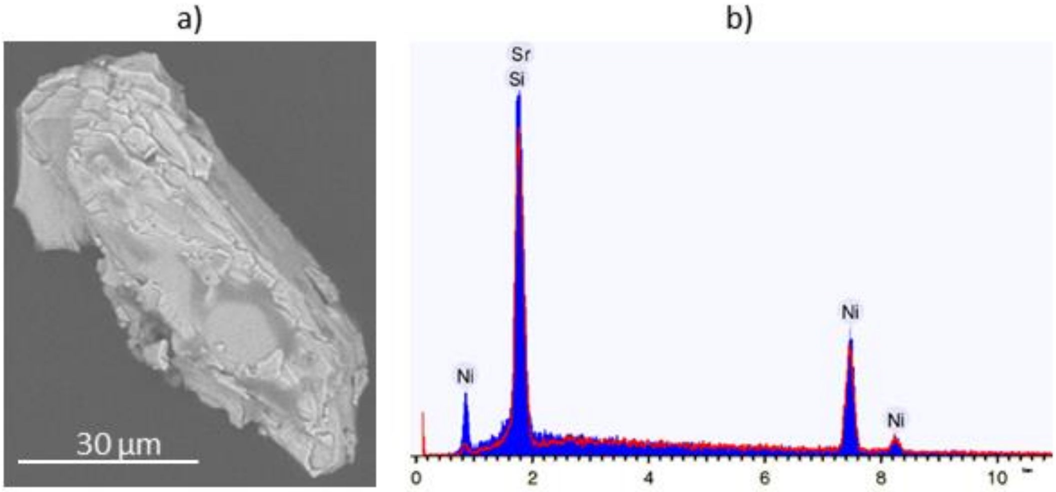

Figure 2 a) SEM image of the single crystal used for X-ray diffraction. b) SEM-EDX spectrum measured on the single crystal, confirming nickel, silicon and strontium, however with overlapping Si/Sr signals.

2.2. X-ray diffraction methods

Selected single crystal has been attached to a glass fiber with nail polish under microscope. Diffraction data were collected at room temperature by a STOE IPDS 2T (Bruker rotating anode, Mo-K_α, λ = 0.71073 Å, graphite monochromator) with image plate detector. Diffraction data were collected, integrated and corrected with the diffractometer software X-Area [23], including numerical absorption correction [24,25]. SHELXS-2014 [26,27] was used to obtain starting atomic parameters via direct methods. These were refined using SHELXL-2014 [28,29] with full-matrix least squares on F_O^2 with anisotropic atomic displacement parameters for all atoms. To check for the correct composition, occupancy parameters of both compounds were refined in a separate series of least-squares cycles, showing that all sites are fully occupied. The ideal occupancies were assumed in the last cycles. A final difference electron-density (Fourier) synthesis did not reveal any significant residual peaks (Table 1). Positional parameters and equivalent anisotropic displacement parameters are given in Table 2.

The single crystal was imaged into a HITACHI TM-1000 scanning electron microscope (SEM), applying 15 keV in high vacuum (Figure 2a) and energy dispersive x-ray (EDX) characterization performed. Due to overlapping X-ray energies of silicon and strontium with 1.740, 1.837 for silicon and 1.806, 1.871 for strontium, the exact ratio of Si:Sr could not be deduced. Nickel content of 60.5% is close to ideal 63.1%.

Phase analysis was done with powder X-ray diffractometer on a Stoe Stadi P (Cu-$K_{\alpha 1}$ source, $\lambda = 1.540598$ Å, DECTRIS MYTHEN 1K detector and curved Ge(111) monochromator). The sample was ground and powder fixed on a Scotch magic tape. External silicon was used for data correction. Rietveld-refinement was done with Fullprof suite [30]. The new compound $SrNi_5Si_3$ is the main phase with about 78 wt.-% and equally amounts of $Ni_{31}Si_{12}$ [31] and $SrNi_{6.3}Si_{6.7}$ [11] are present.

2.3. Electronic structure calculations

Self-consistent field calculations have been performed with Stuttgart-TB-LMTO-ASA software package, using the local density approximation (LDA) [32,33]. Linear muffin-tin orbitals (LMTOs) created with the atomic sphere approximation (ASA) including empty spheres. Radii of the spheres were determined after Jepsen and Andersen by blowing up spheres until volume filling is reached within limited allowed overlap [34,35]. Tight-binding model was used, constructing wave functions by superposition of wave functions from isolated atoms [36]. Inner shells are treated as soft-cores, higher quantum numbers down-folded [34] and all relativistic effects except spin-orbit coupling were included. The exchange-correlation term was parametrized after von Barth and Hedin [37]. Density of States (DOS) were calculated with the tetrahedron method [38]. As basis set, following orbitals have been used: Sr: s, d and down-folded p, f; Ni: s, p, d; Si, P and As: s, p and down-folded d.

Table 1. Crystal data and structure refinement of $SrNi_5Si_3$ with $LaCo_5P_3$-type model. The lattice parameter were taken from powder Rietveld analysis

empirical formula	$SrNi_5Si_3$
formula weight (g mol^{-1})	465.44
temperature (K)	293
crystal system	orthorhombic
space group	*Cmcm*
unit cell dimensions (from powder data)	
a (Å) *b* (Å) c (Å)	3.7251(1) 11.8705(2) 11.7177(2)
volume (Å^3)	518.14(2)
Z	4
ρ_{calcd} (g cm^{-3})	5.97
μ (mm^{-1})	28.548
F(000)	880
crystal size (mm^3)	0.07×0.03×0.02
theta range for data collection (°)	3.4 – 29.1
index ranges in *hkl*	± 5, ± 16, ± 16
reflections collected	4749
independent reflections	412 (R_{int} = 0.019)
Reflections with $I \geq 2\sigma(I)$	358 (R_{sigma} = 0.041)
data/restraints/parameters	412/0/32
goodness-of-fit on F^2	0.943
final *R* indices ($I > 2\sigma(I)$)	R_1 = 0.0109, wR_2 = 0.0195
R indices (all data)	R_1 = 0.0167, wR_2 = 0.0201
Extinction coefficient	0.0017(1)
largest diff. peak and hole (e·Å^{-3})	0.42, −0.51

Table 2. Atomic coordinates and equivalent isotropic displacement parameter of $SrNi_5Si_3$ (*Cmcm*, *Z* = 4).

Atom	Site	*x/a*	*y/b*	*z/c*	$U_{eq}{}^{*}$ /$10^{-3} \cdot Å^2$
Sr1	4*c*	0	0.83309(3)	¼	6.8(1)
Ni1	4*c*	0	0	0	6.9(1)
Ni2	8*f*	0	0.55213(3)	0.14470(3)	6.4(1)
Ni3	8*f*	0	0.19529(3)	0.06352(3)	6.3(1)
Si1	8*f*	0	0.38306(6)	0.03713(6)	5.2(2)
Si2	4*c*	0	0.10536(9)	¼	7.2(2)

* U_{eq} is defined as one third of the trace of the orthogonalized *Uij* tensor.

3. Results

3.1. Crystal Structure

$SrNi_5Si_3$ crystallizes with $LaCo_5P_3$-type (Figure 4), which is one member of several structure types with general formula RT_5X_3 (*R* = alkaline or rare earth element, *T* = transition metal, *X* = Si, P, Ge, As. With the exception of UFe_5Si_3 [39] and $CaNi_5Ge_3$ [3] that represent an intergrowth of $ThCr_2Si_2$- and Cu_3Au-type, these types have a common structural motif: all atoms are situated in two planar layers with *AB* stacking; the *R* and *X* atoms on one layer are surrounded by *T* atoms on adjacent layers and form RT_6X_3 units (Figure 3i), that are linked via shared edges [20]. These units are well common for a compounds with metal (*R* + *T*) to nonmetal (*X*) ratio being exactly or close to 2:1 [40–42]. Figure 3 shows the different kinds of arrangement found for 153-compounds: UCr_5P_3 ($P12_1/m1$, *mP*18) [14], $LaCo_5P_3$ (*Cmcm*, *oS*36) [15], YCo_5P_3 (*Pnma*, *oP*36) [16], YNi_5Si_3 (*Pnma*, *oP*36) [17], UCo_5Si_3 ($P6_3/m$, *hP*54) [18], $CeNi_{5-x}P_3$ (*C*12/*m*1, *mS*71) [19], $LaNi_5As_3$ (*Pnma*, *oP*72) [20] and $SmRh_5Ge_3$ ($P6_3/m$, *hP*108) [21]. $LaCo_5P_3$-type has highest symmetry with only 6 atoms in the asymmetric unit. $SrNi_5Si_3$ is the first representative of $LaCo_5P_3$-type containing a tetrel element. This is remarkable since with the exception of $TbMn_5Ge_3$, which adopts YCo_5P_3-type, no other representative of the structure type was obtained with *X* substituted by an element from the other group.

$SrNi_5Si_3$ consists of a three-dimensional nickel silicide framework that forms parallel channels in *a*-direction. These channels are occupied by strontium atoms. The coordination of Ni1 is shown in Figure 4b. Nickel is the center of a distorted hexagonal N_6Si_6-prism. Two silicon atoms are shared by two polyhedra and has a larger distance to the central atom, forming zigzag-chains. These chains are stacked along a direction via common faces to sheets. Adjacent zigzag sheets are linked via nickel–nickel and nickel–silicon bonds. Every second sheet is shifted by *a*/2 along *a*-direction. Besides other compounds with $LaCo_5P_3$-type, such Ni@Ni_6X_6-polyhedra have been found in e.g. $SrNi_3Ge_2$ and $Ba_2Ni_5Ge_4$ [7,43].

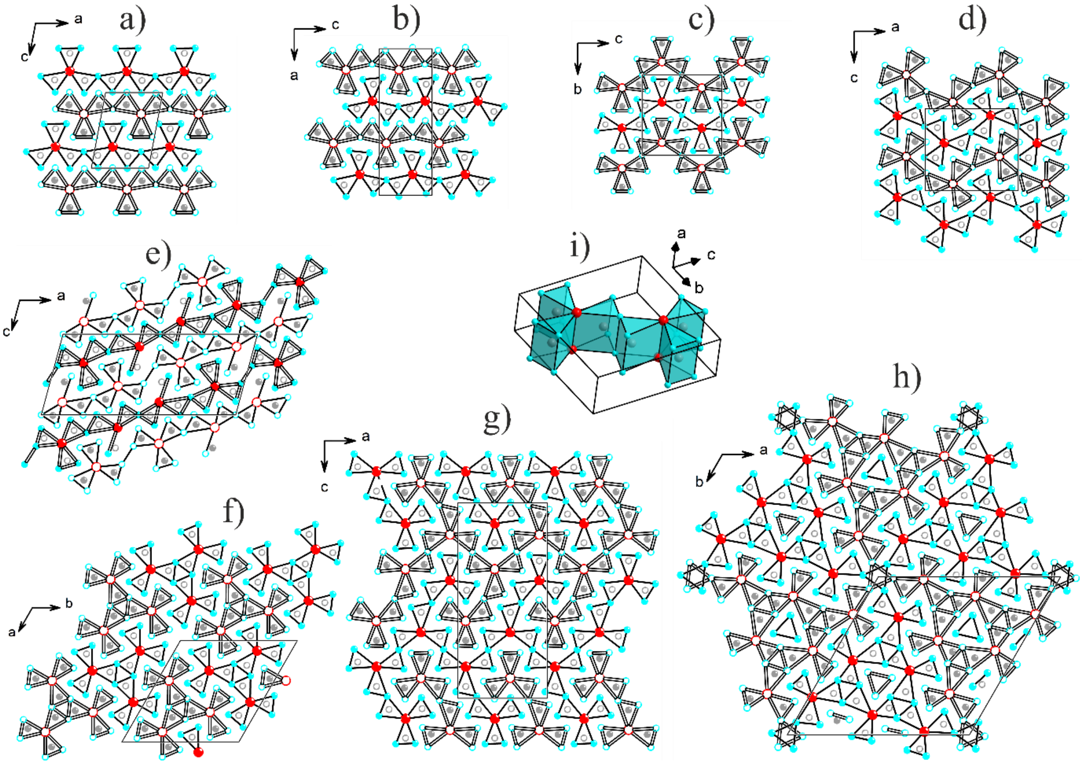

Figure 3 Different arrangements of simple RT_5X_3-compounds. a) UCr_5P_3, b) YNi_5Si_3, c) $LaCo_5P_3$, d) YCo_5P_3, e) $CeNi_{4.57}P_3$, f) UCo_5Si_3, g) $LaNi_5As_3$ and h) $SmRh_5Ge_3$. i) section of $LaCo_5P_3$ with two linked RT_6X_3-units. Cations are red, transition metals cyan blue and main group elements in grey. *T*–*T*-bonds and *R*–*T*-bonds are drawn to illustrate RT_6X_3-units. Atoms and bonds on layers shifted by half a unit cell perpendicular to the paper plane are represented hollow.

Distance between strontium atoms of 3.7251(1) Å corresponds to the shortest unit cell parameter. It is shorter than in elemental, close-packed strontium metal with 4.3 Å. The Sr–Si- and Sr–Ni-distances vary from 3.1690(6) Å to 3.2828(1) Å and 3.3045(3) Å to 3.4281(2) Å respectively. Strontium–nickel contacts are slightly shorter and strontium–silicon contacts close to the sum of elemental radii (3.33 Å and 3.40 Å, respectively). The nickel–nickel distances range between 2.4347(4) Å and 2.7152(4) Å (2.492 Å in elemental nickel). The Si–Si-distances of 2.909(1) Å are much larger than in elemental silicon with 2.352 Å. The silicon atoms are well separated by a Ni–Ni-substructure. The Ni–Si-distances range from 2.2503(8) Å to 2.4319(6) Å and are almost smaller than the sum of the atomic radii (2.422 Å), indicating covalent Ni–Si-bonds. The Ni–Si distance of 3.1852(4) Å can be found between central nickel of hexagonal Ni@Ni_6X_6 prism and the Si-vertex that is shared by two linked polyhedra.

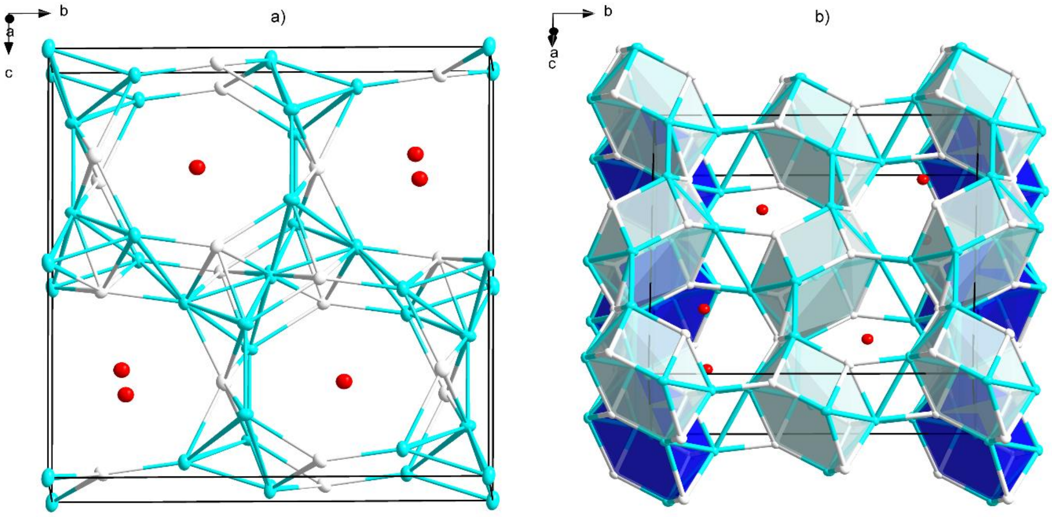

Figure 4 Crystal structure of $SrNi_5Si_3$ (Sr – red, Ni – cyan, Si – white, thermal ellipsoids with 90% probability), two-colored bonds are drawn between Ni–Ni and Si–Si. a) The polyanionic $^3_\infty[Ni_5Si_3]$-framework. b) Hexagonal prisms as coordination polyhedra Ni1@Ni_6Si_6 that form face-sharing chains and are linked via Si to vertex-sharing zigzag-layers. The layers are interconnected via additional Ni–Ni and Ni–Si-bonds. For better visibility, the subjacent polyhedral are blue tinted.

According to the Inorganic Crystal Structure Database [9] $LaCo_5P_3$ is an orthorhombic structure type, so far with 7 representatives: $LaCo_5P_3$, $LaNi_5P_3$, $EuNi_5P_3$, $EuNi_5As_3$, $SrNi_5As_3$, $SrNi_5P_3$ and $YbNi_5P_3$. The tetrelides RT_5Tt_3 (R = rare earth, U; T = d^{10} transition metal; Tt = tetrelide) generally adopt orthorhombic YNi_5Si_3-type structure, with only one exception: $SmPt_5Si_3$, which adopts the UCo_5Si_3-type that is formed by cobalt or rhodium silicides. The heavier rhodium germanides $SmRh_5Ge_3$, $GdRh_5Ge_3$ and $TbRh_5Ge_3$ make their own type. YCo_5P_3-type is formed by most of phosphide and arsenide homologues with cobalt, iron or manganese. $TbMn_5Ge_3$ is the only tetrelide, which has been reported with YCo_5P_3-structure. Few compounds have been found with UCr_5P_3-type: UCr_5P_3, $ZrCr_5P_3$, $CaFe_5As_3$, UV_5P_3 and $SrAu_{3.36}In_{4.64}$. Most interesting are nickel phosphides and arsenides RNi_5X_3 (R = Ca, Sr, La, Eu, Yb; X = P, As). Peculiar structures are formed in $CeNi_{4.85}P_3$, $LaNi_5As_3$ and $CaNi_5Ge_3$. The last as well as $HoZn_5Al_3$ and UFe_5Si_3 make completely different structure types that do not fit the general scheme illustrated in Figure 3. The remaining RNi_5X_3 compounds crystallize with $LaCo_5P_3$-type (also sometimes called $SrNi_5P_3$-type).

It can be summarized that while UCr_5P_3-type and YCo_5P_3-type are flexible on the transition metal, YNi_5Si_3-type and $SrNi_5P_3$-type compounds are formed almost exclusively with d^{10}-metals and UCo_5Si_3-type with d^9. This indicates that for the structure the valence electron concentration is primarily responsible. However whereas YNi_5Si_3-type exists with silicon and germanium, UCo_5Si_3-type is found exclusively with silicon and forms $SmRh_5Ge_3$-type upon substitution. For $SrNi_5P_3$-type, in some cases, the substitution is tolerated ($SrNi_5P_3$, $SrNi_5As_3$, $EuNi_5P_3$, $EuNi_5As_3$ and even $LaCo_5P_3$) but $CeNi_{4.85}P_3$ and $LaNi_5As_3$ leads to new structure types, whereas $LaCo_5P_3$ would be expected to adopt YCo_5P_3-type. Here the dependence does not follow an easy trend. The compound reported in this work, $SrNi_5Si_3$ is the first tetrelide with $SrNi_5P_3$-type atomic arrangement.

There are also other compounds where the replacement of pnicitide with tetrelide does not change the structure. Examples are plenty of compounds with $ThCr_2Si_2$-type [9] and $RERh_6Ge_4$ [8,44] (RE = rare earth). Basically, these compounds occur in the region rich in transition metal, i.e. away from electronically balanced compounds (Zintl phases) and closer to typical intermetallics, where the atomic size plays a greater role in the formation of the structure compared to the electron concentration. This is a confirmation of the general trend observed in going from the Zintl phases through the Hume-Rothery phase to the Laves phases.

With respect to superconducting $SrNi_xSi_{2-x}$ [13], a polycrystalline sample of $SrNi_5Si_3$ was investigated in a MPMS 5XL magnetometer by Quantum Design. No hints of superconductivity were observed.

3.2. Electronic Structure

Electronic structure calculations have been perfomed for $SrNi_5Si_3$ as well as for isostructural homologues $SrNi_5P_3$ and $SrNi_5As_3$ on basis of reported data [42] and are given in Figure 5. General shape of the density of states (DOS) curve is quite similar which is expected for similar structures according to the rigid-band model. Most remarkable is shape and position of a small block mainly containing s-orbitals of the tetrel or pentel element and separated from the other states by a gap of 2 to 3 eV. For silicon it is located between −12 and −8 eV and comparably flat. For phosphorous and arsenic, it is shifted to lower energies between −14 and −12 eV. In contrast to the silicide, a peak around −11 eV is caused by relatively flat bands, that are most likely related to the additional valence electrons that are located in lone pairs. The other block is dominated by Ni-d-states between 2 and −4 eV, crossing the Fermi level. Thus metallic behavior is expected for all three compounds. In addition to nickel, the block also contains p-orbitals of the p-block element and some strontium-states. The region between −4 and −6 eV shows a stronger hybridization of nickel and pentel element than in comparison with silicon. Figure 5d compares all three DOS, near the Fermi level no significant difference occurs upon substitution of pentel with tetrel element. Thus, electronic structures are in agreement with the crystal structural similarities of the three structures. And, as can be seen, the X-element does not play a decisive role in structural stability of this type.

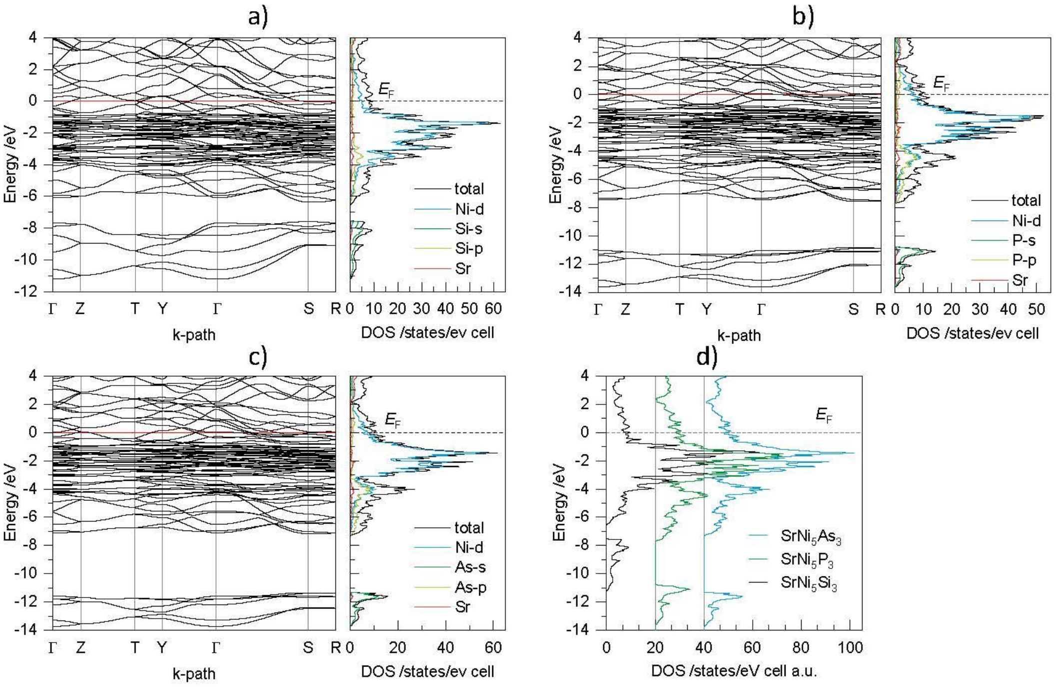

Figure 5 LMTO calculations of band structure and density of states (DOS) and projected DOS for a) $SrNi_5Si_3$, b) $SrNi_5P_3$ and c) $SrNi_5As_3$. Comparison of the DOS is given in d) with zero-line drawn for all three curves.

4. Conclusion

In the 1:5:3 structural family that is well investigated for rare earth elements and few alkaline earth compounds, $SrNi_5Si_3$ is a new member with $LaCo_5P_3$-type. It did not adopt the structure of homologous tetrelides YNi_5Si_3, UFe_5Si_3, UCo_5Si_3, $CaNi_5Ge_3$ or $SmRh_5Ge_3$. $SrNi_5Si_3$ being isostructural to $SrNi_5P_3$ and $SrNi_5As_3$ instead emphasizes the diagonal by the relationship between arsenic and silicon. This compound gives evidence that the formation of to $LaCo_5P_3$ instead of YCo_5P_3-type or YNi_5Si_3-type for strontium, lanthanum and europium variants is most likely caused by the atom's size and not number of electrons, especially from *X*-element that was confirmed by electronic structure calculations.

5. Acknowledgments

This research was financially supported by the German Research Foundation (Deutsche Forschungsgemeinschaft, DFG, Grant HL 62/3-1) and the TUM Graduate School.

6. References

[1] L. Siggelkow, V. Hlukhyy, T.F. Fässler, *Z. Anorg. Allg. Chem.* **2017**, *643*, 1424–1430, https://doi.org/10.1002/zaac.201700180.

[2] V. Hlukhyy, T.F. Fässler, *Z. Anorg. Allg. Chem.* **2010**, *636*, 100–107, https://doi.org/10.1002/zaac.200900487.

[3] L. Siggelkow, V. Hlukhyy, B. Wahl, T.F. Fässler, *Eur. J. Inorg. Chem.* **2011**, *2011*, 4012–4024, https://doi.org/10.1002/ejic.201100347.

[4] V. Hlukhyy, L. Siggelkow, T.F. Fässler, *Z. Anorg. Allg. Chem.* **2012**, *638*, 2029–2034, https://doi.org/10.1002/zaac.201200118.

[5] V. Hlukhyy, L. Siggelkow, T.F. Fässler, *Inorg. Chem.* **2013**, *52*, 6905–6915, https://doi.org/10.1021/ic302681t.

[6] V. Hlukhyy, D. Trots, T.F. Fässler, *Inorg. Chem.* **2017**, *56*, 1173–1185, https://doi.org/10.1021/acs.inorgchem.6b02190.

[7] L. Siggelkow, V. Hlukhyy, T.F. Fässler, *Z. Anorg. Allg. Chem.* **2011**, *637*, 2000–2006, https://doi.org/10.1002/zaac.201100306.

[8] D. Voßwinkel, O. Niehaus, R. Pöttgen, *Z. Anorg. Allg. Chem.* **2013**, *639*, 2623–2630, https://doi.org/10.1002/zaac.201300369.

[9] FIZ Karlsruhe, ICSD: Inorganic Crystal Structure Database, Leibniz Institute for Information Infrastructure, Karlsruhe, Germany, 2022.

[10] Y.M. Prots, W. Jeitschko, *Inorg. Chem.* **1998**, *37*, 5431–5438, https://doi.org/10.1021/ic980397w.

[11] N. Nasir, N. Melnychenko-Koblyuk, A. Grytsiv, P. Rogl, G. Giester, J. Wosik, G.E. Nauer, *J. Solid State Chem.* **2010**, *183*, 565–574, https://doi.org/10.1016/j.jssc.2009.12.023.

[12] O.T. Bodak, E.I. Gladyshevskii, *Dopov. Akad. Nauk Ukr. RSR, Ser. A: Fiz.-Tekh. Mat. Nauki* **1968**, *30*, 944–947.

[13] S. Pyon, K. Kudo, M. Nohara, *J. Phys. Soc. Jpn.* **2012**, *81*, 23702, https://doi.org/10.1143/JPSJ.81.023702.

[14] W. Jeitschko, R. Brink, P.G. Pollmeier, *Z. Naturforsch., B: J. Chem. Sci.* **1993**, *48*, 52–57, https://doi.org/10.1515/znb-1993-0113.

[15] V.N. Davydov, Y.B. Kuz'ma, *Dopov. Akad. Nauk Ukr. RSR, Ser. A: Fiz.-Tekh. Mat. Nauki* **1981**, *1*, 81–84.

[16] U. Meisen, W. Jeitschko, *Z. Kristallogr.* **1984**, *167*, 135–143, https://doi.org/10.1524/zkri.1984.167.1-2.135.

[17] L.G. Akselrud, V.I. Yarovets, O.I. Bodak, Y.P. Yarmolyuk, E.I. Gladyshevskii, *Sov. Phys. Crystallogr.* **1976**, *21*, 210–211.

[18] V.G. Terziev, *Sov. Phys. Crystallogr.* **1978**, *23*, 531–533.

[19] V.S. Babizhet'sky, S.V. Orishchin, S.I. Chikhrii, Y. Kuz'ma, *Sov. Phys. Crystallogr.* **1992**, *37*, 1024–2026.

[20] V. Babizhetskyy, R. Guérin, A. Simon, *Z. Naturforsch., B: J. Chem. Sci.* **2004**, *59*, 1103–1108, https://doi.org/10.1515/znb-2004-1004.

[21] A.V. Morozkin, A.E. Bogdanov, R. Welter, *J. Alloys Compd.* **2002**, *340*, 49–53, https://doi.org/10.1016/S0925-8388(02)00045-2.

[22] T. Braun, S. Zeitz, V. Hlukhyy, *Z. Anorg. Allg. Chem.* **2019**, *645*, 388–395, https://doi.org/10.1002/zaac.201800500.

[23] X-Area, STOE & Cie GmbH, Darmstadt, Germany, 2015.

[24] X-RED32, STOE & Cie GmbH, Darmstadt, Germany, 2016.

[25] X-SHAPE, STOE & Cie GmbH, Darmstadt, Germany, 2015.

[26] G.M. Sheldrick, SHELXS-2014: Program for the Determination of Crystal Structure, University of Göttingen, Göttingen, Germany, 2014.

[27] G.M. Sheldrick, *Acta Crystallogr., Sect. A: Found. Crystallogr.* **2008**, *64*, 112–122, https://doi.org/10.1107/S0108767307043930.

[28] G.M. Sheldrick, SHELXL-2014: Program for Crystal Structure Refinement, University of Göttingen, Göttingen, Germany, 2014.

[29] G.M. Sheldrick, *Acta Crystallogr., Sect. C: Struct. Chem.* **2015**, *71*, 3–8, https://doi.org/10.1107/S2053229614024218.

[30] J. Rodriguez-Carvajal, FullProf: A Program for Rietveld Refinement and Pattern Matching Analysis. At the Satellite Meeting on Powder Diffraction of the XV IUCr Congress, Toulouse, France, 1990.

[31] K. Frank, K. Schubert, *Acta Crystallogr., Sect. B: Struct. Crystallogr. Cryst. Chem.* **1971**, *27*, 916–920, https://doi.org/10.1107/S0567740871003261.

[32] R.W. Tank, O. Jepsen, O.K. Andersen, The STUTTGART TB-LMTO-ASA program, Stuttgart, 1998.

[33] M. van Schilfgarde, T.A. Paxton, O. Jepsen, O.K. Andersen, TB-LMTO-ASA, Stuttgart, Germany, 1994.

[34] O. Jepsen, O.K. Andersen, *Z. Phys. B: Condens. Matter* **1995**, *97*, 35–47, https://doi.org/10.1007/BF01317585.

[35] O.K. Andersen, O. Jepsen, *Phys. Rev. Lett.* **1984**, *53*, 2571–2574, https://doi.org/10.1103/PhysRevLett.53.2571.

[36] W.R.L. Lambrecht, O.K. Andersen, *Phys. Rev. B* **1986**, *34*, 2439–2449, https://doi.org/10.1103/PhysRevB.34.2439.

[37] U.v. Barth, L. Hedin, *J. Phys. C: Solid State Phys.* **1972**, *5*, 1629–1642, https://doi.org/10.1088/0022-3719/5/13/012.

[38] P.E. Blöchl, O. Jepsen, O.K. Andersen, *Phys. Rev. B, Condens. Matter* **1994**, *49*, 16223–16233, https://doi.org/10.1103/physrevb.49.16223.

[39] D. Berthebaud, A.P. Gonçalves, O. Tougait, M. Potel, E.B. Lopes, H. Noël, *Chem. Mater.* **2007**, *19*, 3441–3447, https://doi.org/10.1021/cm070943w.

[40] W. Jeitschko, J.H. Albering, R. Brink, U. Jakubowski-Ripke, E.J. Reinbold, *Z. Anorg. Allg. Chem.* **2014**, *640*, 2449–2457, https://doi.org/10.1002/zaac.201400267.

[41] J.-Y. Pivan, R. Gue´rin, M. Sergent, *J. Solid State Chem.* **1987**, *68*, 11–21, https://doi.org/10.1016/0022-4596(87)90279-9.

[42] H. Probst, A. Mewis, *Z. Anorg. Allg. Chem.* **1991**, *597*, 173–182, https://doi.org/10.1002/zaac.19915970120.

[43] V. Hlukhyy, T.F. Fässler, *Z. Anorg. Allg. Chem.* **2008**, *634*, 2316–2322, https://doi.org/10.1002/zaac.200800272.

[44] D. Voßwinkel, O. Niehaus, U.C. Rodewald, R. Pöttgen, *Z. Naturforsch., B: J. Chem. Sci.* **2012**, *67*, 1241–1247, https://doi.org/10.5560/znb.2012-0265.

5.7 Alkaline Earth Metal Poorest Ordered Compound $BaNi_{16}Si_{12}$ with Catalan Pentakis Dodecahedra—A New Record for Coordination Number

Braun, T.; Henseler, D.; Karttunen, A. J.; Hlukhyy, V.

Manuscript for publication

Alkaline Earth Metal Poorest Ordered Compound $BaNi_{16}Si_{12}$ with Catalan Pentakis Dodecahedra—A New Record for Coordination Number

Thomas Braun[*], David Henseler[*], Antti J. Karttunen[**], Viktor Hlukhyy[*1]

[*] Department of Chemistry, Technische Universität München, Lichtenbergstr. 4, 85747, Garching, Germany, and

[**] Department of Chemistry and Materials Science, Aalto University, FI-00076 Aalto, Finland

Abstract

An alkaline metal poorest polar intermetallic can be synthesized directly by arc melting of the elements. It crystallizes in own structure type with space group $Fd\bar{3}c$, Wyckoff sequence h^2cba, Pearson code $cF464$, a = 18.0482(1) Å, V = 5878.94(8) Å^3, wR_2 = 3.3% (all data), 452 F^2 values, 24 variable parameters. The coordination sphere of barium atoms adopts the shape of catalan pentakis dodecahedron $Ba@Ni_{20}Si_{12}$, composed of fused silicon icosahedron and nickel pentagon dodecahedron. Coordination number CN = 32 is the highest to date for the metal atoms among intermetallic compounds. Full and projected density of states (DOS) calculations, thermal, thermoelectric properties and magnetic properties have been investigated. For the $Ba@Ni_{20}Si_{12}$ fragment, Raman bands have been calculated.

Keywords: Intermetallics, Superstructure, Magnetic Properties, Single Crystal, Thermoelectric properties, Superconductivity

---

[1] Corresponding author.

E-mail address: viktor.hlukhyy@tum.de (V. Hlukhyy)

1. Introduction

With its d^{10}-configuration nickel is structurally versatile in polar intermetallic compounds. It forms corrugated layers like in $BaNi_2Si$ [1], with fused six-rings in boat conformation, with the rings in chair-conformation in $CaNi_2Si$ [2] alike grey arsenic; or planar square layers that can be rigid or distorted (e.g. $BaNi_2Ge_2$ [3], $BaNi_2Si_2$ [4], $CaNi_2Si_2$ [5]). Structural motif might be chains or ribbons of one-dimensional character, two-dimensional layers or three-dimensional network (BaNiGe, CaNiGe or MgNiGe, respectively).[6] And even very complex structures have been found (e.g. $CaNi_5Ge_3$, $Ca_{15}Ni_{18}Ge_{37}$ and $Ca_7Ni_{49}Ge_{22}$) [7]. Besides this structural diversity some compounds of the Ba–Ni–Si-family also exhibit interesting physical properties. Type-I clathrates with general formula $Ba_{8-\delta}Ni_x\square_ySi_{46-x-y}$ and AlB_2-type structures $SrNi_xSi_{2-x}$ show superconductivity up to 6.0 K and 2.8 K respectively [8,9]. Moreover clathrates have been investigated regarding their remarkable thermoelectric properties [10,11]. Searching for polar intermetallic compounds with alkaline earth metal (*Ae*) poor composition, $SrIr_9In_{18}$ represents the lower limit up to date with *Ae* to host atom ratio of 1:27 [12]. $BaNi_{16}Si_{12}$ in this work with a ratio of 1:28 breaks that record. At the same time, in this compound the atom has the largest coordination number (CN = 32) among intermetallic compounds. This number is only topped by fullerenes, where the polyhedra are more a cage than a coordination sphere [13–16]. In this work the novel structure type is discussed, physical properties analyzed and electronic structure calculation presented.

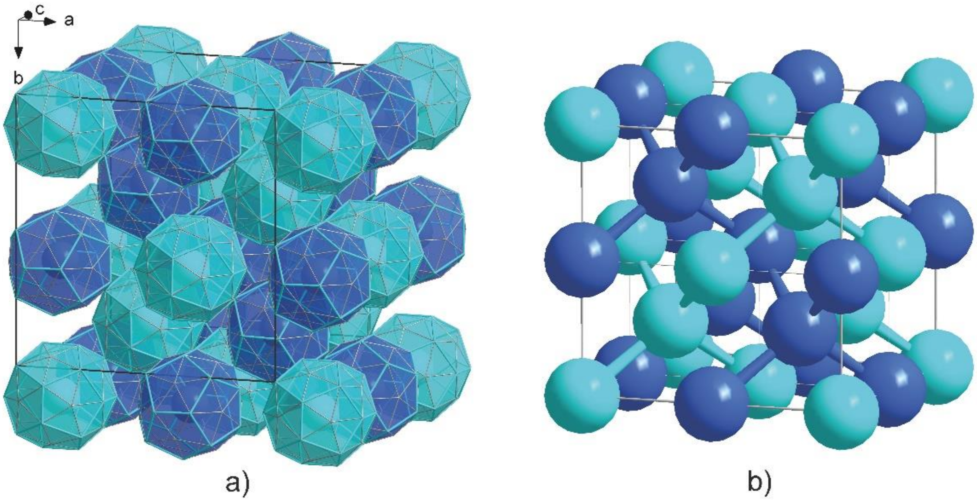

Figure 1 Packing scheme of $Ba@(Ni_{12+8/2}Si_{12})$ polyhedra. Two different orientations (tilted by 90° to each other) are present, marked in deep and cyan blue. They are packing analogue to NaTl-type, forming two interlaced cubic diamond-structures.

2. Experimental Section

2.1. Syntheses

Pieces of barium (ChemPur, 99.5%), nickel wire (Alfa Aesar, 99.98%) and silicon (Alfa Aesar, 99.999%) were arc melted in an argon-filled glovebox. An air stable single crystal of $BaNi_{16}Si_{12}$ was found in a sample with arbitrary composition 1:5:3 of barium to nickel to silicon, where the regulus was sealed in graphitized silica and annealed in a resistance furnace at 1050 °C for two hours, cooled with −6 °C/h to 900 °C with 24 h dwell time and turning off heating to cool down to room temperature. Arc melting of the elements in the stoichiometric composition with 7% barium excess and a total mass of 0.4 g leads to $BaNi_{16}Si_{12}$ with high phase purity (Figure 2).

2.2. X-ray diffraction methods

A single crystal was selected under a microscope and attached to a glass fiber with nail polish. Diffraction data were collected at room temperature by a STOE STADIVARI, equipped with a Genix 3D High Flux microfocus (Mo-K_{α}, $\lambda = 0.71073$ Å), graded multilayer mirror monochromator and DECTRIS Pilatus 300K detector. Data procession has been performed with the diffractometer software X-Area [17], including scaling with Laue Analyzer [18] and numerical absorption correction [19,20], with a crystal model generated with X-Shape [20] on basis of 500 reflection pairs selected by X-RED32 [19]. A structural model was created with direct methods using SHELXS-2014 and atomic parameter refined with SHELXL-2014 [21–24]. As a check for the correct composition, occupancy parameters were refined in separate leastsquares cycles. All sites were fully occupied. In the last cycles, the ideal occupancies were assumed again. No significant residual electron density was observed.

Energy dispersive X-ray spectroscopy of the crystal shown in Figure S1 was performed using a HITACHI TM-1000, applying 15 keV in high vacuum. The resulting composition of 1.1:16:12.9 atom-% (for barium, nickel and silicon, respectively) is very close to the ideal composition of 1:16:12.

Powder X-ray diffraction was performed with a STOE Stadi P (DECTRIS MYTHEN 1K detector, Cu-$K_{\alpha 1}$ source at $\lambda = 1.540598$ Å, and curved Ge(111) monochromator). Homogenized sample was fixed on a Scotch magic tape, the resulting data corrected to external silicon standard. Rietveld-refinement was done with Fullprof suite [25]. It showed high phase purity with some weak reflections that could not be assigned.

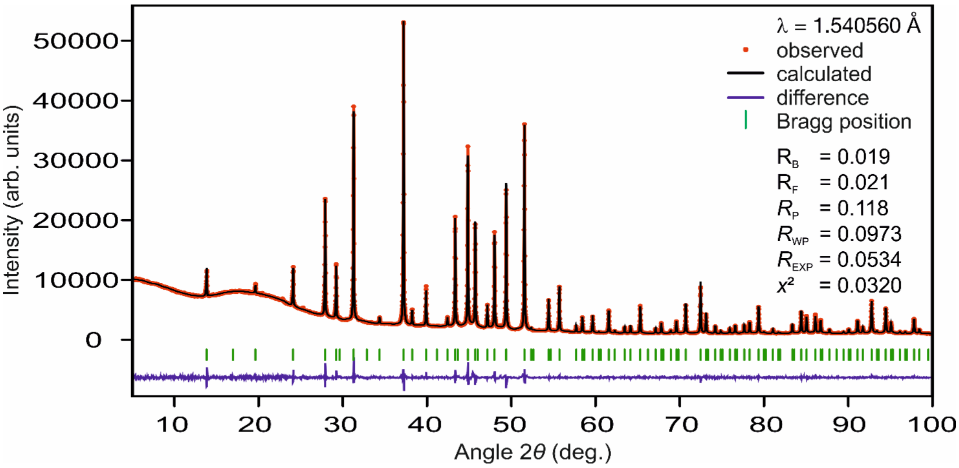

Figure 2 Powder X-ray diffraction data and Rietveld refinement of $BaNi_{16}Si_{12}$.

Table 1 Crystal data and structure refinement of $BaNi_{16}Si_{12}$. The lattice parameter was taken from powder Rietveld analysis

empirical formula	$BaNi_{16}Si_{12}$
formula weight (g mol^{-1})	1413.78
temperature (K)	293
crystal system	cubic
space group	$Fd\bar{3}c$
Pearson code	*cF*464
Wyckoff sequence	h^2cba
unit cell dimensions	
a (Å)	18.0482(1) (from powder data)
volume (Å^3)	5878.94(8)
Z	16
ρ_{calcd} (g cm^{-3})	6.39
μ (mm^{-1})	23.54
$F(000)$	10752
crystal size (mm^3)	0.08×0.08×0.05
theta range for data collection (°)	3.2 – 32.5
index ranges in *hkl*	$-26 \leq h \leq 27$, $-27 \leq k \leq 26$, $-26 \leq l \leq 27$
reflections collected	9531
independent reflections	452 (R_{int} = 0.034)
Reflections with $I \geq 2\sigma(I)$	277 (R_{sigma} = 0.075)
data/restraints/parameters	452/0/24
goodness-of-fit on F^2	0.845
final R indices ($I > 2\sigma(I)$)	R_1 = 0.018,
	wR_2 = 0.031
R indices (all data)	R_1 = 0.048,
	wR_2 = 0.033
Extinction coefficient	—
largest diff. peak and hole (e·Å^{-3})	0.58, −0.69

Table 2 Atomic coordinates and equivalent isotropic displacement parameter of $BaNi_{16}Si_{12}$.

Atom	Site	*x/a*	*y/b*	*z/c*	U_{eq} a) $/10^{-3} \cdot Å^2$
Ba	16	⅛	⅛	⅛	8.6(1)
Ni1	192h	0.05552(2)	0.12318(3)	0.31644(2)	10.1(1)
Ni2	32c	0	0	0	8.3(4)
Ni3	32b	¼	¼	¼	7.5(4)
Si	192h	0.02214(4)	0.28610(4)	0.12701(6)	8.8(2)

a) U_{eq} is defined as one third of the trace of the orthogonalized *Uij* tensor.

Table 3 Atomic distances, count and corresponding integrated −COHP at the Fermi level

Atoms			Distance / Å		−iCOHP / eV × cell
Ni1	–	Si	2.300(1)	2×	2.21
Ni1	–	Si	2.301(1)	2×	2.30
Ni1	–	Si	2.314(1)	2×	2.19
Ni2	–	Si	2.348(1)	7×	2.08
Ni1	–	Si	2.385(1)	2×	1.74
Ni3	–	Si	2.416(1)	7×	1.78
Si1	–	Si	2.454(2)	1×	1.67
Ni1	–	Ni1	2.472(1)	1×	1.30
Ni1	–	Ni1	2.509(4)	1×	1.19
Ni1	–	Ni3	2.717(1)	7×	0.80
Ni1	–	Si	2.729(1)	2×	0.81
Ni1	–	Ni1	2.760(1)	2×	0.68
Ni1	–	Ni2	2.771(1)	7×	0.64
Ni1	–	Si	2.863(1)	2×	0.46
Si	–	Si	3.063(1)	2×	0.16
Ba	–	Si	3.450(1)	12×	0.32
Ba	–	Ni3	3.676(1)	12×	0.21
Ba	–	Ni1/Ni2	3.907(1)	8×	0.16

2.3. *Thermal and thermoelectrical measurements*

Powdered $BaNi_{16}Si_{12}$ was cold-pressed (45 min at 8 t, in argon atmosphere) into a tablet of 1.09 g with 13 mm diameter and 1.75 mm thickness. This corresponds to 73.4% of the ideal crystallographic density. Seebeck coefficient S and electric conductivity σ were measured simultaneously perpendicular to the pressing direction with a NETZSCH SBA 458 Nemesis. In an argon flow rate of 60 ml/min conductivity was measured at 50 mA DC current and Seebeck at a temperature difference of at least ΔT = 2 °C. Temperature range was room temperature up to 500 °C. To calculate $ZT = \frac{S^2\sigma}{\lambda} \cdot T$, thermal conductivity λ = 4 W/mK was assumed, what is in the range of values reported for clathrates $Ba_8Ni_xSi_{46-x}$.[8,11]

2.4. Computational Methods

Stuttgart-TB-LMTO-ASA was used to calculate Band structure, density of states (DOS) and projected pDOS. It uses linear muffin tin orbital (LMTO) method in atomic sphere approximation (ASA) with tight-binding (TB) [26]. Radii were chosen after Jepsen and Andersen [27]. Total and projected density of states (DOS/pDOS) were calculated without spin polarization. Basis was set up with s/d/f orbitals for Ba, s/p/d for Ni and s/p for Si. For Ba 6p downfolding technique was employed [28].

Quantum-chemical calculations on a Ba@$Ni_{20}Si_{12}$ cluster were carried out using the TURBOMOLE program package [29,30]. We used PBE0 hybrid density functional method [31,32] and a triple-zeta-valence quality basis set with polarization functions (def2-TZVP) [33]. Multipole-accelerated resolution-of-the-identity technique was used to speed up the calculations [34–36]. The structure of $BaNi_{20}Si_{12}$ was fully optimized within T_h point group symmetry. The optimized structures of the studied systems in XYZ format are reported as Supporting Information. The cluster was confirmed to be a true local minimum by means of a harmonic frequency calculation. The Raman spectrum calculations were carried out for T = 298.15 K, laser wavelength 632.8 nm, unpolarized radiation, scattering angle of 90° [37,38]. The Raman intensities are given relative to the most intensive peak. The final Raman spectra were convoluted using Lorenzian peak profiles with FWHM of 10 cm^{-1}. The peak assignment was carried out by visual inspection of the normal modes (Jmol program package [39]).

2.5. Magnetic Properties

The powdered sample of 78 mg was placed in a gelatin capsule and fixed within a plastic straw. Field dependent magnetization and temperature dependent susceptibility was measured with a MPMS XL5 SQUID magnetometer from Quantum Design. Field dependent magnetization was measured at 300 and 10 K between ± 50 kOe. Zero-field cooling (ZFC) and field cooling (FC) data were collected between 2 and 300 K at 100 and 1000 Oe, respectively. The sample was first pre-cooled in zero-field, then warmed up and cooled with magnetic field applied, to measure temperature-dependent susceptibility.

3. Results

Via arc melting and subsequent annealing a mixture of barium, nickel and silicon pieces, crystals of $BaNi_{16}Si_{12}$ were found, which crystallizes in own structure type with a large cubic unit cell (space group $Fd\bar{3}c$, Pearson code $cF646$, a = 18.0482(1) Å (powder data), Z = 16). The solved structure model refines to $BaNi_{16}Si_{12}$.

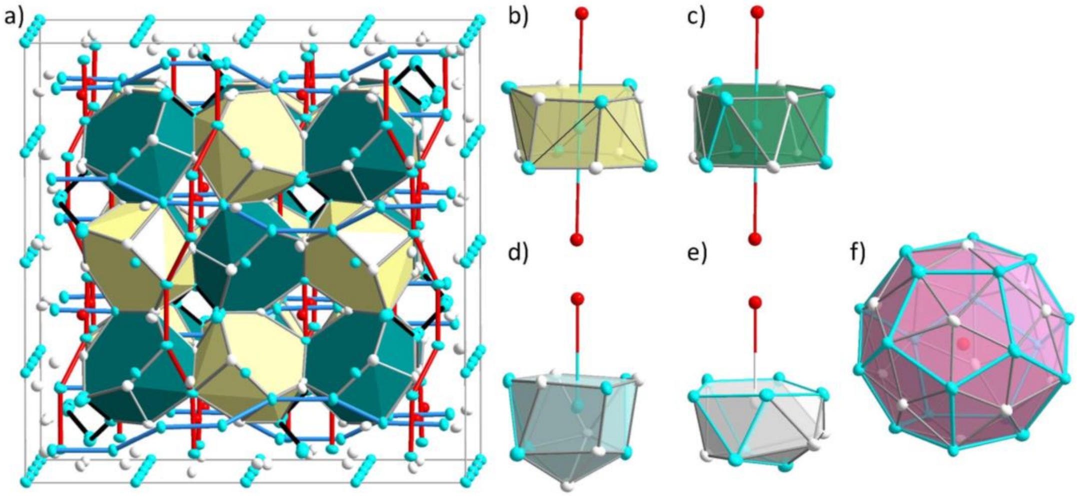

Figure 3 a) Crystal structure of $BaNi_{16}Si_{12}$ with cubic space group $Fd\bar{3}c$. Shortest Ni–Ni-bonds are highlighted in blue, red and black, forming corrugated infinite one-dimensional bands along all three directions. Shortest Si–Si- and Ni–Si-bonds in grey form the edges of $Ni2@Ni_6Si_6$- (yellow) and $Ni3@Ni_6Si_6$-polyhedra (green). b) and c) show isolated views of $Ni2@Ni_6Si_6$ and $Ni3@Ni_6Si_6$ distorted hexagonal prisms, respectively, capped by two barium atoms. d), e) and f) show coordination of $Ni1@Ni_6Si_6$, $Si@Ni_8Si_3$ and $Ba@Ni_{20}Si_{12}$, respectively. The last is shaped as catalan pentakis-dodecahedron, an intergrowth of Ni-pentagon dodecahedron and Si-icosahedron. Color code: red = barium; cyan blue = nickel; white = silicon, phosphorous.

The crystal structure consists of a three-dimensional network of nickel and silicon atoms that enclose barium atoms (Figure 3a). This Ni–Si-network can be regarded as edge-sharing distorted hexagonal prisms, with nickel as central atom. The $Ni@Ni_6Si_6$-prisms have already been observed for other intermetallic nickel-tetrelides, for example $SrNi_5Si_3$ [40], $SrNi_3Ge_2$ [41] and $Ba_2Ni_5Ge_4$ [42] (Figure S2, Supp. Inf.). In $BaNi_{16}Si_{12}$, two sets of prisms occur, one that is similar to other compounds, containing only Ni–Si-bonds between ligand atoms. And another one where nickel and silicon atoms of both hexagons are stacked congruently, resulting in short Ni–Ni- and Si–Si-contacts. The central nickel atom is also part of barium-coordination sphere, the relation of interpenetrating polyhedral is drawn in Figure S3a (Supp. Inf.). By removing Ni2 and Ni3 atoms centered in these prisms to represent the connectivity of prism edges, resulting Ni–Si-framework (Figure S3b) reminds to layers found in SrNiSi [40]. The Ni_2Si_2-rhomb has a close Ni–Ni-contact of 2.509(4) Å that is shorter than in SrNiSi (2.547 Å). In $BaNi_{16}Si_{12}$ nickel and silicon atoms form a $(3^2.6^2)(3.6^2)$ net as finite Ba-polyhedra that are fused with prisms, in SrNiSi the Ni/Si-atoms form a $(3^2.8^2)(3.8^2)$ net as infinite flat layer .

Connecting only shortest Ni–Ni-bonds (d = 2.472(1), 2.509(4) Å), corrugated infinite one-dimensional chains occur that perpetuate in all three directions. Another comprehensive view results regarding the barium coordination polyhedra $Ba@(Ni_{12+8/2}Si_{12})$, polyhedra (shown in

Figure 1a and Figure 3f). These polyhedra are composed of 20 nickel atoms that form a pentagon dodecahedron and 12 silicon atoms, each of them capping one of the five-fold faces. Silicon atoms by itself can be regarded as icosahedron. The complete polyhedron represents a catalan pentakis dodecahedron. Each polyhedron is linked to eight other polyhedra via vertex-sharing nickel atoms, in body centered cubic arrangement. Four polyhedra have the same orientation and four are rotated by 90 degree. Simplifying the polyhedra into two kind of balls, they pack analogue to NaTl-structure, each forming a cubic diamond-structure that is interlaced with the other (Figure 1b).

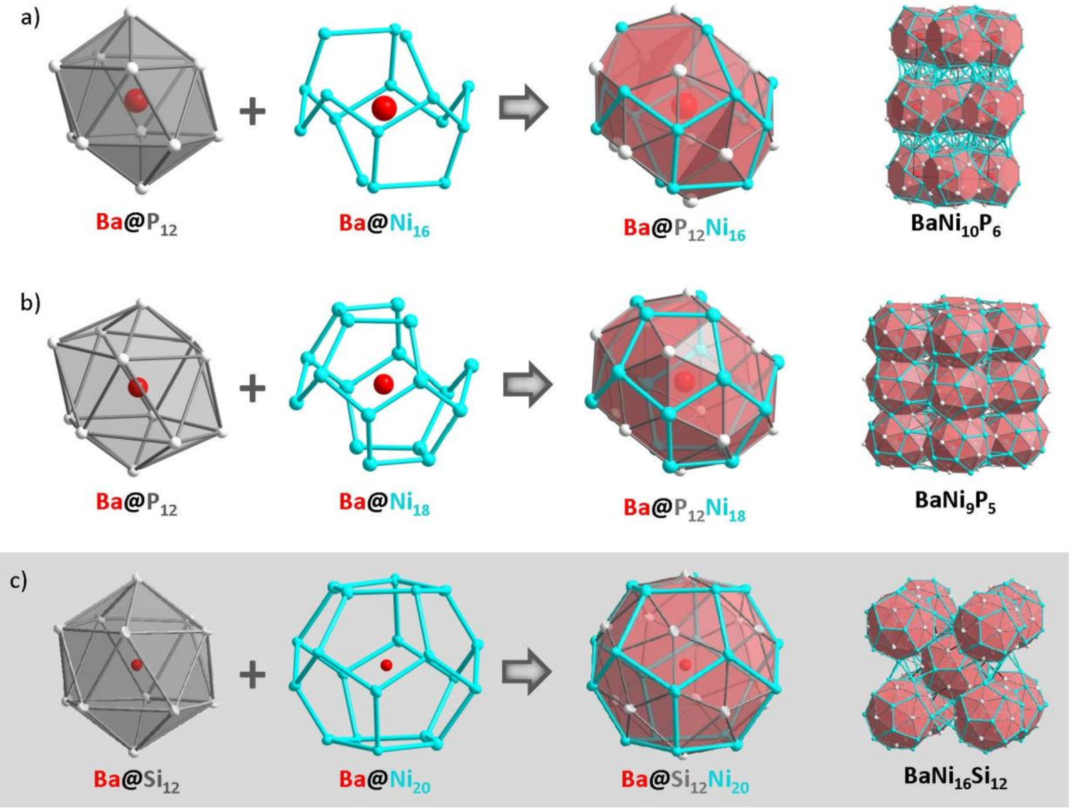

Figure 4 Barium coordination polyhedra in a) $BaNi_{10}P_6$ [43], b) $BaNi_9P_5$ [44] and c) $BaNi_{16}Si_{12}$.

This is the first time, such a large and completely closed and highly symmetrical coordination polyhedron has been observed for an intermetallic compound. Up to date, a catalan pentakis dodecahedron has only been found on theoretical level for hollow $Cu_{20}Si_{12}$ [45], $Au_{20}Si_{12}$ [46] and $B_{12}@Mg_{20}B_{12}$ [47]. With respect to the large size of barium and relatively small nickel and p-block element, our search for comparable alkaline earth metal poor compounds with a high coordination number of barium lead to $Ba@P_{12}Ni_{18}$, found in $BaNi_9P_5$ [44] and $Ba@P_{12}Ni_{16}$, found in $BaNi_{10}P_6$ [43], both shown in Figure 4. They show the same trend of nickel forming pentagons, capped by the main group element, however these units are not complete and exhibit hexagonal faces that are capped by another barium atom. Fully-closed coordination shell is only achieved by alkaline-earth poorest intermetallic compound $BaNi_{16}Si_{12}$. It is related to so-called Matryoshka- or onionskin-like compounds such as $[PBu_4]_3[As@Ni_{12}@As_{20}]$ and $A_{12}Cu_{12}Sn_{21}$ (A = Na, K) [48–50]. An atom-centered icosahedron is enclosed inside a regular pentagon dodecahedron. While this "atom in a cage in a cage" unit also represents an atom surrounded by 32 atoms, coordination spheres are different, as they have an inner and an outer shell. In $BaNi_{16}Si_{12}$ the central atom is larger, which stretches the icosahedron until both shells combine. In addition, the pentakis dodecahedra are not isolated by additional atoms and form a large three-dimensional vertex-sharing framework (Figure 1). Shared vertices are centered in hexagonal prisms that form necks between these large polyhedra (Figure 3).

Atomic distances are listed in Table 3. Ni–Ni-distances split into two groups. The first one (2.472(1) – 2.509(1) Å) is similar to the distance of elemental Ni (2.492(1) Å) and the bonds form one-dimensional corrugated chains that perpetuate parallel to the three crystallographic axes (highlighted in red, blue and black in Figure 3). Each chain alternatingly constitutes part of a polyhedron and bridges to the next. The second group of Ni–Ni-distances (2.717(1) – 2.771(1) Å) is located between Ni1 and Ni2/Ni3 atoms of $(Ni2/Ni3)@Ni_6Si_6$ prisms or as contacts between Ba-polyhedra, respectively. Shortest Si–Si-distances of 2.454(2) Å are formed in $Ni3@Ni_6Si_6$-prism, being necks between Ba-polyhedra of different orientation. This is larger than covalent bonds in elemental silicon (2.352(1) Å). The Ni–Si distances range from 2.300(1) – 2.416(1) Å within Ba-polyhedra and 2.729(1), 2.863 Å between atoms of different Ba-polyhedra, while the Ni-Si-bonds in the $Ni2@Ni_6Si_6$-prism are of 2.385(1) Å. The shortest contacts match the sum of covalent atomic radii. Ba–Si- (3.450(1) Å) and Ba–Ni-distances (3.676(1) Å, 3.907(1) Å) are slightly larger than the sum of atomic radii.

The calculated density of states is shown in Figure 5. Due to numerous atoms many states contribute to the bands and even at low energies no band gaps are found. Around −7.4 eV a kink indicates transition from s-dominated to p/d-dominated states. Near the Fermi level E_F almost all contributions arise from Ni-d and DOS is non-zero at E_F. This would mean the sample to possess metallic properties, however, with filled d-orbitals. Integrated COHP has been calculated for the shortest interatomic distances between barium, nickel and silicon atoms, to estimate their type and strength of bonding. All values are listed in Table 3. As expected coordinative interactions between cationic barium and silicon or nickel of the polyanionic framework is weak. Nickel-silicon bonds between atoms in prisms with values between 1.78

and 2.3 eV/cell indicate covalent character. Nickel–nickel bonds are weaker of about 0.64 to 1.3 eV/cell, giving reason to metallic character both. Interestingly, there are some weak metallic nickel–silicon interactions between adjacent clusters (0.46 and 0.81 eV/cell).

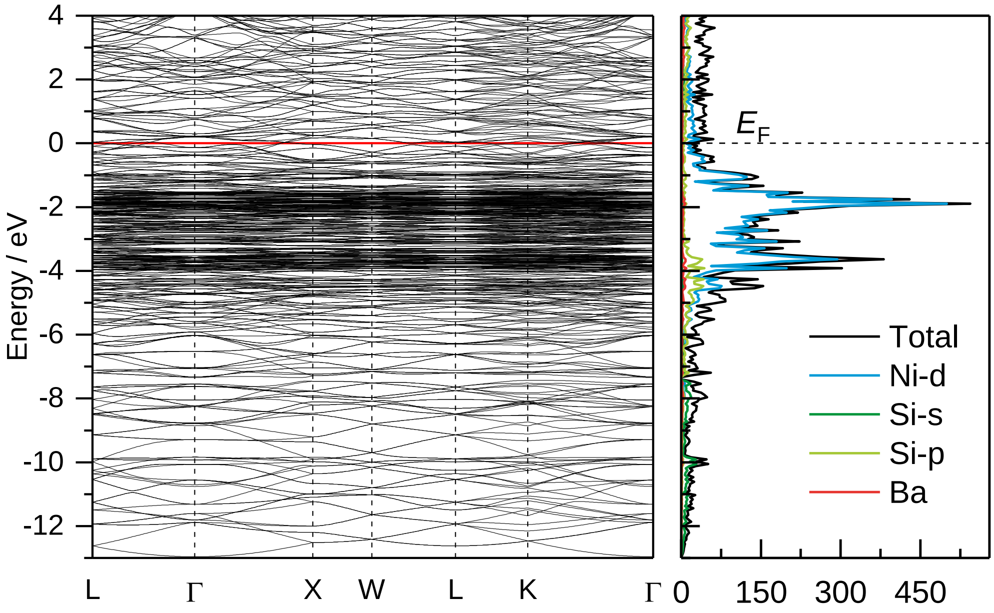

Figure 5 Calculated density of states (DOS) and projected DOS of $BaNi_{16}Si_{12}$.

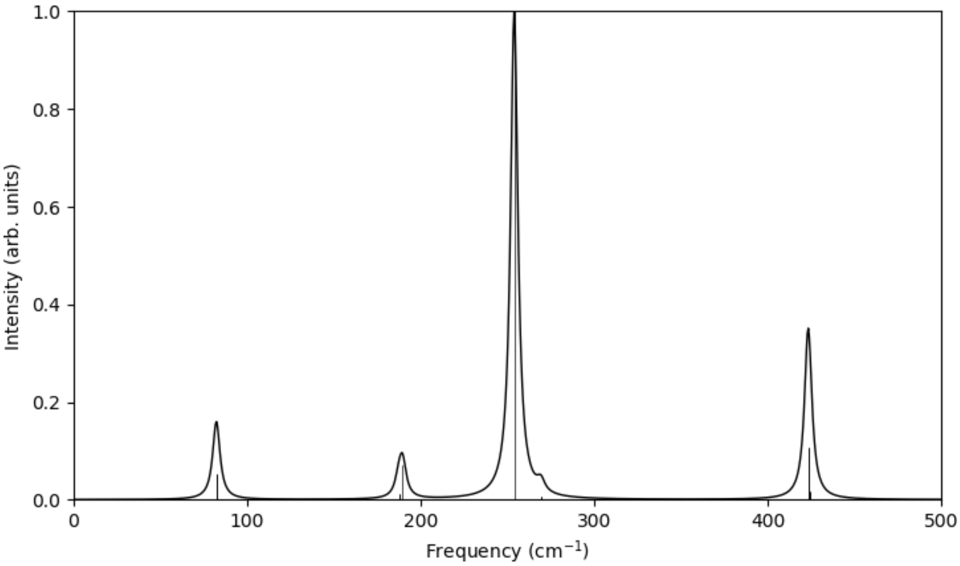

Figure 6 Raman spectrum of $BaNi_{20}Si_{12}$ cluster (laser wavelength 632.8 nm).

The results agree well with calculations on predicted $Cu_{20}Si_{12}$ and $Au_{20}Si_{12}$ pentakis dodecahedra [45,46]. Even though they calculated isolated clusters, they also contain strong bonds between transition metal and silicon, weaker bonds between transition metal atoms. The difference of 12 valance electron between those and the here presented nickel compound might by compensated by interstitial metallic bonds in the necks. We investigated a molecular $BaNi_{20}Si_{12}$ cluster cut from the crystal structure of $BaNi_{16}Si_{12}$ by means of density functional calculations (DFT-PBE0/TZVP level of theory). We studied the cluster within the T_h point group because it had a degenerate electronic ground state within I_h point group. After geometry optimization (Table S1, Supp. Inf.), the key intra-cluster distances are as follows (in Å, averaged distance in the crystal structure in parentheses). Si–Ni: 2.24 (2.34); Ni–Ni: 2.55 (2.70); Ba–Si 3.41 (3.46); Ba–Ni: 3.57 (3.78). The optimized cluster shows a HOMO-LUMO gap of 0.8 eV and a frequency calculation shows it to be a true local minimum. The calculated Raman spectrum of the cluster is shown in Figure 6. The most intense mode at 254 cm^{-1} corresponds to a symmetric breathing mode of the Si atoms, while the next most intense mode at 424 54 cm^{-1} corresponds to Si–Ni stretching.

No reversible phase transition has been observed between 150 and 900 °C (Figure S4). Thermoelectric measurements gave a Seebeck coefficient S between 16 and 21 µV/K and electric conductivity σ around $5 \cdot 10^2$ S/cm (Figure S5). Decreasing σ with increasing temperature confirms metallic properties stated from the DOS. Assuming thermal conductivity to be at the same magnitude than clathrates $BaNi_xSi_{46-x}$ [8,11], ZT can be calculated and compared with values reported for the clathrates (shown in Figure 7). Since Figure of merit ZT scales linearly with σ and S is only moderate, $Ba_8Ni_{16}Si_{12}$ is no suitable thermoelectric material.

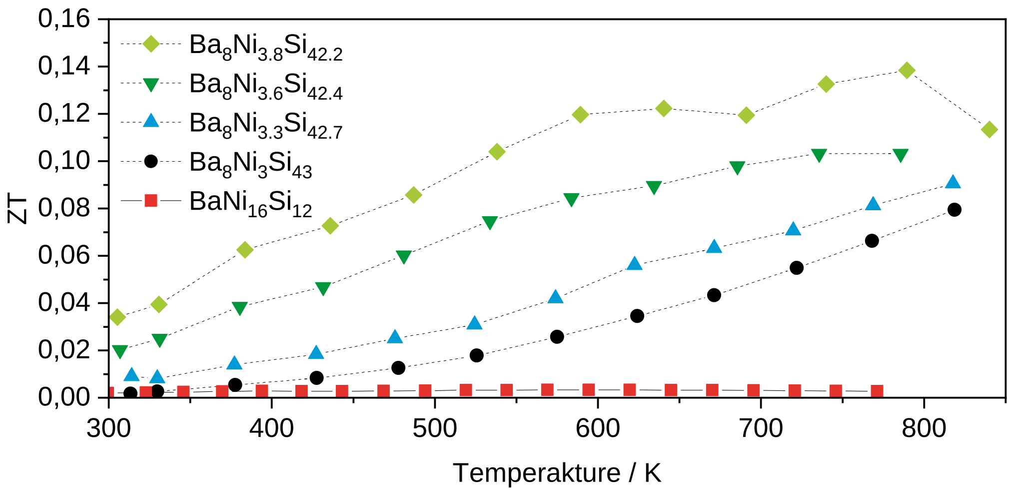

Figure 7 Comparison of obtained data with literature values for $Ba_8Ni_xSi_{46-x}$ [11]. To calculate a ZT-factor for $BaNi_{16}Si_{12}$ thermal conductivity of the clathrates was used.

Clathrates $Ba_8Ni_xSi_{46-x}$ ($x = 1.4, 1.5$, $T_C = 5.5 - 6.0$ K) and AlB_2-type $SrNi_xSi_{2-x}$ ($0.1 \leq x \leq 0.3$, $T_C = 2.3 - 2.8$ K) are known superconductors [8,9]. Magnetic measurements on $BaNi_{16}Si_{12}$ do not exhibit superconductivity in magnetic measurements down to 1.8 K. Magnetization at

300 and 1.8 k (Figure 8) shows weak paramagnetism which is comparable in size to the diamagnetic contribution of core electrons. The absolute magnetization of the sample very weak and thus small traces of ferromagnetic secondary phases can be observed.

Susceptibility at 100 Oe, 1000 Oe and 1000 Oe is shown in Figure 9. A phase transition occurs at 150 K for weak magnetic fields with some spin-glass-behavior below 40 K. However this feature ceases at higher fields and is attributed to a secondary phase that becomes saturated. The main phase has an almost temperature independent susceptibility that does not follow the Curie-Weiss-law. No superconductivity is observed, the sample is pauli-paramagnetic.

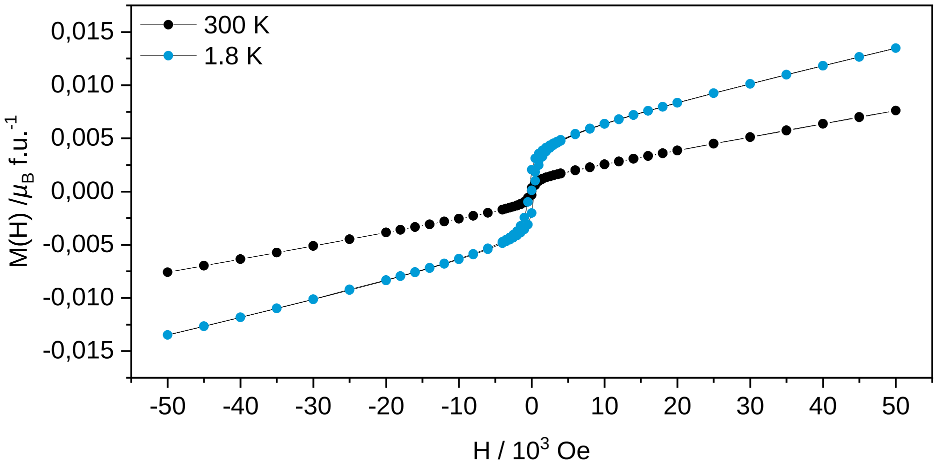

Figure 8 Field-dependent magnetization of $BaNi_{16}Si_{12}$. Data have been corrected for diamagnetic contributions of core electrons assuming $\chi_D = -MW/2\times10^{-6}$ emu mol^{-1} [51].

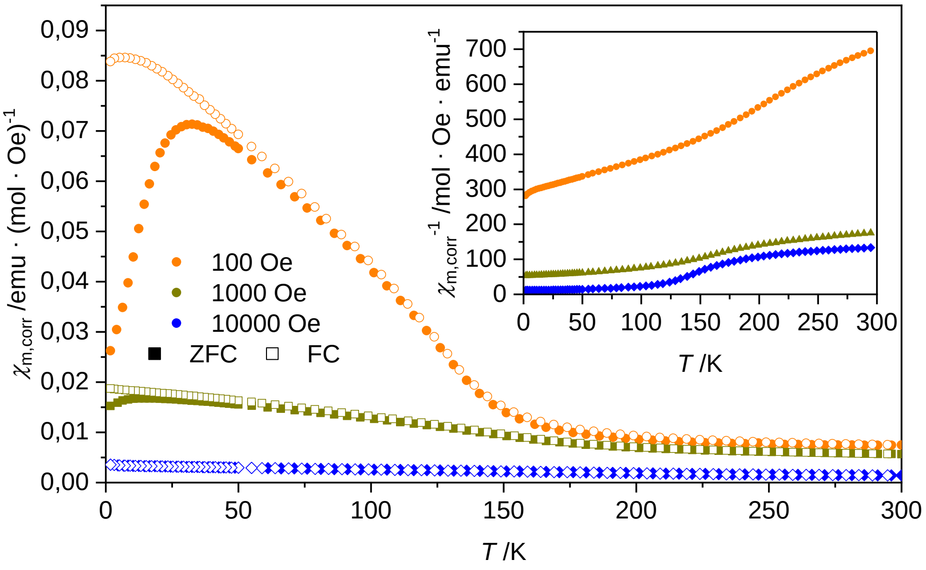

Figure 9 Temperature dependent magnetic susceptibility of $BaNi_{16}Si_{12}$ at different magnetic fields. Samples have been pre-cooled with zero-field, heated and cooled with applied field. The inset shows the Curie-Weiss-plot.

4. Conclusion

$BaNi_{16}Si_{12}$ is a new member of the *Ae*–Ni–Si-compounds. It has the lowest earth alkaline content up to date considering compounds with fully occupied atomic position of *Ae*. It crystallizes in space group $Fd\bar{3}c$ with linked Ba@$Ni_{20}Si_{12}$-polyhedra that have the form of pentakis dodecahedra. These polyhedra pack in cubic NaTl-type. The detailed arrangement of barium, nickel and silicon creates a novel structure type. DOS calculations and electric conductivity measurements show metallic properties, the sample is pauli-paramagnetic and melts congruently. It can be prepared with high phase purity from the elements. A Ba@$Ni_{20}Si_{12}$-fragment has been geometry optimized and Raman bands been calculated.

5. Acknowledgments

This research was financially supported by the German Research Foundation (Deutsche Forschungsgemeinschaft, DFG, Grant HL 62/3-1) and the TUM Graduate School. We thank Prof. Dr. Tom Nilges and his co-workers for performing thermoelectric measurements.

6. References

[1] T. Braun, S. Zeitz, V. Hlukhyy, *Z. Anorg. Allg. Chem.* **2019**, *645*, 388–395, https://doi.org/10.1002/zaac.201800500.

[2] J. Glaser, *Z. Anorg. Allg. Chem.* **2002**, *628*, 1946–1950, https://doi.org/10.1002/1521-3749(200209)628:9/10<1946:AID-ZAAC1946>3.0.CO;2-I.

[3] V. Hlukhyy, D. Trots, T.F. Fässler, *Inorg. Chem.* **2017**, *56*, 1173–1185, https://doi.org/10.1021/acs.inorgchem.6b02190.

[4] W. Dörrscheidt, H. Schäfer, *Z. Naturforsch., B: Anorg. Chem., Org. Chem.* **1980**, *35*, 297–299, https://doi.org/10.1515/znb-1980-0307.

[5] W. Rieger, E. Parthé, *Monatsh. Chem.* **1969**, *100*, 444–454, https://doi.org/10.1007/BF00904086.

[6] V. Hlukhyy, L. Siggelkow, T.F. Fässler, *Inorg. Chem.* **2013**, *52*, 6905–6915, https://doi.org/10.1021/ic302681t.

[7] L. Siggelkow, V. Hlukhyy, B. Wahl, T.F. Fässler, *Eur. J. Inorg. Chem.* **2011**, *2011*, 4012–4024, https://doi.org/10.1002/ejic.201100347.

[8] U. Aydemir, C. Candolfi, A. Ormeci, H. Borrmann, U. Burkhardt, Y. Oztan, N. Oeschler, M. Baitinger, F. Steglich, Y. Grin, *Inorg. Chem.* **2012**, *51*, 4730–4741, https://doi.org/10.1021/ic2027626.

[9] S. Pyon, K. Kudo, M. Nohara, *J. Phys. Soc. Jpn.* **2012**, *81*, 23702, https://doi.org/10.1143/JPSJ.81.023702.

[10] J.H. Roudebush, M. Orellana, S. Bux, T. Yi, S.M. Kauzlarich, *J. Solid State Chem.* **2012**, *192*, 102–108, https://doi.org/10.1016/j.jssc.2012.02.054.

[11] M. Falmbigl, M.X. Chen, A. Grytsiv, P. Rogl, E. Royanian, H. Michor, E. Bauer, R. Podloucky, G. Giester, *Dalton Trans.* **2012**, *41*, 8839–8849, https://doi.org/10.1039/c2dt30279a.

[12] B. Heying, R.-D. Hoffmann, J. Kösters, R. Pöttgen, *Z. Anorg. Allg. Chem.* **2020**, *646*, 631–635, https://doi.org/10.1002/zaac.201900174.

[13] S. Alvarez, *Dalton Trans.* **2005**, 2209–2233, https://doi.org/10.1039/b503582c.

[14] V. Smetana, A. Mudring, A. Ovchinnikov, *J. Phys. Condens. Matter.* **2020**, https://doi.org/10.1088/1361-648X/ab6b87.

[15] A. Hermann, M. Lein, P. Schwerdtfeger, *Angew. Chem. Int. Ed.* **2007**, *46*, 2444–2447, https://doi.org/10.1002/anie.200604148.

[16] A. Reich, M. Panthöfer, H. Modrow, U. Wedig, M. Jansen, *J. Am. Chem. Soc.* **2004**, *126*, 14428–14434, https://doi.org/10.1021/ja0401693.

[17] X-Area, STOE & Cie GmbH, Darmstadt, Germany, 2015.

[18] LANA, STOE & Cie GmbH, Darmstadt, Germany, 2016.

[19] X-RED32, STOE & Cie GmbH, Darmstadt, Germany, 2016.

[20] X-SHAPE, STOE & Cie GmbH, Darmstadt, Germany, 2015.

[21] G.M. Sheldrick, SHELXS-2014: Program for the Determination of Crystal Structure, University of Göttingen, Göttingen, Germany, 2014.

[22] G.M. Sheldrick, SHELXL-2014: Program for Crystal Structure Refinement, University of Göttingen, Göttingen, Germany, 2014.

[23] G.M. Sheldrick, *Acta Crystallogr., Sect. C: Struct. Chem.* **2015**, *71*, 3–8, https://doi.org/10.1107/S2053229614024218.

[24] G.M. Sheldrick, *Acta Crystallogr., Sect. A: Found. Crystallogr.* **2008**, *64*, 112–122, https://doi.org/10.1107/S0108767307043930.

[25] J. Rodriguez-Carvajal, FullProf: A Program for Rietveld Refinement and Pattern Matching Analysis. At the Satellite Meeting on Powder Diffraction of the XV IUCr Congress, Toulouse, France, 1990.

[26] R.W. Tank, O. Jepsen, O.K. Andersen, The STUTTGART TB-LMTO-ASA program, Stuttgart, 1998.

[27] O. Jepsen, O.K. Andersen, *Z. Phys. B: Condens. Matter* **1995**, *97*, 35–47, https://doi.org/10.1007/BF01317585.

[28] W.R.L. Lambrecht, O.K. Andersen, *Phys. Rev. B* **1986**, *34*, 2439–2449, https://doi.org/10.1103/PhysRevB.34.2439.

[29] TURBOMOLE V7.3, a development of University of Karlsruhe and Forschungszentrum Karlsruhe GmbH, 1989-2007, TURBOMOLE GmbH, since 2007, 2018.

[30] R. Ahlrichs, M. Bär, M. Häser, H. Horn, C. Kölmel, *Chem. Phys. Lett.* **1989**, *162*, 165–169, https://doi.org/10.1016/0009-2614(89)85118-8.

[31] J.P. Perdew, K. Burke, M. Ernzerhof, *Phys. Rev. Lett.* **1997**, *78*, 1396, https://doi.org/10.1103/PhysRevLett.78.1396.

[32] C. Adamo, V. Barone, *J. Chem. Phys.* **1999**, *110*, 6158–6170, https://doi.org/10.1063/1.478522.

[33] F. Weigend, R. Ahlrichs, *Phys. Chem. Chem. Phys.* **2005**, *7*, 3297–3305, https://doi.org/10.1039/b508541a.

[34] K. Eichkorn, O. Treutler, H. Öhm, M. Häser, R. Ahlrichs, *Chem. Phys. Lett.* **1995**, *240*, 283–290, https://doi.org/10.1016/0009-2614(95)00621-A.

[35] F. Weigend, *Phys. Chem. Chem. Phys.* **2006**, *8*, 1057–1065, https://doi.org/10.1039/b515623h.

[36] M. Sierka, A. Hogekamp, R. Ahlrichs, *J. Chem. Phys.* **2003**, *118*, 9136–9148, https://doi.org/10.1063/1.1567253.

[37] D. Rappoport, F. Furche, *J. Chem. Phys.* **2007**, *126*, 201104, https://doi.org/10.1063/1.2744026.

[38] F. Furche, R. Ahlrichs, *J. Chem. Phys.* **2002**, *117*, 7433–7447, https://doi.org/10.1063/1.1508368.

[39] Jmol: an open-source Java viewer for chemical structures in 3D. http://www.jmol.org/.

[40] T. Braun, V. Hlukhyy, in preparation.

[41] V. Hlukhyy, T.F. Fässler, *Z. Anorg. Allg. Chem.* **2008**, *634*, 2316–2322, https://doi.org/10.1002/zaac.200800272.

[42] L. Siggelkow, V. Hlukhyy, T.F. Fässler, *Z. Anorg. Allg. Chem.* **2011**, *637*, 2000–2006, https://doi.org/10.1002/zaac.201100306.

[43] V. Keimes, A. Mewis, *Z. Kristallogr.* **1993**, *207*, 81–90, https://doi.org/10.1524/zkri.1993.207.12.81.

[44] J.V. Badding, A.M. Stacy, *J. Solid State Chem.* **1990**, *87*, 10–14, https://doi.org/10.1016/0022-4596(90)90058-6.

[45] H.-Y. Zhao, J. Wang, L.-Y. Ai, Y. Liu, *J. Phys. Chem. A* **2016**, *120*, 6303–6308, https://doi.org/10.1021/acs.jpca.6b05258.

[46] J.J. Guo, H.Y. Zhao, J. Wang, L.Y. Ai, Y. Liu, *J. Chem. Phys.* **2017**, *146*, 64310, https://doi.org/10.1063/1.4975988.

[47] H.-Y. Zhao, L.-Y. Ai, H.-M. Ma, J.-J. Guo, J.-L. Qiu, J. Wang, Y. Liu, *J. Phys. Chem. C* **2019**, *123*, 17639–17643, https://doi.org/10.1021/acs.jpcc.8b12141.

[48] S. Stegmaier, T.F. Fässler, *J. Am. Chem. Soc.* **2011**, *133*, 19758–19768, https://doi.org/10.1021/ja205934p.

[49] F.K. Sheong, W.-J. Chen, H. Kim, Z. Lin, *Dalton Trans.* **2015**, *44*, 7251–7257, https://doi.org/10.1039/C5DT00097A.

[50] M.J. Moses, J.C. Fettinger, B.W. Eichhorn, *Science (New York, N.Y.)* **2003**, *300*, 778–780, https://doi.org/10.1126/science.1082342.

[51] G.A. Bain, J.F. Berry, *J. Chem. Educ.* **2008**, *85*, 532, https://doi.org/10.1021/ed085p532.

Supporting Information

Alkaline Earth Metal Poorest Ordered Compound $BaNi_{16}Si_{12}$ with Catalan Pentakis Dodecahedra—A New Record for Coordination Number

Thomas Braun, David Henseler, Antti Karttunen, Viktor Hlukhyy

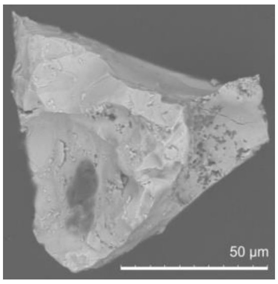

Figure S1 SEM images of the single crystal used for XRD and EDX measurements.

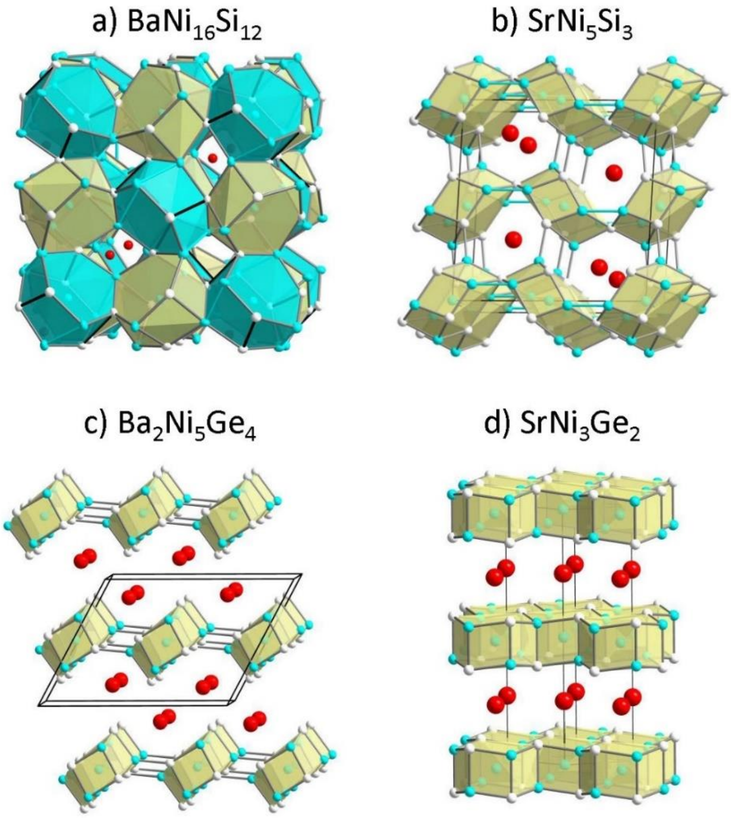

Figure S2 Ni@Ni_3X_3 (X = Si, Ge) found in crystal structures of a) $BaNi_{16}Si_{12}$, b) $SrNi_5Si_3$, c) $Ba_2Ni_5Ge_4$ and $SrNi_3Ge_2$.

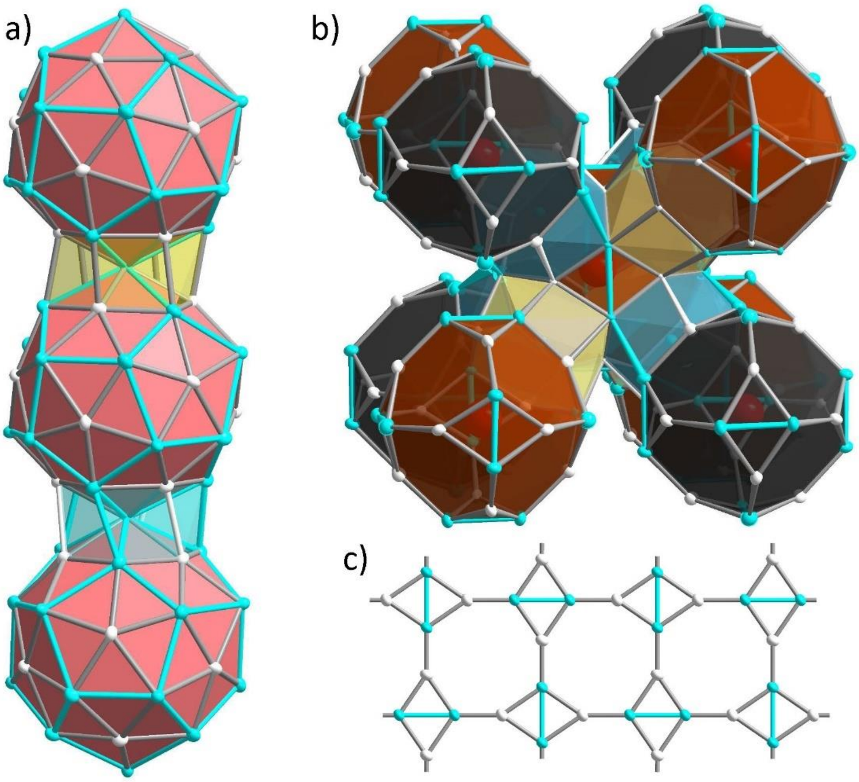

Figure S3 a) Relation of Ni2@Ni_6S_6 (yellow) and Ni3@Ni_6Si_6 prism (green) with Ba@$Ni_{20}Si_{12}$ (red), b) Ni–Si-network formed by edges of the prisms (black and brown represent two different orientations) and c) infinite flat Ni–Si-layer found in SrNiSi.

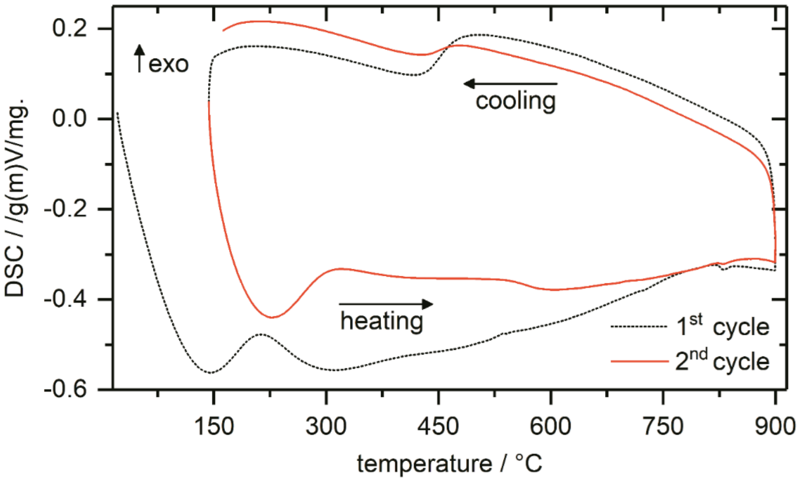

Figure S4 Differential thermal analysis of $BaNi_{16}Si_{12}$ measured in argon atmosphere. No reversible signals or phase change could be observed.

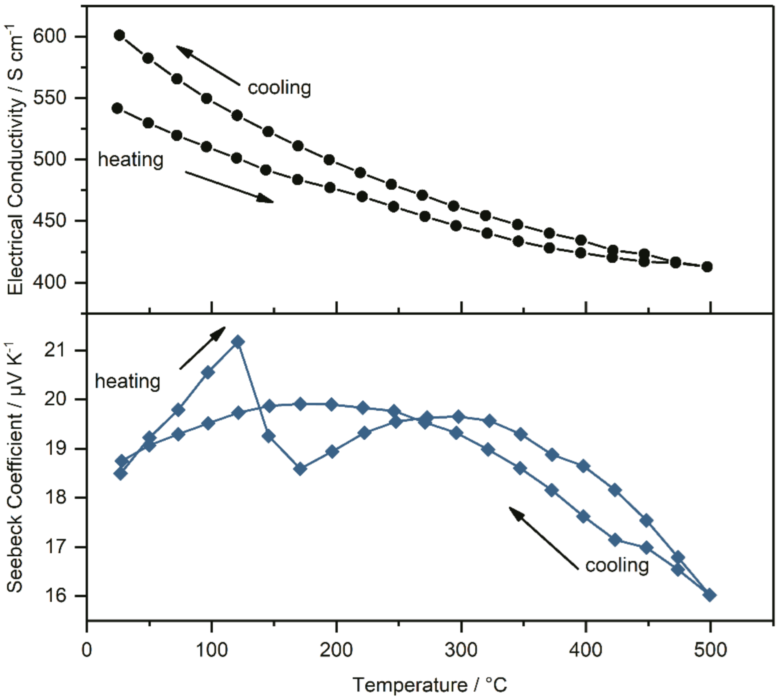

Figure S5 Seebeck coefficient and electrical conductivity of $BaNi_{16}Si_{12}$ between room temperature and 500 °C. Decreasing conductivity demonstrates metallic properties.

Table S1 Optimized structure of $BaNi_{20}Si_{12}$-cluster fragment in XYZ format

33

Energy = -33661.11829721

Ba	0.0000000	0.0000000	0.0000000
Ni	3.3362939	1.2742944	0.0000000
Ni	-2.0617640	2.0617640	-2.0617640
Ni	-0.0000000	-3.3362939	-1.2742944
Ni	-1.2742944	0.0000000	3.3362939
Ni	0.0000000	3.3362939	1.2742944
Ni	2.0617640	-2.0617640	2.0617640
Ni	-3.3362939	-1.2742944	0.0000000
Ni	1.2742944	-0.0000000	-3.3362939
Ni	-2.0617640	-2.0617640	-2.0617640
Ni	3.3362939	-1.2742944	-0.0000000
Ni	2.0617640	-2.0617640	-2.0617640
Ni	-2.0617640	-2.0617640	2.0617640
Ni	-1.2742944	0.0000000	-3.3362939
Ni	-2.0617640	2.0617640	2.0617640
Ni	-0.0000000	-3.3362939	1.2742944
Ni	-3.3362939	1.2742944	0.0000000
Ni	2.0617640	2.0617640	-2.0617640
Ni	0.0000000	3.3362939	-1.2742944
Ni	2.0617640	2.0617640	2.0617640
Ni	1.2742944	-0.0000000	3.3362939
Si	-2.9001245	-0.0000000	-1.7923813
Si	1.7923813	-2.9001245	0.0000000
Si	-1.7923813	-2.9001245	-0.0000000
Si	2.9001245	0.0000000	-1.7923813
Si	0.0000000	-1.7923813	2.9001245
Si	0.0000000	-1.7923813	-2.9001245
Si	-1.7923813	2.9001245	0.0000000
Si	-2.9001245	-0.0000000	1.7923813
Si	1.7923813	2.9001245	-0.0000000
Si	-0.0000000	1.7923813	-2.9001245
Si	2.9001245	0.0000000	1.7923813
Si	-0.0000000	1.7923813	2.9001245

5.8 Synthesis and Crystal Structure of $CaCo_{8.79(1)}Si_{4.21}$ and $SrNi_{9.26(8)}Ge_{3.74}$ with $Ce_2Ni_{17}Si_9$-type

Braun, T.; Hlukhyy, V.

Manuscript for publication

Synthesis and Crystal Structure of $CaCo_{8.79(1)}Si_{4.21}$ and $SrNi_{9.26(8)}Ge_{3.74}$ with $Ce_2Ni_{17}Si_9$-type

Thomas Braun, Viktor Hlukhyy[1]

Department of Chemistry, Technische Universität München, Lichtenbergstr. 4, 85747, Garching, Germany

Abstract

Ternary intermetallic compounds $CaCo_{8.79(1)}Si_{4.21}$ and $SrNi_{9.26(8)}Ge_{3.74}$ were prepared from the elements via arc melting and subsequent annealing in induction furnace. They crystallize with $Ce_2N_{17}Si_9$-type, a distorted colored variant of cubic $NaZn_{13}$. It is closely related to $LaFe_9Si_4$ but has mixed occupied sites. $CaCo_{8.79(1)}Si_{4.21}$ with space group *I4/mcm*, a = 7.785(1) Å, c = 11.589(2) Å, V = 702.4(2) Å^3, $_{W}R_2$ = 2.68% (all data), 551 F^2 values, 26 variable parameters and $SrNi_{9.26(8)}Ge_{3.74}$ with space group *I4/mcm*, a = 7.9903(1) Å, b = 11.8371(2) Å, V = 755.74(2) Å^3, $_{W}R_2$ = 5.38% (all data), 295 F^2 values, 27 variable parameters. Mixed *T/X*-occupancy (T = Co, Ni; X = Si, Ge) was observed for both compounds. The structure is formed by packing of transition metal centered icosahedra and alkaline earth metal centered snub cubes with 24 vertices. Density of States was calculated for the ideal 194 composition, assuming perfect order.

Keywords: Intermetallic Compound, Crystal Structure, Density of States, Magnetic Measurement

1. Introduction

$NaZn_{13}$ is parent structure for ternary polar intermetallic compounds with generalized formula $RT_{13-x}X_x$ (R = rare earth element, T = Fe, Co, Ni, Cu; X = Al, Ga, Si, Ge) [1]. Starting from a hypothetical binary compound RNi_{13}, which do not exist, partial substitution with a third element leads to formation of new phases. Depending on the degree of substitution, these com-

---

[1] Corresponding author.

E-mail address: viktor.hlukhyy@tum.de (V. Hlukhyy)

pounds crystallize with $NaZn_{13}$-type [2,3] in cubic disordered symmetry or they undergo structural distortion to tetragonal or several orthorhombic space groups. Prots et al. [4] have shown a relationship for $LaNi_{11}Ga_2$, $LaNi_9Ga_4$, $LaNi_7Ga_6$, $LaNi_{6.5}Ga_{6.5}$ and $LaNi_{5.5}Ga_{7.5}$ using Bärnighausen formalism. RT_9X_4-structures ($x = 4$) are of special interest, as they can be described with completely ordered structure of $LaFe_9Si_4$ in tetragonal space group *I*4/*mcm* [5]. It contains two magnetic sublattices and substitution can occur either on the iron or silicon position, depending on the degree of substitution. The sharp composition 1:9:4 as edge case marks the point between to different types of interfered sublattices [6]. This compound class is therefore an interesting model to examine and tune magnetic properties [7–10]. In case of mixed occupancy, this structure is known as $Ce_2N_{17}Si_9$-type [11,12], which can be rewritten as $CeNi_{9-x}Si_{4+x}$ (x = 0.5) to demonstrate the relation to $LaFe_9Si_4$. Degree of substitution x may also adopt negative values even though in that case other crystallographic sites are affected. Further substitution lead to orthorhombic $LaNi_7Ga_6$ (*Ibam*) [13] or $LaNi_{6.5}Ga_{6.5}$ (*Fmmm*) [4]. Kranenberg and Mewis [14] have reported four $Ce_2N_{17}Si_9$-type compounds $AeCu_9X_4$ (Ae = Sr, Ba; X = Si, Ge) with alkaline earth metals. In this report, two new compounds are reported that contain an alkaline earth element in combination with cobalt or nickel and tetrels silicon or germanium.

2. Experimental Section

2.1. Syntheses

A modified arc furnace (Mini Arc Melting System, MAM-1, Johanna Otto GmbH) with water-cooled copper hearth was used inside an argon-filled glove box. Pieces of strontium (ChemPur, 98%,), nickel wire (Alfa Aesar, 99.98%) and germanium (Evochem GmbH, 99.999%) or calcium (Alfa Aesar, 99.5%), cobalt shots (Alfa Aesar,99.9+%) and silicon (Alfa Aesar, 99.999%) were arc melted with ratio 1.05:9:4. To enhance homogeneity, the melting regulus was turned over and remelted two more times, alkaline earth metal excess was used to compensate for evaporation losses. For phase purity, the samples were then sealed in a welded tantalum ampoule and annealed in induction furnace (Hüttinger TIG 2.5/300) with water cooled sample space under dynamic argon atmosphere, heating to 1050 °C for 5 minutes, cooling down to circa 700 °C within 20 minutes, dwelling for 70 minutes and cooling to room temperature within 15 minutes. The solids are hard and brittle with grey color, metallic luster and were air- and moisture-stable.

2.2. X-ray Diffraction Methods

Single crystals have been selected under a microscope and been attached to a glass fiber with nail polish. Diffraction data were collected at room temperature either by a STOE IPDS 2T

(Bruker rotating anode, Mo-K_α, $\lambda = 0.71073$ Å, graphite monochromator) with image plate detector for $SrNi_{9.26(8)}Ge_{3.74}$ or a STOE STADIVARI with Genix 3D High Flux microfocus source (Mo-K_α, $\lambda = 0.71073$ Å), graded multilayer mirror monochromator and DECTRIS Pilatus 300K detector for $CaCo_{8.79(1)}Si_{4.21}$. Diffraction data were collected, integrated and corrected with the diffractometer software X-Area [15], including numerical absorption correction [16,17]. SHELXS-2014 [18,19] was used to obtain starting atomic parameters via direct methods. These were refined using SHELXL-2014 [20,21] with full-matrix least squares on F_O^2 with anisotropic atomic displacement parameters for all atoms. To check for the correct composition, occupancy parameters of both compounds were refined in a separate series of least-squares cycles. Mixed occupancy was refined by using restraints on positional and atomic displacement parameters. A final difference electron-density (Fourier) synthesis did not reveal any significant residual peaks. Positional parameters and equivalent anisotropic displacement parameters are given in Table ***2***.

Table 1 Crystal data und structure refinement data of $CaCo_{8.79(1)}Si_{4.21}$ and $SrNi_{9.26(8)}Ge_{3.74}$.

Compound	$CaCo_{8.79(1)}Si_{4.21}$	$SrNi_{9.26(8)}Ge_{3.74}$
formula weight (g mol^{-1})	676.33	903.52
temperature (K)	293	293
crystal system	cubic	Cubic
space group	$I4/mcm$	$I4/mcm$
unit cell dimensions		
a (Å) (= b)	7.785(1)	7.9903(1)
c (Å)	11.589(2)	11.8371(2)
volume (Å^3)	702.4(2)	755.74(2)
Z	4	4
ρ_{calcd} (g cm^{-3})	6.40	7.93
μ (mm^{-1})	21.551	43.990
F(000)	1265	1668
crystal size (mm^3)	0.14×0.05×0.05	0.10×0.06×0.03
theta range for data collection (°)	3.52 – 38.4	5.00 – 29.21
index ranges in hkl	$h \le \pm 13$, $-13 \le k \le 11$, $-20 \le l \le 19$	$h \le \pm 10$, $k \le \pm 10$, $l \le \pm 16$
reflections collected	10834	6661
independent reflections	551 ($R_{int} = 0.017$)	295 ($R_{int} = 0.092$)
Reflections with $I \ge 2\sigma(I)$	511 ($R_{sigma} = 0.009$)	294 ($R_{sigma} = 0.025$)
data/restraints/parameters	551/0/26	295/0/27
goodness-of-fit on F^2	1.106	1.173
final R indices ($I > 2\sigma(I)$)	$R_1 = 0.0114$, $wR_2 = 0.0266$	$R_1 = 0.0313$, $wR_2 = 0.0515$
R indices (all data)	$R_1 = 0.0128$, $wR_2 = 0.0268$	$R_1 = 0.0412$, $wR_2 = 0.0538$
Extinction coefficient	0.0013(1)	0.0009(2)
largest diff. peak and hole (e·Å^{-3})	0.504, −0.422	0.851, −1.331

Table 2 Atomic coordinates and equivalent isotropic displacement parameter of $CaCo_{8.79(1)}Si_{4.21}$ and $SrNi_{9.26(8)}Ge_{3.74}$

Atom	Site	*S.O.F.*	*x/a*	*y/b*	*z/c*	U_{eq} [a] $/10^{-3}\cdot$ Å^2
$CaCo_{8.79(1)}Si_{4.21}$						
Si1	16*l*	1	0.16883(3)	0.66883(3)	0.12297(4)	7.1(1)
Co1	16*l*	1	0.62883(2)	0.12883(2)	0.17965(2)	6.0(1)
Co2	16*k*	0.947(2)	0.07034(2)	0.19857(2)	0	6.4(1)
Si2	16*k*	0.053(2)	0.07034(2)	0.19857(2)	0	6.4(1)
Co3	4*d*	1	0	½	0	5.6(2)
Ca1	4*a*	1	0	0	¼	8.0(2)
$SrNi_{9.26(8)}Ge_{3.74}$						
Ge1	16*l*	0.90(5)	0.17508(9)	0.67508(9)	0.12096(9)	17.5(5)
Ni1	16*l*	0.10(5)	0.17508(9)	0.67508(9)	0.12096(9)	17.5(5)
Ni2	16*l*	1	0.62161(12)	0.12161(12)	0.1804(1)	16.9(3)
Ni3	16*k*	1	0.06700(14)	0.20387(16)	0	16.7(3)
Ni4	4*d*	0.87(8)	0	½	0	17(1)
Ge2	4*d*	0.13(8)	0	½	0	17(1)
Sr1	4*a*	1	0	0	¼	17.2(4)

[a] U_{eq} is defined as one third of the trace of the orthogonalized U^{ij} tensor.

Single crystals used for the diffraction experiments were analyzed via scanning electron microscopy (SEM) and energy dispersive X-ray (EDX) characterization. The crystals were mounted on a sticky carbon disk that had been adhered to an aluminum holder and introduced into the SEM microscope. No impurities heavier than Na have been observed. $CaCo_{8.79(1)}Si_{4.21}$ was investigated with HITACHI TM-1000, applying 15 keV in high vacuum. The single crystal of $SrNi_{9.26(8)}Ge_{3.74}$ was imaged with JEOL model SEM 5900LV. Semiquantitative analyses of well-shaped single crystals revealed the following compositions (in atomic percentages): The composition of Ca:Co:Si = 1.0:8.8:4.2 is in good agreement with refined formula $CaCo_{8.79(1)}Si_{4.21}$ and Sr:Ni:Ge = 0.8:9.5:3.5 are close to $SrNi_{9.26(8)}Ge_{3.74}$.

Phase analysis was done with powder X-ray diffraction on a STOE Stadi P (Cu-$K_{\alpha 1}$ source, λ = 1.540598 Å, DECTRIS MYTHEN 1K detector and curved Ge(111) monochromator). The sample was ground and powder fixed on a Scotch magic tape. External silicon was used for data correction. Figure 1 shows the Rietveld-refinement done with Fullprof suite [22]. Both samples agree well with the structure model and have high phase purity.

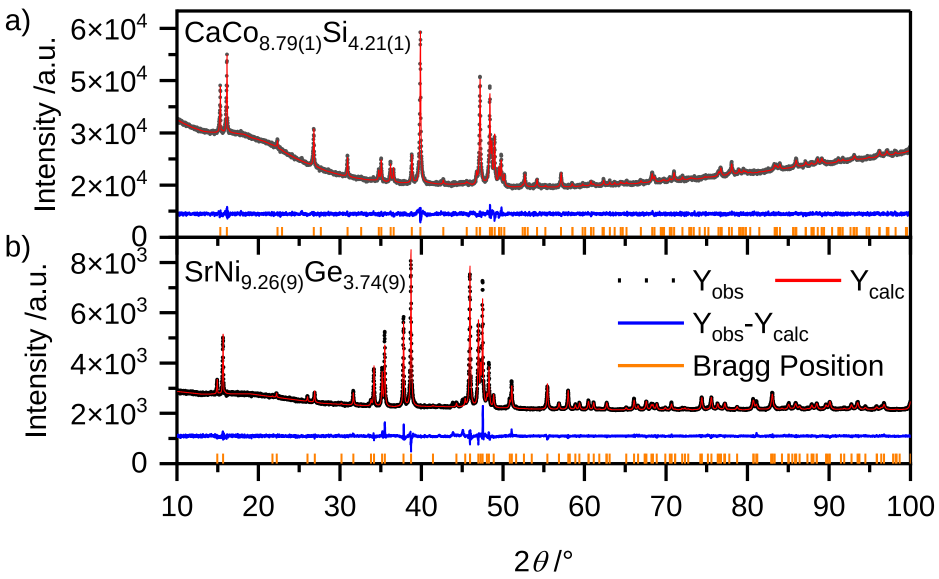

Figure 1 Rietveld refinement of powder X-ray diffraction data of a) $CaCo_{8.79(1)}Si_{4.21}$ or $SrNi_{9.26(9)}Ge_{3.74}$ measured with Cu-K$_{\alpha1}$ radiation.

2.3. Magnetic Measurements

Powdered samples were measured with MPMS XL5 SQUID magnetometer. 57 mg of $CaCo_{8.79(1)}Si_{4.21}$ were placed in a gelatin capsule and fixed within a plastic straw. Field dependent magnetization was recorded between −50 000 Oe and 50 000 Oe at 300 K and 2 K. Data were corrected for diamagnetic contributions of core electrons (Pascal's constants) and the sample holder.

2.4. Electronic Structure Calculations

Self-consistent Field calculations have been performed with Stuttgart-TB-LMTO-ASA software package, using the local density approximation (LDA) [23,24]. Linear muffin-tin orbitals (LMTOs) were created with the atomic sphere approximation (ASA). Radii of the spheres were determined after Jepsen and Andersen by blowing up until volume filling is reached within specified overlap [25,26]. Tight-binding model was used, constructing wave functions by superposition of wave functions from isolated atoms [27]. Inner shells are treated as soft-cores, higher quantum numbers down-folded [25] and all relativistic effects except spin-orbit coupling were included. The exchange-correlation term was parametrized after von Barth and Hedin [28] and density of states (DOS) calculated with tetrahedron method [29]. As basis set, following orbitals have been used: Ca: s, d and down-folded p, f; Sr: s, d and down-folded p, f; Ni and Co: s, p, d; Ge and Si: s, p and down-folded d.

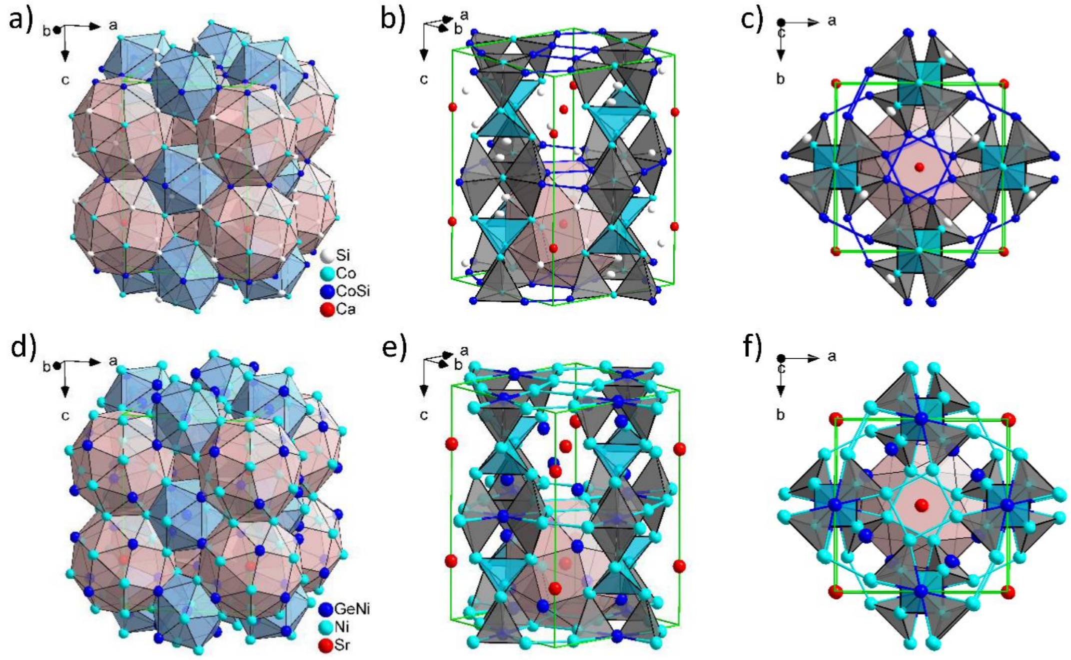

Figure 2 a) Crystal structure of $CaCo_{8.79(1)}Si_{4.21}$, Co3 occupies the 4*d* Wyckoff-position, centered in the blue icosahedra. Co2 shares a mixed 16*k*-position with 5.3% Si2, drawn in dark blue. Co1 and Si1 take independent 16*l*-sites. Calcium is coordinated by a 24-vertex snub cube, shown in red. The side (b) and top view (c) highlighting tetrahedral cobalt-cluster. Particularly short Co–Co-contacts are drawn in blue. d) Crystal structure of $SrNi_{9.26(8)}Ge_{3.74}$, Ni4 in the blue icosahedra is mixed with 13% Ge2, Ge1 position is mixed with 10% Ni1. Ni2 and Ni3 share fully-occupied 16*k* and 16*l* sites. e) and f) give side and top view with Ni-tetrahedra and particular short Ni–Ni-contacts. All atoms are drawn as displacement ellipsoids with 90% probability.

3. Results and Discussion

3.1. Crystal structure

$CaCo_{8.79(1)}Si_{4.21(1)}$ and $SrNi_{9.26(8)}Ge_{3.74(8)}$ both crystalize with tetragonal space group *I*4/mcm in a distorted, coloring variant of $NaZn_{13}$ [2,3]. This structure type is often reported as $Ce_2N_{17}Si_9$-type [11,12] or $LaFe_9Si_4$-type [5]. While the latter shows a fully ordered variant, the other is not stoichiometric and shows mixed occupancy on certain Wyckoff positions. It can also be rewritten as $CeNi_{9-x}Si_{4+x}$ and is derived from $LaFe_9Si_4$ [5]. The transition metal is substituted by additional tetrel atoms at the 16*k* layer for $x > 0$, while for $x < 0$ the transition metal atoms are mixed on the 16*l* site of tetrel element [6,30]. Our investigations follow this trend, as can be seen in Table 2. The additional mixed occupancy of $SrNi_{9.26(8)}Ge_{3.74(8)}$ on the 4*d* site has also been reported for isostructural compounds $BaCu_{8.45}Si_{4.54}$ [14] and $CeNi_{17}Si_9$ [11]. Interestingly, a theoretical investigation of possibly ordered stereoisomers in $LaFe_{13-x}Si_x$ ($1.0 \leq x \leq 5.0$) has shown a correlation between the number of short Si–Si-contacts and relative molecular orbital energy for $[Fe(Fe_{12-n}Si_n)]^{3-}$ clusters (n = 1, 2, 3, 4) [31]. Lowest energy was found for the smallest number of short Si–Si-contacts.

In the structure of AeT_9X_4 (Ae = alkaline earth, T = transition metal, X = tetrel element) the transition metal atom-centered icosahedra $T@T_{8-x}X_{4+x}$ are arranged in primitive cubic packing with the rare earth or alkaline earth atoms in the interstices. By distortion, a symmetry reduction from cubic $NaZn_{13}$ [2,3] to tetragonal $LaFe_9Si_4$-type [5] or orthorhombic $LaNi_7In_6$-type [13] occurs, caused by the substitution effect in these ternary compounds. Figure 2a illustrates the atomic arrangement in $CaCo_{8.79(1)}Si_{4.21}$, consisting of $Co@(Co_{7.79(1)}Si_{4.21})$ icosahedral units and calcium in between. The coordination sphere around calcium represents a snub cube with 24 vertices. Distances between central Ca and coordinating atoms are d(Ca–Co) = 3.1654(4), 3.3293(5) Å and d(Ca–Si) = 3.2468(4) Å. In polyanionic network, Co–Si-distances range from 2.3224(4) – 2.5620(4) Å, Co–Co-distances from 2.3192(4) – 2.8370(4) Å and d(Si–Si) = 2.8507(8) Å. The large silicon-silicon distance supports the hypothesis that close contacts are not favored by this structure [31]. This also explains why mixed occupancy is preferred on 16*k* position that has among cobalt position the largest distance to Si1. All other Co–Si-contacts are shorter than the sum of atomic radii [32,33], indicating covalent character. Figure 2b,e illustrates tetrahedral clusters build by cobalt contacts. Trigonal bipyramidal clusters are formed by sets face-sharing tetrahedra. Two of these clusters form units via shared basal vertex atom and the apical vertices form another tetrahedron with adjacent units. Each face is capped with a silicon atom, forming the *stella quadrangula* [34]. The Co2–Co2-distances of 2.3192(4) Å, connecting the apical vertices of adjacent units, are particularly short, which might be caused by smaller silicon atoms mixing on that position. Ca–Co- and Ca–Si-distances lie all between 3.1545(4) Å and 3.3293(4) Å, similar to that found in corresponding binary compounds. Interatomic distances in RCo_9Si_4-compounds (R = Ce, Gd, La, Nd, Pr, Sm, Tb, Y) with d(R–Co) = 3.14 – 3.32 Å, d(R–Si) = 3.22 – 3.26 Å, d(Co–Co) = 2.30 – 2.56 Å, d(Co–Si) = 2.30 – 2.58 Å and d(Si–Si) = 2.76 – 2.82 Å are very similar to those observed in Ca-compound, however, some Co–Co- and Si–Si-contacts in title compound are slightly larger, which is in agreement with the larger atomic size of calcium.

$SrNi_{9.26(8)}Ge_{3.74}$ (Figure 2d–f) crystallizes in a similar structure with minor differences. The Ni4 atoms centered in the icosahedra are partially substituted with germanium, whereas Ni2 and Ni3 are fully occupied and the Ge1 position is mixed with some additional nickel. The Sr–Ni-contacts of 3.2809(6) and 3.4203(6) Å, Sr–Ge of 3.3212(8) Å, Ge–Ni-distances between 2.403(1) – 2.594(1) Å are slightly shorter than the sum of atomic radii, analogue to the calcium cobalt silicide. The Ni–Ni-distance lie between 2.402(1) – 2.748(1) Å, shortest bonds of similar lengths are found within as well as between tetrahedral cobalt clusters, arranged in layers (Figure 2e,f). This is in contrast to the observation for the silicide and can be explained by the atomic radii, which are closer in number for nickel and germanium. The Ge–Ge-distances of 2.854(2) Å have similar lengths as in the silicon homolog. The Sr–Ni- and Sr–Ge-distances between 3.281(1) – 3.421(1) Å are slightly larger than the sum of atomic radii. *R*Ni_9Ge_4-compounds (R = Ce, Eu, Pr) show the *R*–Ni-distances between 3.24 – 3.38 Å, *R*–Ge-distances between 3.30 and 3.32 Å, Ni–Ni-distances between 2.28 – 2.72 Å, Ni–Ge-distances between 2.38 – 2.58 Å and Ge–Ge-distances between 2.80 – 2.85 Å, while the Ge–Ge distances are similar for Sr compound, some Ni–Ni-contacts are larger due to for larger strontium atoms.

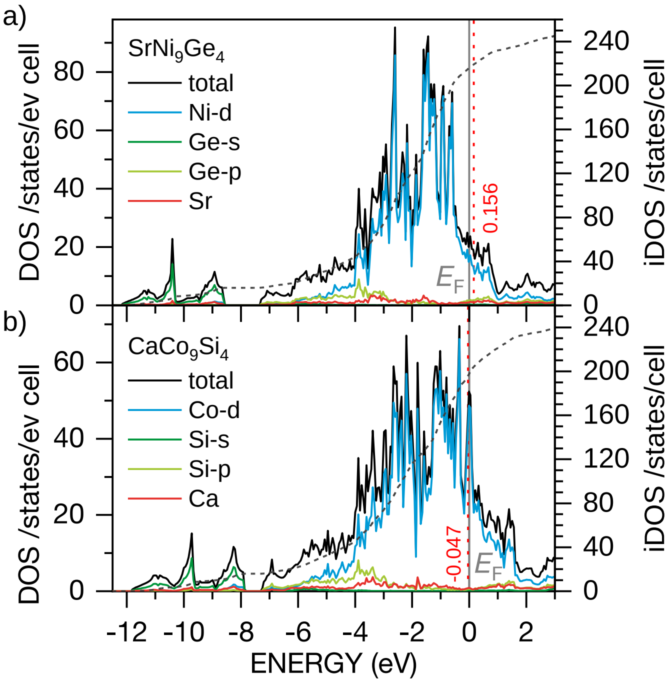

Figure 3 Density of States (DOS) and projected DOS for model structures a) $CaNi_9Ge_4$ and b) $SrNi_9Ge_4$. Integrated DOS is drawn as dashed line. With respect to the refined compositions $CaCo_{8.79(1)}Si_{4.21(1)}$ and $SrNi_{9.26(9)}Ge_{3.74(9)}$, the Fermi level is shifted by +0.156 eV and −0.047 eV, respectively.

3.2. Electronic Structure

Electronic properties of $CaCo_{8.79(1)}Si_{4.21}$ and $SrNi_{9.26(9)}Ge_{3.74}$ were theoretically investigated with TB-LMTO-ASA calculations assuming fully ordered $CaCo_9Si_4$ and $SrNi_9Ge_4$. Corresponding density of states (DOS) and projected DOS are given in Figure 3. $SrNi_9Ge_4$ consists of two blocks, one between −8.5 eV to −12.2 eV, containing primarily Ge-s states, and one large block starting from −7.3 eV. The second block contains mainly Ni-d states between −3 eV and the Fermi level. The lower part shows Ni-s states together with Ge-p and Sr. A similar situation results for $CaCo_9Ge_4$, where the Si-s-block is found between −7.9 eV and −12 eV, however, a sharp peak originated from Co-d states is located at the Fermi level. For both compounds no band gap is observed, indicating metallic behaviour. This is in agreement with investigations for isostructural homologues $BaCu_9Si_4$ [14] and ACo_9Si_4 (A = Y, Gd, Tb) [35]. Assuming the rigid band model, the Fermi level for the non-stoichiometric formulas have been determined via integrated DOS. $CaCo_{8.79(1)}Si_{4.21}$ shows a shift of −0.047 eV and $SrNi_{9.26(9)}Ge_{3.74}$ of +0.156 eV. A remarkable difference between the two compounds is the peak located at the Fermi level for $CaCo_{8.79(1)}Si_{4.21}$. This might indicate magnetic instability.

3.3. Magnetic Properties

Field-dependent measurements have been performed at 2 K and 300 K. The sample is ferromagnetic between 2 and 300 K with a small hysteresis. Magnetic saturation is reached at 1.2 μB per formula unit for 300 K and at 3.4 μB per formula unit for 2 K. This is in contrast to investigation on $LaCo_{13-x}Si_x$ ($3.8 < x < 4.1$) [9], were ferromagnetism was observed only for x smaller than 4, as additional silicon disturbs the order of the cobalt sublattice. For $x = 4$, paramagnetism was observed and attributed to cobalt, since lanthanum has no magnetic order. Atomic radii of lanthanum and calcium are similar in size, so the Co–Co-distances of both homologues are comparable as well (2.35 – 2.57 Å for $LaCo_9Si_5$, 2.32 – 2.59 Å for $CaCo_{8.79(1)}Si_{4.21}$), which does not explain the different behaviour. However, the electronic situation is different due to one additional electron of La. No superconductivity was found down to 2 K. As the sample is ferromagnetic over the full measured temperature range, no susceptibility was investigated.

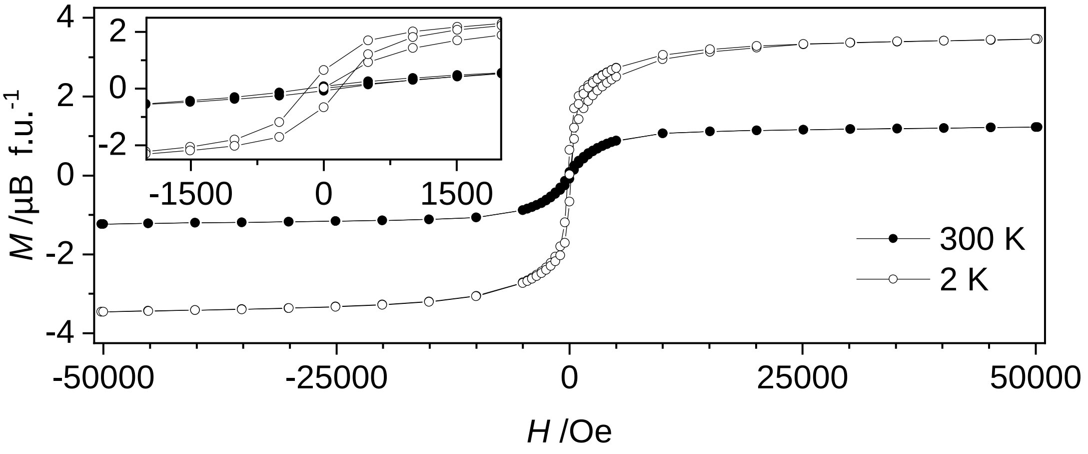

Figure 4 Magnetic measurements of $CaCo_{8.79(1)}Si_{4.21(1)}$ at 300 K and 2 K between −50 000 and 50 000 Oe. The sample showing small hysteresis and ferromagnetic saturation in the measured range.

4. Conclusion

$CaCo_{8.79(1)}Si_{4.21}$ and $SrNi_{9.26(9)}Ge_{3.74}$ crystalize with $Ce_2N_{17}Si_9$-type. They are the first alkaline earth metal containing cobalt silicide and nickel germanide with this structure. Single crystal refinements show that substitution is not randomly but occurs on specific Wyckoff positions. Electronic structure calculations with fully-ordered model structures show a peak for the cobalt silicide that is absent in nickel germanide. Density of states calculations show a sharp peak at the Fermi level of $CaCo_{8.79(1)}Si_{4.21}$, magnetic measurements show ferromagnetism up to 300 K. Detailed investigation of magnetic structure by neutron diffraction is subject for future investigation. Substitution with lanthanum could be promising to create magnetic transition between ferromagnetic and enhanced Pauli paramagnetic properties.

5. Acknowledgments

This research was financially supported by the German Research Foundation (Deutsche Forschungsgemeinschaft, DFG, Grant HL 62/3-1) and the TUM Graduate School.

6. References

[1] P. Villars, K. Cenzual, R. Gladyshevskii, S. Iwata, *Chem. Met. Alloys* **2018**, *11*, 43–76, https://doi.org/10.30970/cma11.0382.

[2] J.A.A. Ketelaar, *J. Chem. Phys.* **1937**, *5*, 668, https://doi.org/10.1063/1.1750098.

[3] E. Zintl, W. Haucke, *Z. Elektrochem. angew. phys. Chem.* **1938**, *44*, 104–111.

[4] Y. Prots, L. Vasylechko, W. Carrillo-Cabrera, C. Drathen, M. Coduri, D. Kaczorowski, U. Burkhardt, Y. Grin, *Dalton Trans.* **2018**, *47*, 12951–12963, https://doi.org/10.1039/c8dt02273a.

[5] W. Tang, J. Liang, X. Chen, G. Rao, *J. Appl. Phys. (Melville, NY, U. S.)* **1994**, *76*, 4095–4098, https://doi.org/10.1063/1.357359.

[6] M. Giovannini, M. Hadwig, R. Pasero, E. Bauer, G. Hilscher, M. Reissner, P. Rogl, H. Michor, *J. Phys. Condens. Matter.* **2010**, *22*, 135601, https://doi.org/10.1088/0953-8984/22/13/135601.

[7] Z.K. Heiba, M. El-Hagary, H. Michor, G. Hilscher, *Intermetallics* **2006**, *14*, 220–223, https://doi.org/10.1016/j.intermet.2005.05.009.

[8] M. El-Hagary, H. Michor, E. Bauer, R. Grössinger, P. Kerschl, D. Eckert, K.-H. Müller, P. Rogl, G. Giester, G. Hilscher, *Phys. B* **2005**, *359-361*, 311–313, https://doi.org/10.1016/j.physb.2005.01.117.

[9] M. El-Hagary, H. Michor, M. Wind, E. Bauer, G. Hilscher, P. Rogl, *J. Alloys Compd.* **2004**, *367*, 239–245, https://doi.org/10.1016/j.jallcom.2003.08.045.

[10] H. Michor, St. Berger, M. El-Hagary, C. Paul, E. Bauer, G. Hilscher, P. Rogl, G. Giester, *Phys. Rev. B, Condens. Matter* **2003**, *67*, https://doi.org/10.1103/PhysRevB.67.224428.

[11] O.I. Bodak, E.I. Gladyshevskii, *Inorg. Mater.* **1969**, *5*, 1754–1758.

[12] O. Moze, C.H. de Groot, F.R. de Boer, K. Buschow, *J. Alloys Compd.* **1996**, *235*, 62–65, https://doi.org/10.1016/0925-8388(95)02098-5.

[13] Y.M. Kalychak, V.I. Zaremba, Y.V. Galadzhun, K.Y. Miliyanchuk, R.-D. Hoffmann, R. Pöttgen, *Chem.* **2001**, *7*, 5343–5349, https://doi.org/10.1002/1521-3765(20011217)7:24<5343:AID-CHEM5343>3.0.CO;2-%23.

[14] C. Kranenberg, A. Mewis, *Z. Anorg. Allg. Chem.* **2003**, *629*, 1023–1026, https://doi.org/10.1002/zaac.200200451.

[15] X-Area, STOE & Cie GmbH, Darmstadt, Germany, 2015.

[16] X-RED32, STOE & Cie GmbH, Darmstadt, Germany, 2016.

[17] X-SHAPE, STOE & Cie GmbH, Darmstadt, Germany, 2015.

[18] G.M. Sheldrick, SHELXS-2014: Program for the Determination of Crystal Structure, University of Göttingen, Göttingen, Germany, 2014.

[19] G.M. Sheldrick, *Acta Crystallogr., Sect. A: Found. Crystallogr.* **2008**, *64*, 112–122, https://doi.org/10.1107/S0108767307043930.

[20] G.M. Sheldrick, SHELXL-2014: Program for Crystal Structure Refinement, University of Göttingen, Göttingen, Germany, 2014.

[21] G.M. Sheldrick, *Acta Crystallogr., Sect. C: Struct. Chem.* **2015**, *71*, 3–8, https://doi.org/10.1107/S2053229614024218.

[22] J. Rodriguez-Carvajal, FullProf: A Program for Rietveld Refinement and Pattern Matching Analysis. At the Satellite Meeting on Powder Diffraction of the XV IUCr Congress, Toulouse, France, 1990.

[23] R.W. Tank, O. Jepsen, O.K. Andersen, The STUTTGART TB-LMTO-ASA program, Stuttgart, 1998.

[24] M. van Schilfgarde, T.A. Paxton, O. Jepsen, O.K. Andersen, TB-LMTO-ASA, Stuttgart, Germany, 1994.

[25] O. Jepsen, O.K. Andersen, *Z. Phys. B: Condens. Matter* **1995**, *97*, 35–47, https://doi.org/10.1007/BF01317585.

[26] O.K. Andersen, O. Jepsen, *Phys. Rev. Lett.* **1984**, *53*, 2571–2574, https://doi.org/10.1103/PhysRevLett.53.2571.

[27] W.R.L. Lambrecht, O.K. Andersen, *Phys. Rev. B* **1986**, *34*, 2439–2449, https://doi.org/10.1103/PhysRevB.34.2439.

[28] U.v. Barth, L. Hedin, *J. Phys. C: Solid State Phys.* **1972**, *5*, 1629–1642, https://doi.org/10.1088/0022-3719/5/13/012.

[29] P.E. Blöchl, O. Jepsen, O.K. Andersen, *Phys. Rev. B, Condens. Matter* **1994**, *49*, 16223–16233, https://doi.org/10.1103/physrevb.49.16223.

[30] FIZ Karlsruhe, ICSD: Inorganic Crystal Structure Database, Leibniz Institute for Information Infrastructure, Karlsruhe, Germany, 2022.

[31] M.-K. Han, G.J. Miller, *Inorg. Chem.* **2008**, 515–528, https://doi.org/10.1021/ic701311b.

[32] L. Pauling, B. Kamb, *Proc. Natl. Acad. Sci. USA* **1986**, *83*, 3569–3571.

[33] J.C. Slater, *J. Chem. Phys.* **1964**, *41*, 3199–3204, https://doi.org/10.1063/1.1725697.

[34] H. Nyman, S. Andersson, *Acta Crystallogr., Sect. A: Cryst. Phys., Diffr., Theor. Gen. Crystallogr.* **1979**, *35*, 934–937, https://doi.org/10.1107/S0567739479002084.

[35] I.D. Shcherba, Y.K. Gorelenko, N.V. Nikolic, V.G. Sinyushko, M.M. Ristic, *J. Serb. Chem. Soc.* **1992**, *57*, 179.

5.9 Synthesis and Crystal Structure of *G*-Phases $Mg_6Co_{15.64(9)}Si_{7.36}$, $Mg_6Co_{16}Ge_7$ and Laves Phase $MgCo_{2-x}Ge_x$

Braun, T.; Schulz, A.; Hlukhyy, V.

Manuscript for publication

Synthesis and Crystal Structure of *G*-Phases $Mg_6Co_{15.64(9)}Si_{7.36}$, $Mg_6Co_{16}Ge_7$ and Laves Phase $MgCo_{2-x}Ge_x$

Thomas Braun, Annika Schulz, Viktor Hlukhyy[1]

Department of Chemistry, Technische Universität München, Lichtenbergstr. 4, 85747, Garching, Germany

Abstract

The family of *G*-phases has been extended by $Mg_6Co_{15.64(9)}Si_{7.36}$, $Mg_6Co_{16}Ge_7$ and new Laves phase $MgCo_{2-x}Ge_x$ was synthesized. All compounds were prepared from the elements via inductive heating. $Mg_6Co_{15.64(9)}Si_{7.36}$ with space group $Fm\bar{3}m$, a = 11.380(2) Å, V = 1473.9(7) Å^3, wR_2 = 3.8% (all data), 241 F^2 values, 15 variable parameters and $Mg_6Co_{16}Ge_7$ with s.g. $Fm\bar{3}m$, a = 11.603(1) Å, V = 1562.2(5) Å^3, wR_2 = 4.8% (all data), 217 F^2 values, 14 refineable parameters) crystallize in $Mg_6Cu_{16}Si_7$-type. The coloring variant of Th_6Mn_{23} contains magnesium octahedra and cobalt stella quadrangula in a germanium supertetrahedra. Laves phase $MgCo_{2-x}Ge_x$ for x = 0.37(2) with s.g. $P6_3/mcm$, a = 4.9490(7) Å, c = 7.992(2), V = 169.53(6) Å^3, wR_2 = 2.1% (all data), 161 F^2 values, 13 variable parameters and x = 0.46(7) with s.g. $P6_3/mcm$, a = 5.0163(7) Å, c = 7.854(2), V = 171.15(6) Å^3, wR_2 = 4.0% (all data), 161 F^2 values, 12 variable parameters crystallizes in $MgZn_2$-type. Mixed occupation is found on all Co-sites, however, the Kagomé-layer is preferred with a higher transition metal content and substitution first occurs in 6^3-net. Electronic structures of all compounds were calculated using TB-LMTO-ASA method to investigate band structure and density of states. For mixed sites an ideal occupation was assumed and true location of the Fermi level estimated by integrated density of states.

Keywords: Intermetallic compounds, G-Phase, Band Structure, Single Crystal

---

[1] Corresponding author.
E-mail address: viktor.hlukhyy@lrz.tum.de (V. Hlukhyy)

1. Introduction

$Mg_6Cu_{16}Si_7$ was first reported by Witte in 1938 [1], and its structure was characterized in more detail in 1956 by Bergman and Waugh [2,3]. In the same year, Beattle and Versnyder [4] investigated precipitates in the ferrite phase of austenitic stainless steel, which they named *G*-phases. They reported a cubic structure for several phases containing nickel, silicon and other transition metal elements, which turned out to be solid solutions and compounds with $Mg_6Cu_{16}Si_7$-type that is an ordering variant of that are an ordering variant of Th_6Mn_{23} [5]. About 100 compounds with the general formula $A_6T_{16-x}X_{7+x}$ with this structure type have been found up to date [6], commonly containing scandium, titanium or hafnium as element *A*, aluminum, nickel or gallium as metal *T* and silicon or germanium as tetrel *X*. However, there are also compounds with *A* = Na, Mg, Y, Dy, Ho, Er, Tm, Yb, Lu, U, Zr, V, Nb, Ta, Cr, Mn; *T* = Fe, Co, Cu, Zn, Cd, P and *X* = Al, As, Au, Co, Cu, Ir, Mn, Os, P, Pd, Pt, Rh, Ru. With respect to superconductivity, Holman et al. [7] have investigated the $A_6Ni_{16}Si_7$-family with *A* = (Mg, Sc, Ti, Nb and Ta). These compounds have been of interest since band-structure calculations showed a coexistence of flat and steep bands, which is a typical property of superconducting compounds [8]. Due to the structural flexibility towards different elements, the Fermi level can be shifted according to the rigid band model.

Another famous structural family are Laves phases, with simple binary composition AB_2 or pseudobinary solid solutions on the *B*-position. Even though they seem very simple, crystal structures vary from simple cubic or hexagonal arrangements to complex structures with different stacking. Most simple are $MgCu_2$, $MgZn_2$ and $MgNi_2$, which have been assigned *Strukturbericht* symbols C15, C14 and C36, respectively. They consist of alternating layers of (3.6.3.6) Kagomé-lattice and honeycomb nets (3^6). By combination of cubic and hexagonal stacking of these layers and/or coloring of certain Wyckoff-positions instead of random occupation, complicated structures can be derived [9]. This has been observed for compounds with stoichiometric composition such as Mg_2Cu_3Si [1], $Mg_2MnGa_{3[10]}$ or Y_2Rh_3Ge [11] as well as for non-stoichiometric solid solution $MgNi_{1.3}Ge_{0.7}$ [12]. As typical for intermetallics, a combination of sterical and electronic factors determine the atomic arrangement [13] and predictions are not reliable [14]. An influence of the valence electron concentration on the structure formation has been observed for solid solution $MgNi_{2-x}Ge_x$ by Siggelkow et al. [12].

In this work the homologues $Mg_6Co_{15.64(9)}Si_{7.36}$ and $Mg_6Co_{16}Ge_7$ were synthesized and investigated. $Mg_6Co_{15.64(9)}Si_{7.36}$ is the first ternary compound in the Mg–Co–Si. As secondary phase the Laves phase $MgCo_{2-x}Ge_x$ was identified and reproduced.

2. Experimental

$Mg_6Co_{15.64(9)}Si_{7.36}$ and $Mg_6Co_{16}Ge_7$ were prepared with 3.45% Mg-excess. Pieces of Mg (Alfa Aesar, 99.8%, granules), Co (Alfa Aesar, 99.9+%, cut from pieces) and Si (Wacker, 99.9+%, granules) or Ge (ChemPur, 99.5%, pieces) were sealed in niobium ampules and placed in an induction furnace. In a short reaction the mixture was heated to 1050 °C and after 5 min cooled to approximately 750 °C within 20 min, kept at that temperature for 20 min, then cooled to room temperature within 15 min. $MgCo_{2-x}Ge_x$ was prepared analogue to previously compounds with 15% magnesium excess and $x = 0.5, 0.75$. Products are stable in air and were crushed to extract single crystals or ground into powder.

Single crystals were selected with an optical microscope under air and fixed on a glass fiber with nail polish. Data were collected at room temperature with a STOE STADIVARI, using Genix 3D High Flux microfocus source (Mo-K_α, $\lambda = 0.71073$ Å), graded multilayer mirror monochromator and DECTRIS Pilatus 300K detector. HKL data were deduced with “X-Area” software package [15] and reflections scaled using Laue Analyzer “LANA” [16]. Structural models were created with direct methods by SHELXS- and refined with SHELXL-2014 [17–20] and full-matrix least squares on F_O^2. In order to check the composition, occupational parameters were refined in separate series of least-squares cycles. For $Mg_6Co_{16}Ge_7$ no mixed sites were observed and ideal occupation was assumed in the last refinement. $Mg_6Co_{15.64(9)}Si_{7.36}$ showed mixed occupation on 32*f* site and $MgCo_{2-x}Ge_x$ on 2*a*, 6*h*. Parameters obtained by refinement are given in Table 1 and Table 2. Interatomic distances are listed in Table 3.

Shape, size and elemental composition of single crystals were imaged by an HITACHI TM-1000 electron microscope (14 keV, high vacuum), equipped with a SWIFT-ED-TM (Oxford) energy dispersive X-ray (EDX) detector. The elemental composition could be confirmed for all single crystals.

Powder of the samples was fixed on a Scotch magic Tape and measured with a STOE Stadi P in transmission geometry. The device was equipped with Cu-$K_{\alpha1}$ source ($\lambda = 1.540598$ Å), DECTRIS MYTHEN 1K detector and curved Ge(111) monochromator. Empirical background correction has been performed and theoretical reflection data simulated with WinXPOW [21], presented in Figure 1. $Mg_6Co_{15.64(9)}Si_{7.36}$ has some CoSi as secondary phase and $Mg_6Co_{16}Ge_7$ contains the Laves phase $MgCo_{2-x}Ge_x$.

Table 1 Crystal data and structure refinement of $Mg_6Co_{15.64(9)}Si_{7.36}$ and $Mg_6Co_{16}Ge_7$ with $Mg_6Cu_{16}Si_7$-type and hexagonal Laves phase $MgCo_{2-x}Ge_x$ (x = 0.37(2), 0.46(2)) with $MgZn_2$-type.

compound	(I) $Mg_6Co_{15.64(9)}Si_{7.36}$	(II) $Mg_6Co_{16}Ge_7$	(III) $MgCo_{1.63(2)}Ge_{0.37}$	(IV) $MgCo_{1.54(7)}Ge_{0.46}$
formula weight (g mol^{-1})	1271.80	1596.87	147.16	147.16
temperature (K)	293	293	293	293
crystal system	cubic	cubic	Hexagonal	Hexagonal
space group	$Fm\bar{3}m$	$Fm\bar{3}m$	$P6_3/mmc$	$P6_3/mmc$
unit cell dimensions				
a (Å)	11.380(2)	11.603(1)	4.9490(7)	5.0163(7)
c (Å)	= a	= a	7.992(2)	7.854(2)
volume (Å^3)	1473.9(7)	1562.2(5)	169.53(6)	171.15(6)
Z	4	4	4	4
ρ_{calcd} (g cm^{-3})	5.73	6.79	5.77	5.76
μ (mm^{-1})	17.83	29.91	22.22	22.75
F(000)	2385	2912	271	273
crystal size (mm^3)	0.08×0.07×0.04	0.10×0.06×0.03	0.07x0.04x0.03	0.11x0.09x0.04
theta range for data collection (°)	3.10 – 37.4	3.04 – 34.8	4.8 – 34.0	4.7 – 34.0
index ranges in hkl	$-17 \leq h \leq 19$, $k \leq \pm 19$, $l \leq \pm 19$	$-18 \leq h \leq 17$, $k \leq \pm 18$, $-18 \leq l \leq 16$	$h \leq \pm 7$, $k \leq \pm 7$, $-12 \leq l \leq 11$	$h \leq \pm 7$, $-7 \leq k \leq 5$, $-8 \leq l \leq 12$
reflections collected	3592	5468	2767	1623
independent reflections	241 (R_{int} = 0.036)	217 (R_{int} = 0.035)	161 (R_{int} = 0.072)	161 (R_{int} = 0.071)
reflections with $I \geq 2\sigma(I)$	202 (R_{sigma} = 0.018)	199 (R_{sigma} = 0.009)	114 (R_{sigma} = 0.034)	113 (R_{sigma} = 0.053)
data/restraints/parameters	241/0/15	217/0/14	161/0/13	161/0/12
goodness-of-fit on F^2	1.06	1.23	0.81	0.87
final R indices ($I > 2\sigma(I)$)	R_1 = 0.017, wR_2 = 0.037	R_1 = 0.017, wR_2 = 0.046	R_1 = 0.015, wR_2 = 0.021	R_1 = 0.024, wR_2 = 0.039
R indices (all data)	R_1 = 0.027, wR_2 = 0.038	R_1 = 0.020, wR_2 = 0.048	R_1 = 0.030, wR_2 = 0.021	R_1 = 0.047, wR_2 = 0.040
extinction coefficient	—	—	0.0060(9)	—
largest diff. peak and hole (e·Å^{-3})	0.86, −0.82	1.16, −0.73	0.52, −0.46	0.87, −0.95

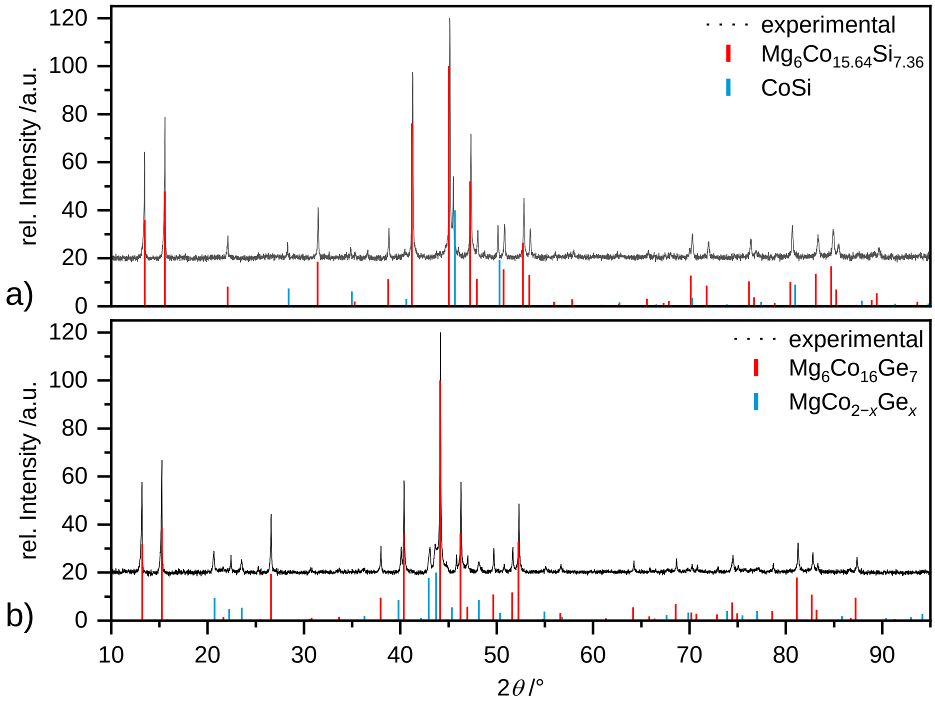

Figure 1 Powder X-ray diffractograms of $Mg_6Co_{16-x}X_{7+x}$. a) X = Si, x = 0.36 with CoSi secondary phase; b) X = Ge, x = 0 with Laves-phase $MgCo_{2-x}Ge_x$.

Table 2 Refined atomic coordinates and equivalent isotropic displacement parameter of $Mg_6Co_{15.64(9)}Si_{7.36}$, $Mg_6Co_{16}Ge_7$ and $MgCo_{2-x}Ge_x$ (x = 0.37(2), 0.46(2)).

Atom	Site	S.O.F.	x/a	y/b	z/c	U_{eq} a) /10^{-3} · Å^2
$Mg_6Co_{15.64(9)}Si_{7.36}$						
Mg	*24e*	1	0.2964(2)	0	0	10.2(3)
Co1	*32f*	1	0.11841(2)	0.11841(2)	0.11841(2)	8.2(1)
Co2/Si3	*32f*	0.945(6)/0.055	0.32713(3)	0.32713(3)	0.32713(3)	7.4(1)
Si1	*24d*	1	0	¼	¼	8.8(2)
Si2	*4a*	1	0	0	0	7.5(5)
$Mg_6Co_{16}Ge_7$						
Mg	*24e*	1	0.2967(2)	0	0	10.3(3)
Co1	*32f*	1	0.11924(2)	0.11924(2)	0.11924(2)	8.2(1)
Co2	*32f*	1	0.32615(3)	0.32615(3)	0.32615(3)	8.0(1)
Ge1	*24d*	1	0	¼	¼	8.2(1)
Ge2	*4a*	1	0	0	0	6.8(2)
$MgCo_{1.63(2)}Ge_{0.37}$						
Mg	*4f*	1	⅓	⅔	0.5643(2)	11.2(4)
Go1/Ge1	*6h*	0.85(2)/0.15	0.17111(7)	0.3422(1)	¼	9.5(2)
Co2/Ge2	*2a*	0.71(3)/0.29	0	0	0	10.0(3)
$MgCo_{1.54(7)}Ge_{0.46}$						
Mg	*4f*	1	⅓	⅔	0.5639(4)	14.4(8)
Go1/Ge1	*6h*	0.88(2)/0.12	0.1732(1)	0.3464(2)	¼	11.1(3)
Co2/Ge2	*2a*	0.55(3)/0.45	0	0	0	11.8(5)

a) U_{eq} is defined as one third of the trace of the orthogonalized *Uij* tensor.

Table 3 Atomic distances (in Å) and count in $Mg_6Co_{15.64(9)}Si_{7.36}$ and $Mg_6Co_{16}Ge_7$ with $Mg_6Cu_{16}Si_7$-type and hexagonal Laves phase $MgCo_{2-x}Ge_x$ ($x = 0.37, 0.46$) with $MgZn_2$-type.

$Mg_6Co_{15.64(9)}Si_{7.36}$				$Mg_6Co_{16}Ge_7$			
Mg	Mg	3.277(2)	4×	Mg	Mg1	3.336(2)	4×
	Co1	2.781(1)	4×		Co1	2.841(1)	4×
	Co2/Si3	2.8040(6)	4×		Co2	2.8733(6)	4×
	Si1	2.8938(6)	4×		Ge1	2.9510(5)	4×
Co1	Co1	2.6951(7)	3×	Co1	Co1	2.7672(7)	3×
	Co2/Si3	2.5319(6)	3×		Co2	2.5625(5)	3×
	Si1	2.5102(5)	3×		Ge1	2.5531(3)	3×
	Si2	2.3340(6)	1×		Ge2	2.3964(6)	1×
Co2/Si3	Co2/SI3	2.4828(9)	3×	Co2	Co2	2.4990(9)	3×
	Si1	2.3262(4)	3×		Ge1	2.3729(3)	3×
$MgCo_{2-x}Ge_x$		$x = 0.37(2)$		$x = 0.46(7)$			
Mg	Mg	2.968(2)	1×	2.923(5)	1×		
		3.0366(8)	3×	3.065(2)	3×		
	Go1/Ge1	2.871(2)	3×	2.831(3)	3×		
		2.8859(9)	6×	2.904(2)	6×		
	Co2/Ge2	2.9033(5)	3×	2.9388(6)	3×		
Co1/Ge1	Co1/Ge1	2.409(1)	2×	2.410(2)	2×		
		2.541(1)	2×	2.606(2)	2×		
	Co2/Ge2	2.4786(5)	2×	2.4737(7)	2×		

Self-consistent Field calculations have been performed with Stuttgart-TB-LMTO-ASA software package, using the local density approximation (LDA) [22,23]. Linear muffin-tin orbitals (LMTOs) were created with the atomic sphere approximation (ASA). Radii of the spheres were determined after Jepsen and Andersen by blowing up until volume filling is reached within specified overlap [24,25]. Tight-binding model was used, constructing wave functions by superposition of wave functions from isolated atoms [26]. Inner shells are treated as soft-cores, higher quantum numbers down-folded [24] and all relativistic effects except spin-orbit coupling were included. The exchange-correlation term was parametrized after von Barth and Hedin [27] and density of states (DOS) calculated with tetrahedron method [28]. As basis set, following orbitals have been used: Mg: s and down-folded p; Co: s, p, d; Ge and Si: s, p and down-folded d. Full occupied sites have been assumed on mixed positions. Integrated DOS has been compared with the number of electrons for different degree of substitution, to estimate the location of the Fermi level.

3. Results and Discussion

3.1. Crystal Structure

$Mg_6Co_{15.64(9)}Si_{7.36}$ (I) and $Mg_6Co_{16}Ge_7$ (II) crystallize with $Mg_6Cu_{16}Si_7$-type [2,3], illustrated in Figure 2. For *G*-phases known mixability [29] on the Co2 position could be observed in the silicide compound but not in the germanide. Cobalt atoms build clusters by forming a central tetrahedron with all four faces capped by another cobalt atom, the arrangement is known as stella quadrangular [30,31]. The vertex atoms are tetrahedrally coordinated by X-atoms (X = Si, Ge), resulting in larger Co_8X_{10}-supertetrahedra. Another way of description are vertex-sharing Co_4X_{10}-supertetrahedra with cobalt-tetrahedron in central octahedral void. These supertetrahedra form a highly symmetrical three-dimensional edge-sharing framework with large octahedral voids that are filled by magnesium-octahedra.

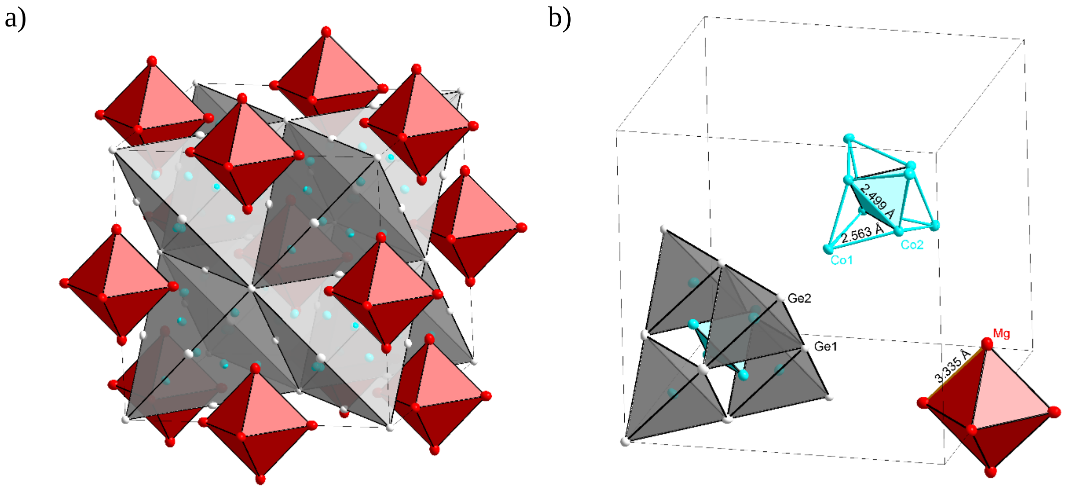

Figure 2 a) Crystal structure of $Mg_6Co_{16}Ge_7$ with isolated Mg_6-octahedra (red) and edge-sharing Co–Ge-supertetrahedra (grey). b) Stella quadrangula of Co-atoms (cyan), a tetrahedron with capped faces; Co-Ge-supertetrahedron with stella quad. in its center; magnesium octahedra with long interatomic distances. Co2-atoms are centered in grey Ge_4-tetrahedra. Atoms are drawn as ellipsoids with 90% probability; magnesium in red, cobalt in cyan and germanium in grey. In isostructural $Mg_6Co_{15.64(9)}Si_{7.36}$ mixed occupation is found on the Co2-site.

Shortest distances between Mg–Mg of 3.277(2) Å (I) or 3.336(2) Å (II), Mg–Co of 2.781(1) Å (I) or 2.841(1) Å (II) and Mg–X of 2.8938(6) (I) or 2.9510(5) (II) are slightly larger than the sum of elemental atomic radii [32]. Thus, magnesium makes no covalent bonded cluster in this structure, which is not surprising due to its low electronegativity and cationic character. Shortest Co–Co-contacts are 2.483(1) Å for (I) or 2.499(1) Å for (II), respectively. The Si–Si- and Ge–Ge closest contacts of 4.0236(5) Å (Si–Si) or 4.1024(3) Å (Ge–Ge) are too long for bonding interaction. They make contacts with cobalt of 2.3262(4)/2.3340(6)/2.4102(5) Å (I) or 2.3729(3)/2.3964(6)/2.5531(3) Å (II). Whereas shortest Co–X-distance indicate covalent interactions, the remaining correspond to the sum of atomic radii, suggesting more metallic bonding character.

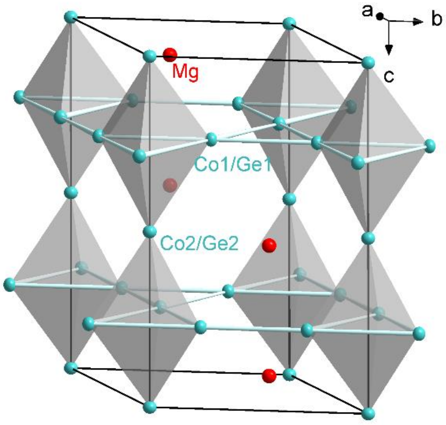

Figure 3 Crystal structure of Laves phase $MgCo_{2-x}Ge_x$ with mixed occupation on all Co-sites. Cobalt prefers to occupy Co1/Ge1, which forms a Kagomé-layer. Co2/Ge2 forms vertices of trigonal bipyramids.

Laves phases $MgCo_{2-x}Ge_x$ with $x = 0.37(2)$ (III) and $x = 0.46(7)$ (IV) both adopt $MgZn_2$-type (C14) with hexagonal AB stacking of Kagomé-nets (3.6.3.6) that are mixed occupied by Co1 and Ge1. Every second triangle in Kagomé-net is capped from both sides by Co2/Ge2 atoms, forming trigonal bipyramidal chains by face- and vertex-sharing of tetrahedra, as illustrated in Figure 3. For transition metal rich Laves phases, Kagomé-lattice positions are mostly occupied by the transition metal, and solid solution is preferred on the other atomic site, as has been observed also for other Laves-phases, e.g. $MgNi_{2-x}Ge_x$ [12] or $NbCr_{2-x}Co_x$ [33]. Within the Kagomé nets, shorter contacts are formed between basal atoms of trigonal bipyramids (2.409(1) Å (III), 2.410(2) Å (IV)), intermediate distances between basal and apical atoms (2.4786(5) (III), 2.4737(7) (IV)) and slightly longer in Kagomé-layer between bipyramids (2.541(1) Å (III), 2.606(2) Å (IV)). Magnesium atoms occupy voids above and below hexagons of Kagomé-hexagons, with Mg–Mg-distance of 2.968(2) Å (III), 2.923(5) Å (IV) being between those for MgCoGe (2.795 Å) [34] and $Mg_6Co_{16}Ge_7$ (3.336(2) Å). The new Laves phases are electronically and sterically very close to $MgNi_{2-x}Ge_x$ ($x = 0.5, 0.7$) [12]. However, while upon increasing degree of substitution x, a change from hexagonal $MgNi_2$-type (C36) over Cubic C15-type to Y_2Rh_3Ge-type and $MgNi_{1.3}Ge_{0.7}$-type were reported [12], no structural change was observed for $MgCo_{2-x}Ge_x$. The found Laves phases with $x = 0.37(2)$ and 0.46(7) adopt $MgZn_2$-type, just like $MgCo_2$ ($x = 0$). Therefore, reported structural dependency on valence electron concentration for nickel-compounds has not been observed for cobalt, even though $x = 0.46$ is very similar to Mg_2Ni_3Ge ($x = 0.5$).

Table 4 Interatomic distances (in Å) in intermetallic compounds MgCoGe [34], $MgCo_4Ge_6$ [35] and $MgCo_6Ge_6$ [36].

	MgCoGe	$MgCo_6Ge_6$	$MgCo_4Ge_6$
d(Mg–Mg)	3.516	–	–
d(Mg–Co)	2.795	3.188	2.894
d(Mg–Ge)	2.778 2.818	2.622 2.928	2.945
d(Co–Co)	2.755	2.535	2.581
d(Co–Ge)	2.405	2.425 2.430 2.627	2.284 2.371 2.419 2.470
d(Ge–Ge)	–	2.501 2.928	2.945 2.906

The only ternary Mg–Co–Ge compounds to compare with are MgCoGe [34], $MgCo_4Ge_6$ [35] and $MgCo_6Ge_6$ [36], listed in Table 4; distances of $Mg_6Co_{15.64(9)}Si_{7.36}$, $Mg_6Co_{16}Ge_7$ and $MgCo_{2-x}Ge_x$ are given in Table 3. Co–Co-bonding in $Mg_6Co_{16}Ge_7$ is the shortest within Mg–Co–Ge-compounds, except for $MgCo_{2-x}Ge_x$, where Co and Ge occupy mixed-positions. Shortest Co–Ge-contacts in $Mg_6Co_{16}Ge_7$ are larger than in $MgCo_4Ge_6$ and shorter than in MgCoGe, $MgCo_6Ge_6$ or $MgCo_{2-x}Ge_x$. The Mg–Ge-distances are similar to $MgCo_4Ge_6$ or $MgCo_{2-x}Ge_x$ and larger than for MgCoGe or $MgCo_6Ge_6$. Mg–Mg-octahedra in $Mg_6Co_{15.64(9)}Si_{7.36}$ or $Mg_6Co_{16}Ge_7$ show shorter distances than in MgCoGe. These octahedral units have been investigated for isostructural compounds with respect to possible guest atoms for $U_6Fe_{16}Si_7C$ [37,38], $Ti_6Ni_{16.7}Si_7$ [39], $Ti_6Ni_{17}Al_7$ [40] and for $Zr_6Sn_{23}Si$ [41], being a filled variant of parent structure type Th_6Mn_{23}. These compounds have additional transition metal, carbon or silicon in the octahedra, however they also observed isostructural compounds with empty octahedra. Whether there is a guest atom or not is indicated by the residual electron density on the 4*b* Wyckoff site, that should be about 16 electrons per Å^3 [39,41]. Largest residual densities given in Table 1 don't give reason for missed atoms in $Mg_6Co_{15.64(9)}Si_{7.36}$ and $Mg_6Co_{16}Ge_7$. Additionally, a solvent-stabilized empty magnesium-octahedron with comparable interatomic distances has been reported by Clegg et al. [42].

3.2. Electronical structure

LMTO-based calculations (Figure 4) have been performed for $Mg_6Co_{15.64(9)}Si_{7.36}$ (I) $Mg_6Co_{16}Ge_7$ (II) and $MgCo_{2-x}Ge_x$ Laves phase (III, IV). As no mixed occupancy was allowed, full occupation was assumed for (I). For the Laves phase, the structural model of an ordered variant was required. Due to similar atomic radii of $MgCo_{2-x}Ge_x$ to $MgNi_{2-x}Ge_x$ [12], ordered model of $MgNi_{1.3}Ge_{0.7}$ [12] was chosen. Lattice parameters of $MgCo_{1.54(7)}Ge_{0.46}$ ($x = 0.47$) and atomic coordinates have been adjusted to keep interatomic distances of the original structure, ideal occupation was assumed to get ordered Mg_2Co_3Ge ($x = 0.5$). The model represents a superstructure of $MgZn_2$, where cobalt occupies the Kagomé-layer and germanium the hexagonal layer.

All three compounds show typical band structure and DOS of polar intermetallics. A block between −8 and −12 eV with mainly Ge-s or Si-s character, separated by small gap. And a large block that crosses the Fermi level, indicating metallic properties. Magnesium and Si-p states contribute essentially at lower energies between −3 and −8 eV, whereas the region around the Fermi level is dominated by Co-d-states. For $Mg_6Co_{15.64(9)}Si_{7.36}$ and $MgCo_{1.54(7)}Ge_{0.46}$ the precise number of valence electrons have been matched with integrated DOS and corresponding lines drawn next to the Fermi level. Zoomed area near the Fermi level shows a narrow maximum close to E_F, followed by a larger block at lower energy and at higher energy by a more flat region with small pseudo-gap at 1 eV. This is in agreement with calculations for $Mg_6Ni_{16}Si_7$ [7], where energy is slightly shifted to higher energy due to additional Ni electrons and a coexistence of flat and steep bands was reported. In (I), the reduced number of electrons in iDOS matches a local DOS minimum, as can be seen in Figure 4a and explains the stability of the non-stoichiometric compound. The two Laves phases locate at two local maxima in Figure 4c, however the DOS corresponds to an ordered model whereas the found crystals showed a mixed occupation of Co/Ge-orbits.

4. Conclusion

$Mg_6Co_{15.64(9)}Si_{7.36}$ and $Mg_6Co_{16}Ge_7$ compounds crystallizing in $Mg_6Cu_{16}Si_7$-type, were identified and characterized. Mixed occupancy, typical for these *G*-phases was observed for the silicide but not for the germanide. The structure contains stella quadrangula composed of cobalt atoms, that are within germanium supertetrahedra. In the voids are octahedral Mg-clusters, which are not filled according to residual electron density but have a large interatomic distance. $MgCo_{2-x}Ge_x$ ($x = 0.37(2)$ and $x = 0.46(7)$) form $MgZn_2$-type (C14) Laves phase with Co–Ge-disorder. Calculated electronic structures show metallic behavior for all three compounds. No superconductivity was observed.

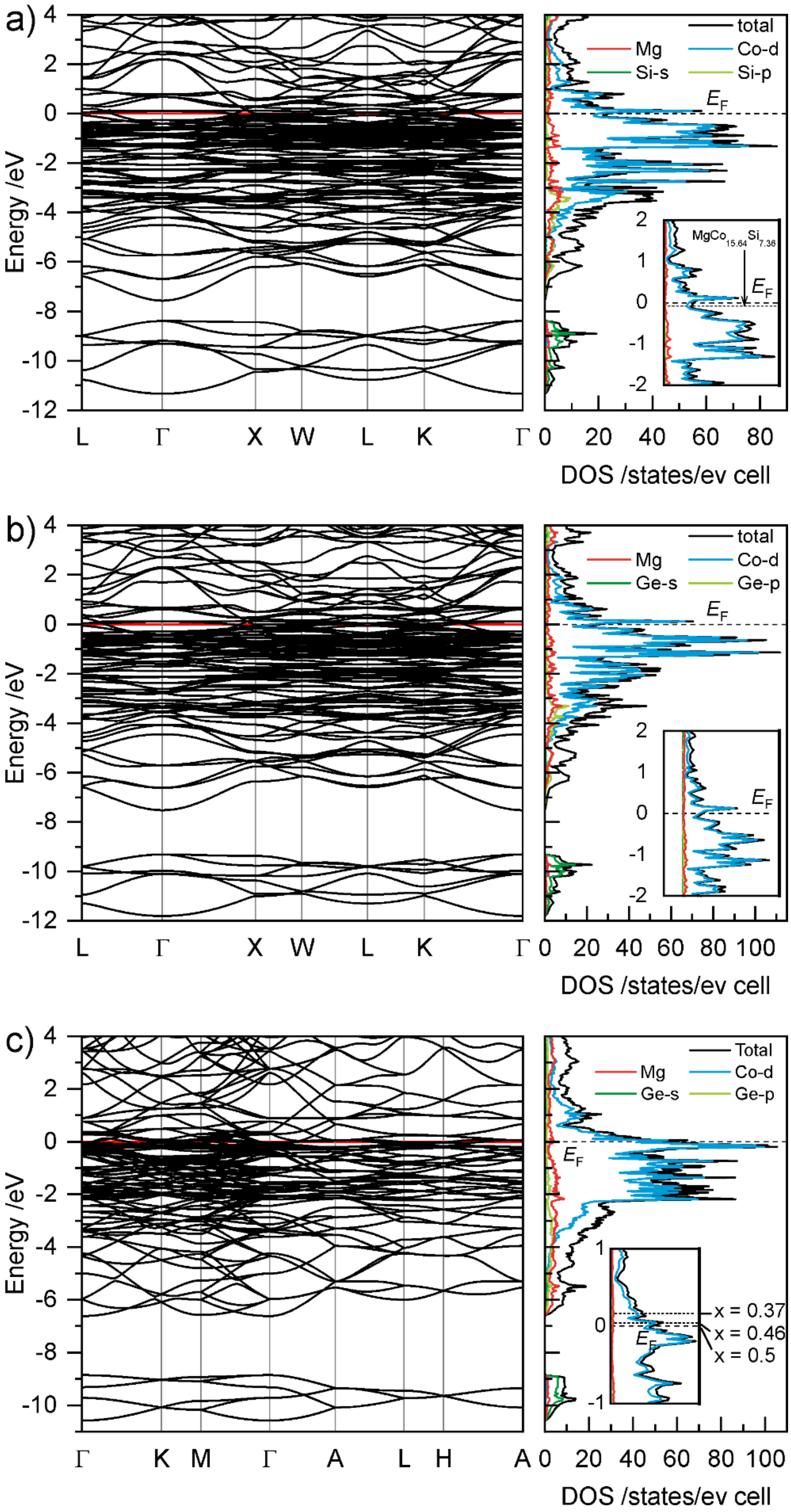

Figure 4 Band structure, projected and total density of states (DOS) calculated for a) Mg$_6$Co$_{16}$Si$_7$, b) Mg$_6$Co$_{16}$Ge$_7$ and c) MgCo$_{2-x}$Ge$_x$ for $x = 0.5$, using ordered structure of of MgNi$_{1.3}$Ge$_{0.7}$-type.[12] Insets show a zoomed view near the Fermi level E_F (dashed line) and shift of E_F (dotted lines) with electron count in solid solution, derived from integrated DOS.

5. Acknowledgments

This research was financially supported by the German Research Foundation (Deutsche Forschungsgemeinschaft, DFG, Grant HL 62/3-1) and the TUM Graduate School.

6. References

[1] H. Witte, *Z. Angew. Mineral.* **1938**, *1*, 255–268.

[2] G. Bergman, J.L.T. Waugh, *Acta Crystallogr.* **1953**, *6*, 93–94, https://doi.org/10.1107/S0365110X53000223.

[3] G. Bergman, J.L.T. Waugh, *Acta Crystallogr.* **1956**, *9*, 214–217, https://doi.org/10.1107/S0365110X56000632.

[4] H.J. Beattie, F.L. Versnyder, *Nature* **1956**, *178*, 208–209, https://doi.org/10.1038/178208b0.

[5] F.X. Spiegel, P.A. Beck, D. Bardos, *Trans. Metall. Soc. AIME* **1963**, *227*, 575.

[6] P. Villars, K. Cenzual, R. Gladyshevskii, S. Iwata, *Chem. Met. Alloys* **2018**, *11*, 43–76, https://doi.org/10.30970/cma11.0382.

[7] K.L. Holman, E. Morosan, P.A. Casey, L. Li, N.P. Ong, T. Klimczuk, C. Felser, R.J. Cava, *Mater. Res. Bull.* **2008**, *43*, 9–15, https://doi.org/10.1016/j.materresbull.2007.09.023.

[8] S. Deng, A. Simon, J. Köhler, *Solid State Sci.* **2000**, *2*, 31–38, https://doi.org/10.1016/S1293-2558(00)00105-9.

[9] Y. Komura, *Acta Crystallogr.* **1962**, *15*, 770–778, https://doi.org/10.1107/S0365110X62002017.

[10] N. Pavlyuk, I. Chumak, V. Pavlyuk, H. Ehrenberg, S. Indris, V. Hlukhyy, R. Pöttgen, Mg_2MnGa_3 – an orthorhombically distorted superstructure variant of the hexagonal Laves phase $MgZn_2$. to be submitted.

[11] K. Cenzual, B. Chabot, E. Parthé, *J. Solid State Chem.* **1987**, *70*, 229–234, https://doi.org/10.1016/0022-4596(87)90061-2.

[12] L. Siggelkow, V. Hlukhyy, T.F. Fässler, *Z. Anorg. Allg. Chem.* **2017**, *643*, 1424–1430, https://doi.org/10.1002/zaac.201700180.

[13] Y. Ohta, D.G. Pettifor, *J. Phys. Condens. Matter* **1990**, *2*, 8189–8194, https://doi.org/10.1088/0953-8984/2/41/006.

[14] B. Seiser, R. Drautz, D.G. Pettifor, *Acta Materialia* **2011**, *59*, 749–763, https://doi.org/10.1016/j.actamat.2010.10.013.

[15] X-Area, STOE & Cie GmbH, Darmstadt, Germany, 2015.

[16] LANA, STOE & Cie GmbH, Darmstadt, Germany, 2016.

[17] G.M. Sheldrick, *Acta Crystallogr., Sect. A: Found. Crystallogr.* **2008**, *64*, 112–122, https://doi.org/10.1107/S0108767307043930.

[18] G.M. Sheldrick, SHELXS-2014: Program for the Determination of Crystal Structure, University of Göttingen, Göttingen, Germany, 2014.

[19] G.M. Sheldrick, SHELXL-2014: Program for Crystal Structure Refinement, University of Göttingen, Göttingen, Germany, 2014.

[20] G.M. Sheldrick, *Acta Crystallogr., Sect. C: Struct. Chem.* **2015**, *71*, 3–8, https://doi.org/10.1107/S2053229614024218.

[21] WinXPOW, STOE & Cie GmbH, Darmstadt, Germany, 2011.

[22] R.W. Tank, O. Jepsen, O.K. Andersen, The STUTTGART TB-LMTO-ASA program, Stuttgart, 1998.

[23] M. van Schilfgarde, T.A. Paxton, O. Jepsen, O.K. Andersen, TB-LMTO-ASA, Stuttgart, Germany, 1994.

[24] O. Jepsen, O.K. Andersen, *Z. Phys. B: Condens. Matter* **1995**, *97*, 35–47, https://doi.org/10.1007/BF01317585.

[25] O.K. Andersen, O. Jepsen, *Phys. Rev. Lett.* **1984**, *53*, 2571–2574, https://doi.org/10.1103/PhysRevLett.53.2571.

[26] W.R.L. Lambrecht, O.K. Andersen, *Phys. Rev. B* **1986**, *34*, 2439–2449, https://doi.org/10.1103/PhysRevB.34.2439.

[27] U.v. Barth, L. Hedin, *J. Phys. C: Solid State Phys.* **1972**, *5*, 1629–1642, https://doi.org/10.1088/0022-3719/5/13/012.

[28] P.E. Blöchl, O. Jepsen, O.K. Andersen, *Phys. Rev. B, Condens. Matter* **1994**, *49*, 16223–16233, https://doi.org/10.1103/physrevb.49.16223.

[29] E. Ganglberger, H. Nowotny, F. Benesovsky, *Monatsh. Chem.* **1966**, *97*, 829–832, https://doi.org/10.1007/BF00932755.

[30] D. Johrendt, A. Mewis, *Z. Anorg. Allg. Chem.* **1992**, *618*, 30–34, https://doi.org/10.1002/zaac.19926180106.

[31] H. Nyman, S. Andersson, *Acta Crystallogr., Sect. A: Cryst. Phys., Diffr., Theor. Gen. Crystallogr.* **1979**, *35*, 934–937, https://doi.org/10.1107/S0567739479002084.

[32] J.C. Slater, *J. Chem. Phys.* **1964**, *41*, 3199–3204, https://doi.org/10.1063/1.1725697.

[33] A. Kerkau, D. Grüner, A. Ormeci, Y. Prots, H. Borrmann, W. Schnelle, E. Bischoff, Y. Grin, G. Kreiner, *Z. Anorg. Allg. Chem.* **2009**, *635*, 637–648, https://doi.org/10.1002/zaac.200801411.

[34] V. Hlukhyy, N. Chumalo, V. Zaremba, T.F. Fässler, *Z. Anorg. Allg. Chem.* **2008**, *634*, 1249–1255, https://doi.org/10.1002/zaac.200700534.

[35] C. Gieck, M. Schreyer, T.F. Fässler, F. Raif, P. Claus, *Eur. J. Inorg. Chem.* **2006**, *2006*, 3482–3488, https://doi.org/10.1002/ejic.200600298.

[36] C. Gieck, M. Schreyer, T.F. Fässler, S. Cavet, P. Claus, *Chem. Eur. J.* **2006**, *12*, 1924–1930, https://doi.org/10.1002/chem.200500411.

[37] D. Berthebaud, O. Tougait, M. Potel, E.B. Lopes, A.P. Gonçalves, H. Noël, *J. Solid State Chem.* **2007**, *180,* 2926–2932, https://doi.org/10.1016/j.jssc.2007.07.030.

[38] P. Qian, Q.-Y. Hu, J. Shen, *J. Solid State Chem.* **2009**, *182*, 3289–3293, https://doi.org/10.1016/j.jssc.2009.09.023.

[39] A. Grytsiv, X.-Q. Chen, P. Rogl, R. Podloucky, H. Schmidt, G. Giester, V. Pomjakushin, *J. Solid State Chem.* **2007**, *180,* 733–741, https://doi.org/10.1016/j.jssc.2006.11.031.

[40] A. Grytsiv, J.J. Ding, P. Rogl, F. Weill, B. Chevalier, J. Etourneau, G. André, F. Bourée, H. Noël, P. Hundegger, G. Wiesinger, *Intermetallics* **2003**, *11,* 351–359, https://doi.org/10.1016/S0966-9795(02)00267-4.

[41] X. Chen, W. Jeitschko, M.H. Gerdes, *J. Alloys Compd.* **1996**, *234*, 12–18, https://doi.org/10.1016/0925-8388(95)01967-7.

[42] W. Clegg, M. Frank, R.E. Mulvey, P.A. O'Neil, *J. Chem. Soc., Chem. Commun.* **1994**, 97–98, https://doi.org/10.1039/c39940000097.

6 Complete List of Publications and Manuscripts

Peer-reviewed manuscripts

$SrNi_2Si$ and $BaNi_2Si$ – New Layered Silicides with Fused Nickel Six-membered Rings in a Boat Conformation
T. Braun, S. Zeitz, V. Hlukhyy, *Z. Anorg. Allg. Chem.* **645**, 388–395 (2019),
DOI: 10.1002/zaac.201800500

$CaFe_2Ge_2$ with square-planar iron layers – Closing a gap in the row of CaT_2Ge_2 (T = Mn–Zn)
T. Braun, V. Hlukhyy, *J. of Solid State Chem.* **276**, 368–375 (2019),
DOI: 10.1016/j.jssc.2019.05.032

Structural Order-Disorder in $CaFe_6Ge_6$ and $Ca_{1-x}Co_6Ge_6$
T. Braun, V. Hlukhyy, *J. of Solid State Chem.* **in press**, 123742 (2022),
DOI: 10.1016/j.jssc.2022.123742

An Intermetallic $CaFe_6Ge_6$ Approach to Unprecedented Ca–Fe–O Electrocatalyst for Efficient Alkaline Oxygen Evolution Reaction
H. Yang, J. N. Hausmann, V. Hlukhyy, T. Braun, K. Laun, I. Zebger, M. Driess and P. W. Menezes, ChemCatChem, 14, e202200293 (2022), DOI: 10.1002/cctc.202200293

Manuscripts prepared for publication

Trends in $ThCr_2Si_2$-Type Tetrelides with Iron, Cobalt or Nickel—Disorder and Distortion
T. Braun, V. Hlukhyy, manuscript for publication

SrNiSi with two Different Stacking Variants—An Electron Deficient Zintl-Phase
T. Braun, V. Hlukhyy, manuscript for publication

$SrNi_5Si_3$—First Tetrelide with $LaCo_5P_3$-Type Structure
T. Braun, V. Hlukhyy, manuscript for publication

Alkaline Earth Metal Poorest Ordered Compound $BaNi_{16}Si_{12}$ with Catalan Pentakis Dodecahedra—A New Record for Coordination Number
T. Braun, D. Henseler, V. Hlukhyy, manuscript for publication

Synthesis and Crystal Structure of $CaCo_{8.79(1)}Si_{4.21}$ and $SrNi_{9.26(8)}Ge_{3.74}$ with $Ce_2Ni_{17}Si_9$-type
T. Braun, V. Hlukhyy, manuscript for publication

Synthesis and Crystal Structure of G-Phases $Mg_6Co_{15.64(9)}Si_{7.36}$, $Mg_6Co_{16}Ge_7$ and Laves Phase $MgCo_{2-x}Ge_x$
T. Braun, A. Schulz, V. Hlukhyy, manuscript for publication

Conference Contribution

$SrNi_2Si$ and $BaNi_2Si$ – new layered nickel silicides with corrugated Ni-6^3 net
T. Braun, V. Hlukhyy, *19. Vortragstagung für Anorganische Chemie der Fachgruppen Wöhler-Vereinigung und Festkörperchemie und Materialforschung*, Regensburg, Germany, September 24th-27th 2018 (P-127 poster, abstract)

$CaFe_2Ge_2$ – a Substitution Variant of the Superconducting Iron Arsenide $CaFe_2As_2$
T. Braun, V. Hlukhyy, *19. Vortragstagung für Anorganische Chemie der Fachgruppen Wöhler-Vereinigung und Festkörperchemie und Materialforschung*, Regensburg, Germany, September 24th-27th 2018 (P-233 poster, abstract)

New Nickel Silicides
T. Braun, V. Hlukhyy, *XIV International Conference on Crystal Chemistry of Intermetallic Compounds*, Lviv, Ukraine, September 22th -26th 2019 (O7 abstract)

New $NaZn_{13}$-Type Related Cobalt Silicide and Germanides: Syntheses, Structures and Properties
T. Braun, V. Hlukhyy, *17th European Conference on Solid State Chemistry*, Lille, France, September 1st – 4th 2019 (C17 abstract)